Friction drag reduction by a perforated plate

by

Van Thuan Hoang

A thesis submitted in total fulfillment for the
degree of Doctor of Philosophy

in the
School of Electrical and Mechanical Engineering
The University of Adelaide
South Australia, 5005

February 2025

Abstract

Turbulence control in wall-bounded flows has gained considerable attention from many researchers. It has the potential to reduce energy consumption in various engineering applications, such as airplanes and cars by reducing skin friction drag. As a result, carbon dioxide (CO_2) emissions from these applications are reduced. The generation of friction drag is directly linked to turbulent coherent structures. Coherent structures, like streamwise vortices and streaks, contribute to turbulent momentum transfer and shear stresses. Streamwise vortices, particularly those exhibiting both ejection and sweep events, dominate these coherent structures in the near-wall region of turbulent boundary layers, causing burst events which are the major contributors to turbulence generation and skin friction drag in turbulent boundary layers.

This project aims to develop an understanding of the mechanisms of drag reduction in turbulent boundary layers due to a perforated plate with a backing cavity. As a passive device, it does not require external energy input and is simpler to install than an active device. The turbulent boundary layer over a perforated plate with a backing cavity has been simulated in a wind tunnel. The flow field was measured by hot-wire anemometry, which was then analysed by a variable-interval time-averaging (VITA) technique, Fourier transformation, and Fourier decomposition. The modification of the near-wall region, the interaction between small and large scales, the turbulence energy spectrum, and the turbulence generation of the turbulent boundary layers were estimated to evaluate if a perforated plate with a backing cavity can decrease the skin friction drag of a fully formed boundary layer.

To develop an understanding of the effect of the perforated plate with a backing cavity on the turbulent characteristics of a turbulent boundary layer, the modification of near-wall turbulence was first investigated using hot-wire measurements. The perforated plate was tested in a low Reynolds number wind tunnel at the University of Adelaide in two flow conditions at momentum-thickness-based Reynolds numbers of 1165 and 2294, which correspond to the viscous-scaled cavity volumes of 2.6×10^6 and 11.5×10^6. Their experiments found a reduction of up to 9% in burst intensity and a decrease of approximately 33.5% in burst frequency within the near-wall region at an viscous-scaled wall-normal location below 30, indicating that the perforated plate weakened burst events in this region. Additionally, the perforated plate transferred turbulence energy away from the wall. Consequently, there was a reduction of up to approximately 9% in turbulence intensity near the wall, contributing to a reduction of 8.7% in local skin friction drag.

After determining the effect of the perforated plate on the near-wall region of turbulent boundary layers, the impact of the perforated plate on the interaction between large-scale motions primarily located in the log region and small-scale motions in the near-wall region of the boundary layer was investigated. The perforated plate was tested at momentum-thickness-based Reynolds numbers from 1165 to 3002, using hot-wire measurements. As a result, the viscous-scaled cavity volume increased from 2.6×10^6 to 27.8×10^6. The results showed that the perforated plate strengthened the large-scale amplitude modulation of small scales. An increase in the viscous-scaled cavity volume increases the large-scale amplitude modulation of the small scales. Consequently, the location where the amplitude modulation is zero moves further away from the wall. The increase in the amplitude modulation is associated with reducing skin friction drag in the turbulent boundary layers over the perforated plate.

The interaction between the backing cavity and the turbulent boundary layer generates unsteady wall-normal velocities through the perforated plate. It is hypothesised that the reduction in turbulence energy and skin friction in the turbulent boundary layers is contributed by the wall-normal velocities. To develop an understanding of the effect of wall-normal velocities through a perforated plate on turbulent boundary layers, a synthetic jet actuator was used to manipulate the turbulent boundary layers. The effect of jet frequency and amplitude on turbulent boundary layers is investigated. Different jet characteristics including an viscous-scaled forcing frequency from 0.025 to 0.063 at two inner-scale amplitudes of 2.23 and 4.47 were considered to manipulate a turbulent boundary layer at a momentum-thickness-based Reynolds number of 1050. The results demonstrate a reduction of up to 5% in burst intensities and a decrease of approximately 20% in burst durations within the near-wall region at viscous-scaled wall-normal locations below 12, indicating that synthetic jets lifted turbulent energy and weakened burst events in this region. Consequently, there was a reduction of up to approximately 12.5% in turbulence intensity near the wall, contributing to diminished shear stresses and local skin-friction drag. Furthermore, the synthetic jets generated a displacement of the inner peak of turbulent energy away from the wall, indicating that the synthetic jets shifted turbulent energy away from the wall. As the jet frequency or amplitude increased, the modification of the boundary layer became more pronounced. These findings show that the wall-normal velocities through the perforated plate can be used to manipulate the turbulent energy in turbulent boundary layers, which supports the hypothesis about the effects of the the wall-normal velocities on the reduction in turbulence energy and skin friction in the turbulent boundary layers.

The interaction between the wall-normal velocities and the pressure at the wall can lead to suppression of the near-wall cycles as well as friction drag. This interaction is represented by wall impdeance of the perforated plate. To understand the impact of the wall impdeance on the near-wall turbulence, different wall impedances generated by a perforated plate with a backing cavity were used to control turbulent boundary layers. Acoustic impedance was varied by the use of a perforated plate with a backing cavity, providing normalised specific acoustic reactance from 5.5 to 69.6 at the angle of the acoustic impedance of approximately $0.25 \times (2\pi)$. The correlation between the wall impedance and the modification of the burst events, turbulence intensity, and turbulence energy of the turbulent boundary layers with the wall impedance also was discussed. The findings indicate that the acoustic impedance of the perforated plate with a backing cavity has a correlation with near-wall turbulence. When the normalised specific acoustic reactance increases, the turbulence intensity in the near-wall region reduces. A maximum reduction of about 7.8% in sweep intensity and 7% in ejection intensity within the near-wall region was observed at a normalised specific acoustic reactance of 69.6. These are associated with a reduction of about 7% in the turbulence intensity in the near-wall region and about 8% in the estimated local friction drag. This indicates that the perforated suppressed the near-wall cycles and consequently reduced the near-wall turbulence. An increase in the normalised specific acoustic impedance affects the relationship between the wall-normal velocities and the pressure at the wall in a way that the wall-normal velocities lift the turbulence kinematic energy further from the wall. These wall-normal velocities also suppress the near-wall cycles by weakening sweep and ejection events in the near-wall region. As a result, friction drag, shear stress in the near-wall area, and turbulence intensity are all decreased.

This research provides an improved understanding of the interaction between a perforated plate and turbulent boundary layers for skin drag reduction. The findings show a correlation between friction drag reduction and the acoustic impedance of the perforated plate. When the normalised specific acoustic reactance of the perforated plate increases, the friction drag reduction to become more pronounced. This evidences that the wall-normal velocities interact with the pressure at the wall in a way that suppresses the near-wall cycles and reduces friction drag. The findings provide recommendations for designing perforated plates with a backing cavity with to generate preferable acoustic impedance to achieve friction drag. Furthermore, the presented research shows the potential of perforated plates to reduce turbulence intensity and skin friction drag in turbulent boundary layers. A reduction of 9% in turbulence intensity near the wall and 8.7% in local skin friction drag were found in the turbulent boundary layers over the perforated plate at the momentum-thickness-based Reynolds number of 2294. The findings highlight that the perforated plate weakens burst events in the near-wall region, which consequently reduces near-wall turbulence, shear stresses near the wall, and friction drag. The perforated plate also increases turbulence energy in the logarithmic region. As a result, the amplitude modulation of the near-wall region small scale by the large scales increases, which contributes to friction drag reduction. These effects of the perforated plate on turbulent boundary layers could result from the wall-normal velocities exchange of the flow inside and outside the backing cavity. A larger backing cavity would dampen kinetic energy more effectively. As a result, an increase in the backing cavity volume is associated with a decrease in the local skin friction drag in the turbulent boundary layers over the perforated plate. The results of this research show the potential of perforated plates for turbulent boundary layer control, which suggests a need for further investigation into the flow inside the backing cavity in the future.

Declaration

I certify that this work contains no material which has been accepted for the award of any other degree or diploma in my name, in any university or other tertiary institution and, to the best of my knowledge and belief, contains no material previously published or written by another person, except where due reference has been made in the text. In addition, I certify that no part of this work will, in the future, be used in a submission in my name, for any other degree or diploma in any university or other tertiary institution without the prior approval of the University of Adelaide and where applicable, any partner institution responsible for the joint-award of this degree.

I acknowledge that copyright of published works contained within this thesis resides with the copyright holder(s) of those works.

I also give permission for the digital version of my thesis to be made available on the web, via the University's digital research repository, the Library Search and also through web search engines, unless permission has been granted by the University to restrict access for a period of time.

I acknowledge the support I have received for my research through the provision of an Australian Government Research Training Program Scholarship.

Signed: ____________________

Name: Van Thuan Hoang

Date: 19/11/2024

Acknowledgements

I would like to thank my principal supervisor, Prof. Maziar Arjomandi, for his unwavering support, relentless encouragement, and invaluable guidance throughout the past three years. I truly appreciate the support of my co-supervisors, Prof. Ben Cazzolato and Dr. Azadeh Jafari. I have learned a lot from you all, and I am very grateful for your insightful supervision without which this thesis would not have been completed. I would also like to thank Dr. Anton Silvestri for his support. I really appreciate the time and effort that you all put into my work.

I would also like to thank the support provided by the technical staff of the Mechanical and Electronic workshops, particularly Phil Schmidt, Thomas Stanef, and Marc Simpson for helping me with the design and manufacturing of my experimental rigs. I would like to thank Marc Simpson for his kind support and help when carrying out my experimental testing at the Thebarton wind tunnel.

I am thankful for the support of the staff of the Adelaide Graduate Research School, especially Dr. Doreen Krumbiegel, Antoinette Brincat, and Mel Lewis. I very much appreciate Dr. Krumbiegel's help with my travel exemption application, allowing me to come to Australia to continue my Ph.D. program during COVID-19 in 2021.

To my family, thank you for your never-ending support. To my father, my mother, my beloved sisters, and my brothers, who have always been my best friends. To my wife, Hang, and my children, Anh and Charles, who have been by my side throughout this journey. Thank you for your unlimited support and encouragement, and for helping me get through difficult times. Thank you for sharing any moment with me. I am extremely grateful for having you in my life at any given time. It would not have been possible to accomplish this without you.

Also, to my friends, thank you for your encouragement and all the good times that we spent together, which were always refreshing throughout the journey of the Ph.D., specifically to Dr. Alison-Jane Hunter. I received a significant amount of help from Dr. Hunter in improving my academic writing. She also shared with me a lot of experience from both studying and living in Australia.

Finally, I would like to acknowledge the financial support I have received for my research through the provision of an Australian Government Research Training Program Scholarship through the University of Adelaide.

Contents

Abstract **i**

Declaration **v**

Acknowledgements **vii**

Contents **ix**

Publications **xi**

Chapter 1: Introduction **1**

- 1.1 Background . . . 1
- 1.2 Aims and objectives . . . 3
- 1.3 Thesis outline . . . 5
- 1.4 Thesis format . . . 8
- References . . . 8

Chapter 2: Literature review **11**

- 2.1 Turbulent boundary layers . . . 11
  - 2.1.1 Near-wall region . . . 13
  - 2.1.2 Outer region . . . 17
  - 2.1.3 Outer region . . . 19
- 2.2 Turbulent boundary layer control . . . 19
  - 2.2.1 Active control . . . 19
    - Opposition control . . . 20
    - Synthetic jet control . . . 21
  - 2.2.2 Passive control . . . 23
    - Riblets . . . 23
    - Permeable surface . . . 25
    - Helmholtz resonators . . . 28
- 2.3 Turbulent boundary layers over a perforated surface . . . 30
  - 2.3.1 Perforated plates . . . 30
  - 2.3.2 Acoustic liners . . . 38
- 2.4 Conclusion of literature and research gaps . . . 43
- References . . . 45

Chapter 3: Near-wall turbulence over a perforated plate **57**

- 3.1 Chapter overview . . . 57
- 3.2 Statement of Authorship . . . 59

3.3 Modification of near-wall turbulence in turbulent boundary layers due to a perforated structure 60

Chapter 4: Turbulent scales in turbulent boundary layers over a perforated plate 97

4.1 Chapter overview 97
4.2 Statement of Authorship 99
4.3 Impacts of a perforated plate on large-scale amplitude modulation in turbulent boundary layers 100

Chapter 5: Wall-normal velocities through a perforated plate 125

5.1 Chapter overview 125
5.2 Statement of Authorship 127
5.3 Modification of burst events in the near-wall region of turbulent boundary layers by synthetic jets 128

Chapter 6: Acoustic impedance of a perforated plate 147

6.1 Chapter overview 147
6.2 Statement of Authorship 149
6.3 Impacts of acoustic impedance of a perforated plate on near-wall turbulence 150

Chapter 7: Conclusions and future work 167

7.1 Near-wall turbulence in the turbulence boundary layers over the perforated plate 168
7.2 Interection between small and large scales in the turbulent boundary layers over a perforated plate 169
7.3 Wall-normal velocities through the perforated plate 170
7.4 Acoustic impedance of the perforated plate 171
7.5 Recommendations for future work 172

Publications

Based on the research in this thesis, four journal manuscripts and three peer-reviewed conference papers have been published as follows:

Journal papers

- Hoang, V. T., Jafari, A., Cazzolato, B., and Arjomandi, M. (2024). Modification of near-wall turbulence in turbulent boundary layers due to a perforated structure. *Physics of Fluids*, 36, 075173. (Published).
- Hoang, V. T., Jafari, A., Cazzolato, B., and Arjomandi, M. (2025). Impacts of a perforated plate on large-scale amplitude modulation in turbulent boundary layers. *Journal of Fluid Mechanics.* (Submitted).
- Hoang, V. T., Jafari, A., Cazzolato, B., and Arjomandi, M. (2024). Modification of burst events in the near-wall region of turbulent boundary layers by synthetic jets. *International Journal of Heat and Fluid Flow*, 112, 109728. (Published).
- Hoang, V. T., Jafari, A., Cazzolato, B., and Arjomandi, M. (2025). Impacts of acoustic impedance of a perforated plate on near-wall turbulence. *Physics of Fluids*, 37, 025102. (Published).

Refereed conference papers

- Hoang, V. T., Jafari, A., Silvestri, A., Cazzolato, B., and Arjomandi, M. (2021). The effect of a micro-cavity array on burst events in a turbulent boundary layer. *ETMM13 conference proceedings.* Hybrid Event in Rhodes, Greece. (Published).

- Hoang, V. T., Jafari, A., Cazzolato, B., and Arjomandi, M. (2022). An improved method for estimation of skin friction in turbulent boundary layers. *The 23rd Australasian Fluid Mechanics Conference*. Sydney, Australia. (Published).
- Hoang, V. T., Jafari, A., Cazzolato, B., and Arjomandi, M. (2024). Attenuation of near-wall turbulence in turbulent boundary layers over a perforated surface. *The 24th Australasian Fluid Mechanics Conference*. Canberra, Australia. (Published).

Chapter 1

Introduction

1.1 Background

Reducing CO_2 emissions is one of the main targets of the aviation industry. Having increased more quickly in recent decades than rail, road, or shipping, aviation accounted for 2% of worldwide energy-related CO2 emissions in 2022 (IEA, 2023). To achieve Net Zero Emissions by 2050, many methods and techniques are used to cut down CO_2 emissions. Drag reduction is one of the effective methods of reducing energy consumption, which consequently results in CO_2 emissions reductions. In aviation, a 10% reduction in the total drag can save approximately 6% of the trip fuel for flights (Heinemann et al., 2017).

In a wall-bounded flow, skin friction drag is mainly generated by the interaction between the flow and the wall in a turbulent boundary layer. Coherent structures, such as quasi-streamwise vortices, streaks, and horseshoe vortices are accounted for by turbulent momentum transfer and shear stress (Hon, 1987). These coherent structures strongly contribute to the Reynold shear stresses in the boundary layer and consequently contribute to the wall shear stresses and friction drag (Guo et al., 2010). Suppressing these coherent structures can reduce friction drag.

Turbulent boundary layer control methods can be classified into active and passive methods. In active methods, energy or momentum is then added or extracted into the turbulent flow, based on the measured signal (Coxe, 2019, Gad-el Hak, 1996). These methods require power, sensors, and actuators, which are complex, difficult to maintain, and expensive. In contrast, passive methods modify turbulent flows without using an external source of energy or flow (Samie et al., 2020). Passive methods, therefore, are cheaper and easier to implement than active methods. However, passive methods are less effective than active methods, and their performance depends highly on the conditions of the wall-bounded flow field (Tiainen et al., 2017).

Passive control by permeable structures has shown the potential to reduce skin friction drag. A 25% reduction in skin friction drag was predicted with a permeable structure at low Reynolds numbers in a direct numerical simulation (DNS) by Gómez-de Segura and García-Mayoral (2019). They suggested that permeable structures with a larger streamwise than spanwise permeability can reduce drag since the resistance to spanwise motions is larger than the resistance to streamwise motions, which lifts quasi-stream vortices away from the wall. This displacement is likely to reduce the skin-friction drag (Chavarin et al., 2021). However, it was also shown that when wall-normal permeability increases over a threshold value, the number of spanwise vortices increases, which can cause the turbulent boundary layer to become unstable, increasing the friction drag (Gómez-de Segura and García-Mayoral, 2019).

A specific type of permeable structure with a large number of vertical holes drilled at specific streamwise and streamwise positions through a plate has recently been found to have the potential to reduce skin friction drag (Gowree et al., 2019, Silvestri et al., 2017). It was shown that perforated structures can reduce sweep and ejection motions in boundary layers, which ultimately can lead to a reduction in skin friction drag. Using wind tunnel experiments, Silvestri et al. (2017) showed a reduction of 14% in the sweep intensity can be achieved by a perforated surface with a backing cavity. This reduction can result in a 5.6% reduction in skin-friction drag (Bhat et al., 2021). Typical perforated structures do not have permeability in either the spanwise or the streamwise directions, so it is suggested that these structures could reduce the spanwise vortices, which can reduce turbulence generation. The turbulence reduction, consequently, is expected to reduce the wall-shear stress and the friction drag.

Recent studies show that adding a backing chamber can increase the turbulence reduction due to a perforated plate in turbulent boundary layers. Silvestri et al. (2018) found that the sweep intensity reduction increases with an increase in the inner-scaled backing chamber volume. The mechanism of sweep reduction is proposed to be caused by the dissipation of sweep energy in the backing chamber and the weakening of the sweeps via the orifices. According to Jafari et al. (2022), at large scales, a backing chamber significantly reduced the pre-multiplied spectrum of streamwise velocity fluctuations by up to 80%. The authors propose that turbulent boundary layers may be reorganised by irregular transpiration via the orifices. Bhat et al. (2021) conducted a DNS of a turbulent boundary layer over a perforated plate with a backing cavity. They observed unsteady blowing and suction through the perforated plate. The mechanisms of unsteady blowing and suction are not clear. It is suggested that the acoustic excitation inside the backing cavity contributes to this unsteady transpiration. Acoustic excitations at a resonant frequency were observed in the literature, such as in the work by Hemon et al. (2004) and Ghanadi et al. (2014). The unsteady transpiration results from the interaction between the wall-normal velocities and the pressure at the wall which is represented by the wall impedance of the perforated plate (Jafari et al., 2023). They observed that the wall impedance with no phase difference between the wall-normal velocities and the pressure at the wall can suppress the near-wall cycles. Jafari et al. (2024) reported a range of wall impedance angles from 0.4π to 1.4π is preferable for drag reduction.

The motivation of this thesis is to enhance the understanding of the mechanisms of drag reduction in turbulent boundary layers over a perforated plate with a backing cavity. This goal can be achieved by characterising the modification of turbulent boundary layers due to the perforated plate. Hence, the interaction between the turbulent boundary layers and the perforated plate with a backing cavity is investigated in this thesis. The findings provide recommendations for designing a perforated plate to achieve friction drag reduction in engineering applications, which saves their fuel consumption and CO_2 emission.

1.2 Aims and objectives

This thesis aims to develop an understanding of the drag reduction mechanisms in the turbulent boundary layers over a perforated plate with a backing cavity. To achieve this aim, the turbulent boundary layers were generated in a wind tunnel and their characterisation were analysed. Hence, the research objectives are defined as follows:

1. To characterise the flow in the near-wall region of the turbulent boundary layers over a perforated plate with a backing cavity. This knowledge enhances understanding of the mechanism of turbulence attenuation in the turbulent boundary layers over the perforated surface. The turbulence attenuation in the near-wall region is associated with a reduction in the wall shear stress and skin friction drag in the turbulent boundary layers. This will be achieved by simulating fully developed turbulent boundary layers in a wind tunnel and measuring the flow velocity and turbulence in the near-wall region of the turbulent boundary with and without the perforated surface.

2. To determine the interaction between small and large scales in the turbulent boundary layers over a perforated plate with a backing cavity. This objective enhances the understanding of large-scale modulation of small scales in the near-wall regions of the turbulent boundary layers over the perforated surface. The large-scale structures in the outer region directly modulate the small-scale structures in the near-wall regions, which consequently affects skin friction drag. This will be achieved by decomposing the turbulence scales into small and large scales and analysing the large-scale modulation of small scales in the turbulent boundary layers over the perforated surface.

3. To evaluate the effect of wall-normal velocities through a perforated plate on turbulent boundary layers. This objective contributes to the understanding of the mechanisms of skin drag reduction in turbulent boundary layers due to a perforated plate. To achieve this objective, a synthetic jet actuator will be developed and used to control the turbulent boundary layers in a wind tunnel. The modification of flow turbulence in the near-wall region will be analysed.

4. To define the effect of acoustic impedance of the perforated plate on turbulent boundary layers. Wall acoustic impedance represents the relationship between the wall-normal velocities and the pressure at the wall. The wall impedance which represents no phase difference between the wall-normal velocities and the pressure can

lead to drag reduction. This objective enhances the understanding of the interaction between the wall-normal velocities and the pressure at the perforated plate which contributes to drag reduction. This will be achieved by testing different acoustic impedance generated by a perforated plate with different backing cavity configurations, estimating skin friction drag, and analysing the modification of the turbulent boundary layers due to the wall impedance.

1.3 Thesis outline

This thesis consists of seven chapters. The sequence of these chapters presents a chronology of knowledge development to meet the project aims. The first chapter provides an overview and introduction to research. Chapter 2 thoroughly reviews the literature on fundamental knowledge and methods and highlights the research gaps in detail to commence research into the potential of using perforated plates as a boundary layer control method. The main body of this thesis which consists of Chapters 3 to 6, investigates the modification of turbulent boundary layers due to a perforated plate with a backing cavity and the mechanisms of friction drag reduction. The main part contains four articles that are direct products of this work, all of which have been published or are pending publication in peer-reviewed journals. The final chapter provides a summary of the research's results, conclusions, and suggestions for future work. The content, scope, and contribution of each chapter are further discussed as follows.

Chapter 2 of this thesis reviews and discusses the turbulent boundary layer's structures and how they affect the near-wall region. Together with this, a thorough literature analysis of earlier control methods is included, in which the benefits and drawbacks of each are evaluated critically. This review also highlights current research on using a perforated plate to control turbulent boundary layers. The effects of a perforated plate on turbulent structures, turbulence intensity, and friction drag in turbulent boundary layers were reviewed. The research gaps are identified in the chapter along with how they can be addressed.

Chapter 3 begins the main body of the thesis by investigating near-wall turbulence in the turbulent boundary layers over a perforated plate with a backing cavity. This consists of the first paper of the thesis and is used to develop an understanding of the mechanisms of turbulence attenuation in the near-wall region due to the perforated plate. Turbulent boundary layers at different Reynolds numbers were simulated in a closed-return wind tunnel at the University of Adelaide. Flow velocities were measured using a Dantec hot-wire probe. The burst events and pre-multiplied power spectral densities (PSD) of velocity fluctuations in the turbulent boundary layers with and without the perforated plate are determined. The results show that the perforated plate weakens the bust events in the near-wall region at the inner-scaled wall-normal locations below 30 but increases them in the outer region of the turbulent boundary layers. The perforated plate also reduces the pre-multiplied PSD in the near-wall region and increases it in the wall-normal locations further from the wall. This indicates that the perforated plate transfers turbulence energy further from the wall. As a result, it reduces the near-wall turbulence intensity and local skin friction drag in the turbulent boundary layers.

In Chapter 4, the interaction between small scales in the near-wall region and large scales in the outer region of the turbulent boundary layers over a perforated plate with a backing cavity is investigated. The purpose of this chapter is to gain an understanding of the effect of the perforated plate on the large scales in the outer region which directly affect the near-wall turbulence and then indirectly alter the skin friction drag. Turbulent boundary layers over the perforated plate at different Reynolds numbers are simulated in a closed-return wind tunnel. The turbulent scales are decomposed into small and large scales and the energy patterns of both small and large scales are analysed. The results show that the perforated plate enhances large scale structures in the outer region of the turbulent boundary layers. This results in an increase in the large-scale modulation of the small scales in the near-wall region. The increase in the large-scale modulation is associated with a decrease in skin friction drag in the turbulent boundary layers over the perforated plate.

Chapter 5 investigates near-wall turbulence in the turbulent boundary layers controlled by wall-normal velocities through a perforated plate. This chapter aims to understand the effect of controlling a particular scale through a perforated plate on turbulence boundary layers. This chapter contributes to knowledge of the mechanics underlying skin drag reduction caused by a perforated plate in turbulent boundary layers. A synthetic jet actuator is developed for turbulent boundary layer control. Different jet amplitudes and frequencies are tested. The modification of velocity profiles, turbulence intensity profiles, burst events, and turbulence energy is analysed. The results illustrate that synthetic jets transfer burst events further from the wall. As a result, the near-wall region experiences a reduction in turbulence intensity, energy, as well as skin friction drag. As the jet frequency increases, the controlling effect becomes more pronounced. In other words, when small scales are controlled, a large reduction in skin friction is achieved. This supports the hypothesis that skin friction and turbulence activity in the turbulent boundary layers are reduced as a result of the wall-normal velocities produced by the perforated plate.

In Chapter 6, the the effect of acoustic impedance of a perforated plate with a backing cavity on near-wall turbulence is investigated. The relationship between the pressure and the wall-normal velocities at the wall is represented by the wall impedance. This chapter aims to improves knowledge of the relationship between the pressure at the perforated plate and the wall-normal velocities for drag reduction. Different wall impedance were generated by the perforated plate with different backing volues. The velocity profiles, turbulence intensity, the burst event, pre-multiplied PSD of velocity fluctuations, and the skin friction drag of the turbulent boundary layers with the wall impedance are analysed. The results show a relationship between near-wall turbulence and the acoustic impedance of the perforated plate with a backing cavity. The turbulence intensity in the near-wall region decreases as the normalised specific acoustic reactance rises. Within the near-wall region, a maximum decrease of roughly 7.8% in sweep intensity and 7% in ejection intensity was observed at a normalised specific acoustic reactance of 69.6. These reductions are associated with an approximate 7% decrease in the near-wall region's turbulence intensity and an approximate 8% decrease in the estimated local friction drag. This suggests that the perforation decreased the near-wall turbulence by suppressing the near-wall cycles. The relationship between the wall-normal velocities and the pressure at the wall is impacted by an increase in the normalised specific acoustic impedance in such a way that the wall-normal velocities lift the turbulence kinematic energy farther away from the wall. By weakening sweep and ejection events in the near-wall region, these wall-normal velocities also reduce the near-wall cycles. Consequently, turbulence intensity, shear stress in the vicinity of the wall, and friction drag are all reduced.

The final chapter documents the conclusions made from the research in this thesis. The research covered in this thesis has taken a significant step forward in developing the perforated plate with a backing cavity as a potential boundary layer control device. Furthermore, key recommendations for future work for the perforated plate to be used in real-life applications are discussed at the end of this chapter.

1.4 Thesis format

This thesis complies with The University of Adelaide's formatting criteria and has been submitted as a portfolio of publications resulting from the study. The print and digital versions of this thesis are identical. This thesis is available as a PDF for online access.

References

Bhat, S., Silvestri, A., Cazzolato, B., and Arjomandi, M. (2021). Mechanism of control of the near-wall turbulence using a micro-cavity array. *Physics of Fluids*, 33(7):075114.

Chavarin, A., Gomez-de Segura, G., Garcia-Mayoral, R., and Luhar, M. (2021). Resolvent-based predictions for turbulent flow over anisotropic permeable substrates. *Journal of Fluid Mechanics*, 913:A24.

Coxe, D. (2019). *Drag Reduction in Turbulent Pipe Flow by Transverse Wall Oscillations at Low and Moderate Reynolds Number.* PhD thesis, Arizona State University.

Gad-el Hak, M. (1996). Modern developments in flow control. *Applied Mechanics Reviews*, 49(7):365–379.

Ghanadi, F., Arjomandi, M., Cazzolato, B., and Zander, A. (2014). Interaction of a flow-excited Helmholtz resonator with a grazing turbulent boundary layer. *Experimental Thermal and Fluid Science*, 58:80–92.

Gómez-de Segura, G. and García-Mayoral, R. (2019). Turbulent drag reduction by anisotropic permeable substrates–analysis and direct numerical simulations. *Journal of Fluid Mechanics*, 875:124–172.

Gowree, E. R., Jagadeesh, C., and Atkin, C. J. (2019). Skin friction drag reduction over staggered three dimensional cavities. *Aerospace Science and Technology*, 84:520–529.

Guo, H., Borodulin, V., Kachanov, Y., Pan, C., Wang, J., Lian, Q., and Wang, S. (2010). Nature of sweep and ejection events in transitional and turbulent boundary layers. *Journal of Turbulence*, 11:N34.

Heinemann, P., Panagiotou, P., Vratny, P., Kaiser, S., Hornung, M., and Yakinthos, K. (2017). Advanced tube and wing aircraft for year 2050 timeframe. In *55th AIAA Aerospace Sciences Meeting*, page 1390.

Hemon, P., Santi, F., and Amandolèse, X. (2004). On the pressure oscillations inside a deep cavity excited by a grazing airflow. *European Journal of Mechanics-B/Fluids*, 23(4):617–632.

Hon, T.-L. (1987). *Analysis of the motions and effects of hairpin vortices.* PhD thesis, Lehigh Univ., Bethlehem, PA (USA).

IEA (2023). Tracking clean energy progress 2023. Technical report, IEA, Paris.

Jafari, A., Cazzolato, B., and Arjomandi, M. (2022). Finite-length porous surfaces for control of a turbulent boundary layer. *Physics of Fluids*, 34(045115):1–34.

Jafari, A., McKeon, B. J., and Arjomandi, M. (2023). Frequency-tuned surfaces for passive control of wall-bounded turbulent flow–a resolvent analysis study. *Journal of Fluid Mechanics*, 959:A26.

Jafari, A., McKeon, B. J., Cazzolato, B. C., and Arjomandi, M. (2024). A resolvent analysis of the effect of passive perforated surfaces on wall-bounded turbulence. *International Journal of Heat and Fluid Flow*, 106:109315.

Samie, M., Baars, W., Rouhi, A., Schlatter, P., Örlü, R., Marusic, I., and Hutchins, N. (2020). Near wall coherence in wall-bounded flows and implications for flow control. *International Journal of Heat and Fluid Flow*, 86:108683.

Silvestri, A., Ghanadi, F., Arjomandi, M., Cazzolato, B., and Zander, A. (2017). Attenuation of sweep events in a turbulent boundary layer using micro-cavities. *Experiments in Fluids*, 58:1–13.

Silvestri, A., Ghanadi, F., Arjomandi, M., Cazzolato, B., Zander, A., and Chin, R. (2018). Mechanism of sweep event attenuation using micro-cavities in a turbulent boundary layer. *Physics of Fluids*, 30(5):055108.

Tiainen, J., Grönman, A., Jaatinen-Värri, A., and Backman, J. (2017). Flow control methods and their applicability in low-reynolds-number centrifugal compressors—a review. *International Journal of Turbomachinery, Propulsion and Power*, 3(1):2.

Chapter 2

Literature review

This chapter provides an overview of turbulent boundary layer control and along with important research on boundary layers over a perforated plate. The first section of the chapter reviews and characterises the literature on turbulent boundary layers and the coherent structures that cause wall-shear stresses. Subsequently, Section 2.2 delves into the methods employed for controlling the boundary layer. Section 2.3 discusses the use of a perforated plate for controlling turbulent boundary layers, followed by the last section which summarises the literature and the main objectives of this thesis.

2.1 Turbulent boundary layers

Boundary layers exist in various wall-bounded engineering applications, such as aircraft, ships, cars, pipelines, heat fans, and reactors. Boundary layers can be categorised into laminar and turbulent flows as shown in Figure 2.1. When fluid flows over a flat plate, it transforms from a laminar to a turbulent flow along with an increase in Reynolds numbers, $Re_x = U_\infty x/\nu$, where U_∞ is the free steam velocity, x is the downstream location from the leading edge of the plate, and ν is the kinematic viscosity of the flow. A boundary layer over a flat plate with a zero-pressure gradient is laminar at $Re_x \leq 10^5$ and turbulent at $Re_x \geq 3 \times 10^6$ (Cengel and Cimbala, 2013).

Turbulent boundary layers are characterised by coherent structures throughout the boundary layer. These structures, such as quasi-streamwise vortices, streaks, and horseshoe

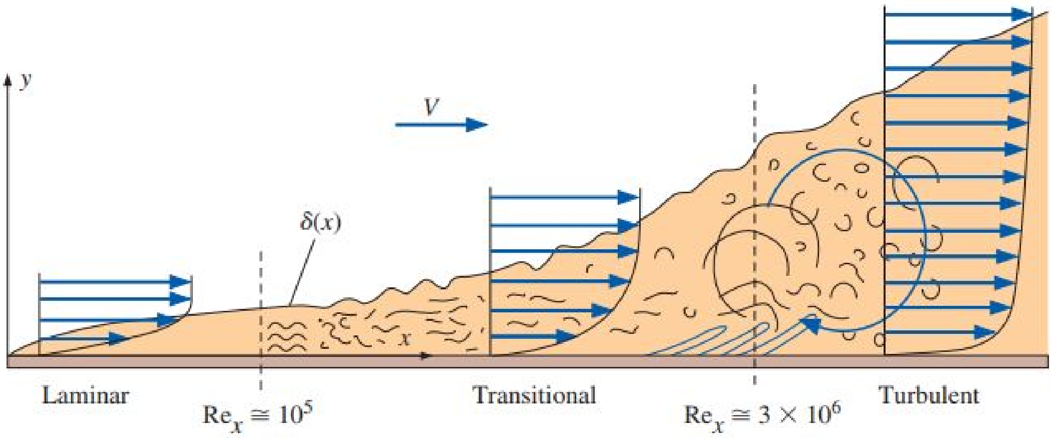

Figure 2.1. Development of a boundary layer over a surface (Cengel and Cimbala, 2013).

vortices as shown in Figure 2.2, rapidly transport mass, momentum, and energy in turbulent boundary layers, which enhances shear stresses, friction drag, heat and mass transfer (Cengel and Cimbala, 2013). The shear stresses and friction drag coefficients of turbulent boundary layers are much higher than those of laminar boundary layers (Von Karman, 1934).

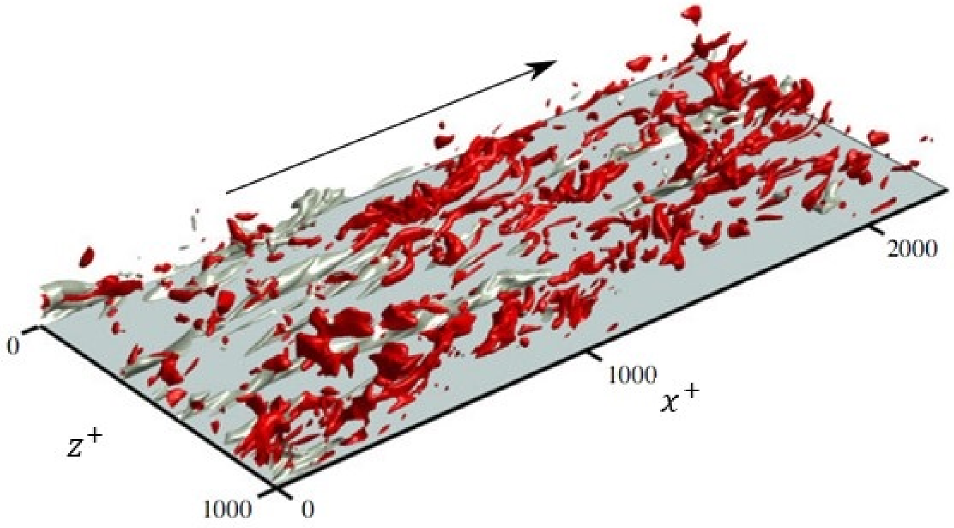

Figure 2.2. Perturbation velocity isosurfaces. Light grey presents low streaks and red presents high streaks of a wall-bounded flow (Jiménez, 2018).

A canonical turbulent boundary layer over a flat plate can be divided into four regions. These regions include the viscous sublayer, buffer layer, logarithmic layer, and wake region as shown in Figure 2.3. The viscous sublayer is close to the wall at $y^+ = yU_\tau/\nu \leq 5$, where y is the wall-normal location and U_τ is the friction velocity. In the viscous sublayer, fluid viscosity is dominant and the mean velocity profile follows the linear law, $U^+ = y^+$, where $U^+ = U/U_\tau$, where U is the mean velocity. Above the viscous sublayer is the buffer region at $5 < y^+ < 30$. This region is between the logarithmic and viscous sublayers, where both viscosity and turbulence shear stress play an important role (Gad-el Hak and Bandyopadhyay, 1994). This region is associated with turbulence generation where the inner peak in the turbulent intensity is observed at $y^+ \approx 15$. The logarithmic layer at $y^+ \geq 30$ is the overlap between the inner region and the outer region of a turbulent boundary layer. In this region, the mean velocity profile is represented by the logarithmic law as

$$U^+ = \frac{1}{\kappa}\ln(y^+) + B, \tag{2.1}$$

where $\kappa = 0.384$ and $B = 4.17$ are the von Kármán constants (Monkewitz et al., 2007). The very outer portion of a turbulent boundary layer is the wake region where the freestream provides the energy for the turbulent energy cascade. This region is characterised by a wake function, $W(\Pi, \eta)$, where Π is the wake parameter; $\eta = y/\delta$; and δ is the boundary layer thickness (Coles, 1956). The mean velocity profile in this region is defined by adding the wake function to the logarithmic law as

$$U^+ = \frac{1}{\kappa}\ln(y^+) + B + W(\Pi, \eta). \tag{2.2}$$

2.1.1 Near-wall region

The near-wall region of a turbulent boundary layer plays an important role in generating skin friction drag. This region includes the viscous sublayer and the buffer layer, so it directly affects skin friction drag and significantly contributes to turbulence generation in the turbulent boundary layer (Kim et al., 1971). The coherent structures including sweep and ejection events in the near-wall region are responsible for the shear stresses and skin friction drag in the turbulent boundary layer (Guo et al., 2010). The sweep and ejection events are involved in the streaks and the quasi-streamwise vortices, which create a self-sustaining generation namely the “near-wall cycle”. Figure 2.4 shows the bubble visualisation of a turbulent boundary layer by Jiang et al. (2020). The top view at $y^+ = 20$

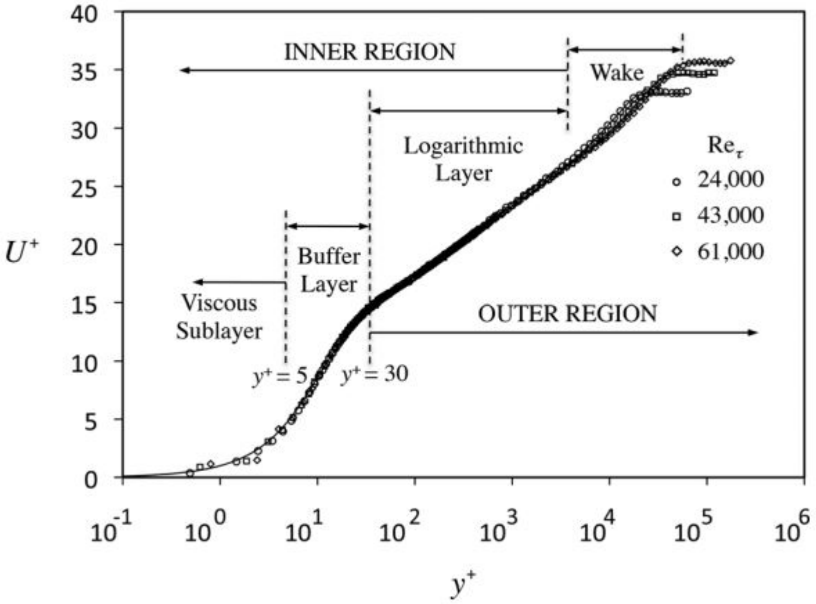

Figure 2.3. Velocity profiles and different regions in turbulent boundary layers (Perlin et al., 2016).

is shown in Figure 2.4(a), which clearly indicates five streaks that are distributed randomly and range from around 80 to 120 in viscous units in the spanwise direction, which agrees with the work by Smith and Metzler (1983) and Klewicki et al. (1995). Figure 2.4(b) shows a side view of the turbulent boundary layer. The figure shows the streaks labeled as “A” and “B” with a length exceeding 1000 viscous units in the streamwise direction in agreement with the work by Smith and Metzler (1983). The sweep and ejection are also presented and labeled as “S” and “E”, respectively.

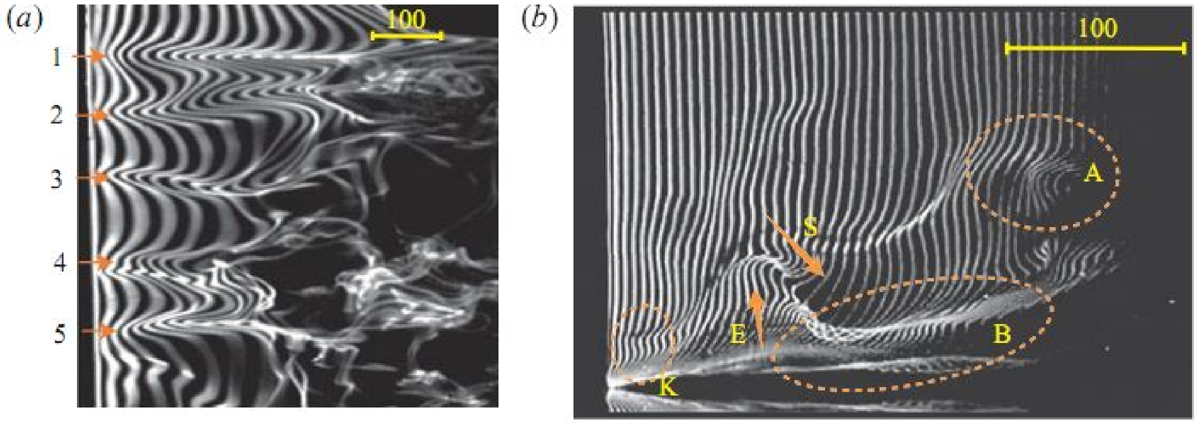

Figure 2.4. (a) The top view at $y^+ = 20$ and (b) a side view of a turbulent boundary layer by bubble visualization. A presents an inflectional pattern in the outer region. B presents a streamwise vortex. E presents an ejection. S presents a sweep (Jiang et al., 2020).

The sweep and ejection events are the main contributors to shear stresses in the near-wall region. The low and high streaks which involve the ejection and sweep events are unstable and quickly break down, which is referred to as the bursting process (Kim et al., 1971). Corino and Brodkey (1969) demonstrated the near-wall region with both sweep and ejection events using Particle Image Velocimetry (PIV). They discovered that the ejection event accounts for 70% of the overall Reynolds stress production in the near wall region, with the sweep event accounting for the remaining portion. Wallace et al. (1972) used a four-quadrant system for the near-wall events in a turbulent boundary layer. They found that there are four possible events namely Q1, Q2, Q3, and Q4. The ejection and sweep events, designated as Q2 and Q4 events, respectively, accounted for roughly 140% of the overall stresses in the vicinity of the wall while the events (Q1 and Q3) are responsible for a negative contribution of 40% of the total Reynolds stresses. (Jiménez, 2018) reported the Q2 and Q4 events as shown in Figure 2.5. They found that a Q2 and a Q4 appeared in a pair which forms a streak. Both low- and high-speed streaks were observed. The high-speed streak is longer, but also taller than the slow-speak streaks. Their width is about 1000 wall units.

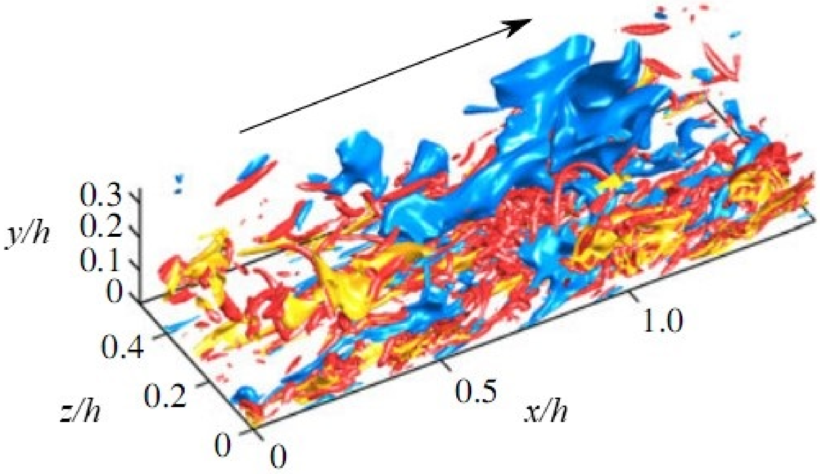

Figure 2.5. Instantaneous ejections and sweeps in a channel turbulent boundary layer. Yellow presents the ejections, Q2, blue presents the sweeps, Q4, and red presents the vortices (Jiménez, 2018).

The sweep and ejection events can be detected by the Variable Interval Time Averaging (VITA) technique (Whalley, 2011). A burst is detected when the local variance, $\mathrm{Var}(t, T_W)$, in a window, T_W, is larger than the variance of an entire signal of velocity fluctuations, $\mathrm{Var}(t)$, manipulated by a threshold, k. The local variance can be given as:

$$\mathrm{Var}(t,T_W) = \widehat{u^2}(t,T_W) - (\hat{u}(t,T_W))^2, \tag{2.3}$$

where $\hat{Q}(t,T_W)$ is the local mean, $\hat{Q}(t,T_W) = \frac{1}{T_W}\int_{t-\frac{1}{2}T_W}^{t+\frac{1}{2}T_W} Q dt$. The detection function, $D(t)$, of burst events can be given as (Whalley, 2011):

$$D(t) = \begin{cases} 1 \ \ \text{if } \mathrm{Var}(t,T_W) \geq k \times \mathrm{Var}(t) \ \& \ du/dt > 0 \text{ (sweeps)} \\ 0 \ \ \text{if } \mathrm{Var}(t,T_W) < k \times \mathrm{Var}(t) \text{ (no events)} \\ -1 \text{ if } \mathrm{Var}(t,T_W) \geq k \times \mathrm{Var}(t) \ \& \ du/dt < 0 \text{ (ejections)} \end{cases} . \tag{2.4}$$

Figure 2.6 shows the burst signatures of the velocity fluctuations for the baseline case at $y^+ = 15$ with VITA parameters, $T_W = 10$ and $k = 1.2$. The velocity signal duration was 30 seconds at a sampling frequency of 40 kHz. Figure 2.6(a) illustrates the instantaneous sweep signatures and Figure 2.6(b) shows the instantaneous ejection signatures. While 32 sweep events were detected, only 7 ejection events were found. This indicates that sweep events were the main contributors to the bursts (Orlandi and Jiménez, 1994, Whalley, 2011).

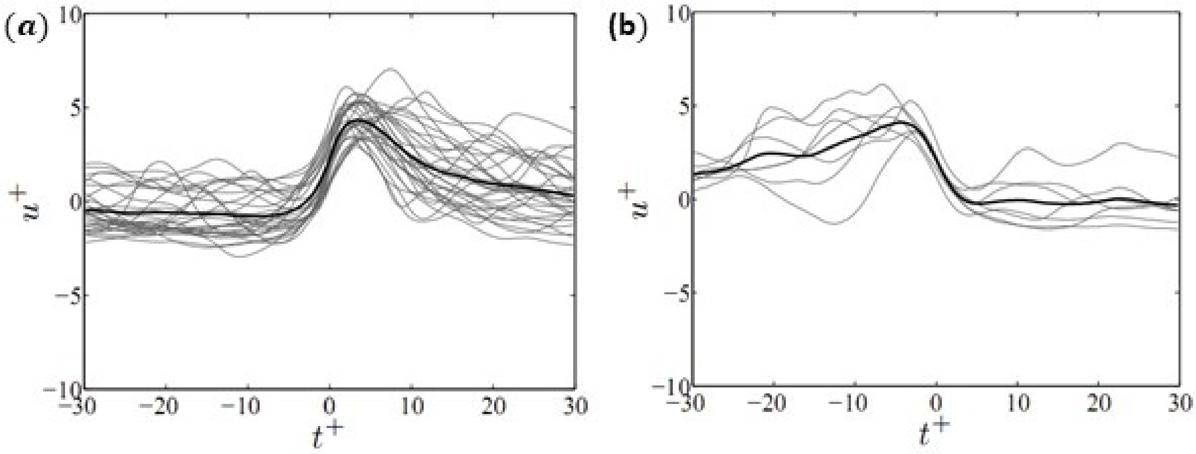

Figure 2.6. Burst signatures: (a) the sweep events and (b) the ejection events. The darked black line present the mean signatures (Whalley, 2011).

Burst events are also detected using other techniques, such as the Quadrant (Luchik and Tiederman, 1987) and the u-level methods (Bogard and Tiederman, 1986). To identify burst events based on the single-component hot-wire velocity signals, Bogard and Tiederman (1986) employed the u-level approach. Through direct comparisons with low visualisation, they assessed the efficacy of the modified u-level, u-level, Quadrant, and

VITA algorithms. They found that the single-component ejection detectors within suitable threshold levels are just as dependable as the Quadrant approaches. More significantly, the bursting process was shown to involve clusters of ejections and associated sweeps based on the detection method (Bogard and Tiederman, 1986, Tardu, 1995). The self-mechanism of wall turbulence is closely related to the active transmission of turbulent momentum during the bursting process. Thus, during the past few decades, there has been a lot of interest in studying the turbulent boundary layer's bursting process.

2.1.2 Outer region

The outer region of a turbulent boundary layer includes the logarithmic layer and the wake region. While the effect of viscosity reduces, the turbulence shear stresses are dominant in this region (Gad-el Hak and Bandyopadhyay, 1994). The logarithmic layer was visualised by smoke in the work by Head and Bandyopadhyay (1981). They observed structures that looked like hairpin shapes at different Reynolds numbers as shown in Figure 2.7(a). The head, neck, and legs are the main components of these hairpin structures. It has been demonstrated that quasi-streamwise vortices are produced by the legs of the hairpin vortex as shown in Figure 2.7(b) (Bernard et al., 1993). These hairpin structures are associated with the sweep and ejection events in the near-wall region where streaks and streamwise vorticity are created. The legs of a hairpin vortex remain fixed to the wall (Perry and Marušić, 1995). As a result, the hairpin legs lengthen and create quasi-streamwise vortices. These are similar to the low-speed streaks that form near walls during ejection events (Robinson et al., 1991).

The hairpin vortices in the outer region have a strong connection to the sweep and ejection events in the near-wall region. Adrian et al. (2000) performed high-speed planar PIV measurements to investigate turbulent structures in turbulent boundary layers. They found that hairpin vortices begin in or above the buffer layer. The hairpin legs involve both sweep and ejection events in the near-wall region. It was found that each individual hairpin traveled at almost the same speed. New quasi-streamwise vortices are also created near the wall during the auto-generation process (Adrian, 2007). Figure 2.8 shows oblique, top, and side views of two hairpin vortices by Jodai and Elsinga (2016). They conducted time-resolved tomographic PIV measurements in a turbulent boundary layer to investigate

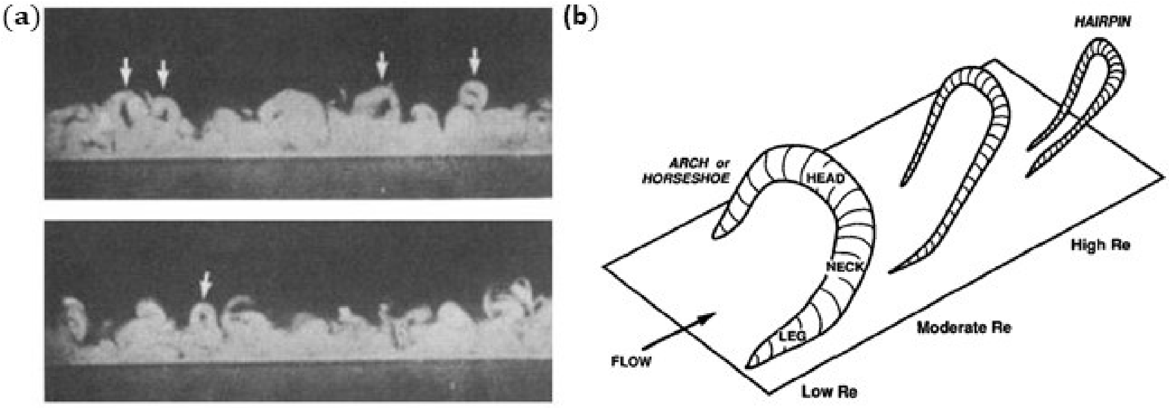

Figure 2.7. (a) Visualisation of turbulent boundary layers (Head and Bandyopadhyay, 1981) and (b) Conceptual model of hairpin-shaped vortical structures (Robinson et al., 1991). The arrows point to horseshoe vortices.

the generation of hairpin vortices. A small hairpin vortex develops just after the big one, which indicates near-wall circles. The legs of these vortices are in the near-wall region, which involves sweeps and ejections. As a result, a considerable portion of the Reynolds shear stress is contributed by the hairpin vortices.

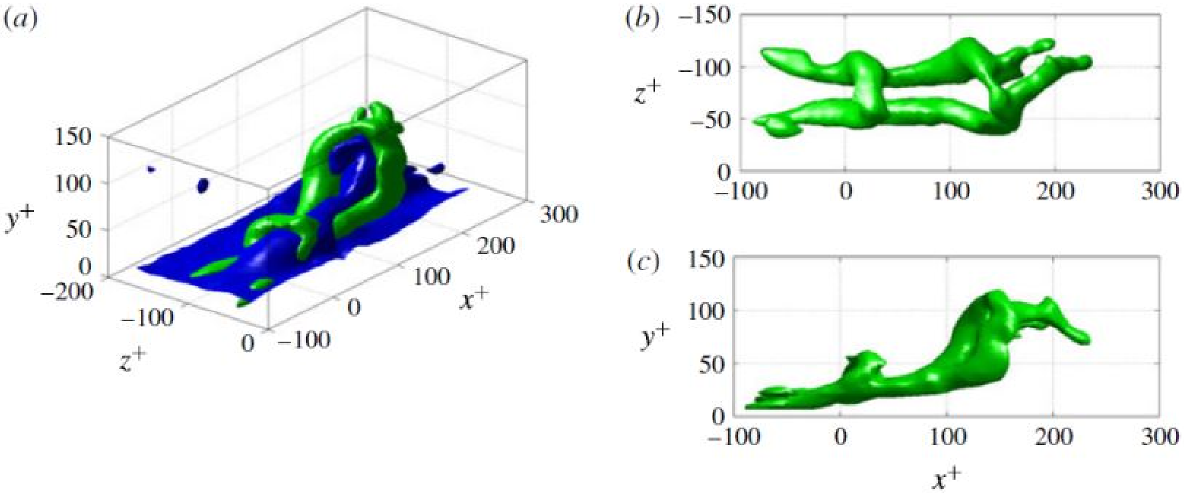

Figure 2.8. (a) The oblinque, (b) top, and (c) side views of a hairpin vortex. The green color presents the swirling strength of $0.08U_\tau^2/\nu$. The blue color presents the streamwise velocities of $14U_\tau$ (Jodai and Elsinga, 2016).

The outer region affects shear stresses and skin friction drag in turbulent boundary layers. The contribution of the outer region to skin friction drag increases as the Reynolds number increases (Hwang, 2013). At high Reynolds numbers, large-scale structures emerge in the outer region, dominantly in the logarithmic region (Hutchins and Marusic, 2007). These large-scale structures directly modulate the small-scale structures in the near-wall regions (Gomit et al., 2018, Hutchins and Marusic, 2007). Mathis et al. (2009) found a strong large-scale amplitude modulation of small-scale structures in the near-wall region in turbulent boundary layers at Reynolds numbers of $Re_\tau \approx 10^3 - 10^4$, where $Re_\tau = \delta U_\tau/\nu$, δ is the boundary layer thickness, U_τ is the friction velocity, and ν is the air viscosity. Hence, turbulent boundary layer control which targets large coherent structures could indirectly affect the near-wall turbulence and reduce skin friction drag (Deshpande et al., 2023, Duvvuri and McKeon, 2016).

2.1.3 Outer region

2.2 Turbulent boundary layer control

Boundary layer control has been of primary interest to researchers for many years. It has numerous applications, such as delaying boundary layer separation, improving heat transfer, lowering skin friction, and suppressing noise (Gad-el Hak et al., 2003, Luchini and Quadrio, 2022). The methods for the control of turbulent boundary layers can be categorised into active or passive (Coxe, 2019, Gad-el Hak et al., 2003). Active methods, such as spanwise wall forcing, pulsed-DC plasma actuation, and blowing/suction and jet control extract or add energy or momentum from an external source to the turbulent flow. Active methods require power, sensors, and actuators, which are complex, difficult to maintain, and expensive (Jahanmiri, 2010). In contrast, passive methods, such as riblets, Helmholtz resonators, permeable surfaces, and perforated plates modify turbulent flows without using any external source of energy or momentum. Passive methods are less efficient than active methods but cheaper and easier to implement and maintain than active methods (Samie et al., 2020).

2.2.1 Active control

Active control alters boundary layer flows by adding or removing mass or energy. There are two categories of active control actuation: interactive and preset (Jahanmiri, 2010). The interactive approaches are based on the application of feedback to build a loop control system by adjusting the actuator based on data from sensors or other sources. Conversely, the preset methods' actuators are preconfigured, and their configuration remains constant throughout the operation, independent of the flow field. For example, there are common active control methods, such as opposition control (Choi et al., 1994, Dacome et al., 2024a, Wang et al., 2022) and jet control (Glezer and Amitay, 2002, Murugan et al., 2016, Zhang et al., 2022).

Opposition control

Opposition control is a promising interactive active control of turbulent boundary layers. In this control, sensors are located at a distance, y_s, from a wall and measure the wall-normal velocity. The measured signal is then transferred to the actuators to create opposite wall-normal velocities, as shown in Figure 2.9. Choi et al. (1994) used opposition control to manipulate boundary layers over a flat plate. They found that the control can significantly reduce sweep and ejection motions in near-wall regions, which will consequently reduce both the turbulence intensity and the wall shear stress. Furthermore, the opposite velocities may also prevent the span-wise vortices' lift from the surface. This will prevent the development of both streamwise vortices and low-speed streaks and consequently reduce skin friction drag. A maximum of a 30% reduction in skin friction in the opposition control case was observed by Choi et al. (1994).

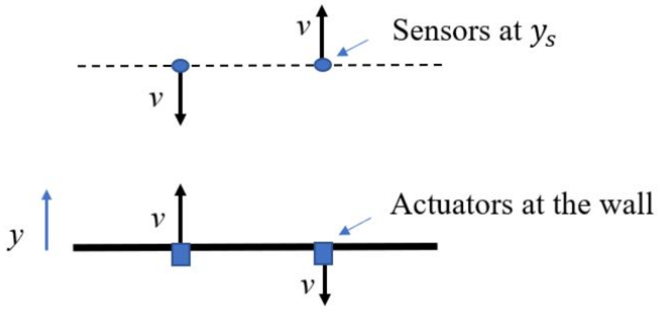

Figure 2.9. Diagram of streamwise-opposition control (Choi et al., 1994).

Fukagata and Kasagi (2003) conducted a DNS of turbulent pipe flow controlled by the opposition control at $Re_\tau = 180$. They discovered that the average drag reduction is related to the area of control, and the highest drag reduction rate, which is roughly 25%, is comparable to that of channel flow. Despite the straightforward relationship for the average drag reduction rate, the local skin friction coefficient shows a complex streamwise fluctuation. Approximately ten times of the pipe diamters downstream of the restricted region, the flow returns to the uncontrolled state. Just downstream of the controlled area, a quick recovery of the skin friction is seen. Luhar et al. (2014) focused on opposition control and used resolvent analysis to examine flow control methods that apply linear control rules. Their findings demonstrate that the amplification characteristics (and wall-normal structures) of the response modes are impacted by opposition control, which is introduced through the boundary condition on wall-normal velocity; a decrease in gain signifies mode suppression, which lowers the drag contribution from that mode. Without the need for high-performance computing tools, Rank-1 mode, under simple assumptions, replicates patterns shown in earlier direct numerical simulation and large eddy simulation. Furthermore, the decline in opposition control performance with increasing sensor elevation and Reynolds number can be explained by a wavenumber–frequency breakdown of control. Dacome et al. (2024a) performed Particle Image Velocimetry (PIV) and Particle Tracking Velocimetry (PTV) measurements of the turbulent boundary layers with opposition control. They found that opposition control can reduce about 40% of turbulent energy in the large-scale motions and approximately 10% of friction drag in comparison with those in the uncontrolled flow.

Synthetic jet control

Synthetic jet control is a preset-active control. Synthetic jets can be generated using piezoelectric actuators or acoustic speakers. Figure 2.10 shows a schematic of a piezoelectric jet actuator. The pressure vibration is created by a vibrating platform that is controlled electrically. The vibrating membrane of the actuator at the operating frequency generates fluctuating pressures, which push the airflow out of or into the cavity. Therefore, an air jet is generated at a particular frequency and amplitude, which can be used to control a turbulent boundary layer (Mossi and Bryant, 2003).

Synthetic jets generate vortex rings in turbulent boundary layers via periodic vortex rings. The membrane moves up and pushes the internal air out of the cavity, which creates a developing vortex ring out of the orifice (Murugan et al., 2016). The vortex rings were observed in the work by Jabbal and Zhong (2010). They conducted PIV measurements of turbulent boundary layers with synthetic jets through a 5 mm diameter orifice at

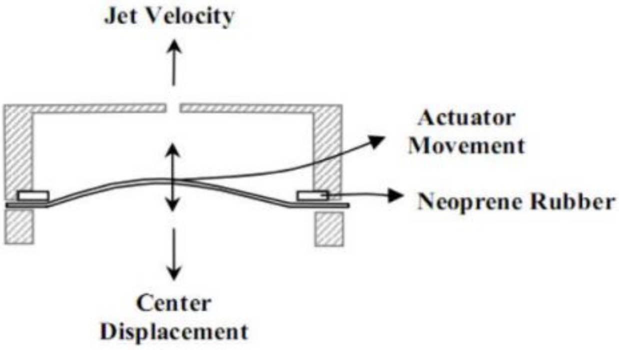

Figure 2.10. Schematic of a piezoelectric jet actuator and synthetic jets (Mossi and Bryant, 2003).

$Re_\delta = U_\infty \delta / \nu = 500$, where U_∞ is the freestream, δ is the boundary layer thickness, and ν is the viscosity of air. The development of the ring vortices is shown in Figure 2.11. The results show that the synthetic jet actuator generated three types of coherent structures including a hairpin vortex, stretched, and tilted vortex rings. Figure 2.11 shows a vortex ring was generated and pushed to a higher location from the wall. This vortex ring was then stretched and lifted out of the boundary layer before transforming into a hairpin vortex (Jabbal and Zhong, 2010).

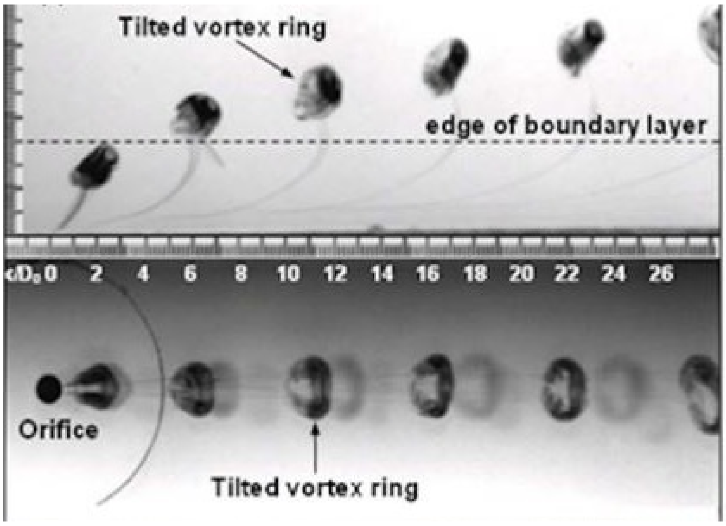

Figure 2.11. Tilted vortex rings generated by synthetic jets (Jabbal and Zhong, 2010).

The application of synthetic jet control has shown potential for reducing friction drag. Park et al. (2001, 2003) experimentally investigated turbulent boundary layers using suction/blowing jets through a slot. The results show that a decrease in velocity near the wall results in reduced skin friction, and the extent of this reduction escalates with higher forcing frequencies as shown in Figure 2.12. The maximum decrease in local skin friction, reaching approximately 45%, was noted at a frequency of $f_c^+ = f\nu/U_\tau^2 = 0.044$ and $x/\delta_0^* = 2$, where f_c is the controlling frequency; x is the downstream location from the actuator; and δ_0^* is the displacement thickness of the uncontrolled boundary layers. As the flow recovers, the drag reduction in downstream locations decreases. Cannata et al. (2020) conducted experiments on synthetic jets at different frequencies and using different actuator configurations at the friction Reynolds number of 180. They also observed a reduction in the instantaneous wall-shear stress by up to 20%. The effect of synthetic jets increases when the jet amplitude and frequency increase (Lu et al., 2020).

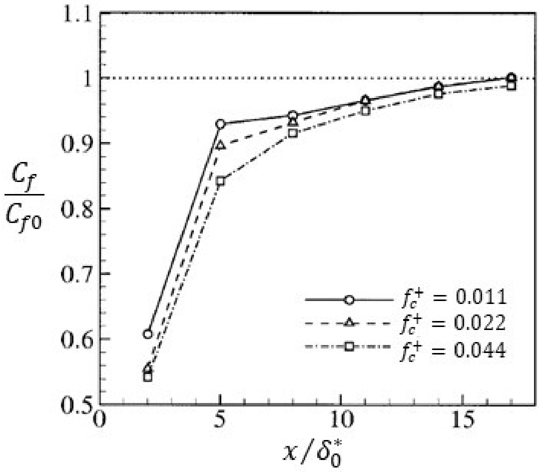

Figure 2.12. Friction drag coefficients as a fuction of downstream locations. C_f and C_{f0} are the friction coefficients in the controlled and uncontrolled cases, respectively. (Park et al., 2001).

2.2.2 Passive control

Passive control alters turbulent boundary layers without adding or extracting energy or momentum from the flow. The configuration of passive control does not change during operation, so its effectiveness depends on the flow condition (Samie et al., 2020). There are common passive methods, such as riblets, permeable surfaces, and Helmholtz resonators.

Riblets

Riblets are one of the passive methods to control boundary layers for drag reduction. Riblets can reduce the skin friction drag in turbulent flows by up to 10% in comparison with the skin friction drag of turbulent flows over smooth walls (Saravi and Cheng, 2013). Simple riblets made of microgrooves along the flow direction with a height, h, and a spanwise spacing, s, are shown in Figure 2.13. Bechert et al. (1997) observed a reduction in spanwise flow fluctuations in turbulent boundary layers over riblets, which contributes to drag reduction. In addition, Choi (1989) and Goldstein et al. (1995) reported that riblets reduce friction drag by damping spanwise rollers. The reduction in the spanwise motion decreases the spanwise motion of low-speed streaks. Consequently, riblets can weaken streamwise vortices and the streamwise motion of these streaks increases, which lifts streamwise vortices and streaks away from the wall (Benschop and Breugem, 2017, Fu et al., 2017, Saravi and Cheng, 2013). Consequently, the riblets weaken turbulent mixing near the surface and reduce friction drag.

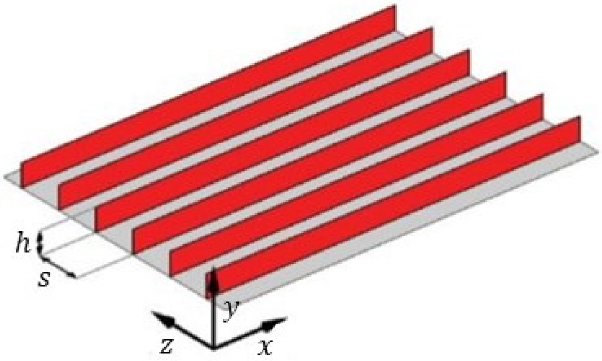

Figure 2.13. Riblet texture aligned with the mean flow (Benschop and Breugem, 2017).

Drag reduction due to riblets depends on the relationship between the riblet spacing and the near-wall turbulent scales. It can be expressed as a function of viscous scaled riblet spacing, $s^+ = sU_\tau/\nu$ (Walsh and Lindemann, 1984). Walsh (1980) reported that drag reduction only happens for $s^+ < 30$ for both curved and sharp forms and the largest reduction was shown at $s^+ \approx 15$. Similarly, Itoh et al. (2006) conducted a comprehensive collection of drag reduction measurements for seal fur and flat-peak riblets. Drag reduction is given as $\Delta\tau/\tau_0$, where $\Delta\tau = \tau - \tau_0$; τ and τ_0 are the wall-shear stresses in the controlled and uncontrolled turbulent boundary layers. They found a relationship between drag reduction and riblet spacings as shown in Figure 2.14. The results show that drag reduction monotonously increases along with an increase in s^+ before reaching the maximum value at $s^+ = 10$. Drag reduction gradually reduces at $10 < s^+ < 20$. The drag increase regime with k-roughness forms may cause the reduction in riblet performance at large spacings (Jiménez, 2004). As riblet performance depends on flow conditions, the challenges in determining the optimal riblet size for minimising drag limit the use of this technique.

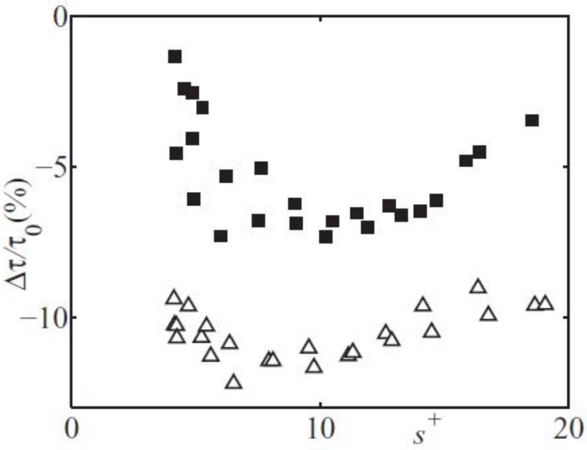

Figure 2.14. Drag reduction as a function of viscous-scaled riblet spacings. Triangles and black solid squares present results for seal fur and flat-peak riblets, respectively (Itoh et al., 2006).

Permeable surface

Anisotropic permeable surfaces have demonstrated the capability to reduce friction drag as a passive flow control method. Luchini et al. (1991) found that permeable surfaces with a larger resistance to the cross-flow than to the streamwise mean flow can reduce drag. When the surface roughness is relatively small, the influence of permeable surfaces can be reduced to an apparent slip in the tangential directions. When the inner-scaled sand equivalent roughness height, k_s^+, of the permeable surfaces is smaller than 1, the roughness have no effect on the wall-bounded flow Nikuradse et al. (1933). Jiménez (1994) adn Luchini et al. (1991) reported that the friction drag is linear to the difference between the streamwise and spanwise slips. This relationship was also reported by Abderrahaman-Elena and García-Mayoral (2017). They conducted an *a priori* analysis to investigate the drag reduction by anisotropic permeable surfaces. They found that the streamwise slip length, l_x, is defined as the distance from the interface at the slip velocity, U_s, to the corresponding virtual walls which act like smooth walls as shown in Figure 2.15(a). The span-wise slip length, l_z, is also defined as the distance from the interface to the corresponding virtual walls which act like smooth walls in the mean spanwise velocity, W, profile as shown in Figure 2.15(b). A drag reduction of about 10% was achieved for anisotropically permeable substrates with anisotropy ratios of $\sqrt{K_x^+/K_y^+} = \sqrt{K_x^+/K_z^+} \approx 5 \div 10$, where K_x, K_y and K_z are the permeabilities in streamwise, wall-normal, and spanwise directions, respectively.

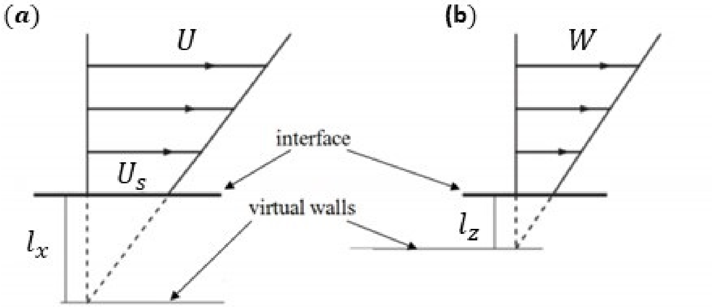

Figure 2.15. Sketch of (a) streamwise slip length and (b) span-wise slip length (Abderrahaman-Elena and García-Mayoral, 2017).

Anisotropic permeable surfaces can be used to reduce friction drag in a turbulent boundary layer. Drag reduction achieved with anisotropic permeable surfaces can be described by a linear function of the characteristic length of the permeable surface. This linear relationship could be similar to the one between drag reduction and riblet spacing observed by Itoh et al. (2006). Abderrahaman-Elena and García-Mayoral (2017) also found that when the streamwise permeability of an anisotropic permeable surface increases, the skin friction of the turbulent boundary layers over the anisotropic permeable surface decreases. When permeable surfaces have permeability in the vertical direction that is lower than that in the wall-parallel planes, drag reductions of up to 20% can be attained (Rosti et al., 2018). Gómez-de Segura and García-Mayoral (2019) conducted direct numerical simulations of channel turbulent boundary layers over anisotropic permeable surfaces with different permeabilities at a low Reynolds number of $Re_\tau = U_\tau \delta/\nu = 180$, where U_τ is the friction velocity. The schematic of a flow over a permeable surface is shown in Figure 2.16. They reported that the drag decrease is proportional to the difference between the streamwise and spanwise permeabilities for small wall-normal permeabilities below a critical threshold. The drag reduction decreases when the wall-normal permeability increases above the critical value. This phenomenon is linked to the creation of spanwise coherent structures that are attributed to Kelvin-Helmholtz-like instability. These spanwise coherent structures eventually overcome the drag-reducing impact of slip and cause drag to develop as they develop in the flow. Their results show a maximum reduction of up to 25% was achieved at $\sqrt{K_y^+} = \sqrt{K_y U_\tau/\nu} = 0.38$, where K_y is the permeability in the wall-normal direction.

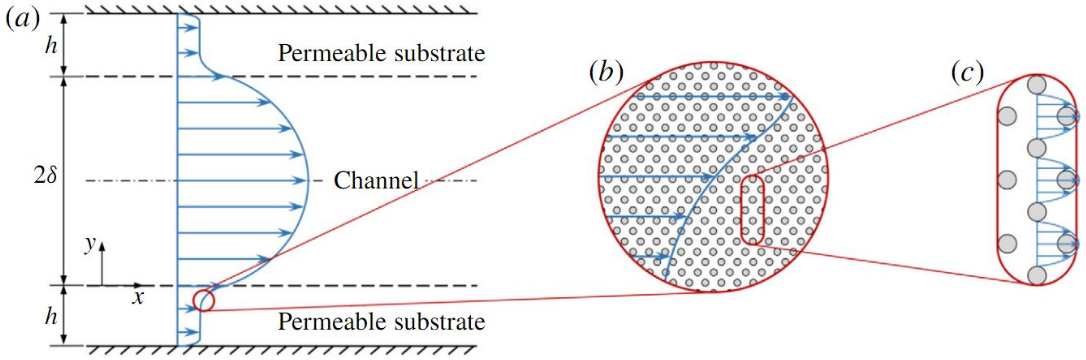

Figure 2.16. (a) Schematic diagram of (a) a channel flow over permeable surfaces, (b) flows inside permeable domain, and (c) detailed flows in inside permeable domain (Gómez-de Segura and García-Mayoral, 2019).

The performance of anisotropic permeable surfaces in reducing drag decreases when their permeabilities increase (Abderrahaman-Elena and García-Mayoral, 2017, Gómez-de Segura et al., 2018). An increase in friction drag was observed for turbulent boundary layers over isotropic permeable surfaces. Breugem et al. (2006) conducted a DNS of turbulent boundary layers over an isotropic permeable surface. Their results show that momentum exchange promotes the development of the Kelvin-Helmholtz (K-H) instability and raises the possibility of spanwise roller formation. The increase in skin friction and local shear stress is caused by strong K-H vortices near the wall and the skin friction for isotropic permeable media rises monotonically as permeability increases (Breugem et al., 2006, Kim et al., 2018). Hence, it is suggested that the performance reduction of anisotropic permeable surfaces is due to K-H vortices. The emergence of these rollers was proposed by Abderrahaman-Elena and García-Mayoral (2017) as a potential drag-degrading process for anisotropic permeable substrates. They used linear stability analysis to investigate the possibility of drag reduction by anisotropic permeable surfaces. Gómez-de Segura et al. (2018) conducted both linear stability analysis and direct numerical simulations to investigate the flow behaviour over anisotropic permeable surfaces. They found that wall-normal permeability primarily determines the generation of K-H rollers. This finding is consistent with the work by Jimenez et al. (2001) who reported that the rollers were triggered by the relaxation of the impermeability requirement at the wall after seeing the creation of Kelvin-Helmholtz rollers over substrates that were permeable only in the wall-normal direction.

Helmholtz resonators

Helmholtz resonators are suggested to manipulate particular turbulent scales in turbulent boundary layers. When a shear layer passes over a Helmholtz resonator as shown in Figure 2.17, the shear layer is affected by pressure fluctuations. This shear layer interacts with the pressure fluctuations to generate periodic vortices. These periodic vortices move towards the trailing edge of the orifice, which generates pressure fluctuations. These pressure fluctuations propagate back towards the leading edge and interact with the moving shear layer to generate other quasi-periodic vortices. These pressure fluctuations propagate into the resonator cavity, which ultimately increase the pressure fluctuations in the resonator. If the frequency of the pressure fluctuations occur at or near the resonant frequency, the resonator releases the air inside the cavity to the shear flow and reduces the internal pressure (Ghanadi et al., 2014). This resonance frequency is a function of both the speed of sound and the resonator geometry, as given by an empirical formula by Howard et al. (2000) as

$$f_r = \frac{c}{2\pi}\sqrt{\frac{S}{l_e V_c + 0.33L^2 S}}, \tag{2.5}$$

where c is the speed of sound; S is the cross-section area of the orifice; l_e is the effective length of the orifice; V_c is the resonator cavity; and L is the cavity depth.

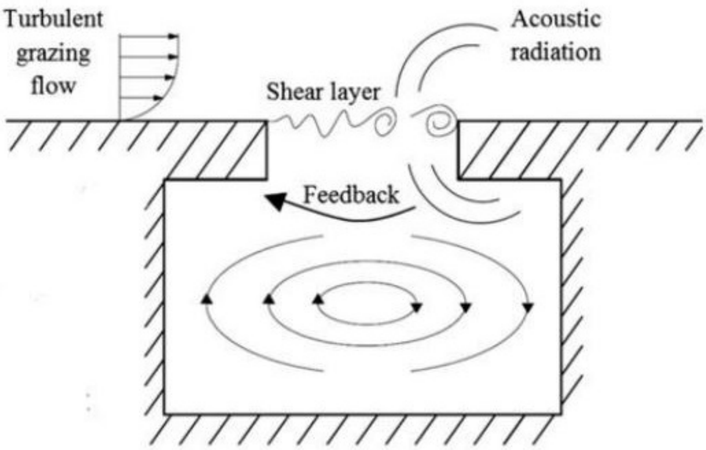

Figure 2.17. Flow behaviour over a cylindrical Helmholtz resonator (Ghanadi et al., 2014).

Resonators have been used to control turbulent boundary layers for drag reduction. Boundary layers can increase the resonant frequency of resonators. Panton and Miller (1975) conducted experiments of nine resonator configurations during a series of experiments with a constant flying speed. They found that the turbulent boundary layer increased the resonant frequency of the resonators. This study, however, considered one flow condition alone with a constant freestream velocity. This increase in the resonant frequency was also reported by Hemon et al. (2004) who investigated the effect of two resonator configurations with the same orifice geometry on a turbulent boundary layer. They also found that when the freestream velocity increases, the resonant frequency slightly increases. This is due to reduce end-correction term as the parcel of air is convected away. Ghanadi et al. (2014) conducted a series of experiments to measure the resonance frequency. Their results show that the power spectral density (PSD) difference between the pressure fluctuations in the no-control case and the resonator case maximises at a resonance frequency of $f_r = 748$ Hz, as shown in Figure 2.18(a). In contrast, the results of the PSD of streamwise velocity fluctuations in this resonator case do not show any noticeable changes at a frequency of 748 Hz as shown in Figure 2.18(b). The PSD of streamwise velocity fluctuations shows a reduction in the resonator case in comparison with the no-control case, throughout the frequency domain. A maximum reduction of 16% in turbulence intensity was observed at one-and-a-half orifice diameters downstream of the resonator in the work by Ghanadi et al. (2015). This reduction, however, vanished at about three orifice diameters downstream of the resonator. The resonator significantly reduced the turbulence intensity in the inner region at $y^+ < 200$ but did not affect the outer region. The impact of small-scale Helmholtz resonators on a turbulent boundary layer at $Re_\tau = 2280$ is examined in Dacome et al. (2024b). They considered two neck-orifice diameters of $d^+ \approx 68$ and 102. Only the streamwise velocity variations in the $y^+ \leq 25$ region are impacted by passive resonance, whereas the vertical velocity fluctuations occur in a layer up to $y^+ \approx 100$. There is a more than 20% attenuation of lower-frequency (larger scale) energy together with a narrow-band increase in streamwise turbulence kinetic energy at the resonance scale.

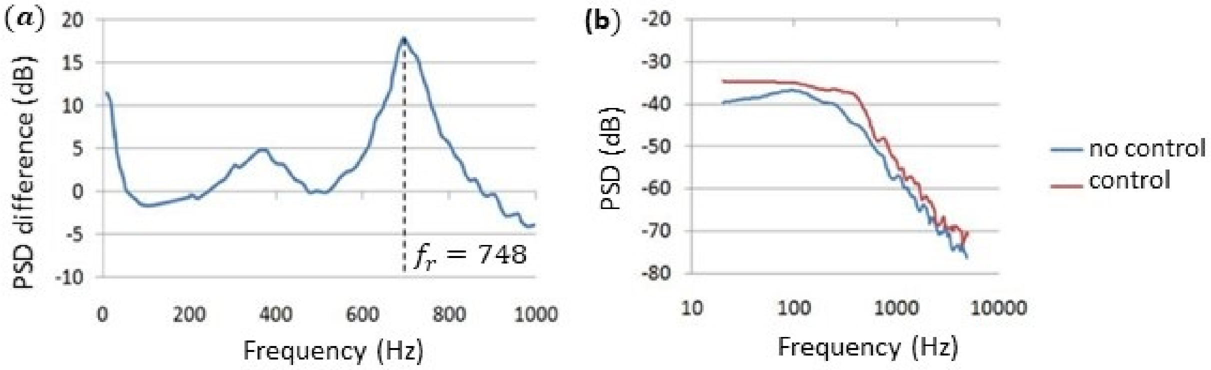

Figure 2.18. (a) PSD differences between the pressure fluctuations in the no control case and the case with Helmholtz resonators and (b) PSD of streamwise velocity fluctuations in both the no control case and the case with Helmholtz resonators (Ghanadi et al., 2014).

2.3 Turbulent boundary layers over a perforated surface

2.3.1 Perforated plates

Perforated surfaces have recently shown potential for turbulent boundary layer control. Silvestri et al. (2017a) conducted experiments to investigate the turbulent boundary layers over a cavity array. Different cavity diameters and spacings as shown in Figure 2.19 were considered. The sweep events were detected by the VITA technique. They found that the cavity array reduces both turbulence intensity and sweep events in the turbulence boundary layers. The reduction in sweep intensity linearly increases along with an increase in the viscous-scaled cavity diameter, $d^+ = dU_\tau/\nu$, where d is the cavity diameter, before maximising at $d^+ \approx 60$. There is no sweep intensity reduction at $d^+ < 20$, as the small cavity diameter limits the effect of the cavity on the sweep event. Moreover, separation of the shear layer and increased turbulence energy production in the near-wall region occurred at $d^+ \geq 145$. The maximum reduction in sweep intensities and turbulence occurs at 13% and 14%, respectively. The authors suggested that the reduction in the sweep event would result in a reduction in skin friction drag. A friction drag reduction due to a perforated plate was then reported by Gowree et al. (2019) who conducted both hot-wire and laser Doppler anemometry (LDA) to investigate turbulent boundary layers over a perforated plate. The friction coefficients were estimated by the Clauser chart method proposed by Clauser (1956). The results show that for $d/h \leq 1$, where h is the orifice depth, the skin friction drag reduces, while for every $d/h \geq 1$, it increases. The authors proposed that the mechanism of skin friction drag reduction of the perforated plate was comparable to that of riblets by adjusting the transverse velocities.

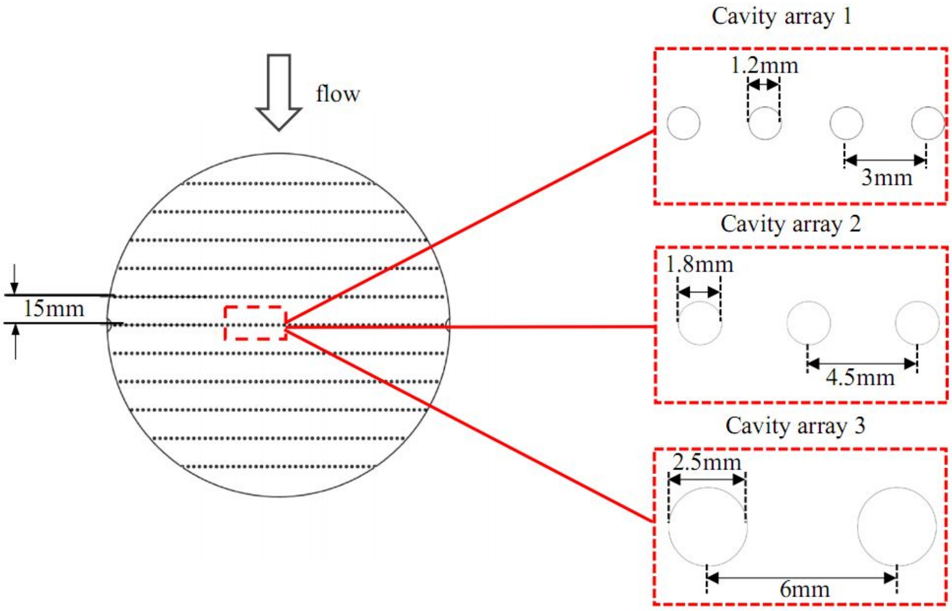

Figure 2.19. Schematic of cavity arrays (Silvestri et al., 2017a).

Scarano et al. (2022, 2023) investigated the modification of turbulent boundary layers and the reduction in skin friction drag due to different perforated plates using hot-wire anemometry. Different open area ratios (OAR) of the perforated plate from 0.12 to 0.47, were considered. The orifice diameter of $80 \leq d^+ \leq 250$ and the orifice spacing of $150 \leq L^+ \leq 1075$, where $L^+ = LU_\tau/\nu$, were tested. They found that an increase in the OAR results in an increase in friction drag reduction, $(C_f - C_{f0})/C_{f0}$, where C_f and C_{f0} are the friction coefficients of the controlled and uncontrolled turbulent boundary layers, respectively, as shown in Figure 2.20. A maximum reduction of 30% in local skin friction drag was achieved. The modification of the boundary layer with an increase in the wake parameter and the shape factor, and a reduction in skin friction drag is similar to the turbulent boundary layers with wall-normal blowing (Kametani et al., 2015) or with an adverse pressure gradient (Monty et al., 2011). Bhat et al. (2021) conducted a numerical simulation on a turbulent boundary layer over a perforated plate with a backing chamber. They noticed instantaneous wall-normal velocity components through the orifices. This unsteady blowing effect could lift the quasi-streamwise vortices, which results in an increase in energy in the outer region and the formation of a second hump in burst intensity. The upward displacement of these structures, carrying low-momentum fluid, then modifies the mean velocity in a manner that reduces skin friction. A similar mechanism of skin friction reduction in turbulent boundary layers due to wall-normal blowing was mentioned by Kornilov (2015). Scarano et al. (2024) recently investigated the effect of a perforated plate on large-scale structures of turbulent boundary layers at the Reynolds number of $Re_\tau = \delta U_\tau/\nu \approx 1000$, where δ is the boundary layer thickness. They discovered that the premultiplied energy spectrogram's contour displayed a two-peak behaviour, with the inner peak shifting higher and towards lower wavelengths, indicating that the cavities in the perforated area were responsible for shortening and raising the streaks. The outer peak may be linked to increased inner/outer layer interaction and turbulent mixing. Measurements of particle image velocimetry, carried out in a streamwise plane downstream of the cavities, revealed a considerable amplification of the ejections contribution along with an increase in Reynolds shear stress. Chen et al. (2024) experimentally studied the amplitude modulation in a turbulent boundary layer over a perforated plate $Re_\tau \approx 300$. Their results show that contrary to the usual phenomenon over the smooth wall scenario, the amplitude modulation effects show that the near-wall small-scale turbulence is suppressed by the positive and enhanced by the negative large-scale velocity streaks, respectively. The porous wall greatly reduces the interaction between the inner small-scale and outside large-scale structures, which helps to lower skin friction overall.

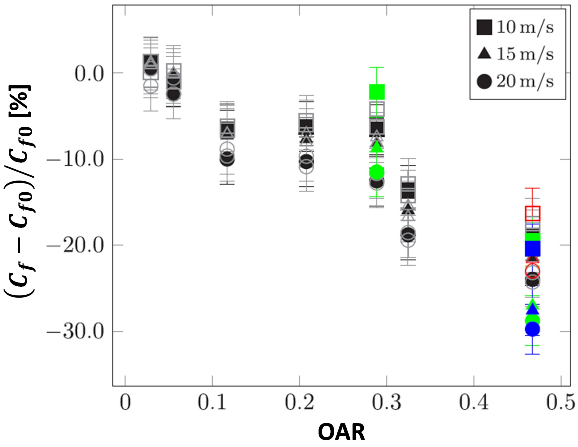

Figure 2.20. Drag reduction as a fuction of the open area ratio (OAR) (Scarano et al., 2023).

Silvestri et al. (2018, 2017b) found that adding a backing chamber under a perforated plate increased the sweep reduction of a turbulent boundary layer. In their study, two types of backing chambers were considered: a common backing chamber and an individual backing chamber with a diameter of 1.2 mm and a depth of 4 mm, $h/D = 3.3$. The backing chamber depth varied from 25 mm to 75 mm, as shown in Figure 2.21. This caused the backing chamber volume for one orifice, V, to vary from $V^+ = V(U_\tau/\nu)^3 = 2.05 \times 10^6$ to 6×10^6, where U_τ is the skin friction velocity and ν is the kinematic viscosity of the air. The results show that the perforated plate with both chamber configurations reduced turbulence intensity and sweep intensity. The largest reduction in sweep intensity accounted for approximately 7% at $Re_\theta = 3771$ and $V^+ = 6 \times 10^6$ in comparison with the sweep intensity of the turbulent boundary layer over a smooth plate. The sweep intensity reduction was reported to increase with an increase in the backing chamber volume before reaching a threshold of $V^+ = 5 \times 10^6$, as shown in Figure 2.22. The mechanism of the sweep reduction could be due to friction loss while the sweep penetrate through the orifices (Silvestri et al., 2018). This is supported by Severino et al. (2022) who investigated the relationship between sweep reduction in turbulent boundary layers over a perforated plate and the orifice length. Results show that the sweep reduction increases with increasing orifice length. Hence, it is suggested that the wall shear stress of the turbulent boundary layer over the perforated plate is reduced by reducing the sweep energy.

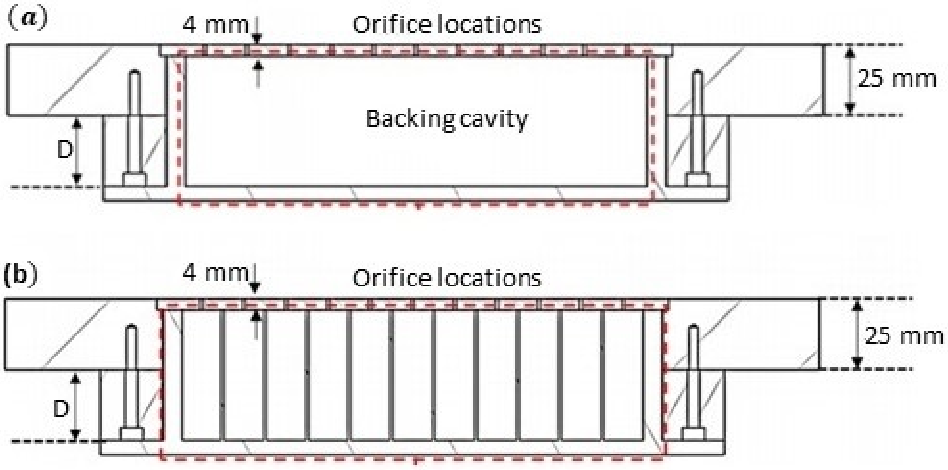

Figure 2.21. Schematic of cavity array with a (a) common backing cavity and (b) individual backing cavities via use of a mesh (Silvestri et al., 2018).

Jafari et al. (2022) reported the effect of different backing chamber configurations under a perforated plate on turbulent boundary layer structures. The backing chamber under the perforated plate had four volume configurations, including chambers that connected all the square orifices in the streamwise direction, chambers that connected all the square orifices in the streamwise direction, individual chambers, and a common chamber that connected all the square orifices as shown in Figure 2.23. The results show that the common and individual chambers reduced more turbulence intensity than the chamber that connected all the square orifices in streamwise and spanwise directions. A maximum reduction of up to 80% in the pre-multiplied spectrum of streamwise velocity fluctuations at large scales was observed in the case of the individual chamber. The authors found a correlation between possible resonant frequency, integral length scales, and turbulence reduction. The individual chamber generated higher resonant frequency but smaller integral length scales than those in the common chamber cases. The authors hypothesised that acoustic excitation inside the chamber affects the unsteady transpiration through the perforated plate. The increase in excitation frequency results in an increase in turbulence reduction in the turbulent boundary layer. This hypothesis was supported by Panton et al. (1987) and Ghanadi et al. (2015) who also reported a reduction in turbulence intensity of turbulent boundary layers due to resonators.

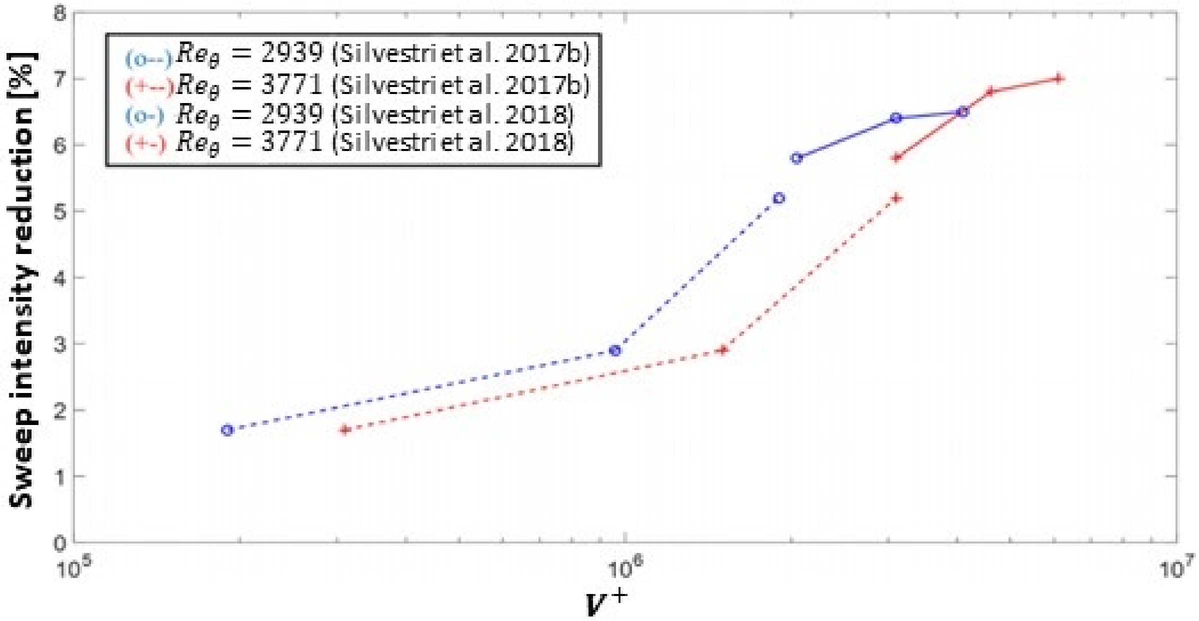

Figure 2.22. Reduction in sweep intensity as a fuction of the viscous-scaled backing volume (Silvestri et al., 2018, 2017b).

The transpiration through the perforated plate was modeled in resolvent analysis as impedance boundary conditions. This wall impedance represent the relationship between the velocity and the force applied to the fluid at the wall via Cauchy stresses and is given as (Jafari et al., 2023):

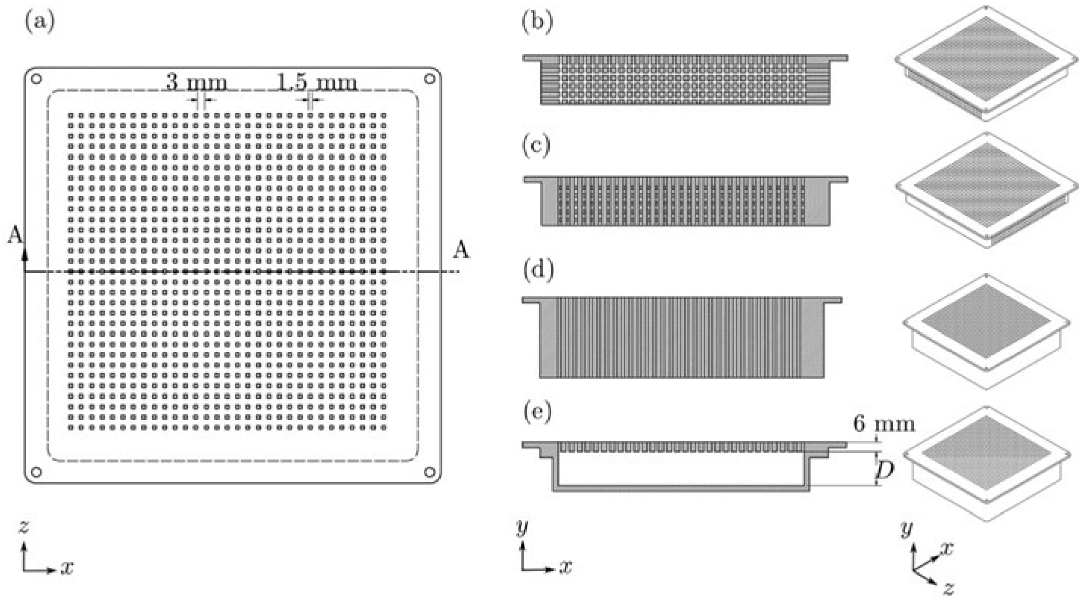

Figure 2.23. Schematics of the porous inserts. (a) Top view of the porous surface, and cross-section A–A for: (b) chambers that connected all the square orifices in the streamwise direction, (c) chambers that connected all the square orifices in the spanwise direction, (d) individual chambers, and (e) a common chamber (Jafari et al., 2022).

$$\overline{Z} = \begin{bmatrix} \overline{Z}_{tt} & \overline{Z}_{tn} \\ \overline{Z}_{nt} & \overline{Z}_{nn} \end{bmatrix}, \tag{2.6}$$

and

$$\overline{Z} \begin{pmatrix} \overline{u}_t \\ \overline{u}_n \end{pmatrix} = \begin{pmatrix} -\overline{\tau}_{nt} \\ \overline{p} - \overline{\tau}_{nn} \end{pmatrix}, \tag{2.7}$$

where — represents dimensional variables, t is a unit vector tangent to the surface and n is the wall-normal unit vector pointing into the surface. $\overline{Z}_{nn}$ represents the relationship between the presure at the wall and the wall-normal velocity. When the tangent impedance is ignored, $\overline{Z}_{tn} = 0$ and $\overline{\tau}_{nn} = 0$, the $\overline{Z}_{nn} = \overline{p}/\overline{u}_n$. The impedance of $\overline{Z}_{nn}$ is defined as pressure-driven impedance. When the tangent impedance is considered, $\overline{Z}_{tn} \neq 0$, then the impedance is refered as the wall-shear-driven impedance.

Jafari et al. (2023) investigated the drag reduction in turbulent boundary layers over a perforated plate using a resolvent analysis with wall-shear-driven impedance boundary conditions. They discovered that the near-wall cycle and very-large-scale motion modes can be suppressed by wall impedance. Consequently, friction drag and Reynolds stress are reduced. Figure 2.24 shows the velocity structures for the near-wall mode of the uncontrolled turbulent boundary layers and the turbulent boundary layers with different wall impedances. The figure shows that the near-wall structures in the turbulent boundary layers were reduced in comparison with those in the uncontrolled turbulent boundary layers. Józsa et al. (2019) used DNSs of turbulent channel flows at $Re_\tau = 180$ and 1000 to study the mechanics of compliant surfaces driven by wall shear stresses with only in-plane velocity response. They discovered that while small-scale passive spanwise wall motions result in significant drag penalties, large-scale passive streamwise wall fluctuations can reduce friction drag by at least 3.7±1%. Jafari et al. (2024) used a resolvent analysis with a measured impedance wall to examine passive perforated surfaces at particular frequencies. It was discovered that the range of 0.4π to 1.4π was the effective angle of impedance for controlling near-wall turbulence. The phase difference between the pressure and wall-normal fields at the wall is determined by the impedance angle. Consequently, the effect of impedance angle on near-wall cycles suggests that the main determinants of the suppression or amplification of the near-wall cycles are the pressure field and wall-normal phase (Jafari et al., 2024).

Fukagata et al. (2008) applied wall-shear-driven impedance in direction number simulations (DNS) of turbulent boundary layers over a compliant surface. Their results show that the wall-shear-driven impedance which accounts for both pressure and wall shear could generate a reduction of up to 8% in friction drag. To achive drag reduction, the wall-normal velocities should be in phase with the pressure fluctuation at the wall. Figure 2.25 shows the Reynolds shear stress profiles near the wall for the turbulent boundary layers over a compliant wall compared with the solid wall. The results show that the compliant wall reduces the Reynolds shear stress near the wall, which is associated with the drag reduction. Luhar et al. (2015) used a Resolvent analysis to investigate the effects of compliant surfaces on wall turbulence. The compliant surfaces are modelled as a complex wall impedance linking pressure and velocity. They found a drag reduction when the wall-normal velocities and the pressure fluctuations are in phase, which consistent with

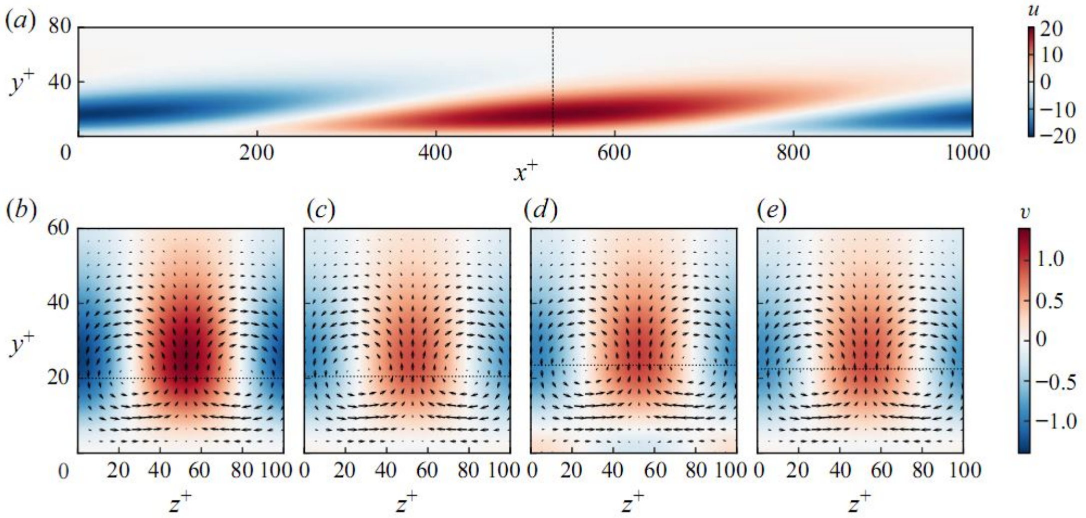

Figure 2.24. Velocity structure for near-wall mode: (a) streamwise velocity amplitude in the streamwise wall-normal plane for uncontrolled flow, (b–e) wall-normal and spanwise velocity fields in the spanwise wall-normal plane. The dashed line in (a) shows the streamwise location where the magnitude of streamwise velocity is maximum and the cross-sections for (b–e) are made.(a,b) Uncontrolled flow, (c) $Z_{yx} = Z_{xy} = 0$, (d) $Z_{yx} = 1 + 5i$ and $Z_{xy} = 0$, (e) $Z_{xy} = 1 + 1i$ and $Z_{yx} = 0$ ($Z_xx = 3$ + 3i, $Z_yy = 0.2$ + 3i). The horizontal dotted line in (b–e) shows the centreline of the streamwise vortices. (Jafari et al., 2023).

the work by Fukagata et al. (2008). They also found that wall impedance of compliant walls with positive damping is correlated with the suppression of the very large scale structures.

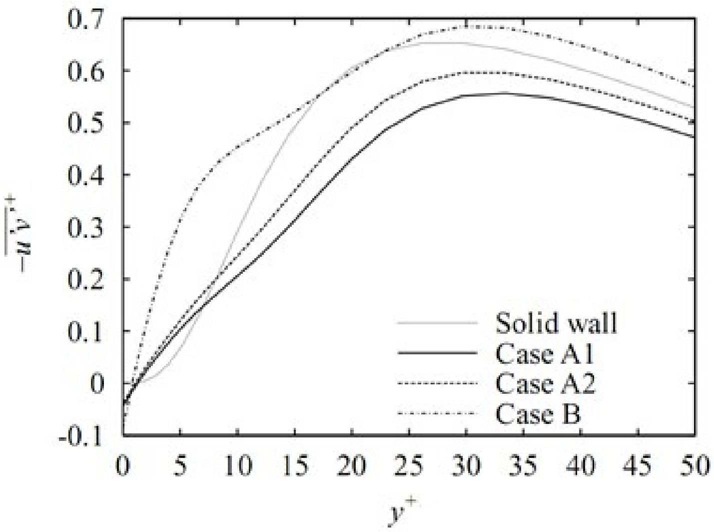

Figure 2.25. Reynolds shear stresses near the wall. Cases A1, A2, and B represent the compliant wall (Fukagata et al., 2008).

2.3.2 Acoustic liners

Acoustic liners are first used to reduce aircraft noise. Covering the interal wall of nacelle of an aircraft engine by acoustic liners can reduce the engine noise Ma and Su (2020). An acoustic liner typically schematic of a perforated plate and a hard-backed honeycomb, which behaves like a quarter-wavelength resonator. In addition to improving the liner's ability to absorb sound, the perforated face plate keeps the aerodynamic flow on the nacelle's internal wall as smooth as feasible. This type of acoustic liners is named single degree of freedom (SDOF) as shown in Figure 2.26(a). The SDOF liner can provide maximum acoustic absorption at the resonant frequency. Larger honeycomb depth results in more efficient noise absorption at low frequencies. However, the noise absorption bandwidth of the SDOF liner is narrow. To increase the noise absorption bandwidth, a septum is utilised to divide the honeycomb into two sections, creating a double degree of freedom (DDOF) arrangement. The DDOF liner's noise absorption bandwidth is increased at the expense of its intricate structure and heavy weight Ma and Su (2020).

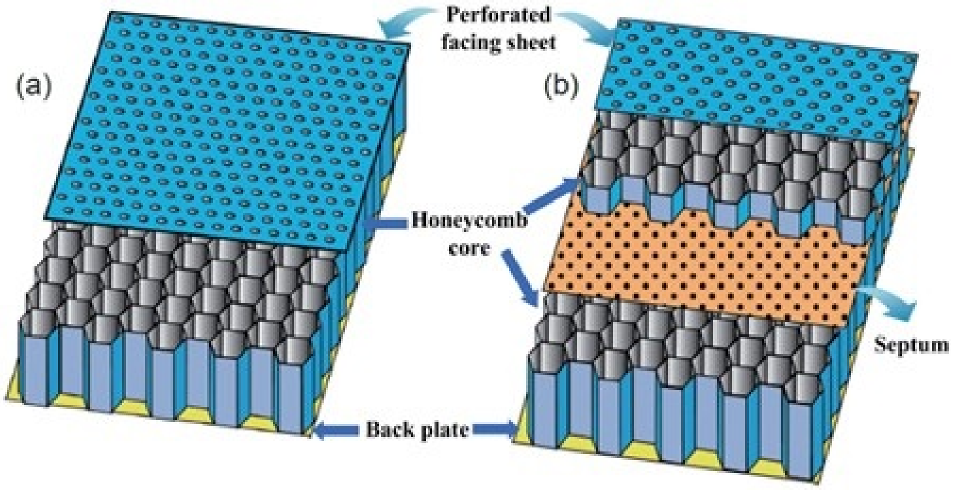

Figure 2.26. Schematics of basic structures of (a) SDOF and (b) DDOF liners (Kempton, 2011).

A conventional SDOF acoustic liner only alow the flow move verticaly to its perforated plate. It, hence, is considered as an array of Helmholtz resonators as shown in Figure 2.27. The resonant frequency of this array of Helmholtz resonators is given as (Ma and Su, 2020):

$$f_r = \frac{c}{2\pi}\sqrt{\frac{S}{V*(l+\Delta l)}}, \tag{2.8}$$

where c is the speed of sound, l is the perforated plate thickness, V is the cavity volume, and Δl is the correction factor of the orifice length, which accounts for the vibration of mass inside the orifices. As the honeycomb creates individual cavities, this acoustic liner is called local reacting acoustic liner (Nayfeh et al., 1975). The viscous and vortical flow in and around the face plate orifices is responsible for the dissipation of sound energy. The highest absorption coefficient occurs when the particle velocity anti-resonance plane passes through the perforated face plate as the excitation frequency moves around the resonance frequency. Insufficient resistance above or below the face plate orifice results in poor absorption performance. Consequently, the sound absorption bandwidth of a local-reacting liner is very limited for this type of acoustic liner. The perforated plate is the major contribution to the acoustical resistance and the cavity provides the dominant portion of acoustical reactance. The orifice diameter, orifice length, and cavity volume are the main parameters of this such liner.

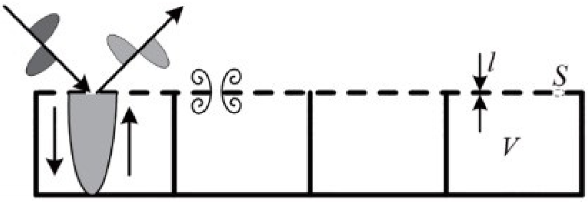

Figure 2.27. Schematics of local-reacting liner (Parrott and Jones, 2006).

Figure 2.28 shows a schematic of exextended-reacting liner. Exextended-reacting liner contains absorber or metal foam instead of a cavity. In exextended-reacting liner, the bulk absorber provides the resistance to the wave motion and the sound wave can travel parallel to the perforated plate. When there is no high particle velocity concentration through the face plate orifice, the distributed energy dissipation shows a more viscous control mechanism. The high particle velocity region still faces resistance when the particle velocity anti-resonance plane is attenuated from the surface of the porous media (such as metal foam) into the bulk material. Hence, extended-reacting liner is known to exhibit broadband sound absorption (Parrott and Jones, 2006).

Acoustic liner can be divided into passive and adaptive acoustic liners (Ma and Su, 2020). The passive acoustic liners have a fixed configuration, such as mesh-cap honeycomb, wide-chamber and variable-depth liners, and metal foam liner. The mesh-cap honeycomb consist of multi-layer liners as shown in Figure 2.29(a). A novel concept of multi-layer liner

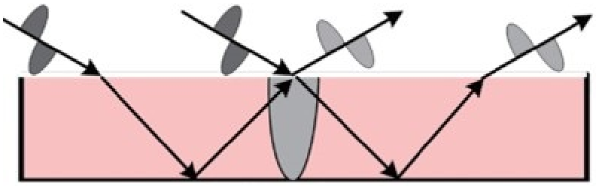

Figure 2.28. Schematics of a local-reacting liner (Parrott and Jones, 2006).

called mesh-cap liner was developed to gain more broadband noise absorption (Ayle, 2013). The mesh caps were secured to the honeycomb cavity wall without separating the honeycomb, in contrast to the inherent septum in a conventional multi-layer acoustic liner. Improving the complete liner's mechanical performance was advantageous (Syed and Ichihashi, 2008). Wide-chamber and variable-depth liners are shown in Figure 2.29(b). According to experimental results by (Jones et al., 2014), the sound absorption performance of variable-depth liners with varying material qualities was comparable. Two mounting designs were found to clearly absorb sound throughout a wide frequency range, although the greatest attenuation was achieved with a significant depth at the leading edge. Mental foam liner shown in Figure 2.29(c) demonstrated a slight increase in sound attenuation compared with untreated hard wall (Bozak et al., 2019). The impact of grazing flow on grooved over-the-rotor acoustic casing treatment was examined by Bozak and Dougherty (2018). According to their findings, as the grazing flow Mach number rose, the foam metal treatment liner expanded the absorption curve and reduced the peak absorption frequency.

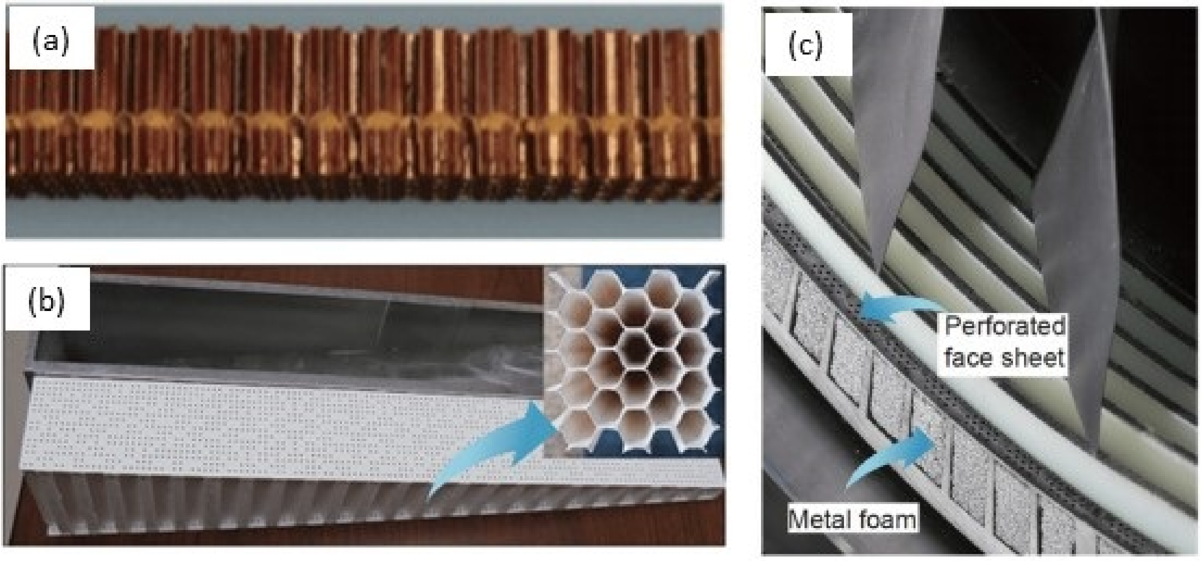

Figure 2.29. Photos of (a) mesh-cap honeycomb (Ayle, 2013), (b) wide-chamber and variable-depth liners (Jones et al., 2014), and (c) metal foam liner (Bozak et al., 2013).

Figure 2.30(a) shows a bias flow liner which is an adaptive acoustic liner. The different bias flow velocities through the aperture of the perforated face plate give the bias flow liner a broad and adjustable sound absorption capability. Bechert et al. (1977) used experiments to demonstrate the bias flow liner's physical mechanism. According to the author, the acoustic energy dissipation was caused by vorticity shedding. The kinetic energy of fluctuating vortices around the orifices was converted from acoustic energy. Acoustic energy was then converted to heat via the vorticity shedding effect. Increasing the bias flow velocity was shown to enhance orifice resistance while decreasing orifice reactance McAuliffe (1950). In Figure 2.30(b), a novel liner idea known as the zero mass flow liner (ZMFL) was introduced. An unstable, oscillating bias flow with zero nett mass flow was created in this liner when high amplitude sound struck a perforated face plate (Heuwinkel et al., 2001). The ZMFL and traditional bias flow liner had a similar sound absorption technique. Without any electrical or mechanical components, the aeroacoustic actuator proved a good substitute for loudspeakers in difficult environments. The trials showed a considerable dependence on frequency and sound pressure level. In comparison to a traditional steady bias flow liner, the driving mass flow rate of ZMFL showed a 60% drop (Lahiri et al., 2011).

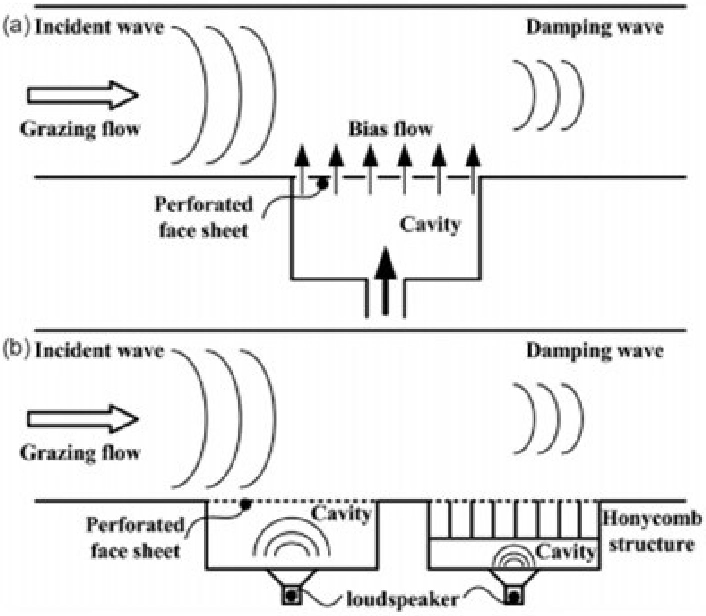

Figure 2.30. Schematics of (a) bias flow liner, (b) ZMFL (left) and hybrid ZMFL (right).

In order to reach the needed noise levels, the aerodynamic drag caused by acoustic liners in an aircraft engine nacelle was accepted as a necessary penalty. Such liners are known to enhance drag in comparison to a smooth surface (Tam et al., 2014). Howerton and Jones (2015) used the static pressure drop inside a lined duct to compute a resistance factor (λ). By using this method, they showed that for a typical liner design, lowering the perforate hole diameter decreased λ. It should be noted that all of the perforates in Figure 2.19 had a higher resistance factor than a hard wall (HW). Schiller et al. (2019) examined the relative drag and acoustic performance of a novel kind of variable depth liner that had resonator pairs connected by shared inlet volumes just beneath the facesheet. Compared to earlier designs, this kind of liner may be able to achieve a targeted impedance with fewer facesheet openings and, thus, less drag. The prototype liner may attain the same impedance as the baseline variable depth liner at discrete frequencies with 50% less open area, according to measurements made in both the normal incidence and grazing flow impedance tubes. In comparison to the baseline design, this results in a 75% reduction in the drag penalty.

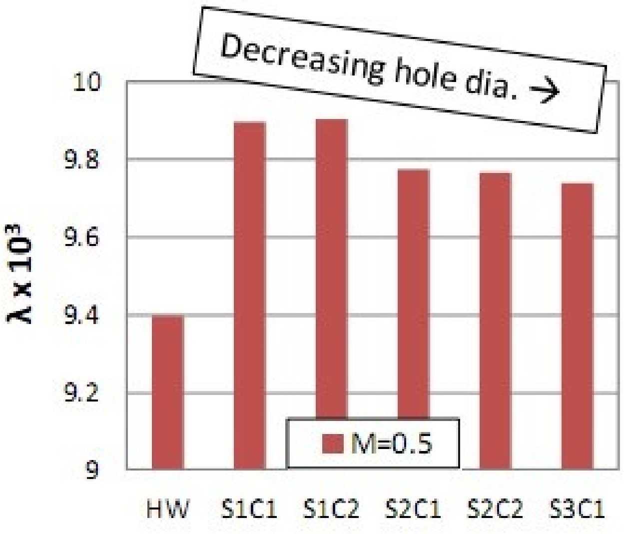

Figure 2.31. The effect of perforate hole diameter on resistance factor (Howerton and Jones, 2023)

Acoustic liners in a grazing flow cause both friction and pressure drag. The actual drag of acoustic liners increased from 2% to 500% in comparison with a smooth wall reported in several works by Howerton and Jones (2015), Jasinski and Corke (2020), Wilkinson (1983). Howerton and Jones (2015, 2016, 2017), Jones et al. (2004) conducted experiments in NASA's Grazing Flow Impedance Tube facility using static pressure drop methods. They tested both conventional and unconventional configurations and observed that the drag increases from 16% to 350% in comparison with a smooth wall. The parameters including the orifice diameter, orifice depths, and plate prosity show a significant impact on the total drag of acoustic liners. Howerton and Jones (2015) found that at a constant prosity, when the orifice diameter reduces, the drag reduces. Howerton and Jones (2017) reported an increase of 50% in drag at a prosity of $\sigma = 0.08$ but an increase of 400% at $\sigma = 0.3$.

The mechanisms of drag increase by acoustic liners could be similar to those over porous surfaces with only wall-normal permeability. When a flow sweeps over acoustic liners, its drag has both roughness and porous components. When a flow moves over a rough surface, the surface topography induces pressure drag (Chung et al., 2021, Leonardi et al., 2003). The surface reaches a fully rough state when pressure drag outweighs viscous drag, causing the skin-friction coefficient to become independent of the Reynolds number (Chung et al., 2021, Leonardi et al., 2003). The flow through various common porous surfaces, including metal foams and conglomerates, can be described using the Darcy and Forchheimer permeability tensors, which quantify how easily fluid moves through the porous material. Shahzad et al. (2023) estimated induced pressure drag due to acoustic liners by DNS simlation at Reynolds numbers of $Re_\tau = 500 - 2000$. They found that the acoustic liners increase the total drag with an increasing relevance of pressure drag. When the inverse of the Forchheimer coefficient reduces,$1/\alpha^+$, the pressure drag reduces. For examples, at $Re_\tau \approx 500$ the pressure drag coefficient reduces from $C_{fp} = 0.539^{-3}$ at $1/\alpha^+ = 1.73$ to $C_{fp} = 0.106^{-3}$ at $1/\alpha^+ = 0.0528$ for the considered liner configurations (Shahzad et al., 2023).

2.4 Conclusion of literature and research gaps

Research in the literature indicates the potential for a perforated plate with a backing cavity to control turbulent boundary layers (Bhat et al., 2021, Jafari et al., 2022, Silvestri et al., 2018, 2017b). However, drag reduction and its mechanisms in turbulent boundary layers due to a perforated plate with a backing cavity have not been fully understood. Hence, there are still several research gaps that must be filled before a device like this can be considered successful and applied in the real world.

Therefore, this thesis aims to investigate the potential of a perforated surface for skin friction drag in turbulent boundary layers and develop an understanding of drag reduction mechanisms. To achieve this aim, the following objectives are defined to address the gaps:

- As discussed in Section 2.1.1 and Section 2.3, the reduction in turbulence intensity due to a perforated plate with a backing cavity has been reported but the mechanisms of turbulence reduction due to the perforated plate have not been fully understood. The near-wall region of turbulent boundary layers plays an important role in turbulence generation as well as the wall shear stress. Ejections and sweep events form burst events which are accounted for by turbulent momentum transfer and shear stress. As a result, these events mainly contribute to turbulence generation and skin friction drag. Hence, an important gap in the research of a perforated plate with a backing cavity is to determine the mechanisms of turbulence reduction due to the perforated plate. To address this gap, the modification of the near-wall region in turbulent boundary layers needs to be determined. Chapter 3 addresses this problem by examining the turbulent boundary layers over a perforated plate with a backing cavity in the near-wall region.

- Section 2.1.2 and Section 2.3 show that perforated plates increase the large scales in turbulent boundary layers even at relatively small Reynolds numbers. However, the interaction between small and large scales in the turbulent boundary layers over perforated plates has received comparatively less attention. When the large-scale energy increases in the outer region, these large-scale structures directly modulate the small-scale structures in the near-wall regions. As a result, the large scales in the outer region affect the near-wall turbulence and reduce skin friction drag. Therefore, determining the interaction between the small and large scales in the turbulent boundary layers over a perforated plate is one of the key research gaps in this field. To address this gap, small and large scales need to be decomposed and their energy patterns need to be analysed. Therefore, Chapter 4 investigates the interaction between small and large scales in turbulent boundary layers to address this gap.

- The discussion in Section 2.2.1 and Section 2.3 shows a significant lack of knowledge about the turbulence characteristics of the turbulent boundary layers with wall-normal velocities through a perforated plate. It was suggested that the wall-normal velocities with a zero-mass flux created by the interaction between the flow inside and outside the backing cavity play a role in reducing turbulence intensity and friction drag. The wall-normal velocities could lift the coherent structures further from the wall, reducing turbulence intensity and wall-shear stresses. The effects of the amplitude and frequency of wall-normal velocities through a perforated plate in near-wall turbulence are not well understood. Therefore, Chapter 5 investigates the effect of jet amplitude and frequency through a perforated plate on turbulent boundary layers.

- Extensive research gaps exist regarding how the relationship between wall-normal velocities and pressure at the wall affects the turbulent boundary layers over a perforated plate with a backing cavity. The relationship between wall-normal velocities and pressure at the wall can be represented by acoustic impedance, but the relationship between the acoustic impedance of the perforated plate and the turbulent boundary layer in a way that reduces friction drag has not been fully understood. To address this gap, different acoustic impedances generated by a perforated plate with a backing cavity were used to control turbulent boundary layers. The correlation between the wall acoustic impedance and the modification of the burst events, turbulence intensity, and turbulence energy of the turbulent boundary layers over the perforated plate also needs to be discussed. Therefore, Chapter 6 addresses this gap by investigating the impact of the acoustic impedance of a perforated plate on near-wall turbulence.

References

Abderrahaman-Elena, N. and García-Mayoral, R. (2017). Analysis of anisotropically permeable surfaces for turbulent drag reduction. *Physical Review Fluids*, 2(11):114609.

Adrian, R. J. (2007). Hairpin vortex organization in wall turbulence. *Physics of Fluids*, 19(4).

Adrian, R. J., Meinhart, C. D., and Tomkins, C. D. (2000). Vortex organization in the outer region of the turbulent boundary layer. *Journal of fluid Mechanics*, 422:1–54.

Ayle, E. (2013). Acoustic honeycomb with perforated septum caps. US Patent 8,413,761.

Bechert, D., Michel, U., and Pfizenmaier, E. (1977). Experiments on the transmission of sound through jets. In *4th Aeroacoustics Conference*, page 1278.

Bechert, D. W., Bruse, M., Hage, W. v., Van der Hoeven, J. T., and Hoppe, G. (1997). Experiments on drag-reducing surfaces and their optimization with an adjustable geometry. *Journal of Fluid Mechanics*, 338:59–87.

Benschop, H. and Breugem, W.-P. (2017). Drag reduction by herringbone riblet texture in direct numerical simulations of turbulent channel flow. *Journal of Turbulence*, 18(8):717–759.

Bernard, P. S., Thomas, J. M., and Handler, R. A. (1993). Vortex dynamics and the production of Reynolds stress. *Journal of Fluid Mechanics*, 253:385–419.

Bhat, S., Silvestri, A., Cazzolato, B., and Arjomandi, M. (2021). Mechanism of control of the near-wall turbulence using a micro-cavity array. *Physics of Fluids*, 33(7):075114.

Bogard, D. and Tiederman, W. (1986). Burst detection with single-point velocity measurements. *Journal of Fluid Mechanics*, 162:389–413.

Bozak, R. and Dougherty, R. P. (2018). Measurement of noise reduction from acoustic casing treatments installed over a subscale high bypass ratio turbofan rotor. In *2018 AIAA/CEAS aeroacoustics conference*, page 4099.

Bozak, R., Hughes, C., and Buckley, J. (2013). *The aerodynamic performance of an over-the-rotor liner with circumferential grooves on a high bypass ratio turbofan rotor*, volume 55225. American Society of Mechanical Engineers.

Bozak, R., Jones, M. G., Howerton, B. M., and Brown, M. C. (2019). Effect of grazing flow on grooved over-the-rotor acoustic casing treatments. In *25th AIAA/CEAS aeroacoustics conference*, page 2564.

Breugem, W.-P., Boersma, B.-J., and Uittenbogaard, R. E. (2006). The influence of wall permeability on turbulent channel flow. *Journal of Fluid Mechanics*, 562:35–72.

Cannata, M., Cafiero, G., and Iuso, G. (2020). Large-scale forcing of a turbulent channel flow through spanwise synthetic jets. *AIAA Journal*, 58(5):2042–2052.

Cengel, Y. and Cimbala, J. (2013). *Ebook: Fluid mechanics fundamentals and applications.* McGraw Hill.

Chen, X., Feng, Z., and Ye, Q. (2024). Amplitude modulation in turbulent boundary layer over anisotropic porous wall. *Physics of Fluids*, 36(2):025127.

Choi, H., Moin, P., and Kim, J. (1994). Active turbulence control for drag reduction in wall-bounded flows. *Journal of Fluid Mechanics*, 262:75–110.

Choi, K.-S. (1989). Near-wall structure of a turbulent boundary layer with riblets. *Journal of Fluid Mechanics*, 208:417–458.

Chung, D., Hutchins, N., Schultz, M. P., and Flack, K. A. (2021). Predicting the drag of rough surfaces. *Annual Review of Fluid Mechanics*, 53(1):439–471.

Clauser, F. H. (1956). The turbulent boundary layer. *Advances in applied mechanics*, 4:1–51.

Coles, D. (1956). The law of the wake in the turbulent boundary layer. *Journal of Fluid Mechanics*, 1(2):191–226.

Corino, E. R. and Brodkey, R. S. (1969). A visual investigation of the wall region in turbulent flow. *Journal of Fluid Mechanics*, 37(1):1–30.

Coxe, D. (2019). *Drag Reduction in Turbulent Pipe Flow by Transverse Wall Oscillations at Low and Moderate Reynolds Number.* PhD thesis, Arizona State University.

Dacome, G., Mörsch, R., Kotsonis, M., and Baars, W. J. (2024a). Opposition flow control for reducing skin-friction drag of a turbulent boundary layer. *Physical Review Fluids*, 9(6):064602.

Dacome, G., Siebols, R., and Baars, W. (2024b). Small-scale Helmholtz resonators with grazing turbulent boundary layer flow. *Journal of Turbulence*, page 2412586.

Deshpande, R., Chandran, D., Smits, A. J., and Marusic, I. (2023). On the relationship between manipulated inter-scale phase and energy-efficient turbulent drag reduction. *Journal of Fluid Mechanics*, 972:A12.

Duvvuri, S. and McKeon, B. (2016). Nonlinear interactions isolated through scale synthesis in experimental wall turbulence. *Physical Review Fluids*, 1(3):032401.

Fu, Y., Yuan, C., and Bai, X. (2017). Marine drag reduction of shark skin inspired riblet surfaces. *Biosurface and Biotribology*, 3(1):11–24.

Fukagata, K. and Kasagi, N. (2003). Drag reduction in turbulent pipe flow with feedback control applied partially to wall. *International Journal of Heat and Fluid Flow*, 24(4):480–490.

Fukagata, K., Kern, S., Chatelain, P., Koumoutsakos, P., and Kasagi, N. (2008). Evolutionary optimization of an anisotropic compliant surface for turbulent friction drag reduction. *Journal of Turbulence*, 9:N35.

Gad-el Hak, M. and Bandyopadhyay, P. R. (1994). Reynolds number effects in wall-bounded turbulent flows. *Applied Mechanics Reviews*, 47(8):307–365.

Gad-el Hak, M., Pollard, A., and Bonnet, J.-P. (2003). *Flow control: fundamentals and practices*, volume 53. Springer Science & Business Media.

Ghanadi, F., Arjomandi, M., Cazzolato, B., and Zander, A. (2014). Interaction of a flow-excited Helmholtz resonator with a grazing turbulent boundary layer. *Experimental Thermal and Fluid Science*, 58:80–92.

Ghanadi, F., Arjomandi, M., Cazzolato, B. S., and Zander, A. C. (2015). Analysis of the turbulent boundary layer in the vicinity of a self-excited cylindrical Helmholtz resonator. *Journal of Turbulence*, 16(8):705–728.

Glezer, A. and Amitay, M. (2002). Synthetic jets. *Annual Review of Fluid Mechanics*, 34(1):503–529.

Goldstein, D., Handler, R., and Sirovich, L. (1995). Direct numerical simulation of turbulent flow over a modeled riblet covered surface. *Journal of Fluid Mechanics*, 302:333–376.

Gómez-de Segura, G. and García-Mayoral, R. (2019). Turbulent drag reduction by anisotropic permeable substrates–analysis and direct numerical simulations. *Journal of Fluid Mechanics*, 875:124–172.

Gómez-de Segura, G., Sharma, A., and García-Mayoral, R. (2018). Turbulent drag reduction using anisotropic permeable substrates. *Flow, Turbulence and Combustion*, 100:995–1014.

Gomit, G., De Kat, R., and Ganapathisubramani, B. (2018). Structure of high and low shear-stress events in a turbulent boundary layer. *Physical Review Fluids*, 3(1):014609.

Gowree, E. R., Jagadeesh, C., and Atkin, C. J. (2019). Skin friction drag reduction over staggered three dimensional cavities. *Aerospace Science and Technology*, 84:520–529.

Guo, H., Borodulin, V., Kachanov, Y., Pan, C., Wang, J., Lian, Q., and Wang, S. (2010). Nature of sweep and ejection events in transitional and turbulent boundary layers. *Journal of Turbulence*, 11:N34.

Head, M. and Bandyopadhyay, P. (1981). New aspects of turbulent boundary-layer structure. *Journal of fluid mechanics*, 107:297–338.

Hemon, P., Santi, F., and Amandolèse, X. (2004). On the pressure oscillations inside a deep cavity excited by a grazing airflow. *European Journal of Mechanics-B/Fluids*, 23(4):617–632.

Heuwinkel, C., Enghardt, L., and Röhle, I. (2001). Concept and experimental investigation of a zero mass flow liner. In *14th AIAA/CEAS Aeroacoustics Conference (29th AIAA Aeroacoustics Conference)*, page 2931.

Howard, C. Q., Cazzolato, B. S., and Hansen, C. H. (2000). Exhaust stack silencer design using finite element analysis. *Noise Control Engineering Journal*, 48(4):113–120.

Howerton, B. M. and Jones, M. G. (2015). Acoustic liner drag: a parametric study of conventional configurations. In *21st AIAA/CEAS Aeroacoustics Conference*, page 2230.

Howerton, B. M. and Jones, M. G. (2016). Acoustic liner drag: measurements on novel facesheet perforate geometries. In *22nd AIAA/CEAS Aeroacoustics Conference*, page 2979.

Howerton, B. M. and Jones, M. G. (2017). A conventional liner acoustic/drag interaction benchmark database. In *23rd AIAA/CEAS Aeroacoustics Conference*, page 4190.

Howerton, B. M. and Jones, M. G. (2023). Low-drag acoustic liner development. Technical report, NASA.

Hutchins, N. and Marusic, I. (2007). Evidence of very long meandering features in the logarithmic region of turbulent boundary layers. *Journal of Fluid Mechanics*, 579:1–28.

Hwang, Y. (2013). Near-wall turbulent fluctuations in the absence of wide outer motions. *Journal of Fluid Mechanics*, 723:264–288.

Itoh, M., Tamano, S., Iguchi, R., Yokota, K., Akino, N., Hino, R., and Kubo, S. (2006). Turbulent drag reduction by the seal fur surface. *Physics of Fluids*, 18(6).

Jabbal, M. and Zhong, S. (2010). Particle image velocimetry measurements of the interaction of synthetic jets with a zero-pressure gradient laminar boundary layer. *Physics of Fluids*, 22(6):063603.

Jafari, A., Cazzolato, B., and Arjomandi, M. (2022). Finite-length porous surfaces for control of a turbulent boundary layer. *Physics of Fluids*, 34(045115):1–34.

Jafari, A., McKeon, B. J., and Arjomandi, M. (2023). Frequency-tuned surfaces for passive control of wall-bounded turbulent flow–a resolvent analysis study. *Journal of Fluid Mechanics*, 959:A26.

Jafari, A., McKeon, B. J., Cazzolato, B. C., and Arjomandi, M. (2024). A resolvent analysis of the effect of passive perforated surfaces on wall-bounded turbulence. *International Journal of Heat and Fluid Flow*, 106:109315.

Jahanmiri, M. (2010). Active flow control: a review. Technical report, Chalmers University of Technology.

Jasinski, C. and Corke, T. (2020). Mechanism for increased viscous drag over porous sheet acoustic liners. *AIAA Journal*, 58(8):3393–3404.

Jiang, X., Lee, C., Smith, C., Chen, J., and Linden, P. (2020). Experimental study on low-speed streaks in a turbulent boundary layer at low Reynolds number. *Journal of Fluid Mechanics*, 903:A6.

Jiménez, J. (1994). On the structure and control of near wall turbulence. *Physics of Fluids*, 6(2):944–953.

Jiménez, J. (2004). Turbulent flows over rough walls. *Annu. Rev. Fluid Mech.*, 36(1):173–196.

Jiménez, J. (2018). Coherent structures in wall-bounded turbulence. *Journal of Fluid Mechanics*, 842:P1.

Jimenez, J., Uhlmann, M., Pinelli, A., and Kawahara, G. (2001). Turbulent shear flow over active and passive porous surfaces. *Journal of Fluid Mechanics*, 442:89–117.

Jodai, Y. and Elsinga, G. E. (2016). Experimental observation of hairpin auto-generation events in a turbulent boundary layer. *Journal of Fluid Mechanics*, 795:611–633.

Jones, M., Watson, W., Parrott, T., and Smith, C. (2004). Design and evaluation of modifications to the nasa langley flow impedance tube. In *10th AIAA/CEAS aeroacoustics conference*, page 2837.

Jones, M. G., Watson, W. R., Nark, D. M., and Howerton, B. M. (2014). Evaluation of a variable-impedance ceramic matrix composite acoustic liner. In *20th AIAA/CEAS Aeroacoustics Conference*, page 3352.

Józsa, T., Balaras, E., Kashtalyan, M., Borthwick, A., and Viola, I. M. (2019). Active and passive in-plane wall fluctuations in turbulent channel flows. *Journal of Fluid Mechanics*, 866:689–720.

Kametani, Y., Fukagata, K., Örlü, R., and Schlatter, P. (2015). Effect of uniform blowing/suction in a turbulent boundary layer at moderate Reynolds number. *International Journal of Heat and Fluid Flow*, 55:132–142.

Kempton, A. (2011). Acoustic liners for modern aero-engines. In *15th CEAS-ASC Workshop and 1st Scientific Workshop of X-Noise EV.*

Kim, H., Kline, S., and Reynolds, W. (1971). The production of turbulence near a smooth wall in a turbulent boundary layer. *Journal of Fluid Mechanics*, 50(1):133–160.

Kim, T., Blois, G., Best, J. L., and Christensen, K. T. (2018). Experimental study of turbulent flow over and within cubically packed walls of spheres: Effects of topography, permeability and wall thickness. *International Journal of Heat and Fluid Flow*, 73:16–29.

Klewicki, J., Metzger, M. M., Kelner, E., and Thurlow, E. (1995). Viscous sublayer flow visualizations at $Re_\theta \approx 1500000$. *Physics of Fluids*, 7(4):857–863.

Kornilov, V. (2015). Current state and prospects of researches on the control of turbulent boundary layer by air blowing. *Progress in Aerospace Sciences*, 76:1–23.

Lahiri, C., Pardowitz, B., Bake, F., and Enghardt, L. (2011). The application of an aeroacoustic actuator in a zero mass flow liner for acoustic damping. In *17th AIAA/CEAS Aeroacoustics Conference (32nd AIAA Aeroacoustics Conference)*, page 2725.

Leonardi, S., Orlandi, P., Smalley, R., Djenidi, L., and Antonia, R. (2003). Direct numerical simulations of turbulent channel flow with transverse square bars on one wall. *Journal of Fluid Mechanics*, 491:229–238.

Lu, L., Li, D., Gao, Z., Cao, Z., Bai, Y., and Zheng, J. (2020). Characteristics of array of distributed synthetic jets and effect on turbulent boundary layer. *Acta Mechanica Sinica*, 36:1171–1190.

Luchik, T. and Tiederman, W. (1987). Timescale and structure of ejections and bursts in turbulent channel flows. *Journal of Fluid Mechanics*, 174:529–552.

Luchini, P., Manzo, F., and Pozzi, A. (1991). Resistance of a grooved surface to parallel flow and cross-flow. *Journal of Fluid Mechanics*, 228:87–109.

Luchini, P. and Quadrio, M. (2022). Wall turbulence and turbulent drag reduction. In *50+ Years of AIMETA: A Journey Through Theoretical and Applied Mechanics in Italy*, pages 349–364. Springer.

Luhar, M., Sharma, A. S., and McKeon, B. (2015). A framework for studying the effect of compliant surfaces on wall turbulence. *Journal of Fluid Mechanics*, 768:415–441.

Luhar, M., Sharma, A. S., and McKeon, B. J. (2014). Opposition control within the resolvent analysis framework. *Journal of Fluid Mechanics*, 749:597–626.

Ma, X. and Su, Z. (2020). Development of acoustic liner in aero engine: a review. *Science China Technological Sciences*, 63:2491–2504.

Mathis, R., Hutchins, N., and Marusic, I. (2009). Large-scale amplitude modulation of the small-scale structures in turbulent boundary layers. *Journal of Fluid Mechanics*, 628:311–337.

McAuliffe, C. E. (1950). *The influence of high speed air flow on the behavior of acoustical elements*. PhD thesis, Massachusetts Institute of Technology.

Monkewitz, P. A., Chauhan, K. A., and Nagib, H. M. (2007). Self-consistent high Reynolds number asymptotics for zero-pressure-gradient turbulent boundary layers. *Physics of Fluids*, 19(11):115101.

Monty, J. P., Harun, Z., and Marusic, I. (2011). A parametric study of adverse pressure gradient turbulent boundary layers. *International Journal of Heat and Fluid Flow*, 32(3):575–585.

Mossi, K. and Bryant, R. (2003). Piezoelectric actuators for synthetic jet applications. *MRS Online Proceedings Library*, 785:1181–1186.

Murugan, T., Deyashi, M., Dey, S., Rana, S. C., and Chatterjee, P. (2016). Recent developments on synthetic jets. *Defence Science Journal*, 66(5):489–498.

Nayfeh, A. H., Kaiser, J. E., and Telionis, D. P. (1975). Acoustics of aircraft engine-duct systems. *Aiaa Journal*, 13(2):130–153.

Nikuradse, J. et al. (1933). Laws of flow in rough pipes. Technical report, National Advisory Committee for Aeronautics Washington.

Orlandi, P. and Jiménez, J. (1994). On the generation of turbulent wall friction. *Physics of Fluids*, 6(2):634–641.

Panton, R., Flynn, K., and Bogard, D. (1987). Control of turbulence through a row of Helmholtz resonators. In *25th AIAA Aerospace Sciences Meeting*, page 436.

Panton, R. L. and Miller, J. M. (1975). Excitation of a Helmholtz resonator by a turbulent boundary layer. *The Journal of the Acoustical Society of America*, 58(4):800–806.

Park, S., Lee, I., and Sung, H. J. (2001). Effect of local forcing on a turbulent boundary layer. *Experiments in Fluids*, 31:384–393.

Park, Y.-S., Park, S.-H., and Sung, H. J. (2003). Measurement of local forcing on a turbulent boundary layer using PIV. *Experiments in Fluids*, 34:697–707.

Parrott, T. and Jones, M. (2006). Cascaded perforates as one-dimensional, bulk absorbers. In *12th AIAA/CEAS Aeroacoustics Conference (27th AIAA Aeroacoustics Conference)*, page 2402.

Perlin, M., Dowling, D. R., and Ceccio, S. L. (2016). Freeman scholar review: passive and active skin-friction drag reduction in turbulent boundary layers. *Journal of Fluids Engineering*, 138(9):091104.

Perry, A. and Marušić, I. (1995). A wall-wake model for the turbulence structure of boundary layers. part 1. extension of the attached eddy hypothesis. *Journal of Fluid Mechanics*, 298:361–388.

Robinson, S. et al. (1991). Coherent motions in the turbulent boundary layer. *Annual Review of Fluid Mechanics*, 23(1):601–639.

Rosti, M. E., Brandt, L., and Pinelli, A. (2018). Turbulent channel flow over an anisotropic porous wall–drag increase and reduction. *Journal of Fluid Mechanics*, 842:381–394.

Samie, M., Baars, W., Rouhi, A., Schlatter, P., Örlü, R., Marusic, I., and Hutchins, N. (2020). Near wall coherence in wall-bounded flows and implications for flow control. *International Journal of Heat and Fluid Flow*, 86:108683.

Saravi, S. S. and Cheng, K. (2013). A review of drag reduction by riblets and micro-textures in the turbulent boundary layers. *European Scientific Journal*, 9(33):62–81.

Scarano, F., Jacob, M. C., Gojon, R., Carbonneau, X., and Gowree, E. R. (2022). Modification of a turbulent boundary layer by circular cavities. *Physics of Fluids*, 34(6):065134.

Scarano, F., Jacob, M. C., and Gowree, E. R. (2023). Drag reduction by means of an array of staggered circular cavities at moderate Reynolds numbers. *International Journal of Heat and Fluid Flow*, 102:109142.

Scarano, F., Jacob, M. C., and Gowree, E. R. (2024). Large scale structures modification of a spatially evolving turbulent boundary layer grazing over circular cavities. *International Journal of Heat and Fluid Flow*, 108:109486.

Schiller, N. H., Jones, M. G., Howerton, B. M., and Nark, D. M. (2019). Initial developments of a low-drag, variable-depth acoustic liner. In *25th AIAA/CEAS Aeroacoustics Conference*, page 2749.

Severino, G. F., Silvestri, A., Cazzolato, B. S., and Arjomandi, M. (2022). Sensitivity analysis of orifice length of micro-cavity array for the purpose of turbulence attenuation. *Experiments in Fluids*, 63:1–10.

Shahzad, H., Hickel, S., and Modesti, D. (2023). Turbulence and added drag over acoustic liners. *Journal of Fluid Mechanics*, 965:A10.

Silvestri, A., Ghanadi, F., Arjomandi, M., Cazzolato, B., and Zander, A. (2017a). Attenuation of sweep events in a turbulent boundary layer using micro-cavities. *Experiments in Fluids*, 58:1–13.

Silvestri, A., Ghanadi, F., Arjomandi, M., Cazzolato, B., Zander, A., and Chin, R. (2018). Mechanism of sweep event attenuation using micro-cavities in a turbulent boundary layer. *Physics of Fluids*, 30(5):055108.

Silvestri, A., Ghanadi, F., Arjomandi, M., Chin, R., Cazzolato, B., and Zander, A. (2017b). Attenuation of turbulence by the passive control of sweep events in a turbulent boundary layer using micro-cavities. *Physics of Fluids*, 29(11):115102.

Smith, C. and Metzler, S. (1983). The characteristics of low-speed streaks in the near-wall region of a turbulent boundary layer. *Journal of Fluid Mechanics*, 129:27–54.

Syed, A. and Ichihashi, F. (2008). The modeling and experimental validation of the acoustic impedance of multi-degrees-of-freedom liners. In *14th AIAA/CEAS Aeroacoustics Conference (29th AIAA Aeroacoustics Conference)*, page 2927.

Tam, C. K., Pastouchenko, N. N., Jones, M. G., and Watson, W. R. (2014). Experimental validation of numerical simulations for an acoustic liner in grazing flow: self-noise and added drag. *Journal of Sound and Vibration*, 333(13):2831–2854.

Tardu, S. (1995). Characteristics of single and clusters of bursting events in the inner layer: Part 1: VITA events. *Experiments in Fluids*, 20(2):112–124.

Von Karman, T. (1934). Turbulence and skin friction. *Journal of the Aeronautical Sciences*, 1(1):1–20.

Wallace, J. M., Eckelmann, H., and Brodkey, R. S. (1972). The wall region in turbulent shear flow. *Journal of Fluid Mechanics*, 54(1):39–48.

Walsh, M. and Lindemann, A. (1984). Optimization and application of riblets for turbulent drag reduction. In *22nd Aerospace Sciences Meeting*, page 347. AIAA.

Walsh, M. J. (1980). Drag characteristics of v-groove and transverse curvature riblets. In *Symposium on Viscous Flow Drag Reduction*, pages 168–184. AIAA.

Wang, Y., Choi, K.-S., Gaster, M., Atkin, C., Borodulin, V., and Kachanov, Y. (2022). Opposition control of turbulent spots. *Journal of Fluid Mechanics*, 943:A3.

Whalley, R. D. (2011). *Turbulent boundary-layer control with DBD plasma actuators using spanwise travelling-wave technique*. PhD thesis, University of Nottingham.

Wilkinson, S. (1983). Influence of wall permeability on turbulent boundary-layer properties. In *21st Aerospace Sciences Meeting*, page 294.

Zhang, X., Wong, C., Cheng, X., and Zhou, Y. (2022). Dependence of skin-friction reduction on the geometric parameters of blowing jet array. *Physics of Fluids*, 34(10):105125.

Chapter 3

Near-wall turbulence over a perforated plate

3.1 Chapter overview

The near-wall turbulence has a strong relationship with turbulence generation and skin friction drag in the turbulent boundary layers. As mentioned in Sections 2.1.1 and 2.3, a perforated plate with a backing cavity has been shown to reduce turbulence intensity; however, the mechanisms underlying this reduction in turbulence are not entirely understood. Shear stresses and turbulent generation account for burst events, which are formed by ejections and sweep events. Consequently, these events primarily contribute to the creation of turbulence and skin friction drag. As a result, an understanding of how a perforated plate with a backing cavity modifies burst events in the near-wall region is developed in this chapter. To explore the mechanisms of turbulence attenuation in the turbulent boundary layers over the perforated plate, turbulent boundary layers at various Reynolds numbers were simulated in a closed-return wind tunnel. Hot-wire measurements of flow velocities were conducted with a Dantec boundary-layer-type probe. The turbulence intensity, burst events, and pre-multiplied power spectral densities (PSD) of velocity fluctuations in the turbulent boundary layers with and without the perforated plate were estimated.

The results show that the near-wall turbulence of the turbulent boundary layers experienced a decrease of approximately 9% in sweep intensity, 9.3% in ejection intensity, 25% in ejection frequency, and up to 33.5% in sweep frequency within the near-wall region, $y^+ \leq 30$, indicating that the perforated structure weakened turbulent activities near the wall. Consequently, the turbulence intensity in this region decreased by nearly 9%. Moreover, a decrease in turbulent kinetic energy near the wall, coupled with an increase at $y^+ \geq 30$, implies that the perforated structure redistributes turbulent energy from the near-wall region to the outer region, probably leading to a reduction in shear stresses and skin friction drag.

The backing chamber plays an important role in reducing near-wall turbulence. The increase in the chamber volume results in a decrease in the estimated local friction drag, suggesting that the larger the backing chamber, the more kinetic energy is damped. Consequently, the sweeps are weakened and the near-wall turbulence intensity is reduced. It is suggested that the wall-normal velocities at the perforated surface exchange the energy between the inside and outside of the chamber and play an important role in reducing the near-wall turbulence of the turbulent boundary layers over the perforated structure.

3.2 Statement of Authorship

Statement of Authorship

Title of Paper	Modification of near-wall turbulence in turbulent boundary layers due to a perforated structure.		
Publication Status	☑ Published ☐ Submitted for Publication	☐ Accepted for Publication ☐ Unpublished and Unsubmitted work written in manuscript style	
Publication Details	Hoang, V., Jafari, A., Cazzolato, B., and Arjomandi, M. (2024). Modification of near-wall turbulence in turbulent boundary layers due to a perforated structure. *Physics of Fluids*, 36, 075173.		

Principal Author

Name of Principal Author (Candidate)	Van Thuan Hoang		
Contribution to the Paper	Modification of near-wall turbulence in turbulent boundary layers due to a perforated structure.		
Overall percentage (%)	75		
Certification:	This paper reports on original research I conducted during the period of my Higher Degree by Research candidature and is not subject to any obligations or contractual agreements with a third party that would constrain its inclusion in this thesis. I am the primary author of this paper.		
Signature		Date	04/02/2025

Co-Author Contributions

By signing the Statement of Authorship, each author certifies that:

i. the candidate's stated contribution to the publication is accurate (as detailed above);

ii. permission is granted for the candidate in include the publication in the thesis; and

iii. the sum of all co-author contributions is equal to 100% less the candidate's stated contribution.

Name of Co-Author	Azadeh Jafari		
Contribution to the Paper	Supervised the development of the research, helped in developing ideas, contributed in academic discussion and manuscript review.		
Signature		Date	19/02/2025

Name of Co-Author	Benjamin Cazzolato		
Contribution to the Paper	Supervised the development of the research, helped in developing ideas, contributed in academic discussion and manuscript review.		
Signature		Date	19/02/2025

Name of Co-Author	Maziar Arjomandi		
Contribution to the Paper	Supervised the development of the research, participated in developing ideas and concepts, helped in interpretation of results, provided critical revision of		
Signature		Date	19/02/2025

3.3 Modification of near-wall turbulence in turbulent boundary layers due to a perforated structure

This chapter consists of the following published journal article:

Hoang, V.T., Jafari, A., Cazzolato, B., and Arjomandi, M. (2024). Modification of near-wall turbulence in turbulent boundary layers due to a perforated structure. *Physics of Fluids*, 36, 075173. (Published)

The article is identical to its published format with the following exceptions:

- The numbering of figures, tables and equations have been altered to include the chapter number.
- The position of some figures and tables have been changed to improve legibility.

The article in its published format is available at: https://doi.org/10.1063/5.0213907

Modification of near-wall turbulence in turbulent boundary layers due to a perforated structure

V.T. Hoang,[1] A. Jafari,[1] B. Cazzolato,[1] and M. Arjomandi[1]
The University of Adelaide, Adelaide, 5005, South Australia, Australia.

(*Electronic mail: vanthuan.hoang@adelaide.edu.au)

(Dated: 18 February 2025)

This study investigates the potential of a perforated structure for the control of near-wall turbulence in turbulent boundary layers. The perforated structure consists of a perforated plate, underneath of which is a backing chamber. The near-wall turbulent structures were analysed using hot-wire measurements. Different inner-scaled chamber volumes from $V^+ = 2.4 \times 10^6$ to 11.5×10^6 were considered to manipulate turbulent boundary layers at two Reynolds numbers of Re_θ = 1165 and 2294. The findings reveal significant effects of the perforated structure on near-wall turbulent structures. Statistical analysis utilising a variable-interval time-averaging (VITA) technique illustrated a reduction of up to about 9% in sweep and ejection intensity, a decrease of about 25% in ejection frequency, and a decrease of approximately 33.5% in sweep frequency within the near-wall region, $y^+ \leq 30$, indicating that the perforated structure weakened burst events in this region. In addition, the perforated structure lifted the turbulence energy further from the wall. Consequently, there was a reduction of up to approximately 9% in turbulence intensities near the wall, contributing to locally diminished shear stresses and skin friction drag. When the inner-scaled chamber volume increased, the reduction in near-wall turbulence became more pronounced.

Modification of near-wall turbulence in turbulent boundary layers due to a perforated structure

I. INTRODUCTION

Carbon dioxide (CO_2) emissions are a global issue. One target of the aviation industry is to reduce CO_2 emissions. The Advisory Council for Aeronautics Research in Europe (ACARE) has recently mandated a 75% reduction in CO_2 emissions per passenger mile, which is aimed to be achieved by 2050[25]. Drag reduction is an effective method of reducing energy consumption in diverse applications, such as aircraft, road vehicles, or ships, which consequently results in CO_2 emissions reductions. In aviation, a 10% reduction in the total drag can save approximately 6% of the trip fuel for flights[14]. Civil aircraft have friction drag of approximately 48% of the total drag[29].

In a wall-bounded flow, skin friction drag is mainly generated by the interaction between the flow and the wall-bounded surface in a turbulent boundary layer. Turbulence is mainly generated in the near-wall region of turbulent boundary layers[23]. Coherent structures, such as quasi-streamwise vortices, streaks, and horseshoe vortices are accounted for by turbulent momentum transfer and shear stress[15]. These streamwise vortices, which spin along the streamwise direction and contain both ejection and sweep events, are the major components of these coherent structures in the near-wall region. The ejections lift the streamwise vortices away from the wall, while the sweeps transfer the turbulent momentum towards the wall. Ejections and sweep events form burst events that mainly contribute to skin friction drag[13]. Hence, suppressing burst events is an efficient way to reduce turbulence in the near-wall region, leading to a reduction in skin friction drag.

The methods for the control of turbulent boundary layers can be categorised into active or passive[5,9]. Active methods, such as opposition control, and blowing and suction control, use an appropriate sensor to measure turbulent flow characteristics and then extract or add energy or momentum from an external source to the turbulent flow. Active methods require power, sensors, and actuators, which are potentially complex, difficult to maintain, and expensive. In contrast, passive methods, such as riblets and perforated plates, modify turbulent flows without using any external source of energy or momentum[39]. Passive methods are less efficient than active methods but cheaper and easier to implement and maintain. The use of perforated plates, which is a passive method to control turbulent boundary layers, has recently shown potential for skin friction drag reduction[40,41].

Gowree et al.[12] observed a reduction in skin friction drag of a turbulent boundary layer over a perforated plate with staggered orifices. The experiments used a fixed orifice depth of h = 3 mm, with the diameter varying from D = 2 to 5 mm, which equates to h/D from 0.6 to 1.5. Both sealed and opened orifices were considered. They found that while the skin friction drag increased with $h/D \leq 1$, it decreased with $h/D > 1$. Similar effects were observed in both open and sealed orifices. The maximum reduction in skin friction drag was found for $h/D = 1.5$ at a Reynolds number based on an orifice diameter of about 2500. Their results based on Laser Doppler Anemometer (LDA) measurements showed a reduction in the transverse velocity fluctuation of the boundary layer for $h/D = 1$ compared with that for $h/D = 0.6$, so the authors suggested that the mechanism of skin friction drag reduction of the perforated plate was similar to that of riblets, by manipulating the transverse velocities.

Scarano et al.[40,41] investigated the modification of turbulent boundary layers and the reduction in skin friction drag due to different perforated plates. Different orifice diameters, h/D from 0.75 to 1.75, different Open Area Ratio (OAR) from 0.12 to 0.47, and different Reynolds numbers, $1750 \leq Re_\theta \leq 3430$, were considered. Their results show a considerable reduction of up to about 30% in local skin friction drag. Increases in the OAR resulted in more pronounced modifications of the boundary layer and reductions in skin friction. The modification of the boundary layer with an increase in the wake parameter and the shape factor, and a reduction in skin friction drag is similar to the turbulent boundary layers with wall-normal blowing[22] or with an adverse pressure gradient[31]. Bhat et al.[3] conducted a numerical simulation on a turbulent boundary layer over a perforated plate with a backing chamber. They noticed instantaneous upward and downward components through the orifices. This unsteady blowing effect could lift the quasi-streamwise vortices, which results in an increase in energy in the outer region and the formation of a second hump in burst intensity. The upward displacement of these structures, carrying low-momentum fluid, then modifies the mean velocity in a manner that reduces skin friction. A similar mechanism of skin friction reduction in turbulent boundary layers due to wall-normal blowing was mentioned by Kornilov[24].

Silvestri et al.[49] found that adding a backing chamber under a perforated plate increased the sweep reduction of a turbulent boundary layer. In their study, two types of backing chambers were considered: a common backing chamber and an individual backing chamber with a diameter of 1.2 mm and a depth of 4 mm, $h/D = 3.3$. The backing chamber depth varied from 25 mm to 75 mm. This caused the backing chamber volume for one orifice, V, to vary from $V^+ = V(U_\tau/\nu)^3 = 2.05 \times 10^6$ to 6×10^6, where U_τ is the skin friction velocity and ν is the kinematic viscosity of the air. The results show that the perforated plate with both chamber configurations reduced turbulence intensities and sweep intensities. The largest reduction in sweep intensity accounted for approximately 7% at Re_θ = 3771 and $V^+ = 6 \times 10^6$ in comparison with the sweep intensity of the turbulent boundary layer over a smooth plate. The sweep intensity reduction was reported to increase with an increase in the backing chamber volume before reaching a threshold of $V^+ = 5 \times 10^6$. It is suggested that the mechanism of the sweep reduction is due to the sweeps being weakened by penetrating through the orifices and the sweep energy dissipating in the backing chamber[49]. It is expected that the wall shear stress of the turbulent boundary layer over the perforated plate reduces by reducing the sweep energy.

Jafari et al.[21] reported the effect of different backing chamber configurations under a perforated plate on turbulent boundary layer structures. The perforated plate includes orifices with a cross-section of 1.5 mm × 1.5 mm and a depth of 6 mm at a spacing of 3 mm. The backing chamber under the perforated plate had three volume configurations, including a common chamber that connected all the square orifices, an individual chamber under each orifice, and chambers that connected all the square orifices in streamwise and spanwise directions. The results showed that the backing chambers played a role in the reduction in the turbulence intensity of the turbulent boundary layers over the perforated plate. Both the common and individual chambers resulted in a considerable reduction of up to 80% in the pre-multiplied spectrum of streamwise velocity fluctuations at large scales. The authors suggested that unsteady transpiration through the orifices could reorganise the turbulent boundary layers. The unsteady transpiration may result from acoustic excitation inside the chamber when the turbulent boundary layer flows over the orifices. When the chamber is strongly excited, it functions as a resonator, which creates flow suction and ejection through the orifices[10,37].

Research in the literature indicates the potential for a perforated plate with a backing chamber to reduce turbulence Bhat et al.[3], Jafari et al.[21], Silvestri et al.[49]. However, the mechanisms of turbulence reduction due to the perforated plate have not been fully understood. This study aims to investigate the effect of the perforated structure on near-wall turbulence to enhance understanding of the mechanism of turbulence attenuation. The main focus is the modification of turbulent behaviors and burst events in the near-wall region due to the perforated structure. Burst characteristics, such as intensity, duration, and frequency, were estimated by the Variable Interval Time Averaging (VITA) technique. The subsequent section provides a thorough overview of the experimental setup. Following that, Section 3 presents the turbulent statistics and activities, while the concluding remarks are outlined in Section 4.

II. EXPERIMENTAL METHODS

A. Experimental rig and flow conditions

A closed-return wind tunnel at the University of Adelaide was used to conduct the experiments. The wind tunnel can operate at a maximum velocity of 30 ms^{-1} with a low-level turbulence intensity of approximately 0.5%. The wind tunnel has a rectangular test section with a cross-section of 600 mm $\times$ 500 mm and 2000 mm in length, as shown in Figure 1. As the wind tunnel width is more than 10 times larger than the boundary layer thickness in these experiments, the effect from the extra strain-rate effect caused by the finite width is negligible, as recommended by Nickels et al.[33]. To minimise the bluff body separation due to the finite plate thickness, a super elliptical edge was attached to the leading edge of the plate. At the trailing edge of the plate, a circulation flap of 125 mm in length was mounted to reduce the development of any circulation and the effect of back pressure. To achieve a zero pressure gradient along the test section, the side walls were adjusted to achieve an acceleration parameter, $K = (\nu/U_\infty^2)(dU_\infty/dx)$, in the order of 10^{-8}, which is similar to the value for the turbulent boundary layers with a zero pressure gradient in the previous works, such as by De Graaff and Eaton[6], Hyun Shin and Jin Song[20], Schultz and Flack[43]. The achieved acceleration parameters are smaller than the threshold of 3.5×10^{-6} suggested for relaminarisation of a turbulent boundary layer[32]. To ensure the boundary layer is fully developed, the inlet flow was tripped using a 3 mm rod placed 140 mm from the leading edge, as recommended by Silvestri et al.[48].

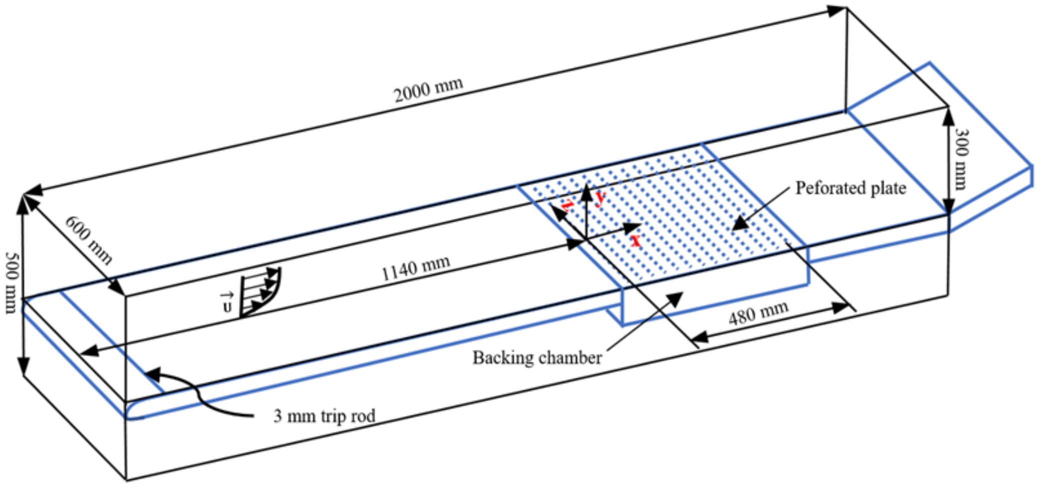

FIG. 1. Schematic diagram of the test section and the perforated plate with a backing chamber.

A single Dantec wire probe, 55P15, with a 5 μm diameter and 1.25 mm length, operated by a Dantec Dynamics Streamline Pro, was used to measure flow velocities and turbulence. The ratio of the wire length to the diameter was about 240, which was larger than the 200 recommended by Ligrani and Bradshaw[27] and Hutchins et al.[19]. The length of the hot-wire probe in viscous units, $l^+ = lU_\tau/\nu$, where l is the probe length, was from 19 to 45. The sampling frequency, f_s, of the measurements was 40 kHz, and the measurement duration was 30 s, equal to a viscous-scaled sample interval of $\Delta t^+ = (U_\tau^2)/(\nu f_s)$, from 0.1 to 0.5. This non-dimensional sample interval is smaller than the minimum timescale, $t^+ = (tU_\tau^2)/\nu = 3$, for resolving energetic turbulent fluctuations, as recommended by Hutchins et al.[19]. A third-order Butterworth filter was used to low-pass filter the measured signals at the filtering frequency, $f_c = 19$ kHz. The non-dimensional filtering frequency, $f_c^+ = f_c\nu/(U_\tau^2)$, from 1.8 to 10, is larger than the threshold of 0.33 recommended by Hutchins et al.[18]. The probe calibration was conducted with a Pitot-static tube connected to a 10 Torr Baratron pressure transducer. Twenty-two free-stream velocities ranging from 0 ms^{-1} to 25 ms^{-1} were measured by both the hotwire probe and the Pitot-static tube. A 5th-order polynomial fit was used to estimate the calibration coefficients, which were then used to convert the voltage measured by the probe to the velocity. The variance of the ambient temperature during calibration and measurements was less than 1^o C, hence the ambient temperature was assumed to be constant during the experiments. To place the probe at different normal-wall locations, a Mitutoyo dial/mechanical-digit counter height gauge with a travel range from 0 to 300 mm and an accuracy of ±0.03 mm was used. The gauge motor was controlled by a Matlab code. To reduce the effect of gear backlash, a Wenglor CP35MHT80 Laser displacement sensor with an accuracy of ± 0.05 mm was used to detect the gauge location.

The experiments were conducted at two free stream velocities, U_∞, of 5.5 m/s and 9.7 m/s. For the turbulent boundary layers over a smooth plate, the measurement positions were at S1, x = -40 mm, and S2, x = 480 mm. These two measurement positions were located before the leading edge and after the trailing edge of the perforated plate, respectively. The Reynolds numbers based on momentum thicknesses, $Re_\theta = \theta U_\infty/\nu$, varied from 1165 to 2815. The main flow parameters of the turbulent boundary layers over a smooth flat plate can be found in Table I, where θ is the momentum thickness, δ^* is the displacement thickness, H is the shape factor, l^+ is the how-wire probe length in viscous units, and C_f is the friction coefficient estimated by using hotwire measurements and the near-wall velocity gradient technique developed by Hutchins and Choi[16]. This method involves determining wall-shear stresses in boundary layers by measuring the instantaneous velocity gradient at the wall and requires precise measurement of the velocity profile within the viscous sublayer. The wall-shear stress was given as $\tau_w = \mu \frac{du}{dy}$, where μ is the dynamic viscosity of air, u is the instantaneous velocities in the viscous sublayer of turbulent boundary layers, $3.5 \leq y^+ \leq 5.5$, and y^+ is the inner-scaled wall-normal location, $y^+ = yU_\tau/\nu$. On average six data points at $3.5 \leq y^+ \leq 5.5$ in the measurements were used to estimate the wall-shear stress. The friction coefficient is estimated from the mean wall shear stress as $C_f = \tau_w/(\rho U_\infty^2/2)$, where ρ is the density of air. This formula necessitates two simultaneous measurements within the viscous sublayer of turbulent boundary layers, which can be quite challenging. Therefore, to simplify the technique, an assumption of a non-slip condition at the wall was applied. The unperturbed turbulent boundary layers at S1 were considered as baseline cases for comparison with those controlled by the perforated structure.

TABLE I. Flow parameters for the two turbulent boundary layers over a smooth plate.

U_∞ (m/s)	locations	K (10^{-8})	Re_θ	Re_τ	θ (mm)	δ^* (mm)	δ_{99} (mm)	H	l^+	ν/U_τ (μm)	U_τ (m/s)	C_f (10^{-3})	τ_w (N/m^2)
5.51	S1	0.29	1165	500	3.25	4.72	36.3	1.45	16.2	61.5	0.251	4.11	0.075
5.51	S2	0.29	1510	715	4.20	6.06	45.6	1.44	15.7	63.8	0.242	3.80	0.070
9.71	S1	0.71	2294	1026	3.64	5.14	38.9	1.41	26.4	37.9	0.408	3.49	0.198
9.68	S2	0.71	2815	1251	4.44	6.20	48.6	1.40	25.8	38.8	0.398	3.31	0.188

In Figure 2(a), the inner-scaled velocity profiles, $U^+ = U/U_\tau$, of the unperturbed turbulent boundary layer as a function of the inner-scaled wall-normal locations, $y^+ = yU_\tau/\nu$, are presented alongside the DNS data by Schlatter et al.[42] at a similar range of Reynolds numbers. The velocity profiles exhibit good agreement with both the DNS and experimental data. A large scatter was shown at $y^+ \leq 3$, which could result from the wall effect as noted by Hutchins and Choi[16], but the measured profiles are identical to the DNS profiles at $3.5 \leq y^+ 5.5$. In Figure 2(b), the friction coefficients of the turbulent boundary layers over a smooth flat plate are shown as a function of Reynolds numbers, comparing them with the experimental data[36]. The calculated friction coefficients for the turbulent boundary layers exhibit good agreement with both the DNS and experimental data within the uncertainties of the measurements.

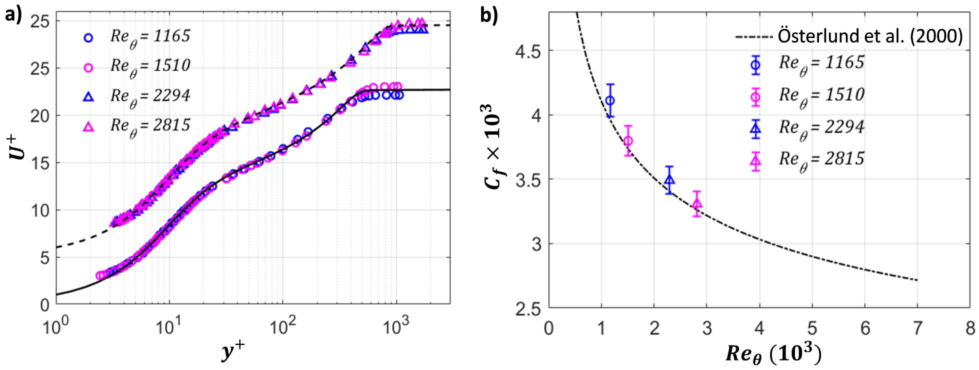

FIG. 2. Turbulent boundary layers over a smooth flat plate: a) Mean velocity profiles and b) friction coefficients. The dashed and black solid lines are reproduced from the DNS data of Schlatter et al.[42] at similar Reynolds numbers. The black dashed-dotted line is reproduced from the semi-empirical relationship, $C_f = 1/2 \times (1/0.384 \times \ln(Re_\theta) + 4.08)^{-2}$ of Österlund et al.[36].

B. Perforated Structure Geometries and Test cases

The perforated structure was located at 1140 mm from the leading edge of the test section, as shown in Figure 1. It contains 64 rows and 340 columns of circular orifices with a diameter, $d = 1$ mm, a depth, $h = 5$ mm, and spacings, $\Delta x = 7.5$ mm in the streamwise and $\Delta z = 1.7$ mm in the spanwise directions, as shown in Figure 3. The orifice diameter in viscous units, $d^+ = d \times U_\tau/\nu$, was from 15 to 26, which would not generate any separation of the flow at the wall because the orifice diameter was below a threshold of 60, as recommended by Silvestri et al.[46]. The orifice spacing in viscous units, $\Delta x^+ = \Delta x \times U_\tau/\nu$, in the streamwise direction was from 113 to 192. The orifice spacing in viscous units, $\Delta z^+ = \Delta z \times U_\tau/\nu$, in the span-wise direction was from 25 to 44. These spacings were selected to manipulate turbulent boundary layers' low-speed streaks. The separation between two neighboring low-speed streaks is distributed randomly and ranges from around 80 to 120 in viscous units in the spanwise direction[51]. This spacing is not affected by Reynolds numbers. Additionally, the length of these streaks in the streamwise direction can exceed 1000 viscous units Smith and Metzler[51]. To prevent thermal conductivity between the hot-wire probe and the wall, the perforated plate was made of acrylic. The backing chamber has a box shape with a length of 598 mm, a width of 500 mm, and a depth of 50 mm, which equates to the chamber volume for each orifice, $V^+ = V/(\nu/U_\tau)^3/N$, from 2.7×10^6 to 11.5×10^6, where $N = 21760$ is the number of orifices. In the perforated plate cases, the measurements were conducted at five locations over the perforated plate from C1 to C5, x = 121.6, 182.4, 243.2, 304.0, 364.8 mm, from the leading edge of the perforated plate. This equates to $x/\Delta x$ = 16, 24, 32, 40, and 48 as shown in Figure 4. These measurement locations were selected to reduce the effect of the leading and trailing edges of the perforated plate on the measured data. The geometrical parameters of the perforated plate in the wall unit, $d^+, h^+, V^+, \Delta x^+$, and Δz^+, are presented in Table II, which were computed using local friction velocities. The local friction velocities of the turbulent boundary layers over the perforated structure were estimated as $U_\tau = \sqrt{\tau_w/\rho}$, where τ_w was computed by the wall-shear stress by the near-wall velocity gradient technique developed by Hutchins and Choi[16] as discussed in Section II A.

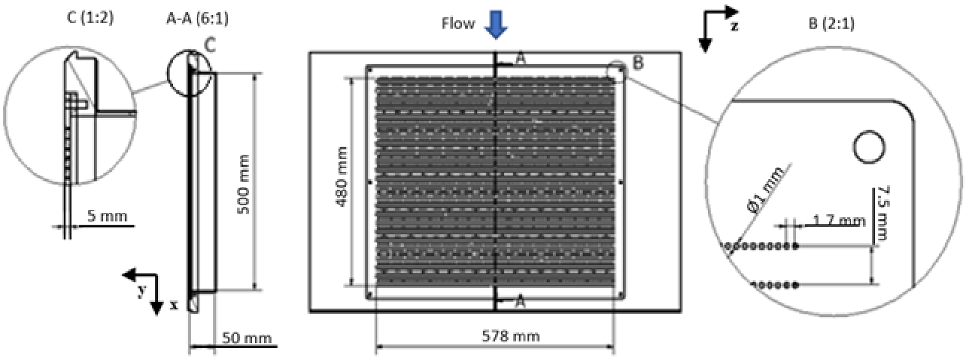

FIG. 3. Schematic of the perforated plate with a backing chamber and the main dimensions.

III. RESULTS AND DISCUSSION

A. Turbulent boundary layer statistics and integral parameters

The momentum thickness as a function of the downstream locations for both the perforated cases and the smooth cases at U_∞ = 5.5 m/s are shown in Figure 5(a). The results show an increase in the momentum thickness of the turbulent boundary layers due to the perforated structure. The increase in the momentum thicknesses would result in an increase in the momentum thickness based Reynolds numbers, Re_θ, as observed in the work by Scarano et al.[41]. Figure 5(b) shows the increases in the momentum thicknesses of the turbulent boundary layers over the perforated structure at two free stream velocities, $(\theta_{cav} - \theta_{sm})/\theta_{sm}$, where θ_{cav} is the momentum thickness for the perforated cases and θ_{sm} is a linearly-interpolated momentum thickness from the two turbulent boundary layers over a smooth flat plate at S1 and S2. The results show a gradual increase when the

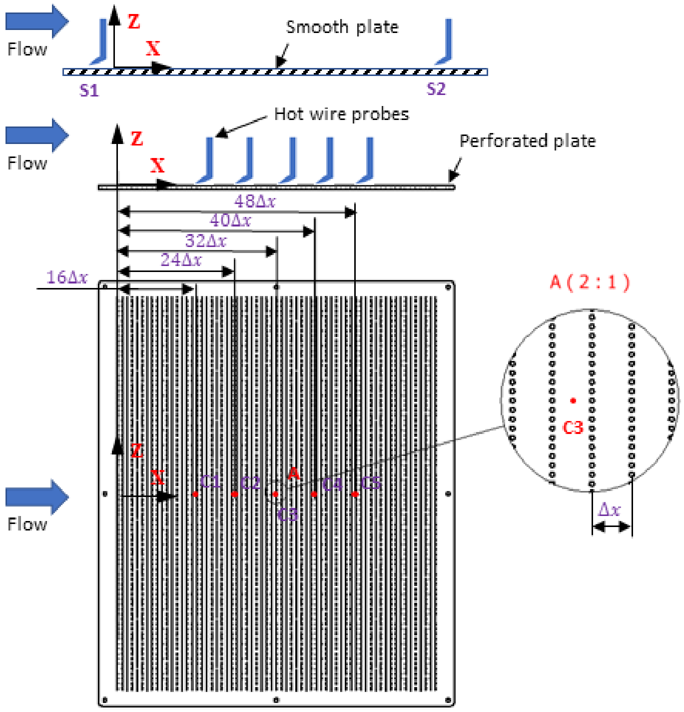

FIG. 4. Schematic of the measurement locations for the turbulent boundary layers over the smooth plate including S1 and S2, and the ones over the perforated structures including C1, C2, C3, C4, and C5.

turbulent boundary layer passes the leading edge of the perforated plate. The maximum increases of about 9% and 4.4% in the momentum thickness were found at $x/\Delta x$ = 48 and U_∞ = 5.5 and 9.7 m/s, respectively. The increase in the momentum thickness of the turbulent boundary layer over a perforated plate was also observed in the work by Scarano et al.[41].

Figure 6(a) shows the increase in the shape factor of the turbulent boundary layers over the perforated structure measured at C3 as a function of the open area ratio (OAR). The results are in agreement with the work by Scarano et al.[41] at the same OAR. The increase in the shape factor of turbulent boundary layers was also observed in turbulent boundary layers with an adverse pressure gradient by Monty et al.[31] or unsteady wall-normal blowing by Kametani et al.[22]. Figure 6(b) shows the increase in the shape factors of the turbulent boundary layers over the perforated structure as a function of the downstream locations from the leading edge of the perforated plate. The increase became less pronounced when the turbulent boundary layer passed the leading edge of the perforated plate. For example, the increase in the shape factor reduces from about 1.3% at $x/\Delta x$ = 16 to about 0.8% at $x/\Delta x$ = 48. One hypothesis is that the perforated structure generates a local adverse pressure gradient in the vicinity of the orifice, which causes the behaviour of

TABLE II. Geometrical parameters for different test conditions and downstream measurement locations.

U_∞ (m/s)	Locations	Δx^+	Δz^+	d^+	h^+	V^+ (10^6)
5.46	C1	118.0	26.7	15.7	78.7	2.7
5.48	C2	118.0	26.7	15.7	78.7	2.7
5.47	C3	116.8	26.5	15.6	77.8	2.6
5.48	C4	115.0	26.1	15.3	76.7	2.5
5.46	C5	113.0	25.6	15.1	75.4	2.4
9.66	C1	191.9	43.5	25.6	127.9	11.5
9.68	C2	191.7	43.5	25.6	127.8	11.5
9.66	C3	188.7	42.8	25.2	125.8	11.0
9.68	C4	185.5	42.0	24.7	123.6	10.4
9.67	C5	184.2	41.8	24.6	122.8	10.2

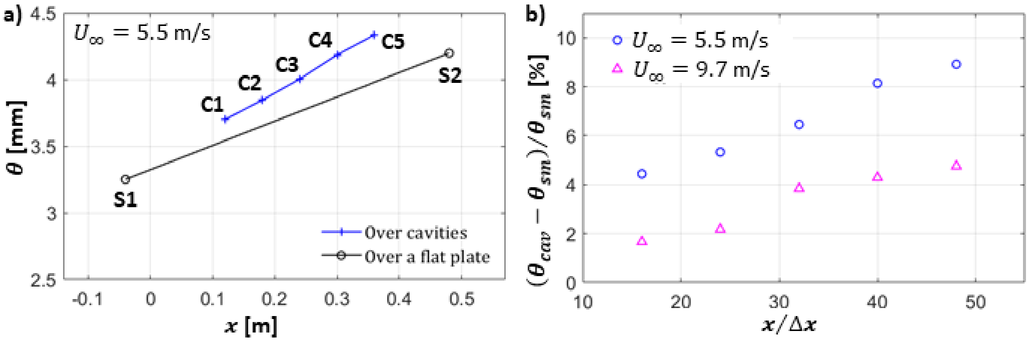

FIG. 5. a) Momentum thicknesses as a function of the downstream locations at the free stream velocity of 5.5 m/s and b) Variations in the momentum thickness as a function of the downstream locations. S1 and S2 indicates the two measured locations for the smooth cases. C1, C2, C3, C4 and C5 indicate the five measured locations for the perforated cases.

the shape factors of the turbulent boundary layers over the perforated structure similar to those of the turbulent boundary layers with an adverse pressure gradient. If a local pressure gradient exists, it would reduce along downstream locations. This would then cause a decrease in the shape factor to reduce from $x/\Delta x = 16$ to 48, as shown in Figure 6(b). As there were no pressure measurements in this study, there is no evidence to confirm this hypothesis. Another hypothesis is that the wall-normal jets created by the possible excitation inside the backing chamber increase the shape factors. Bhat et al.[3] observed unsteady wall-normal velocities through the orifices in the turbulent boundary layer over the perforated structure with a common backing chamber at a similar Reynolds number. The wall-normal jets would result in an increase in the shape factor of the turbulent boundary layer as reported in the work by Park et al.[38] and Lu et al.[28].

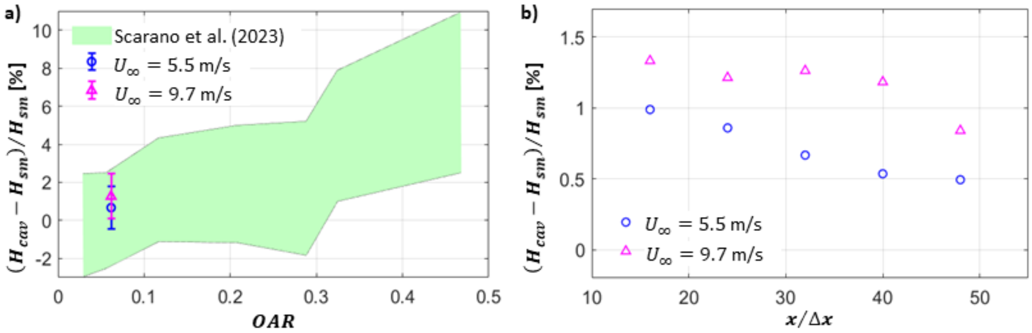

FIG. 6. a) Shape factors of the turbulent boundary layers measured at C3 as a function of the open area ratio (OAR) and b) Shape factors of the turbulent boundary layers over the perforated structure as a function of the downstream locations. The green area is reproduced from the experimental data of Scarano et al.[41]. The error bars represent the variation in downstream measurement locations.

Acceleration factors can be used to characterize pressure gradients in turbulent boundary layers. Figure 7 shows the acceleration parameters developing over the perforated structure from $x/\Delta x$ = 16 to 48 at two free stream velocities of $U_\infty = 5.5$ and 9.7 m/s. The results show a gradual increase in the acceleration parameters when the turbulent boundary layers pass the leading edge of the perforated plate. For example, the acceleration parameter increased from about -5×10^{-8} at $x/\Delta x$ = 16 to about -1.2×10^{-8} at $x/\Delta x$ = 48 for the cases of U_∞ = 9.7 m/s. This increase indicates that the adverse pressure gradient of the turbulent boundary layer reduces when the turbulent boundary layer passes the leading edge of the perforated plate. This was consistent with the reduction of the shape factors shown in Figure 6b, supporting the hypothesis that the perforated structure generates a local adverse pressure gradient in the turbulent boundary layers and this gradient reduces along downstream locations. Consequently, the friction coefficient would increase along downstream location due to the reduction in the adverse pressure gradient.

In Figure 8(a), the increase in the friction coefficient of the turbulent boundary layers over the perforated structure measured at C3 as a function of the open area ratio (OAR) is compared with the work by Scarano et al.[41]. The results are in agreement with the published work at the same OAR within the experiment uncertainties. Figure 8b illustrates the reduction in the local friction

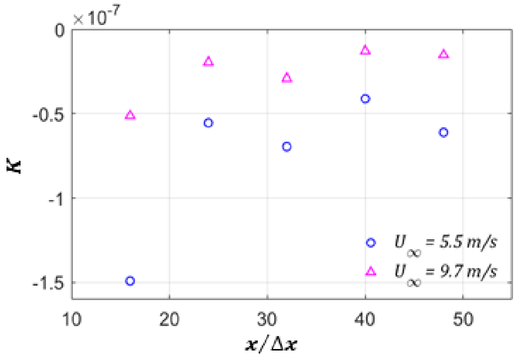

FIG. 7. a) Acceleration parameters of the turbulent boundary layers as a function of the measured locations from the leading edge of the perforated plate.

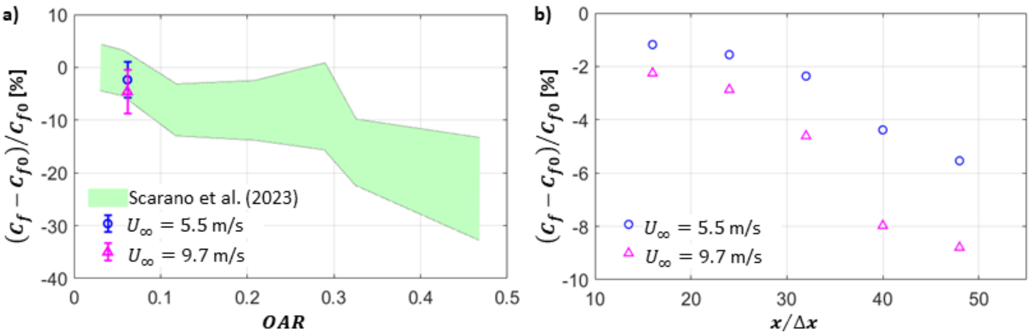

FIG. 8. a) Friction coefficients of the turbulent boundary layers measured at C3 as a function of the open area ratio (OAR) and b) friction coefficients of the turbulent boundary layers over the perforated structure as a function of the downstream locations. The green area is reproduced from the experimental data of Scarano et al.[41]. The error bars represent the variation in downstream measurement locations.

coefficients of turbulent boundary layers over the perforated structure at two free stream velocities of U_∞ = 5.5 and 9.7 m/s as a function of the downstream locations. The friction coefficient is estimated from the mean wall-shear stress as $C_f = \tau_w/(\rho U_\infty^2/2)$, where τ_w was computed by the wall-shear stress by the near-wall velocity gradient technique developed by Hutchins and Choi[16] as discussed in Section II A. It is observed that as the turbulent boundary layer progresses over the leading edge of the perforated plate, the reduction in the friction coefficients increases. For the perforated cases with U_∞ = 5.5 m/s, the reduction in the friction coefficients rises from about 1% at $x/\Delta x$ = 16 to approximately 5.9% at $x/\Delta x$ = 48. Similarly, for the perforated cases with U_∞ = 9.7 m/s, the reduction in friction coefficients increases from around 2% at $x/\Delta x$ = 16 to approximately 8.7% at $x/\Delta x = 48$. This increase in the friction reduction along downstream locations does not agree with Figure 6 and Figure 7 where the friction reduction is expected to reduce along downstream locations. Hence, it is suggested that the possible local adverse pressure gradient is not a main contributor to the friction drag reduction in the turbulent boundary layers over the perforated structure for the considered flow conditions and geometries.

The effect of geometrical parameters including the orifice diameter and chamber volume on the reduction in local skin friction drag is shown in Figure 9. Figure 9(a) shows the reduction in the local friction coefficient of the turbulent boundary layers over the perforated structure measured at C3 as a function of the inner-scale orifice diameter. The result shows that when the inner-scale orifice diameter increases from $d^+ = 15.6$ to 25.2, the reduction in the local friction drag increases from about 5.9% to 8.5%. This finding agrees with the work by Silvestri et al.[46] who reported that the effect of perforated plates increases with an increase in the inner-scale orifice diameter when it is below a threshold of $d^+ = 60$. The larger the inner-scale orifice is, the more sweeps penetrate through the orifices, which enhances the reduction in the sweep intensities and probably leads to a higher reduction in the skin friction drag[46]. In contrast, when the inner-scaled orifice diameter is larger than 60, an increase in the inner-scaled orifice diameter causes the reduction in the sweep intensities to become less pronounced. This probably leads to an increase in skin friction drag[46]. Scarano et al.[40] reported that when the inner-scaled orifice diameter increases from about $d^+ = 130$ to 250, the reduction in the skin friction drag of the turbulent boundary layers over a perforated plate reduces from about 14.5% to about 11%, as shown in Figure 9(a). Figure 9(b) shows the effect of the inner-scaled chamber volumes on the reduction in the local skin friction drag of the turbulent boundary layers measured at C5. The result shows that when the inner-scaled chamber volume increases from $V^+ = 2.6 \times 10^6$ to 11×10^6, the reduction in the local friction drag increases from about 2.2% to 4.6%. The larger the inner-scaled chamber volume is, the more energy of the sweeps is damped, which results in a larger reduction in the sweep intensities and turbulence production Silvestri et al.[47,49]. As a result, the larger reduction in the sweep intensities and turbulence production probably leads to a larger reduction in the local skin friction drag.

The turbulent statistics and integral parameters show significant effects of the perforated structures on the turbulent boundary layers. The increases in the shape factor and momentum thickness of the turbulent boundary layers over the perforated structure support a reduction in the local skin friction drag compared to those of the undisturbed turbulent boundary layers. The increases in the shape factors and the results of the acceleration parameters suggest that the perforated structure

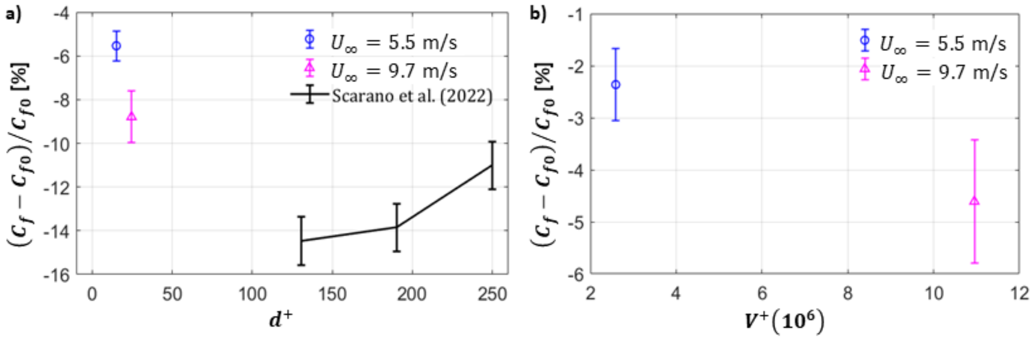

FIG. 9. a) Friction coefficients of the turbulent boundary layers measured at C5 as a function of the inner-scale orifice diameters and b) friction coefficients of the turbulent boundary layers over the perforated structure as a function of the inner-scale chamber volumes. The black solid line is reproduced from the experimental data of Scarano et al.[40]. The error bars represent the variation in downstream measurement locations.

generates an adverse pressure gradient in the turbulent boundary layers. However, the disagreement between the distribution of the shape factors and the friction coefficients along downstream locations suggests that the possible adverse pressure gradient is not a key contributor to the reduction in local skin friction drag of the turbulent boundary layers over the perforated structure. Another hypothesis is that the perforated structure generates wall-normal velocities through the orifices, leading to a reduction in local skin friction drag.

B. Time-averaged flow field

The effects of the perforated structure on the inner-scaled mean velocity profiles of the turbulent boundary layers at two free stream velocities of U_∞ = 5.5 and 9.7 m/s were shown in Figure 10. There was an increase in the mean velocity profiles in the wake region of the turbulent boundary layers over the perforated structure compared with those in the baseline case. This effect was more pronounced when the boundary layers passed the leading edge of the perforated plate. When the Reynolds number increased, the effect became more significant. The increase in the wake region due to a perforated plate was also observed in the work by Scarano et al.[40,41]. It is noticed that the mean velocity profiles of the turbulent boundary layers over the perforated structure experience a reduction in the logarithmic region in comparison with those of the baseline cases. A similar reduction in the mean velocity profiles of the turbulent boundary layers manipulated by suction/blowing jets was observed in the work by Lu et al.[28], Park et al.[38]. It, hence, is suggested that the wall-normal velocities of transpiration as discussed in Section III A cause a significant effect on the mean velocity profile of the turbulent boundary layers over the perforated structure.

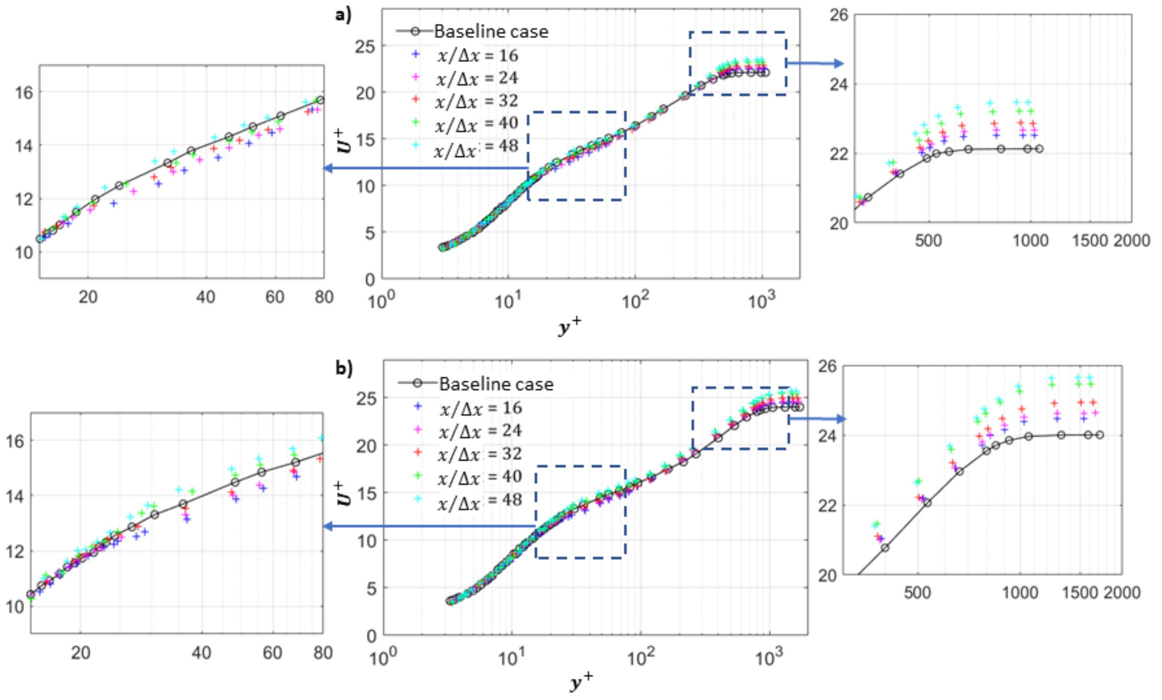

FIG. 10. Inner-scaled velocity profiles of turbulent boundary layers over a perforated structure compared with those of the baseline cases at a) U_∞ = 5.5 m/s and b) U_∞ = 9.7 m/s.

Figure 11(a) shows the Hama roughness function, $\Delta U^+ = U^+_{e-sm} - U^+_{e-cav}$, where U^+_{e-sm} is the inner-scaled mean velocity at the edge of the undisturbed boundary layers over a smooth plate and U^+_{e-cav} is the inner-scaled mean velocity at the edge of the boundary layers over the perforated structure, as a function of the downstream locations from the leading edge of the perforated plate. The findings indicate a reduction in the roughness function of the boundary layers over the leading edge of the perforated plate. Moreover, with an increase in Reynolds number, the roughness function also decreased. This finding agrees with the effect of the perforated structure on local skin friction as shown in Figure 8(b).

The perforated structure can be considered as an anisotropic permeable material. The permeability of the perforated structure in the wall-normal direction can be estimated as[2]:

$$K_y = \varepsilon d^2 h/(32h + 15d), \tag{1}$$

where ε is the porosity or the OAR for the perforated plate. As the depth of the backing chamber is much larger than the depth of the perforated plate, the permeability of the perforated structure in both the spanwise and streamwise directions is assumed to be infinity, $K_x = K_z \approx \infty$. Figure 11(b) shows the roughness function as a function of the inner-scale root square of the permeability, $\sqrt{K_y}^+ = \sqrt{K_y}U_\tau/\nu$ for the turbulent boundary layers over the perforated structure at different thicknesses of the perforated structures, H. Gómez-de Segura and García-Mayoral[11] found that the effect of wall-normal permeability on the roughness function depends on the thicknesses of the perforated structures. When the non-dimensional thickness, $H/\sqrt{K_x}$, reduces, the minimum roughness function increases and is observed at a larger wall-normal permeability. The non-dimensional thickness of the perforated structures of the current study is approximately zero. Hence, the current results agree with the data by Gómez-de Segura and García-Mayoral[11].

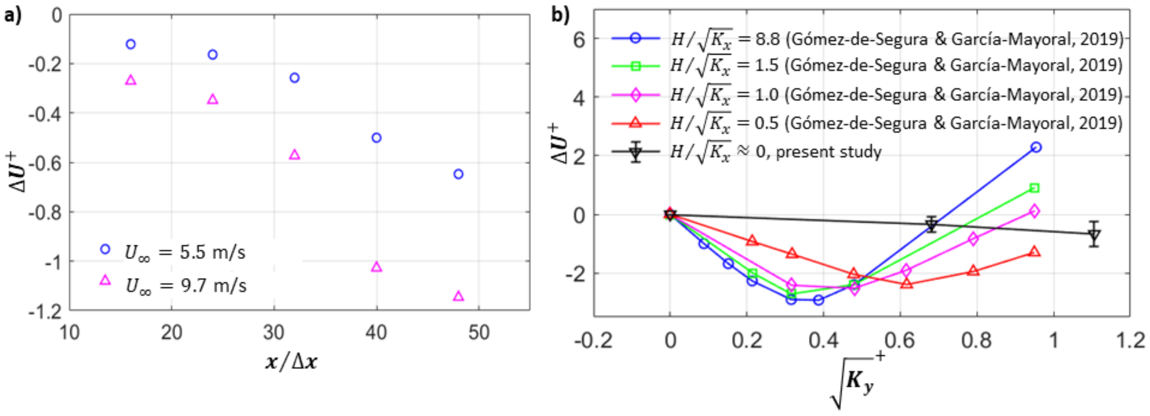

FIG. 11. Roughness functions of the turbulent boundary layers over the perforated structure as a function of a) the downstream location from the leading edge of the perforated plate and b) the permeability at different thicknesses.

Roughness heights would also play a role in the effect of the perforated structure on the turbulent boundary layers. The equivalent sand roughness height, k_s, of a perforated structure is equivalent to the Forchheimer coefficient,$1/\alpha_y$, where $\alpha_y = 1/(OAR^2h)$[44]. The inner-scaled equivalent sand roughness heights of the perforated structure are relatively small, $k_s^+ \leq 0.5$, while the rough wall with a small inner-scaled sand equivalent roughness height, $k_s^+ \leq 1$, could be considered as a smooth wall as mentioned in the work by Nikuradse et al.[34]. Hence, the perforated structure behaves more similar to a smooth wall than a rough wall due to a relatively small equivalent roughness. Figure 12 shows the roughness function of turbulent boundary layers over a perforated plate as a function of the inner-scaled orifice diameter. The perforated plate with a backing cavity can be considered an acoustic liner. The literature shows that acoustic liners increase the total drag with the increasing relevance of pressure drag. However, the pressure drag reduces when the inverse of the Forchheimer coefficient reduces,$1/\alpha^+$, reduces Shahzad et al.[45]. At $Re_\tau \approx 500$ the pressure drag coefficient of $C_{fp} = 0.106^{-3}$ which is about 45 times smaller than the viscous drag coefficient of $C_{fp} = 4.492^{-3}$ at $1/\alpha^+ = 0.0528$ and $d^+ \approx 40$. In addition, Shahzad et al.[44] found that at $d^+ \leq 40$, the roughness effect of acoustic liners is very small. In my research, the orifice diameter of $d^+ \approx 26$ and the equivalent sand roughness height of $k_s \leq 1$ are small, so it suggested that the pressure drag was caused by the perforated plate but it is small and can be negligible.

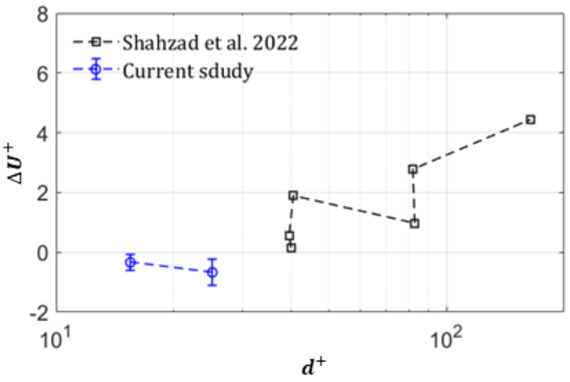

FIG. 12. Roughness functions of the turbulent boundary layers over the perforated structure as a function of inner-scaled orifice diameters. The black square dashed line is reproduced from the data of Shahzad et al.[44].

The leading edge of the perforated plate could be considered as a step change where the turbulent boundary layers start their transition from a smooth wall to a rough wall. This transition would generate an internal layer inside the turbulent boundary layers as discussed by Antonia and Luxton[1] and Efros and Krogstad[7]. The flow within this internal layer is not in energy equilibrium, disrupting the concept of similarity within it[1]. Figure 13(a) shows the definition of the internal layer thickness, δ_i, of the turbulent boundary layer at $x/\Delta x$ = 16 and U_∞ =5.5 m/s by using a half-power method which uses the unit of the internal layer thickness in inches as proposed by Antonia and Luxton[1]. The mean profile experienced a linear trend within the internal layer and another linear trend within the outer layer. The point where these two lines intersected was found to be close to the internal layer edge. Figure 13(b) shows the comparison between the boundary layer thickness and the internal layer thickness of the turbulent boundary layers over the perforated structure at U_∞ = 5.5 m/s as a function of the downstream location from the step change. The result shows that the internal layer thickness is proportional to $X^{0.73}$, which is close to $X^{0.72}$ by Antonia and Luxton[1], $X^{0.7}$ by Krogstad and Nickels[26], and $X^{0.73}$ by Efros and Krogstad[7]. The results also show that it would take about 400δ for the internal thickness to reach the boundary layer thickness, which is much larger than a distance of 15δ reported by Efros and Krogstad[7]. Although the difference in Reynolds number could contribute to this distance scatter, the rough height could play an important role. While the equivalent sand roughness of $k_s^+ \approx 110$ was used in the work by Efros and Krogstad[7], the equivalent sand roughness of $k_s^+ \leq 1$ was used in this study. Hence, the roughness effect of the perforated plate can be negligible.

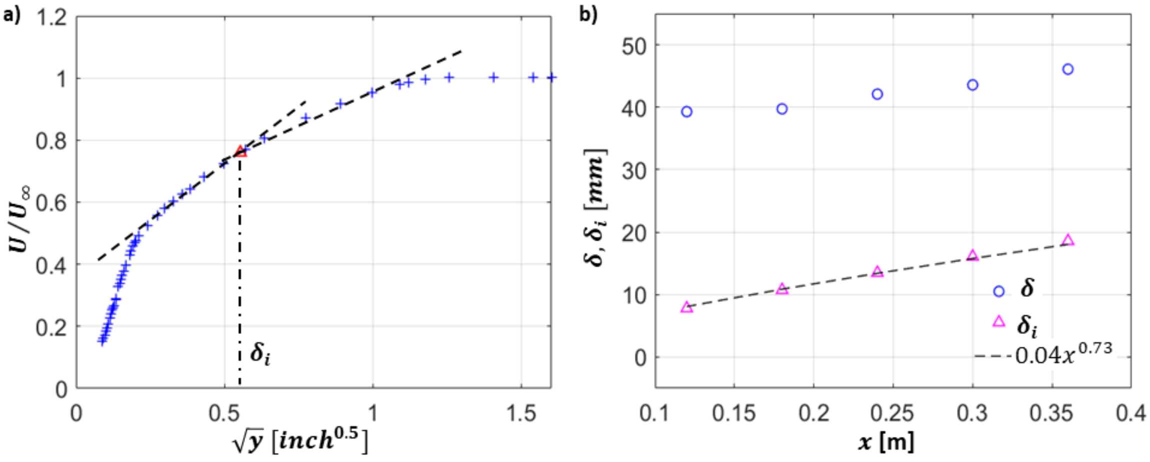

FIG. 13. a) Definition of the internal boundary layer thickness, δ_i, and b) variation of boundary layer thicknesses and internal layer thicknesses as function of the distance from the step for turbulent boundary layers at U_∞ = 5.5 m/s. The black dashed lines present the logarithmic law in the inner and outer regions.

Figure 14 shows the inner-scaled root mean square of the instantaneous velocity, $\mathrm{rms}(u)^+ = \mathrm{rms}(u)/U_\tau$, of the inner-scale wall-normal locations of the turbulent boundary layers over the perforated structure compared with those in the baseline case. The results show that the turbulence intensity profiles in the baseline case exhibit an inner peak at $y^+ = 15$ associated with near-wall cycles in the streamwise direction. The turbulent intensity profiles in the controlled cases experienced an increase in the turbulence intensity at the downstream location of the leading edge of the perforated plate. This agrees with the increase in Reynolds numbers when the turbulent boundary layer passes the leading edge of the perforated plate. The results also show a clear reduction in the inner peak of the turbulence intensities of the turbulent boundary layers over the perforated structure in comparison with those in the baseline case. The results show a hump in the logarithmic region of the turbulence boundary layer. This could result from the wall-normal velocities generated by the interaction between the inside and outside of the backing chamber. The reduction in the near-wall region and the increase in the logarithmic region suggest that the perforated structure transfers the turbulence energy away from the wall in a way that reduces skin friction. A similar mechanism was reported for wall-normal jets by Kametani et al.[22], Lu et al.[28], Zhang et al.[54].

The turbulence intensity profiles shown in Figure 14 also experienced an inflection point at $y^+ \approx 30$ where the inflection in the streamwise velocities also occurred, which generated a hump in turbulence intensities at $y^+ \geq 30$. The hump at $30 \leq y^+ \leq 100$ for U_∞ = 5.5 m/s and $30 \leq y^+ \leq 150$ for U_∞ = 9.7 m/s is reduced when the turbulent boundary layer passes over the leading edge of the perforated plate. A reduction in the hump of the turbulence intensities associated with a reduction in adverse pressure gradient was observed in the turbulent boundary layers with an adverse pressure gradient[31]. It therefore suggests that the pressure gradient increased at a downstream location from the leading edge of the perforated plate. In contrast, the hump at $y^+ \geq 100$ for U_∞ = 5.5 m/s and $y^+ \geq 150$ for U_∞ = 9.7 m/s increased when the turbulent boundary layer passes the leading edge of the perforated plate, which suggests that the perforated structure may only generate a local adverse pressure gradient in the near-wall region of the turbulent boundary layer.

Figure 15 shows the reduction in the averaged turbulence intensities of the turbulent boundary layers due to the perforated structure in the near wall region, $y^+ \leq 30$. The averaged turbulence intensity in the near-wall region is given as:

$$TI = \frac{1}{y^+_{max}} \int_0^{y^+_{max}} \mathrm{rms}(u)^+ dy^+, \tag{2}$$

where $y^+_{max} = 30$ is the selected upper limit of the near-wall region. The results show that when the turbulent boundary layer passed the leading edge of the perforated plate, the reduction in the turbulence intensities in the near wall region became larger at both the free streamwise velocities, U_∞ = 5.5 m/s, and 9.7 m/s. For example, the reduction increased from about 1.9% at $x/\Delta x$ = 16 to about 7% at $x/\Delta x$ = 48 for the cases with a free streamwise velocity of U_∞ = 5.5 m/s. The maximum reduction of about 9% was observed at $x/\Delta x$ = 48 and U_∞ = 9.7 m/s. The reduction in the turbulence intensities in the near-wall region would result in a reduction in the shear stresses and friction drag.

The time-averaged flow field in the turbulent boundary layers over the perforated structure shows the effect of the perforated structure on the mean velocity and turbulence intensity profiles.

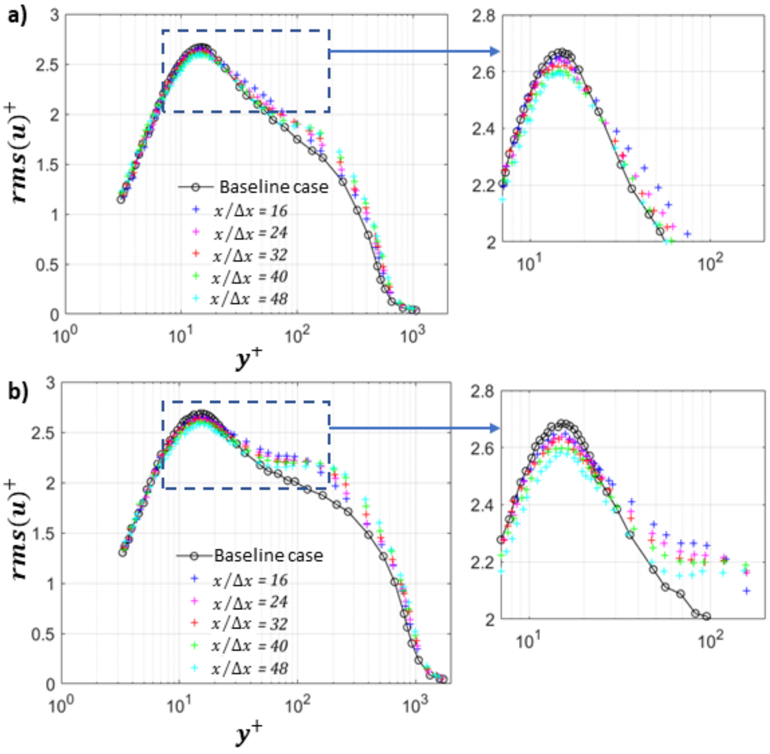

FIG. 14. Turbulence intensity profiles of the turbulent boundary layers over the perforated structure compared with those of the unperturbed turbulent boundary layer at a) U_∞ = 5.5 m/s and b) U_∞ = 9.7 m/s.

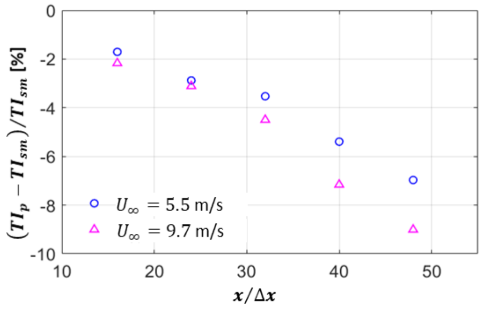

FIG. 15. Reductions in the averaged turbulence intensity in the near-wall region, $y^+ \leq 30$, of the turbulent boundary layers, TI_p, over the perforated structure compared to those of the undisturbed turbulent boundary layer, TI_{sm}.

The relatively small values of permeability and the equivalent sand roughness of the perforated structure suggest a small effect of permeability and roughness on the turbulent boundary layers. This agrees with the long distance for the internal layer to reach the boundary layer edge. In contrast, the turbulence intensity profiles of the turbulent boundary layers over the perforated structure illustrate a clear reduction in the near-wall region. The perforated structure reduced the turbulence generation in the near-wall region, probably leading to a reduction in the shear stresses and friction drag.

C. Burst events

Burst events such as ejections and sweeps are significant contributors to the generation of turbulence within turbulent boundary layers. They are closely linked to turbulence intensities in the near-wall region as identified by Kim et al.[23]. Analysis of turbulence intensities reveals a distinct decrease in turbulence generation near the wall. Therefore, this subsection explores how the perforated structure alters burst events.

Burst events, encompassing both sweep and ejection events, can be identified using the Variable Interval Time Averaging (VITA) technique, as described by Whalley[53]. A burst is identified when the local variance, Var(t,T_W), within a window T_W, exceeds the variance of the entire velocity fluctuations signal, Var(t), adjusted by a threshold, k. The local variance is defined as:

$$\mathrm{Var}(t,T_W) = \widehat{u^2}(t,T_W) - (\hat{u}(t,T_W))^2, \tag{3}$$

where $\hat{Q}(t,T_W)$ is the local mean, $\hat{Q}(t,T_W) = \frac{1}{T_W}\int_{t-\frac{1}{2}T_W}^{t+\frac{1}{2}T_W} Q dt$. The detection function, $D(t)$, of burst events can be given as[53]:

$$D(t) = \begin{cases} 1 \text{ if } \mathrm{Var}(t,T_W) \geq k \times \mathrm{Var}(t) \text{ and } du/dt > 0 \text{ (sweep events)} \\ 0 \text{ if } \mathrm{Var}(t,T_W) < k \times \mathrm{Var}(t) \text{ (no events)} \\ -1 \text{ if } \mathrm{Var}(t,T_W) \geq k \times \mathrm{Var}(t) \text{ and } du/dt < 0 \text{ (ejection events)} \end{cases} . \tag{4}$$

Changing the VITA parameters, k and T_W^+, has no impact on the conclusions reported here, so $k = 1.2$ and $T_W^+ = 20$ were selected in this current study.

Figure 16 presents the burst signatures of velocity fluctuations for the baseline case at y^+ =15 using VITA parameters T_W^+ = 10 and k = 1.2. The velocity signal duration was 30 seconds with a sampling frequency of 40 kHz. Figure 16(a) depicts the instantaneous sweep signatures, while Figure 16(b) shows the instantaneous ejection signatures. A total of 247 sweep events were detected, whereas 48 ejection events were identified. The number of sweep events is much larger than the number of ejection events, which is consistent with findings from Whalley[53]. The intensity of bursts was computed from peak-to-peak values, while the duration of bursts was determined from the time separation of the peaks of the mean signature of the events, as illustrated in Figure 16.

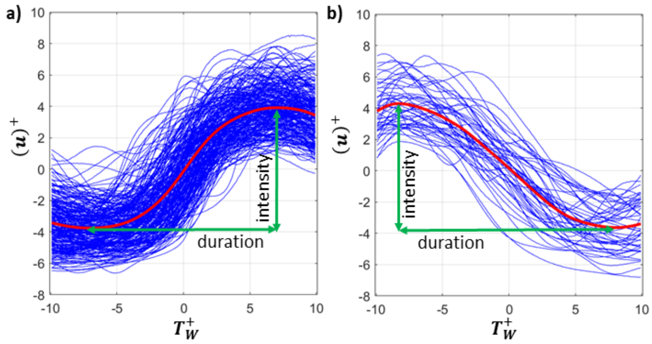

FIG. 16. Burst signatures with VITA parameters, $T_W^+ = 20$ and $k = 1.2$ for the baseline data at $y^+ = 15$. a) the sweep events and b) the ejection events. The red lines present the mean signatures.

In Figure 17, the sweep and ejection profiles of the turbulent boundary layers over the perforated structure compared with those of the baseline cases at a stream velocity, $U_\infty = 9.7$ m/s are shown. Figures 17(a, d) demonstrate the impact of the perforated structure on sweep and ejection intensities, respectively. It is observed that as the turbulent boundary layer passed the leading edge of the perforated plate, both the sweep and ejection intensities decreased at $y^+ \approx 30$. These effects agree with those observed in the turbulence intensities of velocity fluctuations, as shown in Figure 14. Figures 17(c, f) show the effect of the perforated structure on the sweep and ejection frequency profiles. The results indicate a reduction in both sweep and ejection frequencies throughout the turbulent boundary layers as the turbulent boundary layer passes the leading edge of the perforated plate. Given the reduction in the intensity and duration of both the sweep and ejection events near the wall, a corresponding decrease in turbulence intensities in the near-wall region was expected, consistent with Figure 14. In contrast, Figures 17(b, e) do not indicate an effect of the perforated structure on the sweep and ejection durations.

The effect of the perforated structure on the sweep and ejection events in the near-wall region of the turbulent boundary layers over the perforated structure compared to those of the undisturbed turbulent boundary layers as a function of the downstream location at two free streamwise velocities of $U_\infty = 5.5$ and 9.7 m/s are shown in Figures 18. The averaged burst intensity, $\overline{I}_b$, and averaged burst frequency, $\overline{f}_b$, in the near-wall region, $y^+ \leq 30$, are given as:

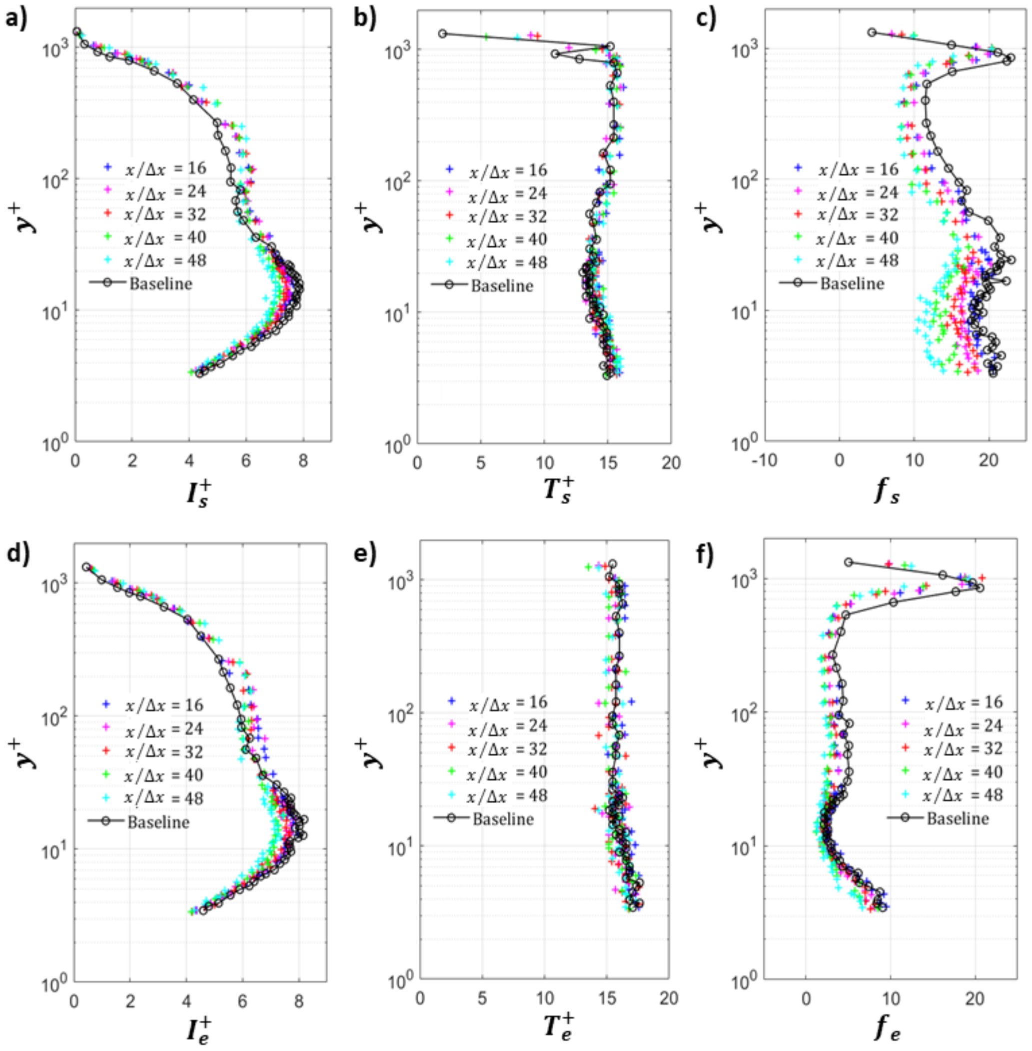

FIG. 17. a, d) The burst intensity, b, e) the burst durations, and c, f) the burst frequencies as a function the wall-normal locations for the turbulent boundary layers over the perforated structure compared with those in the baseline cases for the cases with a free stream velocity of U_∞ = 9.7 m/s. The top figure row presents the sweep events. The bottom figure row presents the ejection events.

$$\bar{I}_b = \frac{1}{y^+_{max}}\int_0^{y^+_{max}} I_b^+ dy^+ ; \bar{f}_b = \frac{1}{y^+_{max}}\int_0^{y^+_{max}} f_b dy^+ . \qquad (5)$$

where $y^+_{max} = 30$.

Figure 18(a, c) show that when the turbulent boundary layer passed the leading edge of the perforated plate, the reduction in both the sweep and ejection intensity became more pronounced. For instance, the reduction in sweep intensity increased from about 3.5% at $x/\Delta x$ = 16 to about

7.5% at $x/\Delta x = 48$ for the cases with a free streamwise velocity of $U_\infty = 5.5$ m/s. A similar effect on the ejection intensity was observed. The maximum sweep intensity reduction of about 9% and the maximum ejection intensity reduction of about 9.3% were observed at $x/\Delta x = 48$ and $U_\infty = 9.7$ m/s. Figure 18(b, d) show the effect of the perforated structure on the sweep and ejection frequencies in the near-wall region of the turbulent boundary layers. The results show that the sweep frequency reduces when the turbulent boundary layer passes the leading edge of the perforated plate, which is similar to the effect on the ejection frequencies. For example, the reduction in the sweep frequency increases from about 1% at $x/\Delta x = 16$ to about 21% at $x/\Delta x = 48$ and the reduction in the ejection frequencies increases from about 7% at $x/\Delta x = 16$ to about 25% at $x/\Delta x = 48$ for the cases with a free streamwise velocity of $U_\infty = 5.5$ m/s. The sweep and ejection frequency reduction maximises at about 33.5% and 25% at $x/\Delta x = 48$ and $U_\infty = 9.7$ m/s, respectively. Therefore, the impact of the perforated structure on sweep and ejection events mirrors its effect on turbulence intensities in the near-wall region, as shown in Figure 15. This indicates a strong correlation between sween and ejection events and turbulence generation in the near-wall region of the turbulent boundary layers. This relationship has also been reported in prior research[23,52].

Figure 19(a) shows the effect of the inner-scaled orifice diameter on the reduction in the burst intensity due to the perforated structure measured at C5 in comparison with the work by Silvestri et al.[46]. The result shows that when the inner-scaled orifice diameter increases from about 15 to 26, the reduction in burst intensity increases from about 7.5% to 9%. This finding agrees with the work by Silvestri et al.[46]. Figure 19(b) shows the reduction in burst intensity due to the perforated structure as a function of the inner-scaled chamber volume. The results show that when the inner-scaled chamber volume increases, the reduction in burst intensity becomes more pronounced. The increase in the burst intensity reduction along with an increase in the inner-scaled chamber volume was also reported by Silvestri et al.[49,50]. It is believed that the kinematic energy of the sweeps is damped when the sweeps penetrate through the orifices into the chamber. The larger the chamber volume is, the more sweep energy is damped. As a result, the sweeps become weaker when the chamber volume increases, which reduces the turbulence intensity in the near-wall region of the turbulence boundary layers over the perforated plate.

The near-wall region of the turbulent boundary layers experienced a significant effect of the perforated structure. The clear reduction in burst intensity and frequencies would result in a reduction in turbulence intensities in the near-wall region as discussed in Subsection III B. This also indicates that the perforated structure weakened the ejection and sweep events in the near-wall

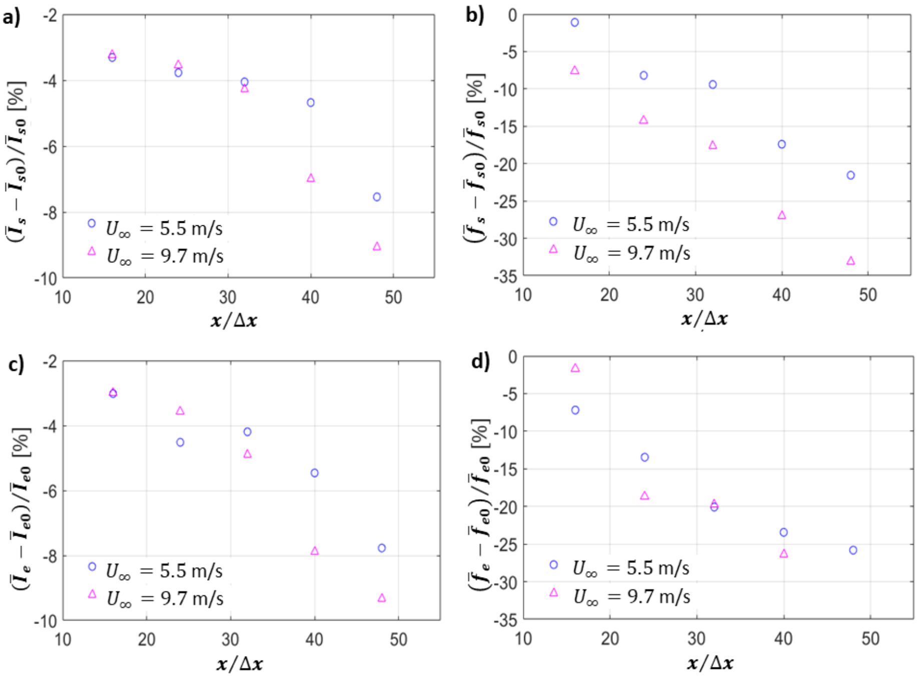

FIG. 18. Reductions in a) the averaged sweep intensities, $\bar{I}_s$, b) the averaged sweep frequencies, $\bar{f}_s$, c) the averaged ejection intensity, $\bar{I}_e$, and d) the averaged ejection frequencies, $\bar{f}_e$, of the turbulent boundary layers over the perforated structure compared to those of the undisturbed turbulent boundary layers in the near-wall region, $y^+ \leq 30$. The subscript of '0' presents the values of the undisturbed turbulent boundary layers.

region, which probably resulted in a reduction in the shear stress and skin friction drag.

D. Spectral content

The power spectral densities (*PSD*), Φ_{uu} of streamwise velocity fluctuations in turbulent boundary layers were computed from the time signal of 2^{20} samples, employing the Welch algorithm. The calculation utilised a 50% overlap, a Hamming window, and a window size of 2^{17} samples. The resulting energy spectrum provides insight into the distribution of turbulent kinetic energy among eddies of various sizes.

Figures 20(a-c, g-i) show the pre-multiplied PSDs, $k_x\Phi^+_{uu} = k_x\Phi_{uu}/U^2_\tau$, with k_x being the wave number in the downstream direction of the turbulent boundary layers for both the baseline and controlled cases, as a function of the inner-scaled wave length, λ^+, and the inner-scaled

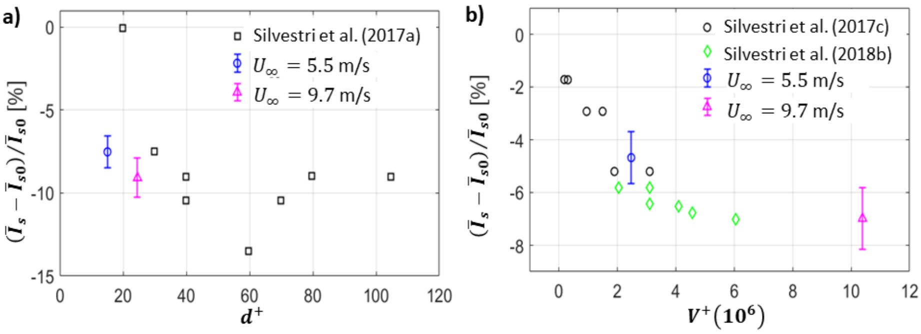

FIG. 19. a) Variance in the averaged sweep intensity as a function of the inner-scaled orifice diameter and b) variance in averaged sweep frequencies as a function of the inner-scaled chamber volume for the turbulent boundary layers over the perforated structure measured at C5 compared to the undisturbed turbulent boundary layer in the near-wall region, $y^+ \leq 30$. The black squares are reproduced from the data of Silvestri et al.[46]. The black circles are reproduced from the data of Silvestri et al.[50]. The green diamonds are reproduced from the data of Silvestri et al.[49]. The error bars represent the variation in downstream measurement locations.

normal-wall locations at three downstream locations, $x/\Delta x$ = 16, 32, and 48, respectively. The pre-multiplied PSDs were smoothed for better visualisation. The results show a clear increase in the pre-multiplied PSDs at $y^+ \geq 30$ but the location of the inner peak at $y^+ \approx 15$ experiences a mirror effect due to the perforated structure. Figures 20(d-f, k-m) show the difference between the pre-multiplied PSDs of the streamwise velocity fluctuations of the turbulent boundary layers over the perforated structure, $(k_x\Phi^+_{uu})_{cav}$, and those of the undisturbed boundary layer, $(k_x\Phi^+_{uu})_{sm}$. The difference is given as:

$$\Delta(k_x\Phi^+_{uu}) = (k_x\Phi^+_{uu})_{cav} - (k_x\Phi^+_{uu})_{sm}. \tag{6}$$

The results show a clear reduction in the pre-multiplied PSD of the turbulent boundary layers over the perforated structure in the near wall region, $y^+ \leq 30$, compared with those of the undisturbed boundary layers over a smooth flat plate. In contrast, there was an increase in the pre-multiplied PSD at $y^+ \geq 30$ for the perforated cases compared with those for the baseline cases. It is suggested that the turbulent kinetic energy was transferred from the near wall region to the outer region, which could probably result from the weakened bursts in the near wall region as shown in Figure 17. When the turbulent boundary layer passed the leading edge of the perforated plate, the reduction in the pre-multiplied PSD became more pronounced. This is consistent with the reduction in the burst events and the turbulence intensity at the downstream location of the leading edge of the perforated plate. As the turbulent kinetic energy reduces in the near wall region of the turbulent boundary layers over the perforated structure, it was expected that the wall-shear stresses would reduce in the perforated cases in comparison with those in the baseline cases.

Figure 21 shows the pre-multiplied PSDs, $k_x\Phi_{uu}/U_\tau^2$, with k_x being the wave number in the downstream direction, as a function of the inner-scaled wave length, λ^+ at y^+ = 15 for both the perforated and baseline cases at U_∞ = 5.5 and 9.7 m/s. The results illustrate a peak in the pre-multiplied PSDs for the baseline case at $\lambda^+ \approx 1000$ when the turbulent boundary layer was over a smooth flat plate. This inner peak was associated with the near-wall cycles of the turbulent boundary layers. The inner peak in the pre-multiplied PSDs of the turbulent boundary layers over a smooth plate was also observed in the work by Mathis et al.[30] and Hutchins and Marusic[17]. The results show a reduction in the pre-multiplied PSDs in the perforated cases compared with those in the baseline cases, which agrees with the reduction in turbulence intensities, as shown in Figure 14, and in the burst events, as shown in Figure 17, of the turbulent boundary layers over the perforated structure in the near wall region. When the turbulent boundary layer passed the leading edge of the perforated plate, this effect became more pronounced. The reduction in the pre-multiplied PSDs at the inner peak of the turbulent boundary layers over the perforated structure illustrates the reduction in turbulence generation in the near-wall region, which would result in a reduction in the wall-shear stresses.

IV. CONCLUSION

In this paper, hot-wire experiments were conducted to investigate how a perforated plate with a backing chamber affects the near-wall turbulences of turbulent boundary layers at two Reynolds numbers, Re_θ = 1165 and 2294. Different inner-scaled chamber volumes from $V^+ = 2.4 \times 10^6$ to 11.5×10^6 were used to manipulate turbulent boundary layers. The study's findings are outlined below.

The near-wall turbulence of the turbulent boundary layers experienced a decrease of approximately 9% in sweep intensity, 9.3% in ejection intensity, 25% in ejection frequency, and up to 33.5% in sweep frequency within the near-wall region, $y^+ \leq 30$, indicating that the perforated structure weakened turbulent activities near the wall. Consequently, the turbulence intensity in

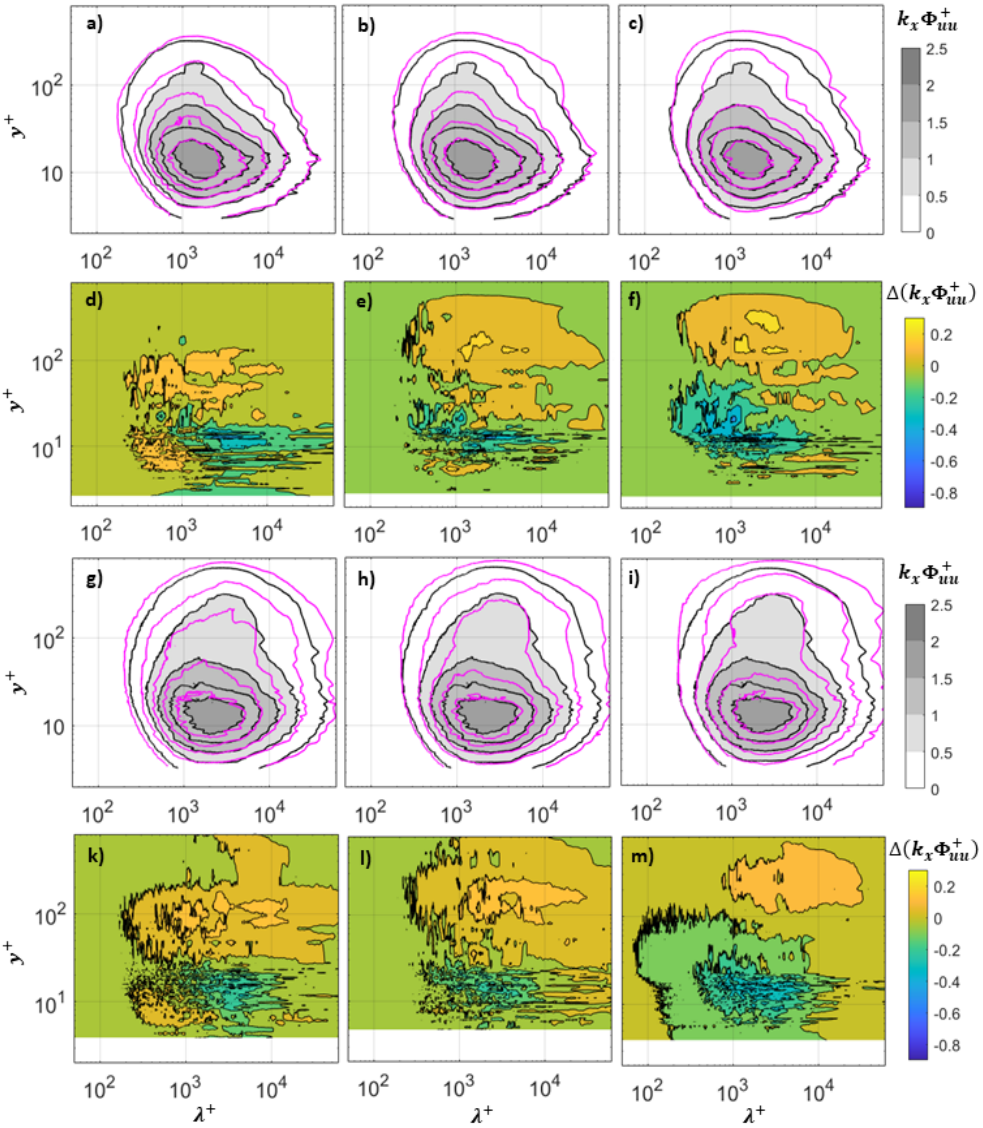

FIG. 20. Pre-multiplied PSDs, $k_x\Phi_{uu}^+$; a-c) U_∞ = 5.5 m/s; g-i) U_∞ = 9.7 m/s; and difference between the pre-multiplied PSDs of the turbulent boundary layers over the perforated structure respect to the one of the undisturbed boundary layers, $\Delta(k_x\Phi_{uu}^+)$; d-f) U_∞ = 5.5 m/s; k-m) U_∞ = 9.7 m/s. The magenta lines present for the controlled cases with $k_x\Phi_{uu}^+$ from 0 to 2.5 in steps of 0.5. The black contours presents for the baseline case. The columns from left to right present the cases from $x/\Delta x$ = 16, 32, and 48, respectively.

this region decreased by nearly 9%. Moreover, a decrease in turbulent kinetic energy near the wall, coupled with an increase at $y^+ \geq 30$, implies that the perforated structure redistributes turbulent energy from the near-wall region to the outer region, probably leading to a reduction in shear stresses and skin friction drag.

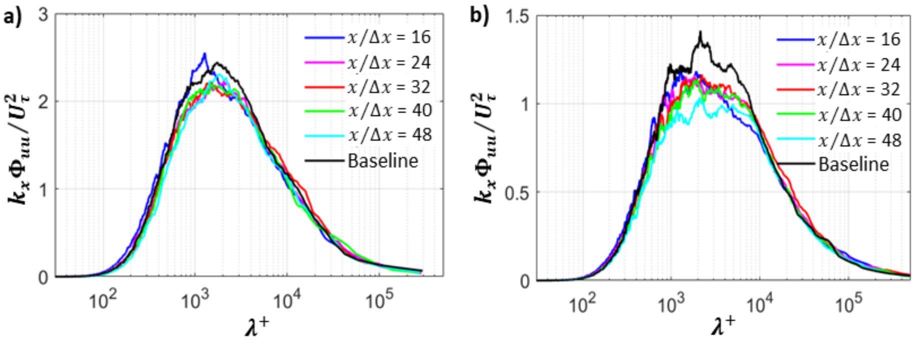

FIG. 21. Pre-multiplied PSDs of the velocity fluctuations as a function of the inner-scaled wave length at y^+ = 15 for both the perforated and baseline cases at a) U_∞ = 5.5 m/s and b) U_∞ = 9.7 m/s.

The backing chamber plays an important role in reducing near-wall turbulence. The increase in the chamber volume results in a decrease in the local skin friction drag, suggesting that the larger the backing chamber, the more kinetic energy is damped. Consequently, the sweeps are weakened and the near-wall turbulence intensity is reduced. It is suggested that the wall-normal velocities at the perforated surface exchange the energy between the inside and outside of the chamber and play an important role in reducing the near-wall turbulence of the turbulent boundary layers over the perforated structure. Future research will carefully examine the near-wall region by using methods like μ-PIV or a comprehensive DNS model of the perforated structure to investigate the wall-normal velocities at the perforated surface for understanding the energy exchange between the inside and outside of the chamber and to confirm the hypotheses in this study.

ACKNOWLEDGMENTS

This research was supported by the Australian Government Research Training Program (RTP) and the Australian Government through the Australian Research Council (ARC DP-200101961).

AUTHOR DECLARATIONS

Conflict of Interest

The authors have no conflicts to disclose.

Author Contributions

Van Thuan Hoang: Conceptualization (equal); Data curation (equal); Formal analysis (equal); Investigation (equal); Methodology (equal); Project administration (equal); Validation (equal); Visualization (equal); Writing - original draft (equal); Writing - review, and editing (equal). Azadeh Jafari: Conceptualization (equal); Formal analysis (equal); Investigation (equal); Project administration (equal); Methodology (equal); Supervision (equal); Writing - review, and editing (equal). Benjamin Cazzolato: Conceptualization (equal); Investigation (equal); Project administration (equal); Supervision (equal); Writing - review, and editing (equal). Maziar Arjomandi: Conceptualization (equal); Formal analysis (equal); Investigation (equal); Methodology (equal); Project administration (equal); Supervision (equal); Writing - review, and editing (equal)

DATA AVAILABILITY

The data that support the findings of this study are available from the corresponding author upon reasonable request.

REFERENCES

[1] Antonia, R. and Luxton, R. (1971). The response of a turbulent boundary layer to a step change in surface roughness part 1. smooth to rough. *Journal of Fluid Mechanics*, 48(4):721–761.

[2] Bae, Y. and Kim, Y. I. (2016). Numerical modeling of anisotropic drag for a perforated plate with cylindrical holes. *Chemical Engineering Science*, 149:78–87.

[3] Bhat, S., Silvestri, A., Cazzolato, B., and Arjomandi, M. (2021). Mechanism of control of the near-wall turbulence using a micro-cavity array. *Physics of Fluids*, 33(7).

[4] Cheng, X., Qiao, Z., Zhang, X., Quadrio, M., and Zhou, Y. (2021). Skin-friction reduction using periodic blowing through streamwise slits. *Journal of Fluid Mechanics*, 920:A50.

[5] Coxe, D. (2019). *Drag Reduction in Turbulent Pipe Flow by Transverse Wall Oscillations at Low and Moderate Reynolds Number*. PhD thesis, Arizona State University.

[6] De Graaff, D. B. and Eaton, J. K. (2000). Reynolds-number scaling of the flat-plate turbulent boundary layer. *Journal of Fluid Mechanics*, 422:319–346.

[7] Efros, V. and Krogstad, P.-Å. (2011). Development of a turbulent boundary layer after a step from smooth to rough surface. *Experiments in Fluids*, 51:1563–1575.

[8]Fukagata, K., Iwamoto, K., and Kasagi, N. (2002). Contribution of reynolds stress distribution to the skin friction in wall-bounded flows. *Physics of fluids*, 14(11):L73–L76.

[9]Gak-El-Hak, M. (1996). Modern development in flow control. *Applied Mechanics Review*, 9:365–379.

[10]Ghanadi, F., Arjomandi, M., Cazzolato, B. S., and Zander, A. C. (2015). Analysis of the turbulent boundary layer in the vicinity of a self-excited cylindrical Helmholtz resonator. *Journal of Turbulence*, 16(8):705–728.

[11]Gómez-de Segura, G. and García-Mayoral, R. (2019). Turbulent drag reduction by anisotropic permeable substrates–analysis and direct numerical simulations. *Journal of Fluid Mechanics*, 875:124–172.

[12]Gowree, E. R., Jagadeesh, C., and Atkin, C. J. (2019). Skin friction drag reduction over staggered three dimensional cavities. *Aerospace Science and Technology*, 84:520–529.

[13]Guo, H., Borodulin, V., Kachanov, Y., Pan, C., Wang, J., Lian, Q., and Wang, S. (2010). Nature of sweep and ejection events in transitional and turbulent boundary layers. *Journal of Turbulence*, 11:N34.

[14]Heinemann, P., Panagiotou, P., Vratny, P., Kaiser, S., Hornung, M., and Yakinthos, K. (2017). Advanced tube and wing aircraft for year 2050 timeframe. In *55th AIAA Aerospace Sciences Meeting*, page 1390.

[15]Hon, T.-L. (1987). *Analysis of the motions and effects of hairpin vortices*. PhD thesis, Lehigh Univ., Bethlehem, PA (USA).

[16]Hutchins, N. and Choi, K.-S. (2002). Accurate measurements of local skin friction coefficient using hot-wire anemometry. *Progress in Aerospace Sciences*, 38(4-5):421–446.

[17]Hutchins, N. and Marusic, I. (2007). Evidence of very long meandering features in the logarithmic region of turbulent boundary layers. *Journal of Fluid Mechanics*, 579:1–28.

[18]Hutchins, N., Monty, J., Hultmark, M., and Smits, A. (2015). A direct measure of the frequency response of hot-wire anemometers: temporal resolution issues in wall-bounded turbulence. *Experiments in Fluids*, 56(1):1–18.

[19]Hutchins, N., Nickels, T. B., Marusic, I., and Chong, M. (2009). Hot-wire spatial resolution issues in wall-bounded turbulence. *Journal of Fluid Mechanics*, 635:103–136.

[20]Hyun Shin, J. and Jin Song, S. (2015). Pressure gradient effects on smooth and rough surface turbulent boundary layers—part i: Favorable pressure gradient. *Journal of Fluids Engineering*, 137(1):011203.

[21] Jafari, A., Cazzolato, B., and Arjomandi, M. (2022). Finite-length porous surfaces for control of a turbulent boundary layer. *Physics of Fluids*, 34(045115):1–34.

[22] Kametani, Y., Fukagata, K., Örlü, R., and Schlatter, P. (2015). Effect of uniform blowing/suction in a turbulent boundary layer at moderate Reynolds number. *International Journal of Heat and Fluid Flow*, 55:132–142.

[23] Kim, H., Kline, S., and Reynolds, W. (1971). The production of turbulence near a smooth wall in a turbulent boundary layer. *Journal of Fluid Mechanics*, 50(1):133–160.

[24] Kornilov, V. (2015). Current state and prospects of researches on the control of turbulent boundary layer by air blowing. *Progress in Aerospace Sciences*, 76:1–23.

[25] Krein, A. and Williams, G. (2012). *Flightpath 2050: Europe's vision for aeronautics*. Innovation for Sustainable Aviation in a Global Environment: Proceedings of the Sixth European Aeronautics Days.

[26] Krogstad, P. and Nickels, T. (2006). Turbulent boundary layer with a step change in surface roughness. In *13th International Conference on Fluid Flow Technologies*, pages 6–9.

[27] Ligrani, P. and Bradshaw, P. (1987). Spatial resolution and measurement of turbulence in the viscous sublayer using subminiature hot-wire probes. *Experiments in Fluids*, 5(6):407–417.

[28] Lu, L., Li, D., Gao, Z., Cao, Z., Bai, Y., and Zheng, J. (2020). Characteristics of array of distributed synthetic jets and effect on turbulent boundary layer. *Acta Mechanica Sinica*, 36:1171–1190.

[29] Marec, J.-P. (2001). Drag reduction: a major task for research. In *Aerodynamic drag reduction technologies*, pages 17–27. Springer.

[30] Mathis, R., Hutchins, N., and Marusic, I. (2009). Large-scale amplitude modulation of the small-scale structures in turbulent boundary layers. *Journal of Fluid Mechanics*, 628:311–337.

[31] Monty, J. P., Harun, Z., and Marusic, I. (2011). A parametric study of adverse pressure gradient turbulent boundary layers. *International Journal of Heat and Fluid Flow*, 32(3):575–585.

[32] Moretti, P. and Kays, W. (1965). Heat transfer to a turbulent boundary layer with varying free-stream velocity and varying surface temperature—an experimental study. *International Journal of Heat and Mass Transfer*, 8(9):1187–1202.

[33] Nickels, T., Marusic, I., Hafez, S., and Chong, M. (2005). Evidence of the k_{-1}^{1} law in a high-Reynolds-number turbulent boundary layer. *Physical Review Letters*, 95(7):074501.

[34] Nikuradse, J. et al. (1933). Laws of flow in rough pipes. Technical report, National Advisory Committee for Aeronautics Washington.

[35] Orlandi, P. and Jiménez, J. (1994). On the generation of turbulent wall friction. *Physics of Fluids*, 6(2):634–641.

[36] Österlund, J. M., Johansson, A. V., Nagib, H. M., and Hites, M. H. (2000). A note on the overlap region in turbulent boundary layers. *Physics of Fluids*, 12(1):1–4.

[37] Panton, R., Flynn, K., and Bogard, D. (1987). Control of turbulence through a row of Helmholtz resonators. In *25th AIAA Aerospace Sciences Meeting*, page 436.

[38] Park, S., Lee, I., and Sung, H. J. (2001). Effect of local forcing on a turbulent boundary layer. *Experiments in Fluids*, 31:384–393.

[39] Samie, M., Baars, W., Rouhi, A., Schlatter, P., Örlü, R., Marusic, I., and Hutchins, N. (2020). Near wall coherence in wall-bounded flows and implications for flow control. *International Journal of Heat and Fluid Flow*, 86:108683.

[40] Scarano, F., Jacob, M. C., Gojon, R., Carbonneau, X., and Gowree, E. R. (2022). Modification of a turbulent boundary layer by circular cavities. *Physics of Fluids*, 34(6):065134.

[41] Scarano, F., Jacob, M. C., and Gowree, E. R. (2023). Drag reduction by means of an array of staggered circular cavities at moderate Reynolds numbers. *International Journal of Heat and Fluid Flow*, 102:109142.

[42] Schlatter, P., Li, Q., Brethouwer, G., Johansson, A. V., and Henningson, D. S. (2010). Simulations of spatially evolving turbulent boundary layers up to $Re_\theta = 4300$. *International Journal of Heat and Fluid Flow*, 31(3):251–261.

[43] Schultz, M. P. and Flack, K. A. (2003). Turbulent boundary layers over surfaces smoothed by sanding. *Journal of Fluids Engineering*, 125(5):863–870.

[44] Shahzad, H., Hickel, S., and Modesti, D. (2022). Permeability and turbulence over perforated plates. *Flow, Turbulence and Combustion*, 109(4):1241–1254.

[45] Shahzad, H., Hickel, S., and Modesti, D. (2023). Turbulence and added drag over acoustic liners. *Journal of Fluid Mechanics*, 965:A10.

[46] Silvestri, A., Ghanadi, F., Arjomandi, M., Cazzolato, B., and Zander, A. (2017a). Attenuation of sweep events in a turbulent boundary layer using micro-cavities. *Experiments in Fluids*, 58:1–13.

[47] Silvestri, A., Ghanadi, F., Arjomandi, M., Cazzolato, B., and Zander, A. (2017b). The effect of the backing cavity on the control of the turbulent boundary layer by the application of a cavity array. In *Tenth International Symposium on Turbulence and Shear Flow Phenomena*, pages 293–298. Begel House Inc.

[48] Silvestri, A., Ghanadi, F., Arjomandi, M., Cazzolato, B., and Zander, A. (2018a). The application of different tripping techniques to determine the characteristics of the turbulent boundary layer over a flat plate. *Journal of Fluids Engineering*, 140(1).

[49] Silvestri, A., Ghanadi, F., Arjomandi, M., Cazzolato, B., Zander, A., and Chin, R. (2018b). Mechanism of sweep event attenuation using micro-cavities in a turbulent boundary layer. *Physics of Fluids*, 30(5):055108.

[50] Silvestri, A., Ghanadi, F., Arjomandi, M., Chin, R., Cazzolato, B., and Zander, A. (2017c). Attenuation of turbulence by the passive control of sweep events in a turbulent boundary layer using micro-cavities. *Physics of Fluids*, 29(11).

[51] Smith, C. and Metzler, S. (1983). The characteristics of low-speed streaks in the near-wall region of a turbulent boundary layer. *Journal of Fluid Mechanics*, 129:27–54.

[52] Tang, Z. and Jiang, N. (2020). The effect of a synthetic input on small-scale intermittent bursting events in near-wall turbulence. *Physics of Fluids*, 32(1).

[53] Whalley, R. D. (2011). *Turbulent boundary-layer control with DBD plasma actuators using spanwise travelling-wave technique*. PhD thesis, University of Nottingham.

[54] Zhang, X., Wong, C., Cheng, X., and Zhou, Y. (2022). Dependence of skin-friction reduction on the geometric parameters of blowing jet array. *Physics of Fluids*, 34(10).

Chapter 4

Turbulent scales in turbulent boundary layers over a perforated plate

4.1 Chapter overview

The large scales in the outer region directly modulate the small-scale structures in the near-wall regions and consequently affect friction drag in turbulent boundary layers. As discussed in Section 2.1.2 and Section 2.3, a perforated plate increases the large scales in turbulent boundary layers even at relatively small Reynolds numbers. However, the interaction between small and large scales in the turbulent boundary layers over perforated plates has received comparatively less attention. Therefore, this chapter investigates the large-scale amplitude modulation of small scales in turbulent boundary layers over a perforated plate with a backing cavity. To gain an understanding of the effect of the perforated plate on the large-scale amplitude modulation of the small scales, turbulent boundary layers over the perforated plate at different Reynolds numbers were conducted in a closed-return wind tunnel. The turbulent scales are decomposed into small and large scales and the energy patterns of both small and large scales are analysed.

The results demonstrated that the perforated surface significantly increases the turbulence energy of the large-scale structures in the outer region of the turbulent boundary layers. Consequently, the large-scale amplitude modulation of small-scale structures in the turbulent boundary layers was pronounced in the turbulent boundary layers over the perforated surface. A clear increase in the modulation was observed at $20 \leq y^{+}150$ in comparison with those in the baseline cases. In addition, the modulation was reduced at $y^{+} \leq 10$. This suggests that the perforated surface lifts the large-scale motions further from the wall, which diminishes large-scale structures in the near-wall region but increases them in the outside region. When the Reynolds number increased, the effects of the perforated surface on modulation became more significant. The wall-normal location at which the amplitude modulation is zero increases further from the wall in the turbulent boundary layer over the perforated surface, which results in a reduction in skin friction drag compared with those in the unperturbed turbulent boundary layer.

4.2 Statement of Authorship

Statement of Authorship

Title of Paper	Impacts of a perforated plate on large-scale amplitude modulation in turbulent boundary layers
Publication Status	☐ Published ☐ Accepted for Publication ☑ Submitted for Publication ☐ Unpublished and Unsubmitted work written in manuscript style
Publication Details	Hoang, V., Jafari, A., Cazzolato, B., and Arjomandi, M. (2024). Impacts of a perforated plate on large-scale amplitude modulation in turbulent boundary layers. *Journal of Fluid Mechanics*.

Principal Author

Name of Principal Author (Candidate)	Van Thuan Hoang		
Contribution to the Paper	Impacts of a perforated plate on large-scale amplitude modulation in turbulent boundary layers		
Overall percentage (%)	75		
Certification:	This paper reports on original research I conducted during the period of my Higher Degree by Research candidature and is not subject to any obligations or contractual agreements with a third party that would constrain its inclusion in this thesis. I am the primary author of this paper.		
Signature		Date	04/02/2025

Co-Author Contributions

By signing the Statement of Authorship, each author certifies that:

i. the candidate's stated contribution to the publication is accurate (as detailed above);

ii. permission is granted for the candidate in include the publication in the thesis; and

iii. the sum of all co-author contributions is equal to 100% less the candidate's stated contribution.

Name of Co-Author	Azadeh Jafari		
Contribution to the Paper	Supervised the development of the research, helped in developing ideas, contributed in academic discussion and manuscript review.		
Signature		Date	19/02/2025

Name of Co-Author	Benjamin Cazzolato		
Contribution to the Paper	Supervised the development of the research, helped in developing ideas, contributed in academic discussion and manuscript review.		
Signature		Date	19/02/2025

Name of Co-Author	Maziar Arjomandi		
Contribution to the Paper	Supervised the development of the research, participated in developing ideas an helped in interpretation of results, provided critical revision		
Signature		Date	19/02/2025

4.3 Impacts of a perforated plate on large-scale amplitude modulation in turbulent boundary layers

This chapter consists of the following published journal article:

Hoang, V.T., Jafari, A., Cazzolato, B., and Arjomandi, M. (2024). Impacts of a perforated plate on large-scale amplitude modulation in turbulent boundary layers. *Journal of Fluid Mechanics.* (Submitted).

The article is identical to its published format with the following exceptions:

- The numbering of figures, tables and equations have been altered to include the chapter number.
- The position of some figures and tables have been changed to improve legibility.

Impacts of a perforated plate on large-scale amplitude modulation in turbulent boundary layers

V.T. Hoang,[1] A. Jafari,[2] B. Cazzolato,[1] and M. Arjomandi[1]

[1]*School of Electrical and Mechanical Engineering, The University of Adelaide, Adelaide, South Australia 5005, Australia*

[2]*School of Mechanical and Mining Engineering, The University of Queensland, St Lucia, Queensland 4072, Australia*

(*Electronic mail: vanthuan.hoang@adelaide.edu.au)

(Dated: 18 February 2025)

This study investigates the large-scale amplitude modulation of small scales in turbulent boundary layers over a perforated plate with a backing cavity. Various viscous-scaled cavity volumes ranging from $V^+ = 2.7 \times 10^6$ to 31.3×10^6 were examined for the purpose of manipulating turbulent boundary layers at different Reynolds numbers from $Re_\theta = 1449$ to 4409. The results measured using hot-wire anemometry show that the shear stresses were reduced throughout the boundary layers due to the perforated surface, resulting in a decrease in turbulence production, particularly at $y^+ \leq 30$. This is associated with the redistribution of the turbulent kinetic energy with a reduction in the near-wall region and an increase in the outer region. Statistical analysis using scale decomposition and the Hilbert transformation shows that the large-scale amplitude modulation was reduced at $y^+ \leq 10$ but increased at $20 \leq y^+ \leq 150$ compared with those in the baseline cases. This implies that the perforated surface elevates large-scale structures, such as quasi-streamwise vortices and streaks away from the wall, reducing large-scale structures in the near-wall region but increasing them in the outer region. The impact of the perforated surface on large-scale amplitude modulation was more pronounced at higher Reynolds numbers.

I. INTRODUCTION

Turbulence control in wall-bonded flows has been an interesting topic for numerous researchers. It aims to reduce friction drag in various engineering applications, such as airplanes and cars, which consequently reduces energy consumption. As a result, carbon dioxide (CO_2) emissions from these applications are reduced. In wall-bounded flows, the interaction between the turbulent boundary layer and the wall creates skin friction drag. Coherent structures including ejections and sweep events in the near-wall region mainly contribute to shear stresses and skin friction drag in turbulent boundary layers (Guo et al., 2010). However, the contribution of the outer region to skin friction drag increases as the Reynolds number increases (Hwang, 2013). At high Reynolds numbers, large-scale structures emerge in the outer region, especially in the logarithmic region (Hutchins and Marusic, 2007). These large-scale structures directly modulate the behaviour of small-scale structures in the near-wall regions (Gomit et al., 2018; Hutchins and Marusic, 2007). Mathis et al. (2009a) found a strong large-scale amplitude modulation of small-scale structures in the near-wall region in turbulent boundary layers at Reynolds numbers of $Re_\tau \approx 10^3 \div 10^4$, where $Re_\tau = \delta U_\tau/\nu$, δ is the boundary layer thickness, U_τ is the friction velocity, and ν is the viscosity. Hence, turbulent boundary layer control which targets large coherent structures could indirectly affect the near-wall turbulence and reduce skin friction drag (Duvvuri and McKeon, 2016; Deshpande et al., 2023).

Perforated surfaces have recently shown potential for skin friction drag reduction in turbulent boundary layers. Silvestri et al. (2017) experimentally investigated the effect of perforated surfaces on turbulence intensity and sweep events in turbulent boundary layers. Their findings demonstrate that the sweep events are limited and that the array does not record any events for a viscous-scaled orifice diameter of $d^+ = dU_\tau/\nu \leq 20$, where d is the orifice diameter. Moreover, separation of the shear layer and increased turbulence energy production in the near-wall region occurred at $d^+ \geq 145$. The maximum reduction in sweep intensities and turbulence occurs at 13% and 14%, respectively for $d^+ \approx 60$. Gowree et al. (2019) found that perforated surfaces could reduce drag by as much as 10%. They discovered that for $d/h \leq 1$, where h is the orifice depth, the skin friction drag reduces, while for $d/h \geq 1$, it increases. The authors proposed that the mechanism of skin friction drag reduction by the perforated plate was comparable to that by riblets by adjusting the transverse velocities. Scarano et al. (2022, 2023) examined how a perforated plate affected turbulent boundary layer modification and skin friction drag reduction. The friction drag is estimated by using the near-wall velocity gradient technique by Hutchins and Choi (2002). Their findings demonstrate a notable decrease in local skin friction drag of up to approximately 30%. Skin friction decreased and boundary layer modification became more pronounced as the open area ratio (OAR) increased. The instantaneous upward and downward velocity components were observed in the numerical simulation of a turbulent boundary layer over a perforated plate by Bhat et al. (2021). They proposed that quasi-streamwise vortices could potentially be lifted by this erratic blowing effect, increasing energy in the outer region and creating a second burst intensity hump. Consequently, the low-momentum fluid carried by these structures as they move upward then alters the mean velocity in a way that decreases skin friction. Kornilov (2015) proposed a similar process of skin friction decrease in turbulent boundary layers due to wall-normal blowing.

Recent studies show that adding a backing cavity can increase the performance of a perforated plate in controlling turbulent boundary layers. Silvestri et al. (2018b) found that the sweep intensity reduction increases with a rise in the backing cavity volume, V, before reaching a threshold of $V^+ = V(U\tau/\nu)^3 = 5 \times 10^6$. The sweep intensity reduction is due to the dissipation of sweep energy in the backing cavity and the friction loss through the orifices (Silvestri et al., 2018b). According to Jafari et al. (2022), at large scales of $\lambda_x \geq \delta$, a backing cavity significantly reduced the pre-multiplied spectrum of streamwise velocity fluctuations by up to 80%. The authors proposed that turbulent boundary layers may be reorganised by irregular transpiration via the orifices. Hoang et al. (2024) found that near-wall turbulent structures are significantly affected by the presence of a backing cavity. Within the near-wall region, $y^+ \leq 30$, there was a reduction of up to about 9% in sweep and ejection intensity, a decrease of about 25% in ejection frequency, and a decrease of roughly 33.5% in sweep frequency. As a result, turbulence intensities were reduced by up to about 9% in the vicinity of the wall, which helped to locally reduce shear stresses and skin friction drag. Scarano et al. (2024) recently reported an increase in large-scale structures of turbulent boundary layers due to a perforated plate even at moderate Reynolds number of $Re_\tau \approx 1000$. Their results show a clear outer peak in the turbulence energy spectrum due to the perforated plate, suggesting that the large-scale structures are dominant in the outer region of the turbulent boundary layers over the perforated plate.

The published studies have shown an increase in the turbulent energy of large-scale structures in turbulent boundary layers over a perforated plate at moderate Reynolds numbers. However, how this increase in the large-scale structures affect the near-wall region has received comparatively less attention. The analysis of this effect would contribute to understanding the mechanisms of friction drag reduction in turbulent boundary layers due to a perforated plate. Hence, the purpose of this work is to examine the large-scale amplitude modulation of small scales in the near-wall region of turbulent boundary layers over a perforated plate. The amplitude modulation impact was quantified using the Hilbert transformation and scale decomposition proposed by Mathis et al. (2009a). An esxtensive description of the experimental configuration is given in the section that follows. The modulation results are then shown in Section III, and Section IV contains closing thoughts.

II. EXPERIMENTAL METHODS

A. Experimental rig and flow conditions

Boundary layer measurements were conducted in a closed-return wind tunnel at the University of Adelaide. The wind tunnel's test section is rectangular, measuring 2000 mm in length and 600 mm × 500 mm in cross-section, which is similar to the experimental setup in the work by Hoang et al. (2024). In these studies, the test section width is greater than ten times the boundary layer thickness. An elliptical edge was fastened to the leading edge of the plate to avoid the bluff body separation due to the finite plate thickness. To lessen the formation of any circulation and the impact of back pressure, a 125 mm-long flap was installed at the trailing edge of the plate. The side walls were adjusted to achieve an acceleration parameter in the order of 10^{-8} which is similar to the value for the turbulent boundary layers with a zero pressure gradient (Schultz and Flack, 2003; Hyun Shin and Jin Song, 2015). This was done to achieve a zero pressure gradient along the test section. As suggested by Silvestri et al. (2018a), the inlet flow was tripped using a 3 mm rod positioned 140 mm downstream of the leading edge of the flat plate to guarantee the boundary layer is fully developed.

To analyse flow statistics related to the near-wall cycle, stream-wise velocities were measured using a Dantec single probe, model number 55P15, with a 5 μm diameter and a 1.25 mm length. The hot-wire probe length ranged from 19 to 45 in viscous units, denoted by $l^+ = lU_\tau/\nu$, where l represents the probe length. The measurements were conducted for 30 s at a sampling frequency of $f_s = 40$ kHz and repeated three times to estimate the measurement uncertainties. The variance parameters of the turbulent boundary layers were then calculated and then represented by error bars in the result section. A Pitot-static tube that was attached to a 10 Torr Baratron pressure transducer was used to calibrate the probe. It was assumed that the ambient temperature was constant throughout the experiments because the variance of the temperature during calibration and measurements was less than 1° C. A Mitutoyo dial/mechanical-digit counter height gauge with a travel range of 0 to 300 mm and an accuracy of ±0.03 mm was utilised to position the probe at various normal-wall locations.

Three free stream velocities, U_∞, of 5.5, 9.7, and 14 m/s were considered. The measurement points for the turbulent boundary layers over the smooth plate were S1, x = -40 mm, and S2, x = 480 mm where the x origin is in the first orifice row of the perforated plate. Based on momentum thicknesses, $Re_\theta = \theta U_\infty/\nu$, the Reynolds numbers ranged from 1499 to 4409. Table I contains the main flow parameters of the turbulent boundary layers over a smooth flat plate. Friction coefficients are given as $C_f = \overline{\tau_w}/(\rho U_\infty^2/2)$ with ρ, the air density and $\overline{\tau_w}$, the averaged wall-shear stress. The wall-shear stresses were determined using the near-wall velocity gradient method created by Hutchins and Choi (2002) as shown in Section II C. In order to compare the turbulent boundary layers controlled by the perforated surface, the unperturbed turbulent boundary layers at S2 were considered as baseline cases.

TABLE I. Flow parameters for the turbulent boundary layers over a smooth plate.

U_∞ (m/s)	locations	Re_θ	Re_τ	θ (mm)	δ^* (mm)	δ_{99} (mm)	H	l^+	ν/U_τ (μm)	U_τ (m/s)	C_f (10^{-3})	τ_w (N/m^2)
5.5	S1	1154	501	3.25	4.73	31.1	1.45	20.1	62.1	0.249	4.11	0.074
5.5	S2	1499	587	4.20	6.08	37.8	1.44	19.4	64.3	0.240	3.80	0.069
9.7	S1	2267	870	3.64	5.14	33.4	1.41	32.6	38.4	0.403	3.49	0.193
9.7	S2	2802	1022	4.44	6.21	39.9	1.40	32.1	39.0	0.395	3.31	0.187
13.9	S1	3639	1242	4.07	5.67	35.1	1.39	44.2	28.3	0.549	3.13	0.358
14.0	S2	4409	1482	4.90	6.74	42.4	1.38	43.7	28.6	0.541	3.01	0.348

Figure 1(a) shows the viscous-scaled velocity profiles, $U^+ = U/U_\tau$, of the unperturbed turbulent boundary layer as a function of the viscous-scaled wall-normal locations, $y^+ = yU_\tau/\nu$ compared with the DNS data of Schlatter et al. (2010) at a similar range of Reynolds numbers. The results show good agreement between the current results and the published data. The friction coefficients of turbulent boundary layers over a smooth flat plate are shown in Figure 1(b) as a function of Reynolds numbers and are compared to the experimental results (Österlund et al., 2000). Within the measurement uncertainties, the computed friction coefficients for the turbulent boundary layers show good agreement with the experimental data. The verification of the baseline cases was presented in detail by Hoang et al. (2024).

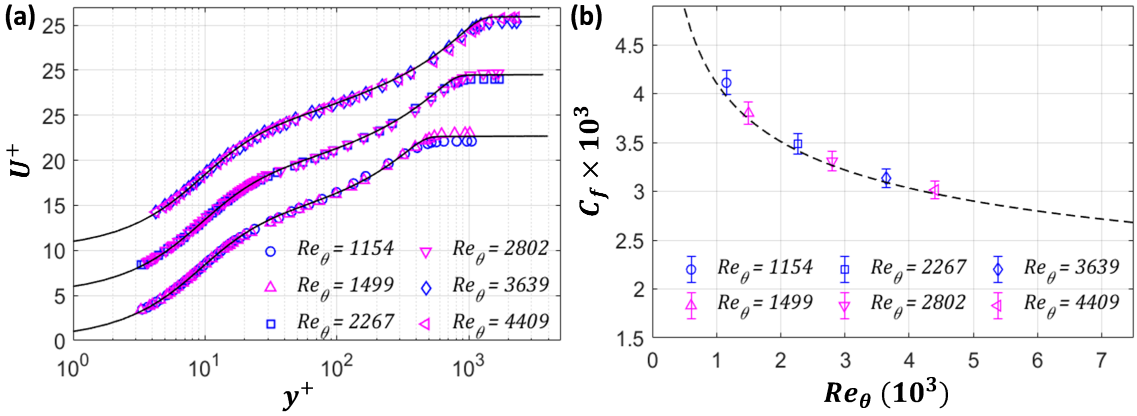

FIG. 1. Turbulent boundary layers over a smooth flat plate: (a) Mean velocity profiles and (b) friction coefficients. The black solid lines are reproduced from the DNS data of Schlatter et al. (2010) at similar Reynolds numbers, Re_θ = 1410, 2540, and 4060. The black dashed line is reproduced from the semi-empirical relationship, $C_f = 1/2 \times (1/0.384 \times \ln(Re_\theta) + 4.08)^{-2}$ of Österlund et al. (2000).

B. Perforated surface Geometries and Test cases

The perforated surface was located at 1140 mm from the leading edge of the test section. The plate has 64 rows and 340 columns of circular orifices with a diameter of $d = 1$ mm, a depth of $h = 5$ mm, and spacings of $\Delta x = 7.5$ mm in the streamwise and $\Delta z = 1.7$ mm in the spanwise directions. In viscous units, $d^+ = d \times U_\tau/\nu$, the orifice diameter ranged from 15 to 35. In the streamwise direction, the orifice spacing ranged from 122 to 268 in viscous units, $\Delta x^+ = \Delta x \times U_\tau/\nu$. In the span-wise direction, the orifice spacing ranged from 27 to 61 in viscous units, $\Delta z^+ = \Delta z \times U_\tau/\nu$. The reasons for selecting these geometries were reported in the work by Hoang et al. (2024). The box-shaped backing cavity is 500 mm in length, 598 mm in width, and 50 mm in depth. The cavity volume for each orifice, $V^+ = V/(\nu/U_\tau)^3/N$ with $N = 21760$ representing the number of orifices, is from 2.7×10^6 to 31.3×10^6. These volumes were selected based on the threshold of $V^+ = V(U\tau/\nu)^3 = 5 \times 10^6$ proposed by Silvestri et al. (2018b). Measurements were conducted in the case of perforated plates at three different locations, C1, C2, and C3, corresponding to $x =$

243.2, 304.0, and 364.8 mm, from the leading edge of the perforated plate, which equates to $x/\Delta x$ = 32, 40, and 48 as shown in Figure 2. These measurement positions are located between two consecutive rows. The local friction velocities were estimated as $U_\tau = \sqrt{\tau_w/\rho}$, where τ_w was the wall-shear stress estimated using the near-wall velocity gradient technique developed by Hutchins and Choi (2002) as discussed in Section II A.

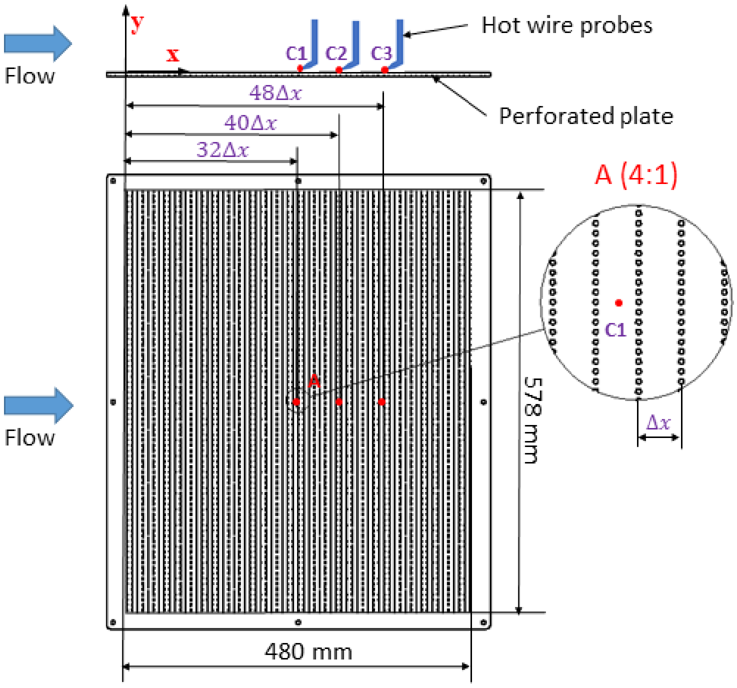

FIG. 2. Schematic of the measurement locations for the turbulent boundary layers the ones over the perforated plate and the measurement locations, C1, C2, and C3.

C. Determination of wall-shear stresses

Wall-shear stresses can be calculated by $\tau_w = \mu \frac{du}{dy}$, where u represents the instantaneous velocities in the viscous sublayer of turbulent boundary layers, and μ represents the dynamic viscosity of air. Since it can be difficult to conduct two simultaneous measurements in the viscous sublayer of turbulent boundary layers, an assumption of a non-slip condition at the wall was made. This means that $\tau_w = \mu u/y$ can be used to estimate the wall-shear stress. Through hotwire measurements in the near-wall region of y^+ = 3.5 to 5.5, the wall-shear stresses were indirectly estimated. This method is named the "near-wall velocity gradient technique" proposed by (Hutchins and

Choi, 2002). They found that the standard error of friction coefficients estimated by this technique is about 1%. Fig. 3(a) shows a sample of instantaneous wall-shear stresses in the controlled case at C3 with U_∞ = 5.5 m/s and the baseline case. For the baseline case, the ratio between the variance and mean of the instantaneous wall-shear stresses, $\mathrm{rms}(\tau_W^{'})/\overline{\tau_W} = 0.39$ was observed, in agreement with a universal value of 0.4 suggested by Örlü and Schlatter (2011). Because of the perforated surface, the instantaneous wall-shear stresses in the controlled case had a mean value of $\overline{\tau_W}/\overline{\tau_{W0}} \approx 0.94$, which was less than that of the baseline case. Figure 3(b) shows the dimensional velocity profiles of the turbulent boundary layers over the perforated surface at C2 and C3 with U_∞ = 5.5 m/s in comparison with the baseline case in the near-wall region. The results show that the dimensional velocity profiles for the controlled cases were smaller than those for the baseline case. These dimensional velocities were normalised by the viscous units and shown in Figure 3(c). The non-dimensional velocity profiles for both the controlled and baseline cases were collapsed to the DNS data by Schlatter et al. (2010) in the region of $3.5 \leq y^+ \leq 5.5$. Those profiles agree with the linear law in this region.

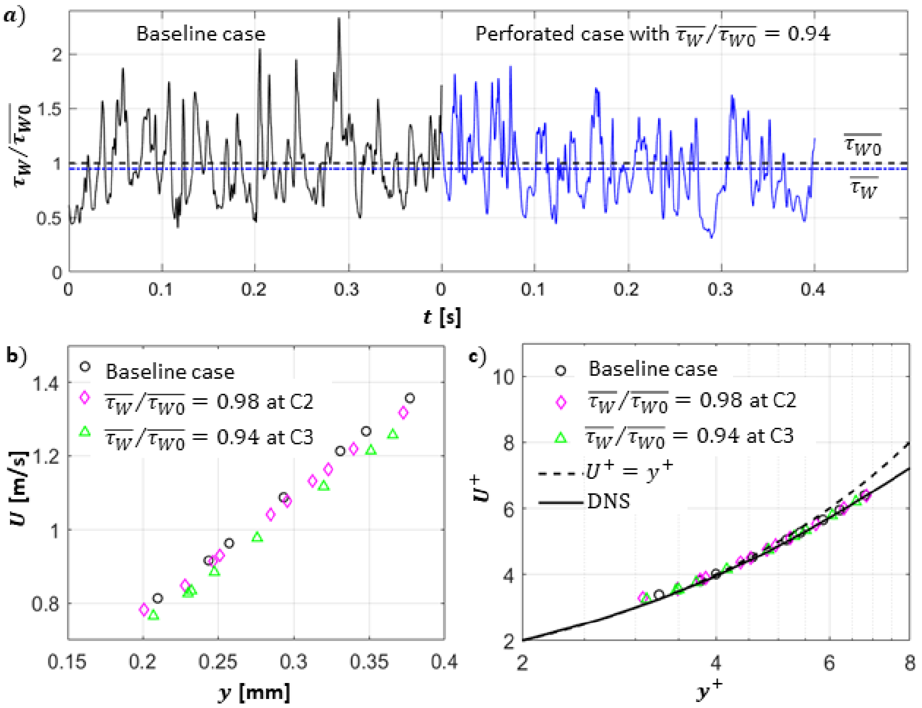

FIG. 3. A sample of instantaneous wall-shear stresses of the turbulent boundary layers in the baseline case and the controlled cases at Locations S2 and C3 with U_∞ = 5.5 m/s.

III. RESULTS AND DISCUSSION

A. Mean velocity and turbulence intensity profiles

The viscous-scaled velocity profiles of the turbulent boundary layers over the perforated surface at different downstream locations compared with the baseline at U_∞ = 14 m/s are shown in Figure 4(a). In comparison to the baseline case, there is an upward shift in the viscous-scaled velocity profiles in the outer region of the turbulent boundary layers over the perforated surface. The effect is more pronounced when the boundary layer crosses the leading edge of the perforated plate. Figures 4(b–d) compare the viscous-scaled velocity profile of the disturbed boundary layers and the baseline case at different Reynolds numbers at Location C2. The results show that when the Reynolds number increases, the effect of the perforated surface on the turbulent boundary layer becomes more pronounced. Similar effects were found at Locations C1, and C3. This finding agrees with the work by Scarano et al. (2022) and Hoang et al. (2024). The upward shift in the viscous-scaled velocity profiles that is often linked with a drag reduction has been largely reported in the literature for different turbulent boundary layer control, such as riblets (Choi, 1989; Cafiero and Iuso, 2022; Endrikat et al., 2021), vortex generators (Aider et al., 2010; Chan and Chin, 2022; Kong et al., 2024), and spanwise wall forcing (Baron and Quadrio, 1995; Quadrio et al., 2009; Chandran et al., 2023).

Figure 5(a) shows the turbulence intensity profiles, $\overline{u'}^{+} = \overline{u'}/U_\tau$, of the turbulent boundary layers over the perforated surface at different downstream locations compared with the baseline at U_∞ = 14 m/s where $\overline{u'}$ is the root mean square of the streamwise velocity fluctuations, u'. The results show that the inner peak at $y^+ \approx 15$ of the turbulence intensity profile for the perforated cases is lower than the one for the baseline case, which clearly shows the reduction in the turbulence generation in the near-wall region of the turbulent boundary layers. In contrast, the turbulence intensity profiles experienced an increase in the logarithmic region, $y^+ \approx 150$, due to the perforated surface. This increase in the large-scale structures in the outer region is potentially due to the wall-normal velocities generated by the interaction between the inside and outside of the backing chamber. The reduction in the near-wall region and the increase in the logarithmic region suggest that the perforated structure transfers turbulence energy away from the wall in a way that reduces skin friction. A similar mechanism was reported for wall-normal jets by Kametani et al. (2015); Lu et al. (2020); Zhang et al. (2022). A reduction of the inner peak and an increase in the outer

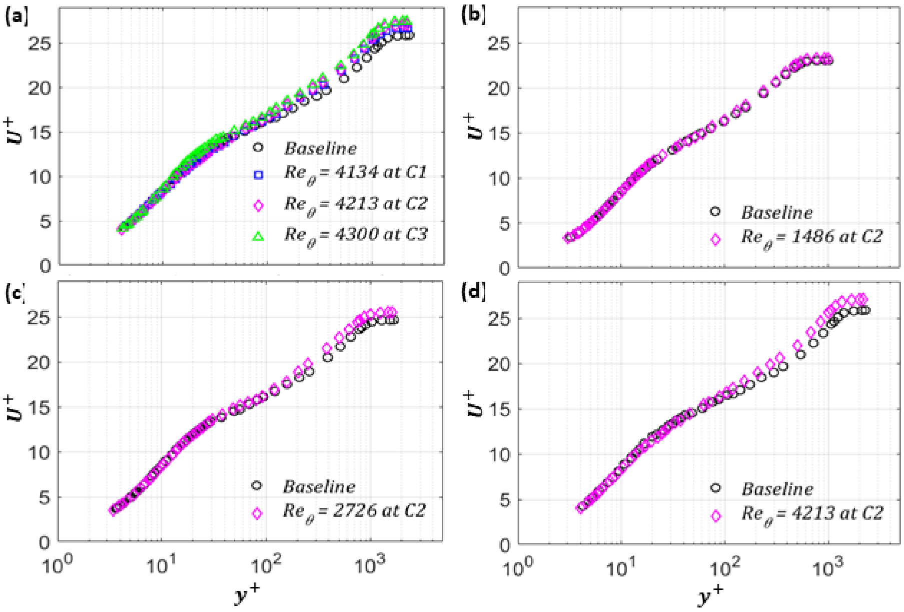

FIG. 4. Viscous-scaled velocity profiles of turbulent boundary layers over a perforated surface (a) at different downstream locations of C1, C2 and C3 compared to the baseline case at U_∞ = 14 m/s, and (b–d) at Location C2 compared to the baseline case at U_∞ = 5.5, 9.7, and 14 m/s, respectively.

peak in the turbulence intensity profiles due to perforated surfaces were also observed in the work by Gowree et al. (2019) and Scarano et al. (2023, 2024). The shift of energy away from the wall, as indicated by the reduction in the near-wall region and the increase in the logarithmic region is associated with a drag reduction for the turbulent boundary layers with wall-normal jets (Kametani et al., 2015; Zhang et al., 2022). Figures 5(b–d) show the turbulence intensity profiles of the turbulent boundary layers over the perforated surface at Location C2 in comparison with those of the baseline case at different Reynolds numbers. The turbulence intensity profiles at Locations C1 and C3 experienced similar effects. The results show that when the Reynolds number increases, the effect of the perforated surface becomes more pronounced. These results agree with the work by Scarano et al. (2022) and Hoang et al. (2024).

B. Turbulence production

The viscous-scaled turbulence production, P^+, in turbulent boundary layers can be given as (Harun et al., 2013):

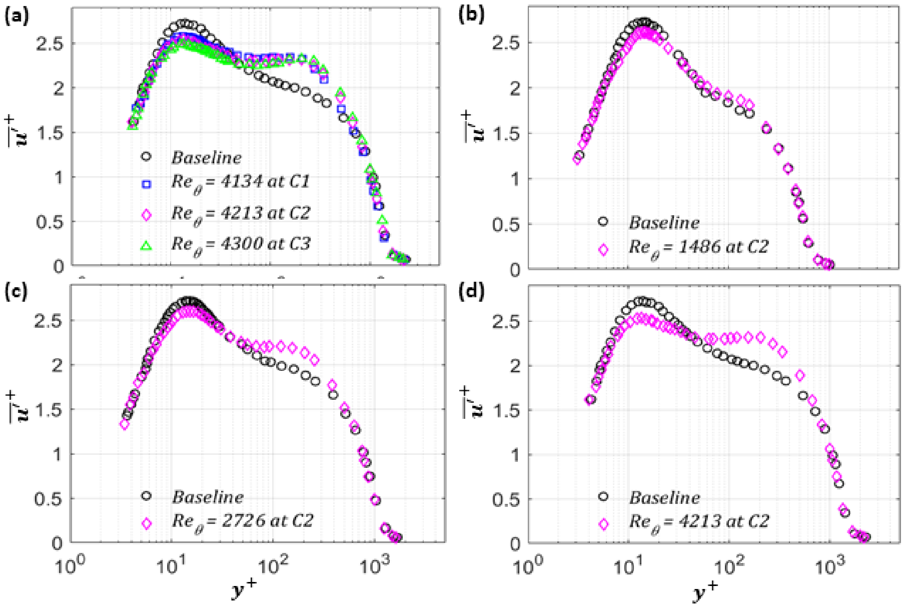

FIG. 5. Turbulence intensity profiles of the turbulent boundary layers over the perforated surface (a) at different downstream locations of C1, C2 and C3 compared to the baseline case at U_∞ = 14 m/s, and (b–d) at Location C2 compared to the baseline case at U_∞ = 5.5, 9.7, and 14 m/s, respectively.

$$P^+ = -\overline{u'v'}^+ \frac{\partial U^+}{\partial y^+} - \overline{u'^2}^+ \frac{\partial U_1^+}{\partial x^+} + \overline{v'^2}^+ \frac{\partial U_1^+}{\partial x^+} - \overline{u'v'}^+ \frac{\partial V^+}{\partial x^+} \qquad (1)$$

where v' is the wall-normal velocity fluctuation, V is the averaged wall-normal velocity, and U_1 is the local freestream velocity. According to Harun et al. (2013), it is sufficient to assume that v'^{2+} is O(1). The second, $\overline{u'^2}^+ \frac{\partial U_1^+}{\partial x^+}$, and third, $\overline{v'^2}^+ \frac{\partial U_1^+}{\partial x^+}$, terms are $\mathrm{O}(10^{-4})$. The fourth term, $\overline{u'v'}^+ \frac{\partial V^+}{\partial x^+}$, is $\mathrm{O}(10^{-6})$. Hence, the second, third, and fourth terms of Equation (1) can be considered negligible. The Reynolds shear stress distribution, $\overline{u'v'}^+$, can be obtained using classical similarity laws and the attached eddy hypothesis by Perry et al. (1994). Perry et al. (2002) applied the Perry formulations to both equilibrium and non-equilibrium boundary layers. Their results show a good agreement between the results estimated by the formulations and those obtained by experiments. Figure 6 shows the Reynolds shear stress profiles for the baseline cases at different freestream velocities, U_∞ = 5.5, 9.5, and 14 m/s in comparison with those calculated from the DNS data of Harun et al. (2013). The results show a good agreement between the current results and the DNS data.

Figures 7(a–c) show the estimated Reynolds shear stress profiles of the controlled cases at C2

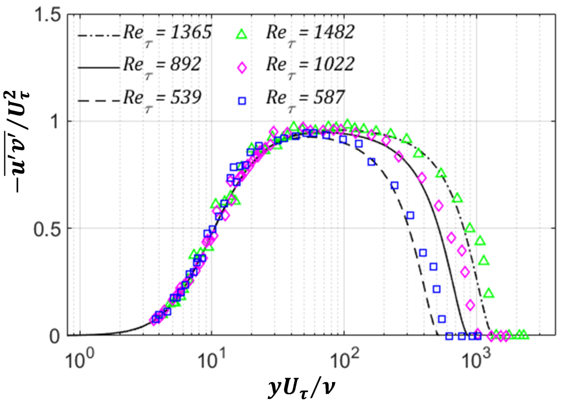

FIG. 6. Reynolds shear stress profiles for the baseline cases at different freestream velocities, $U_\infty = 5.5$, 9.5 and 14 m/s, compared with those which are calculated from the DNS data at similar Reynolds numbers. The black lines represent the reynolds shear stress profiles calculated from the DNS data of Schlatter et al. (2010).

compared with those of the baseline cases at different Reynolds numbers. The results illustrate that the perforated surface reduces the Reynolds shear stress in the region of $20 \leq y^+ \leq 400$. The reduction becomes more pronounced when the Reynolds number increases, which would result in a reduction in skin friction drag. Figures 7(d–f) show the turbulence production profiles of the controlled cases at Location C2 in comparison with those of the baseline cases at different Reynolds numbers. The turbulence production was normalised by the viscous scale of the baseline case. The results show that turbulence is mainly generated in the region of $y^+ \leq 100$. This agrees with the work by Kim et al. (1971). The peak in the turbulence production profiles is associated with the inner peak in the turbulence intensity profiles as shown in Figure 5. When the Reynolds number increases, the reduction in turbulence production becomes more pronounced. Similar effects were observed at Locations C1 and C3. This agrees with the reduction in sweep and ejection events in the near-wall region due to a perforated surface (Hoang et al., 2024).

C. Energy spectra

The energy spectra, Φ_{uu} shows the energy distribution of streamwise velocity fluctuations in turbulent boundary layers. The energy spectra was computed using the Welch algorithm with no overlap, a Hamming window, and a window size of 2^{14}. Figures 8(a–f) show the contours of the

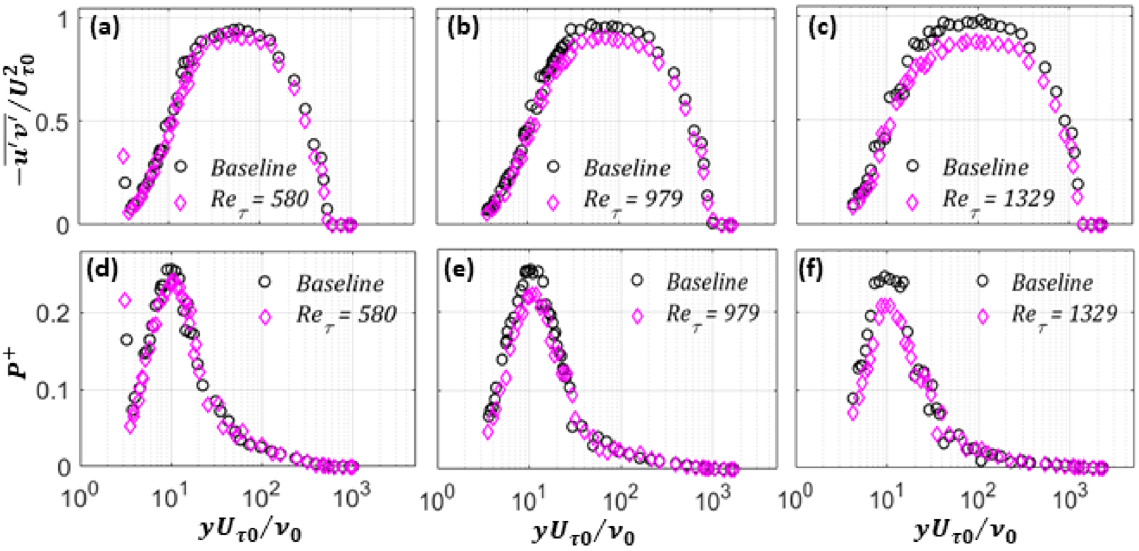

FIG. 7. (a–c) Reynolds shear stress profiles and (d–f) turbulence production profiles. Columns from left to right represent the cases at U_∞ = 5.5 m/s, 9.7 m/s, and 14 m/s, respectively. Black circular markers represent the baseline cases. Diamon magenta markers represent the perforated cases at C2.

Pre-multiplied energy spectra of the streamwise velocity fluctuations, $k_x\Phi_{uu}^+ = k_x\Phi_{uu}/U_{\tau 0}^2$, with k_x being the wavenumber and $U_{\tau 0}$ being the friction velocity in the baseline cases, as a function of the viscous-scaled wall-normal locations and the viscous-scaled wave length, $\lambda_x^+ = \lambda_x U_{\tau 0}/\nu$. The results clearly show an inner peak at $y^+ \approx 15$ and $\lambda_x^+ \approx 1000$, which indicates the dominance of the quasi-streamwise vortices and streaks in this region. The perforated surface reduces the inner peak but increases the turbulence energy in the outer region of $y^+ \geq 50$. A hump in the energy was observed at $y^+ \approx 150$, which is in agreement with the hump in the turbulence intensity as shown in Figure 5. The hump is mainly contributed by large-scale structures, which indicates that the perforated surface promotes these large-scale structures in the outer region. When the Reynolds number increases, both the reduction in the inner peak and the outer hump becomes more pronounced. This indicates that the perforated surface lifts the quasi-streamwise vortices and streaks, which results in a reduction in turbulence intensity and shear stresses in the near-wall region but an increase in the energy of the large-scale structures in the outer region. While the reduction in the turbulence intensity and shear stresses in the near-wall region directly reduces skin friction drag, the increase in the energy of the large-scale structures in the outer region would affect the near-wall region in a way that reduces skin friction drag. The increase in the large-scale energy associated with a friction drag reduction was also reported in the opposition control which controls the large scales in turbulent boundary layers (Abbassi et al., 2017; Dacome et al., 2024).

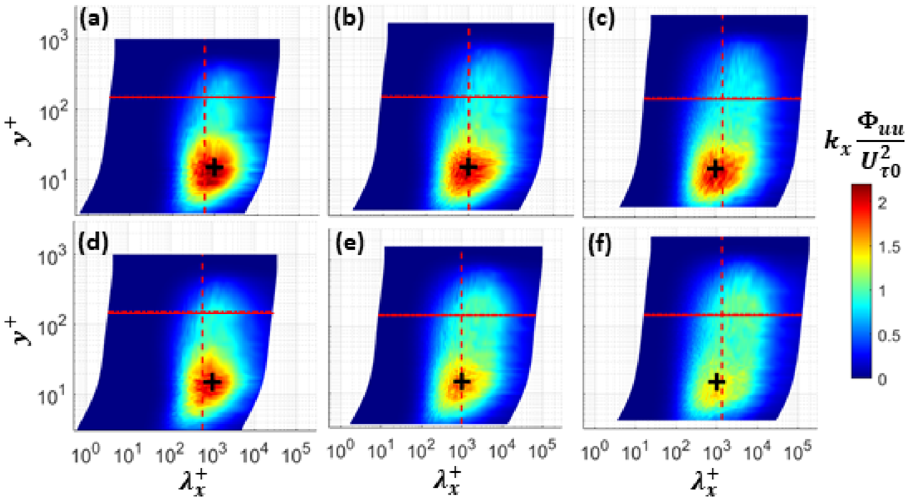

FIG. 8. Pre-multiplied energy spectra, $k_x\Phi_{uu}^+$, for (a–c) the baseline cases and (d–f) the the perforated cases at Location C2. From left to right, the columns represent for the cases with U_∞ = 5.5, 9.7, and 14 m/s. Black plus markers locate at $y^+ \approx 15$ and $\lambda_x^+ \approx 1000$. Red dashed lines represent the wavelength of $\lambda^+ = \delta^+$. Red solid lines represent the wall-normal location of $y^+ = 150$.

Figure 9 shows the pre-multiplied energy spectra for the perforated cases at Location C2 compared with those of the baseline cases at (a–c) y^+ = 15 and (d-f) y^+ = 150 at different Reynolds numbers. The energy spectra are normalised by the freestream velocity. The results show that the energy spectra of all scales for the perforated cases were smaller than those of the baseline cases at $y^+ = 15$, where the inner peak in the energy is located. However, the energy spectra of all scales for the perforated cases increase at y^+ = 150 in comparison with those for the baseline cases. When the Reynolds number increases, the effect of the perforated surface on the energy spectra becomes more significant.

D. Large-scale modulation

The large-scale modulation of small-scale structures illustrates the interaction between small- and large-scale structures in turbulent boundary layers. The large-scale structures in the logarithmic region significantly modulate the amplitude of the small-scale in the near-wall region (Mathis

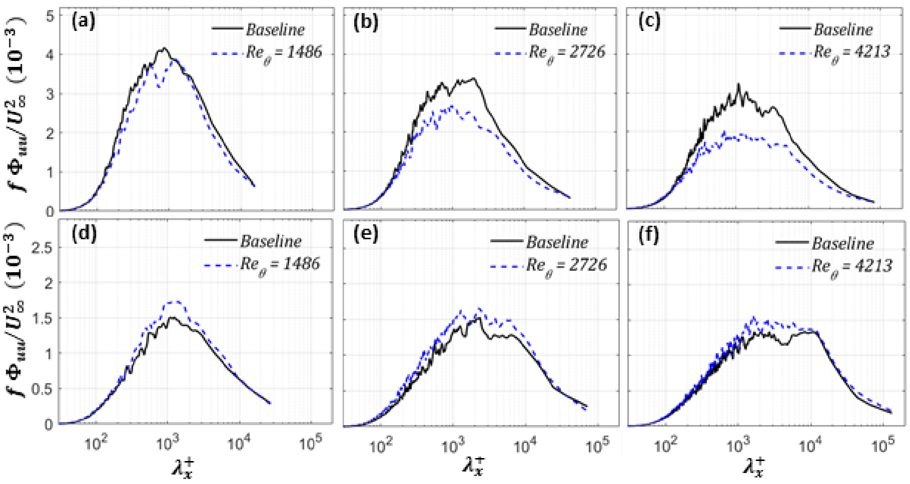

FIG. 9. Pre-multiplied energy spectra for the perforated cases at C2 compared with those of the baseline cases at (a–c) y^+ = 15 and (d–f) y^+ = 150 at different Reynolds numbers.

et al., 2009a,b). The large-scale modulation was estimated using the procedure proposed by Mathis et al. (2009a). Intantaneous velocity fluctuations were decomposed as $u' = u'_S + u'_L$, where u'_S is the small-scale components and u'_L is the large-scale components. This decomposition uses a cut-off wavelength of $\lambda_c = \delta$ (Mathis et al., 2009a,b), which is selected to separate the small and large structures. The small structures contribute to the inner peak in the energy distribution while the large ones contribute to the outer peak (Mathis et al., 2009a,b).

Figure 10(a) shows a sample of viscous-scaled instantaneous velocity fluctuations, $u'^+ = u'/U_\tau$, compared with its viscous-scaled large-scale components, $u'^+_L = u'_L/U_\tau$, as a function of viscous-scaled time, $t^+ = tU_\tau^2/\nu$ at $y^+ = 15$. shows the viscous-scaled small-scale components, $u'^+_S = u'_S/U_\tau$, compared with the viscous-scaled large-scale components which are decomposed from the velocity fluctuations at one wall-normal location of $y^+ = 15$. The results show that the amplitude of small scales is correlated with the sign of large-scale amplitudes. It is attenuated by negative large-scale fluctuations and strengthened by positive large-scale fluctuations. A similar result was reported by Tang et al. (2016). Figures 10(c,d) show the turbulence intensity profiles for the baseline cases at different Reynolds numbers compared to the work by Harun et al. (2013) for small- and large-scale structures, respectively. The results show that the turbulence intensity of small-scale structures increases throughout the boundary layer with an increase in the Reynolds number. In contrast, the turbulence intensity of large-scale structures reduces in the near-wall region but increases in the outer region as the Reynolds number increases, which indicates a good

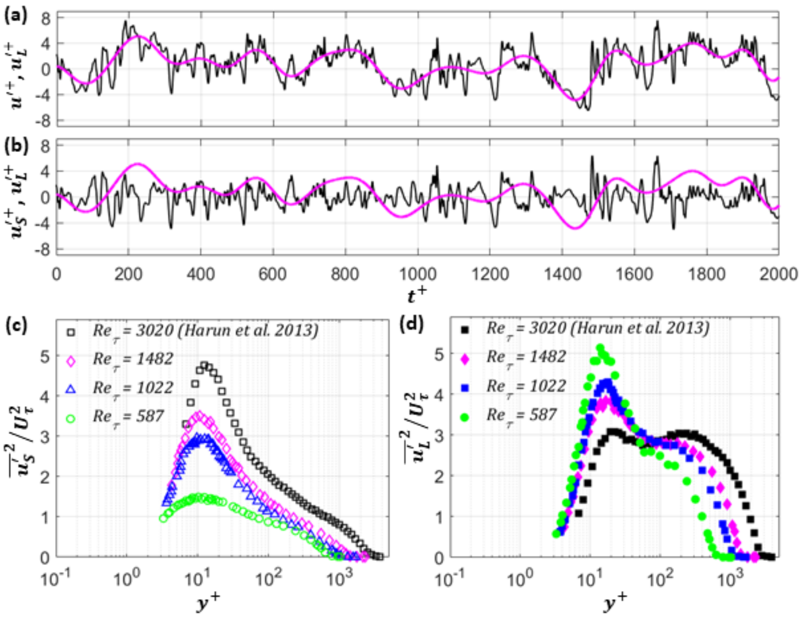

FIG. 10. (a) A sample of instantaneous velocity fluctuations and its large-scale components; (b) Small-scale components; (c) Turbulence intensity profiles of the baseline cases at different Reynolds numbers decomposed into (c) small- and (d) large-scale components. The magenta line represents the large-scale components. Square markers represent the reproduced data by Harun et al. (2013).

agreement between the curent results and the published work by Harun et al. (2013).

Figure 11(a) shows the distribution of the pre-multiplied velocity spectra of streamwise velocity fluctuations in the turbulent boundary layer over a smooth case at a Reynolds number of $R_\tau = 1482$. At this low Reynolds number, the high-energy peak of the large-scale structures is not obvious in the outer region (Mathis et al., 2009b,a). However, the figure shows that there is an increase in the energy in an outer region of $y^+ \approx 200$ at $\lambda_x \geq \delta$. As the wavelength increases from $\lambda_x = \delta$ to $\lambda_x = 3\delta$, the energy in the outer region increases. Different cut-off wavelengths to separate small- and large-scale structures were used in the literature. while Mathis et al. (2009b,a) used a cut-off wavelength of $\lambda_c = \delta$, others used $\lambda_c = 2\delta$, such as Pathikonda and Christensen (2015); Tang et al. (2016). Hence, three cut-off wavelengths of $\lambda_c = \delta, 2\delta$, and 3δ were used to estimate the effects of cut-off wavelengths on the large-scale amplitude modulation in the turbulent boundary layers. Figures 11(b-d) show the comparison between the amplitude modulation of undisturbed and controlled boundary layer with the cut-off wavelength of $\lambda_c = \delta, 2\delta$, and 3δ, respectively. Similar results were observed for different cut-off wavelengths, which shows an reduction in the near-wall region but an increase in the logarithmic region in the amplitude modulation of the controlled boundary layer in comparison with the undisturbed one. Therefore, to distinguish between large- and small-scale structures, a cut-off wavelength of $\lambda_c = \delta$ was selected in this study.

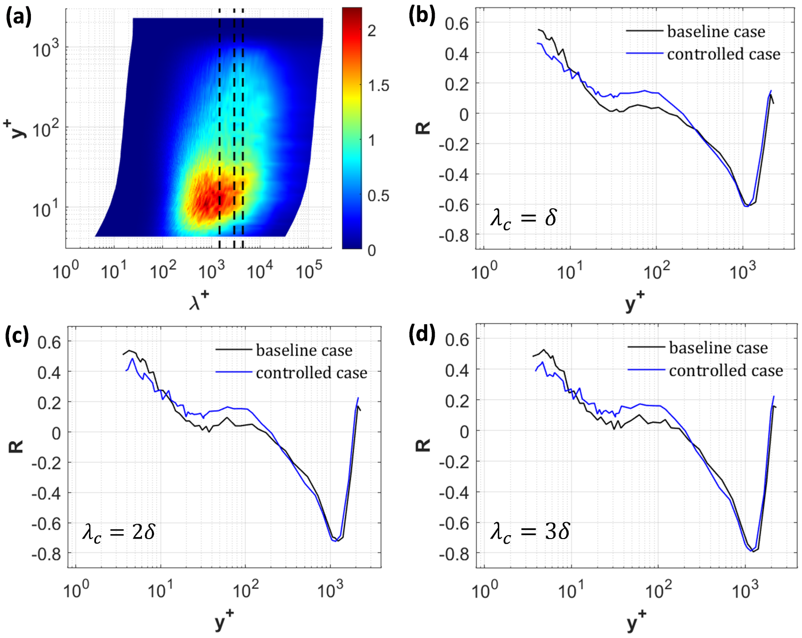

FIG. 11. (a) Pre-multiplied energy spectra of the streamwise velocity fluctuations as a function of length scale and wall-normal heights. The dashed black vertical lines at λ_c/δ = 1, 2 and 3 show the different cut-off length filters separating the large and small scales. (b-c) show the amplitude modulation profiles with different cut-off length filters.

Figure 12(a) shows the large-scale amplitude modulation of small-scale structures in the baseline cases at different Reynolds numbers compared to the work by Harun et al. (2013). The results show that as the Reynolds number increases, the modulation gets stronger, and the location where the modulation is zero moves further from the wall. This is due to the increase in large-scale structures along with an increase in Reynolds numbers. Similar results were reported by (Marusic et al., 2011). Figures 12(b,c,d) show the large-scale amplitude modulation of small-scale structures in the perforated cases at C2 compared with those in the baseline cases at U_∞ = 5.5, 9.7, and 14 m/s, respectively. The results show that the perforated surface enhances the large-scale amplitude modulation of small-scale structures in the turbulent boundary layers at $20 \leq y^+ \leq 150$ which is from the buffer region to the logarithmic region. As the Reynolds number increases, the

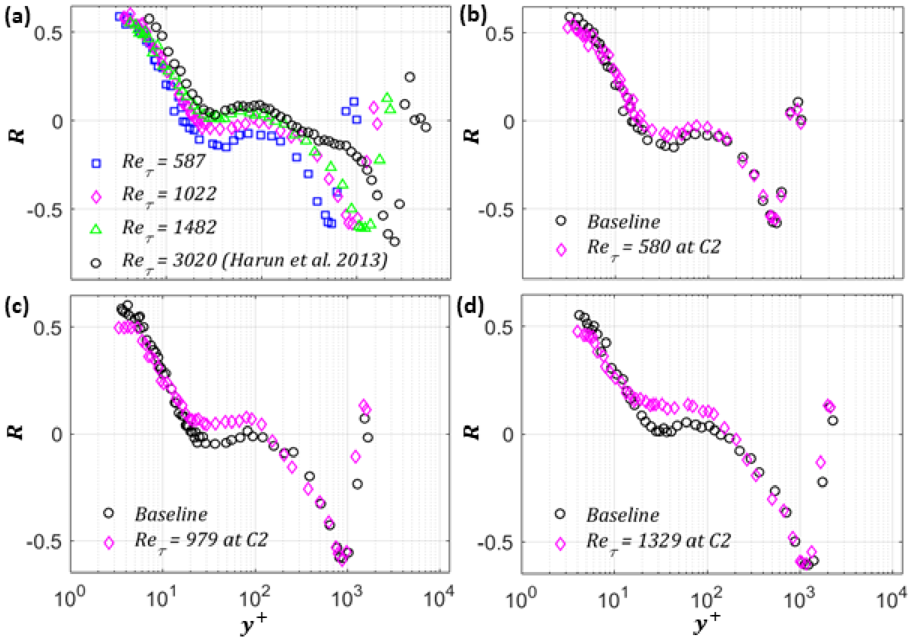

FIG. 12. (a) Amplitude modulation profiles for the baseline cases at different freestream velocities, U_∞ = 5.5, 9.5 and 14 m/s. Black square markers represent the reproduced data of Harun et al. (2013); Amplitude modulation profiles for the perforated cases at C2 compared with those for the baseline cases with (b) U_∞ = 5.5 m/s, (c) U_∞ = 9.7 m/s, and (d) U_∞ = 14 m/s.

increase in modulation becomes more significant. This modulation increase is associated with an increase the boundary layer thickness due to the perforated surface. In contrast, there is a reduction in the large-scale amplitude modulation of small-scale structures due to the perforated surface in the near-wall region of $y^+ \leq 10$ which is transferred from the viscous sublayer to the buffer region. This indicates that the perforated surface reduces the large-scale structures in the near-wall region but increases them in the outer region. The increase in the large-scale amplitude modulation of small-scale structures is associated with a reduction in skin friction drag in the turbulent boundary layers, which is similar to the effect of an adverse pressure gradient on the large-scale amplitude modulation as shown in the work by Harun et al. (2013).

IV. CONCLUSIONS

This paper investigates the effect of a perforated plate with a backing cavity on the large-scale amplitude modulation of small-scale structures in turbulent boundary layers at different Reynolds numbers, Re_θ = 1499, 2802, and 4409 using hot-wire experiments. Turbulent boundary layers were manipulated using varying viscous-scaled cavity volumes ranging from $V^+ = 2.7 \times 10^6$ to 31.3×10^6. The results of the study are summarised here.

The perforated surface reduces turbulence intensity in the near-wall region, $y^+ \leq 30$, but creates a hump in the turbulence energy in the outer region at $y^+ \approx 150$. The analysis of the shear stresses and turbulence production shows that the shear stresses were weakened throughout the boundary layers, which results in a reduction in the turbulence production due to the perforated surfaces, notably in the near-wall region at $y^+ \leq 30$. These agree with the redistribution of the turbulent kinetic energy of the turbulent boundary layers due to the perforated surface. The turbulent energy was reduced in the near-wall region and increased in the outer region at all scales. When the Reynolds number increased, these effects became more pronounced. The reduction in the turbulence energy and the shear stresses in the near-wall region is associated with a reduction in skin friction drag due to the perforated surface.

The perforated surface significantly increases the turbulence energy of large-scale structures in the outer region of the turbulent boundary layers. Consequently, the large-scale amplitude modulation of small-scale structures in the turbulent boundary layers was pronounced in the turbulent boundary layers over the perforated surface. A clear increase in the modulation was observed at $20 \leq y^+150$ in comparison with those in the baseline cases. In addition, the modulation was reduced at $y^+ \leq 10$. This suggests that the perforated surface lifts the large-scale motions further from the wall, which diminishes large-scale structures in the near-wall region but increases them in the outside region. When the Reynolds number increased, the effects of the perforated surface on modulation became more significant. The wall-normal location at which the amplitude modulation is zero increases further from the wall in the turbulent boundary layer over the perforated surface, which results in a reduction in skin friction drag compared with those in the unperturbed turbulent boundary layer.

To better understand the energy exchange between the inside and outside of the cavity and validate this study's hypotheses, future research will closely examine the near-wall region using techniques like PIV and DNS models of the perforated surface.

ACKNOWLEDGMENTS

This research was supported by the Australian Government Research Training Program (RTP) and the Australian Government through the Australian Research Council (ARC DP-200101961).

AUTHOR DECLARATIONS

Conflict of Interest

The authors have no conflicts to disclose.

Author Contributions

Van Thuan Hoang: Conceptualization (equal); Data curation (equal); Formal analysis (equal); Investigation (equal); Methodology (equal); Project administration (equal); Validation (equal); Visualization (equal); Writing - original draft (equal); Writing - review, and editing (equal). Azadeh Jafari: Conceptualization (equal); Formal analysis (equal); Investigation (equal); Project administration (equal); Methodology (equal); Supervision (equal); Writing - review, and editing (equal). Benjamin Cazzolato: Conceptualization (equal); Investigation (equal); Project administration (equal); Supervision (equal); Writing - review, and editing (equal). Maziar Arjomandi: Conceptualization (equal); Formal analysis (equal); Investigation (equal); Methodology (equal); Project administration (equal); Supervision (equal); Writing - review, and editing (equal)

DATA AVAILABILITY

The data that support the findings of this study are available from the corresponding author upon reasonable request.

REFERENCES

Abbassi, M., Baars, W. J., Hutchins, N., and Marusic, I. (2017). Skin-friction drag reduction in a high-Reynolds-number turbulent boundary layer via real-time control of large-scale structures. *International Journal of Heat and Fluid Flow*, 67:30–41.

Aider, J.-L., Beaudoin, J.-F., and Wesfreid, J. E. (2010). Drag and lift reduction of a 3D bluff-body using active vortex generators. *Experiments in Fluids*, 48:771–789.

Baron, A. and Quadrio, M. (1995). Turbulent drag reduction by spanwise wall oscillations. *Applied Scientific Research*, 55:311–326.

Bhat, S., Silvestri, A., Cazzolato, B., and Arjomandi, M. (2021). Mechanism of control of the near-wall turbulence using a micro-cavity array. *Physics of Fluids*, 33(7):075114.

Cafiero, G. and Iuso, G. (2022). Drag reduction in a turbulent boundary layer with sinusoidal riblets. *Experimental Thermal and Fluid Science*, 139:110723.

Chan, C. and Chin, R. (2022). Investigation of the influence of miniature vortex generators on the large-scale motions of a turbulent boundary layer. *Journal of Fluid Mechanics*, 932:A29.

Chandran, D., Zampiron, A., Rouhi, A., Fu, M. K., Wine, D., Holloway, B., Smits, A. J., and Marusic, I. (2023). Turbulent drag reduction by spanwise wall forcing. part 2. High-Reynolds-number experiments. *Journal of Fluid Mechanics*, 968:A7.

Choi, K.-S. (1989). Near-wall structure of a turbulent boundary layer with riblets. *Journal of Fluid Mechanics*, 208:417–458.

Dacome, G., Mörsch, R., Kotsonis, M., and Baars, W. J. (2024). Opposition flow control for reducing skin-friction drag of a turbulent boundary layer. *Physical Review Fluids*, 9(6):064602.

Deshpande, R., Chandran, D., Smits, A. J., and Marusic, I. (2023). On the relationship between manipulated inter-scale phase and energy-efficient turbulent drag reduction. *Journal of Fluid Mechanics*, 972:A12.

Duvvuri, S. and McKeon, B. (2016). Nonlinear interactions isolated through scale synthesis in experimental wall turbulence. *Physical Review Fluids*, 1(3):032401.

Endrikat, S., Modesti, D., MacDonald, M., García-Mayoral, R., Hutchins, N., and Chung, D. (2021). Direct numerical simulations of turbulent flow over various riblet shapes in minimal-span channels. *Flow, Turbulence and Combustion*, 107(1):1–29.

Gomit, G., De Kat, R., and Ganapathisubramani, B. (2018). Structure of high and low shear-stress events in a turbulent boundary layer. *Physical Review Fluids*, 3(1):014609.

Gowree, E. R., Jagadeesh, C., and Atkin, C. J. (2019). Skin friction drag reduction over staggered three dimensional cavities. *Aerospace Science and Technology*, 84:520–529.

Guo, H., Borodulin, V., Kachanov, Y., Pan, C., Wang, J., Lian, Q., and Wang, S. (2010). Nature of sweep and ejection events in transitional and turbulent boundary layers. *Journal of Turbulence*, 11:N34.

Harun, Z., Monty, J. P., Mathis, R., and Marusic, I. (2013). Pressure gradient effects on the large-scale structure of turbulent boundary layers. *Journal of Fluid Mechanics*, 715:477–498.

Hoang, V., Jafari, A., Cazzolato, B., and Arjomandi, M. (2024). Modification of near-wall turbulence in turbulent boundary layers due to a perforated structure. *Physics of Fluids*, 36(7):075173.

Hutchins, N. and Choi, K.-S. (2002). Accurate measurements of local skin friction coefficient using hot-wire anemometry. *Progress in Aerospace Sciences*, 38(4-5):421–446.

Hutchins, N. and Marusic, I. (2007). Evidence of very long meandering features in the logarithmic region of turbulent boundary layers. *Journal of Fluid Mechanics*, 579:1–28.

Hwang, Y. (2013). Near-wall turbulent fluctuations in the absence of wide outer motions. *Journal of Fluid Mechanics*, 723:264–288.

Hyun Shin, J. and Jin Song, S. (2015). Pressure gradient effects on smooth and rough surface turbulent boundary layers—part i: Favorable pressure gradient. *Journal of Fluids Engineering*, 137(1):011203.

Jafari, A., Cazzolato, B., and Arjomandi, M. (2022). Finite-length porous surfaces for control of a turbulent boundary layer. *Physics of Fluids*, 34(045115):1–34.

Kametani, Y., Fukagata, K., Örlü, R., and Schlatter, P. (2015). Effect of uniform blowing/suction in a turbulent boundary layer at moderate Reynolds number. *International Journal of Heat and Fluid Flow*, 55:132–142.

Kim, H., Kline, S., and Reynolds, W. (1971). The production of turbulence near a smooth wall in a turbulent boundary layer. *Journal of Fluid Mechanics*, 50(1):133–160.

Kong, J., Nugroho, B., Bennetts, L. G., Chan, C., and Chin, R. (2024). Friction velocity determination techniques in turbulent boundary layers with miniature vortex generators. *Experiments in Fluids*, 65(5):1–21.

Kornilov, V. (2015). Current state and prospects of researches on the control of turbulent boundary layer by air blowing. *Progress in Aerospace Sciences*, 76:1–23.

Lu, L., Li, D., Gao, Z., Cao, Z., Bai, Y., and Zheng, J. (2020). Characteristics of array of distributed synthetic jets and effect on turbulent boundary layer. *Acta Mechanica Sinica*, 36:1171–1190.

Marusic, I., Mathis, R., and Hutchins, N. (2011). Reynolds number dependence of the amplitude modulated near-wall cycle. In *Progress in Wall Turbulence: Understanding and Modeling: Proceedings of the WALLTURB International Workshop held in Lille, France, April 21-23, 2009*, pages 105–112.

Mathis, R., Hutchins, N., and Marusic, I. (2009a). Large-scale amplitude modulation of the small-scale structures in turbulent boundary layers. *Journal of Fluid Mechanics*, 628:311–337.

Mathis, R., Monty, J. P., Hutchins, N., and Marusic, I. (2009b). Comparison of large-scale amplitude modulation in turbulent boundary layers, pipes, and channel flows. *Physics of Fluids*, 21(11).

Örlü, R. and Schlatter, P. (2011). On the fluctuating wall-shear stress in zero pressure-gradient turbulent boundary layer flows. *Physics of fluids*, 23(2):021704.

Österlund, J. M., Johansson, A. V., Nagib, H. M., and Hites, M. H. (2000). A note on the overlap region in turbulent boundary layers. *Physics of Fluids*, 12(1):1–4.

Pathikonda, G. and Christensen, K. T. (2015). Structure of turbulent channel flow perturbed by a wall-mounted cylindrical element. *AIAA journal*, 53(5):1277–1286.

Perry, A., Marusic, I., and Jones, M. (2002). On the streamwise evolution of turbulent boundary layers in arbitrary pressure gradients. *Journal of Fluid Mechanics*, 461:61–91.

Perry, A., Marušić, I., and Li, J. (1994). Wall turbulence closure based on classical similarity laws and the attached eddy hypothesis. *Physics of Fluids*, 6(2):1024–1035.

Quadrio, M., Ricco, P., and Viotti, C. (2009). Streamwise-travelling waves of spanwise wall velocity for turbulent drag reduction. *Journal of Fluid Mechanics*, 627:161–178.

Scarano, F., Jacob, M. C., Gojon, R., Carbonneau, X., and Gowree, E. R. (2022). Modification of a turbulent boundary layer by circular cavities. *Physics of Fluids*, 34(6):065134.

Scarano, F., Jacob, M. C., and Gowree, E. R. (2023). Drag reduction by means of an array of staggered circular cavities at moderate Reynolds numbers. *International Journal of Heat and Fluid Flow*, 102:109142.

Scarano, F., Jacob, M. C., and Gowree, E. R. (2024). Large scale structures modification of a spatially evolving turbulent boundary layer grazing over circular cavities. *International Journal of Heat and Fluid Flow*, 108:109486.

Schlatter, P., Li, Q., Brethouwer, G., Johansson, A. V., and Henningson, D. S. (2010). Simulations of spatially evolving turbulent boundary layers up to $Re_\theta = 4300$. *International Journal of Heat and Fluid Flow*, 31(3):251–261.

Schultz, M. P. and Flack, K. A. (2003). Turbulent boundary layers over surfaces smoothed by sanding. *Journal of Fluids Engineering*, 125(5):863–870.

Silvestri, A., Ghanadi, F., Arjomandi, M., Cazzolato, B., and Zander, A. (2017). Attenuation of sweep events in a turbulent boundary layer using micro-cavities. *Experiments in Fluids*, 58:1–13.

Silvestri, A., Ghanadi, F., Arjomandi, M., Cazzolato, B., and Zander, A. (2018a). The application of different tripping techniques to determine the characteristics of the turbulent boundary layer over a flat plate. *Journal of Fluids Engineering*, 140(1).

Silvestri, A., Ghanadi, F., Arjomandi, M., Cazzolato, B., Zander, A., and Chin, R. (2018b). Mechanism of sweep event attenuation using micro-cavities in a turbulent boundary layer. *Physics of Fluids*, 30(5):055108.

Tang, Z., Jiang, N., Zheng, X., and Wu, Y. (2016). Bursting process of large-and small-scale structures in turbulent boundary layer perturbed by a cylinder roughness element. *Experiments in Fluids*, 57:1–14.

Zhang, X., Wong, C., Cheng, X., and Zhou, Y. (2022). Dependence of skin-friction reduction on the geometric parameters of blowing jet array. *Physics of Fluids*, 34(10):105125.

Chapter 5

Wall-normal velocities through a perforated plate

5.1 Chapter overview

A perforated plate with a backing cavity creates wall-normal velocities with a zero-mass flux in turbulent boundary layers. As discussed in Section 2.2.1 and Section 2.3, wall-normal velocities with a zero-mass flux can reduce the near-wall turbulence as well as friction drag. However, there is a significant lack of knowledge about the turbulence characteristics of the turbulent boundary layers with wall-normal velocities through a perforated plate. The wall-normal velocities could lift the coherent structures further from the wall, reducing turbulence intensity and wall-shear stresses. The effects of the amplitude and frequency of wall-normal velocities through a perforated plate in near-wall turbulence are not well understood. Therefore, this chapter investigates the effect of jet amplitude and frequency through a perforated plate on the near-wall turbulence of turbulent boundary layers. To explore the effect of wall-normal velocities caused by the perforated plate on the near-wall turbulence, a synthetic jet actuator will be developed and used to control the turbulent boundary layers in a wind tunnel. Different jet amplitudes and frequencies are tested. The modification of velocity profiles, turbulence intensity profiles, burst events, and turbulence energy is analysed.

The results show that the synthetic jets reduced up to 5% burst intensities and about 20% burst durations in the near-wall region at inner-scaled wall-normal positions below 12. This indicates that the synthetic jets lifted turbulent energy and weakened burst events. As a result, there was a decrease in turbulence intensity close to the wall of up to around 12.5%, which helped to reduce shear stresses and local skin-friction drag. In addition, the displacement of the turbulent energy's inner peak away from the wall due to the wall-normal jets show that they moved turbulent energy away from the wall, which results in a reduction in turbulence intensity in the near-wall region as well as the wall-shear stress. Section 2.2.1 and Section 2.3 shows that perforated plates with a backing cavity generate wall-normal velocities due to the interaction between the fluid inside and outside of the cavity. The wall-normal velocities can weaken the near-wall cycles and reduce the turbulence intensity in the near-wall region as well as the wall-shear stresses. Hence, these results support the hypothesis that a perforated plate with a backing cavity produces wall-normal velocities with a zero-mass flux, which reduce skin friction and turbulence energy.

5.2 Statement of Authorship

Statement of Authorship

Title of Paper	Modification of burst events in the near-wall region of turbulent boundary layers by synthetic jets
Publication Status	☑ Published ☐ Accepted for Publication ☐ Submitted for Publication ☐ Unpublished and Unsubmitted work written in manuscript style
Publication Details	Hoang, V., Jafari, A., Cazzolato, B., and Arjomandi, M. (2025). Modification of burst events in the near-wall region of turbulent boundary layers by synthetic jets. *International Journal of Heat and Fluid Flow*, 112, 109728.

Principal Author

Name of Principal Author (Candidate)	Van Thuan Hoang		
Contribution to the Paper	Modification of burst events in the near-wall region of turbulent boundary layers by synthetic jets		
Overall percentage (%)	75		
Certification:	This paper reports on original research I conducted during the period of my Higher Degree by Research candidature and is not subject to any obligations or contractual agreements with a third party that would constrain its inclusion in this thesis. I am the primary author of this paper.		
Signature		Date	04/02/2025

Co-Author Contributions

By signing the Statement of Authorship, each author certifies that:

i. the candidate's stated contribution to the publication is accurate (as detailed above);

ii. permission is granted for the candidate in include the publication in the thesis; and

iii. the sum of all co-author contributions is equal to 100% less the candidate's stated contribution.

Name of Co-Author	Azadeh Jafari		
Contribution to the Paper	Supervised the development of the research, helped in developing ideas, contributed in academic discussion and manuscript review.		
Signature		Date	19/02/2025

Name of Co-Author	Benjamin Cazzolato		
Contribution to the Paper	Supervised the development of the research, helped in developing ideas, contributed in academic discussion and manuscript review.		
Signature		Date	19/02/2025

Name of Co-Author	Maziar Arjomandi		
Contribution to the Paper	Supervised the development of the research, participated in developing ideas ar , helped in interpretation of results, provided critical revision t.		
Signature		Date	19/02/2025

5.3 Modification of burst events in the near-wall region of turbulent boundary layers by synthetic jets

This chapter consists of the following published journal article:

Hoang, V.T., Jafari, A., Cazzolato, B., and Arjomandi, M. (2024). Modification of burst events in the near-wall region of turbulent boundary layers by synthetic jets. *International Journal of Heat and Fluid Flow*, 112, 109728. (Published)

The article is identical to its published format with the following exceptions:

- The numbering of figures, tables and equations have been altered to include the chapter number.
- The position of some figures and tables have been changed to improve legibility.

International Journal of Heat and Fluid Flow 112 (2025) 109728

Contents lists available at ScienceDirect

International Journal of Heat and Fluid Flow

journal homepage: www.elsevier.com/locate/ijhff

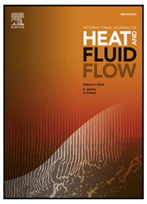

Modification of burst events in the near-wall region of turbulent boundary layers by synthetic jets

Van Thuan Hoang *, Azadeh Jafari, Benjamin Cazzolato, Maziar Arjomandi

School of Electrical and Mechanical Engineering, University of Adelaide, Adelaide, 5005, South Australia, Australia

ARTICLE INFO

Keywords:
Boundary layer control
Skin-friction drag
Synthetic jets

ABSTRACT

Burst events in the near-wall region of turbulent boundary layers are the main contributors to skin friction drag in wall flows. This paper shows how synthetic jets modify the near-wall burst events in turbulent boundary layers, leading to local drag reduction. Different characteristics of synthetic jets including various non-dimensional jet frequencies, ranging from 0.025 to 0.063, at two non-dimensional jet amplitudes of 0.1 and 0.2 were examined by conducting hot-wire measurements at a Reynolds number of $Re_\theta \approx 1050$. Statistical analysis utilizing a variable-interval time-averaging (VITA) technique illustrated a reduction of up to 15% in burst intensity and a decrease of approximately 10% in burst durations within the near-wall region, $y^+ \leq 12$, indicating that synthetic jets lifted turbulent kinetic energy and weakened burst events in this region. Consequently, there was a reduction of up to approximately 14% in turbulence intensity near the wall, contributing to diminished shear stresses and local skin-friction drag. Furthermore, the synthetic jets generated a displacement of the inner peak of turbulent energy away from the wall, indicating that the synthetic jets shifted turbulent kinetic energy away from the wall. As the jet frequency or amplitude increased, the modification of the boundary layer became more pronounced.

1. Introduction

Reducing carbon dioxide (CO_2) emissions is a key objective for the aviation sector. The Advisory Council for Aeronautics Research in Europe (ACARE) has recently set a goal to decrease CO_2 emissions per passenger mile by 75%, with the target year being 2050 (Krein and Williams, 2012). Lowering drag is an effective way to reduce energy consumption across various modes of transport, including aircraft, road vehicles, and ships, which in turn helps to reduce CO_2 emissions. In the aviation industry, a 10% decrease in total drag can lead to a roughly 6% reduction in fuel consumption for flights (Heinemann et al., 2017).

In wall-bounded flows, skin friction drag primarily arises from the interaction between the flow and the wall-bounded surface within a turbulent boundary layer. The generation of turbulence predominantly occurs in the near-wall region of these boundary layers (Kim et al., 1971). Coherent structures such as quasi-streamwise vortices, streaks, and horseshoe vortices play a significant role in turbulent momentum transfer and shear stress (Guo et al., 2010). These streamwise vortices, which rotate along the direction of the flow and encompass both ejection and sweep events, are key elements of coherent structures near the wall. Ejections lift the streamwise vortices away from the wall, while sweeps generate flow momentum towards the wall. These ejection and sweep events create burst events that significantly contribute to skin friction drag (Guo et al., 2010). Therefore, reducing burst events is an effective strategy for minimizing turbulence in the near-wall region, which in turn reduces skin friction drag.

There are several methods for turbulent boundary layer control. These methods weaken streaks and streamwise vortices in turbulent boundary layers, which reduce the near-wall cycles in the turbulence and consequently reduce turbulence production and wall-shear stresses. Reviews of these methods have been extensively conducted in the work by White and Mungal (2008) and Corke and Thomas (2018). The techniques for flow control can be categorized as active or passive. The passive techniques modify turbulent flows without using any external source of energy or momentum, such as riblets (Soleimani and Eckels, 2021), vortex generators (Aider et al., 2010), and perforated plates (Scarano et al., 2023). The active techniques extract or add energy or momentum from an external source to turbulent flows by using actuators, such as spanwise wall forcing (Aider et al., 2010) and pulsed-DC plasma actuation (Thomas et al., 2023). Synthetic jet control is an active method for flow control. A synthetic jet involves alternating phases of blowing and suction in a symmetrical manner, resulting in zero net mass flux (Murugan et al., 2016). A synthetic

---

* Corresponding author.
E-mail address: vanthuan.hoang@adelaide.edu.au (V.T. Hoang).
URL: https://sites.google.com/view/vanthuan-hoang (V.T. Hoang).

https://doi.org/10.1016/j.ijheatfluidflow.2024.109728
Received 22 March 2024; Received in revised form 16 December 2024; Accepted 17 December 2024

Nomenclature

$A = \frac{1}{N}\sum_{j=1}^{N} v_{bj,max}$	Jet amplitude
$A^+ = A/U_{\tau 0}$	Viscous-scaled amplitude in the baseline case
b	Subscript denotes burst
C_f	Friction coefficients
d	Orifice diameter
f	Jet frequency
$f^+ = f\nu/U_\tau^2$	Viscous-scaled frequency
f_c	Filtering frequency
$f_c^+ = f_c\nu/(U_\tau^2)$	Viscous-scaled filtering frequency
f_s	Sampling frequency
f_S	Signal frequency
h	Orifice depth
H	Shape factor
H_c	Channel half height
I_b	Burst intensity
$I_b^+ = I_b/U_\tau$	Viscous-scaled burst intensity
$\langle I_b\rangle$	Mean burst intensity
$\langle I_b^+\rangle = \langle I_b\rangle/U_\tau$	Mean viscous-scaled burst intensity
k	VITA threshold
k_x	Wavenumber in the streamwise direction
l	Probe length
$l^+ = lU_\tau/\nu$	Viscous-scaled probe length
$l_v = \nu/U_\tau$	Viscous length scale
N	Number of jet cycles
$Re_\theta = \theta U_\infty/\nu$	Reynolds number based on momentum thickness
$Re_\tau = \delta U_\tau/\nu$	Friction Reynolds number
t	Time
$t^+ = tU_\tau^2/\nu$	Viscous-scaled time
T_b	Burst duration
$T_b^+ = T_bU_\tau^2/\nu$	Viscous-scaled burst duration
$\langle T_b\rangle$	Mean burst duration
$\langle T_b^+\rangle = \langle T_b\rangle U_\tau^2/\nu$	Mean viscous-scaled burst duration
T_W^+	VITA window
T_s	Signal period
TI	Turbulence intensity
u	Instantaneous velocity
u'	Velocity fluctuations
$u'^+ = u'/U_\tau$	Viscous-scaled velocity fluctuations
u_b'	Burst signature
$u_b'^+ = u_b'/U_\tau$	Viscous-scaled burst signature
$\tilde{u}_b'^+$	Mean viscous-scaled burst signature
U_e	Mean streamwise velocity at the edge of a boundary layer
U_∞	Freestream velocity
U_τ	Friction velocity
$v_{b,max}$	Maximum blowing velocity of a jet cycle
V_S	Input voltage
x	Downstream location from the leading edge of the perforated plate
$x^+ = xU_\tau/\nu$	Viscous-scaled downstream location
X	Downstream location from the leading edge of the test section
y	Wall-normal location
$y^+ = yU_\tau/\nu$	Viscous-scaled wall-normal location

y^+_{max}	Selected upper limit of the near-wall region
z	Spanwise location
δ	Boundary layer thickness
δ_{99}	Boundary layer thickness with $U_e = 0.99U_\infty$
δ^*	Displacement thickness
θ	Momentum thickness
λ_x	Wavelength
$\lambda^+_x = \lambda_x U_\tau/\nu$	Viscous-scaled wavelength
μ	Dynamic viscosity of air
ν	Kinematic viscosity of air
ρ	Density of air
τ_w	Wall-shear stress
Φ_{uu}	Power spectrum density
$\Delta t^+ = (1/f_s)U^2_\tau/\nu$	Viscous-scaled sample interval
Δx	Streamwise spacing of orifices
Δz	Spanwise spacing of orifices
$\wedge$	Acceleration parameter
0	Subscript denotes the smooth baseline case

jet can be produced using piezoelectric, acoustic, electromagnetic, or mechanical means without requiring an external air supply (Murugan et al., 2016). Consequently, it is a favored method for flow control and is extensively researched.

Synthetic jets with a zero net mass flux for active flow control have caught the attention of researchers. Park et al. (2001, 2003) experimentally investigated turbulent boundary layers using suction/blowing jets through a slot. Their results showed a reduction in local skin friction in downstream of the slot. A maximum reduction of approximately 45% was observed at a frequency of $f^+_c = f\nu/U^2_\tau = 0.044$ and $x/\delta^*_0 = 2$, where f_c is the controlling frequency; x is the downstream location from the actuator; and δ^*_0 is the displacement thickness of the uncontrolled boundary layers. As the flow recovers, the drag reduction decreases in the downstream locations. Cannata and Iuso (2008), Cannata et al. (2020) and Iuso and Di Cicca (2007) investigated the interaction between a spanwise synthetic jet array and a turbulent boundary layer. The interaction periodically generates counter-rotating vortices which persist along the channel and reduce wall turbulence. A reduction of up to 12% in turbulence intensity peak and approximately 15% in friction drag was observed. Schatzman et al. (2016) studied the effect of a jet slot with different jet angles on both zero and adverse pressure gradient turbulent boundary layers. The effect of jet angles on the turbulent boundary layer was more sensitive at angles from 60 to 90 degrees than at angles from 30 to 60 degrees. The boundary layer was blocked at an angle of 90 degrees while an attached wall jet was observed at other angles. An increase in skin friction at downstream locations was associated with the increasing jet Reynolds number. Ye et al. (2019) used a streamwise synthetic jet array to control turbulent boundary layers. A reduction in both turbulence intensity and friction drag was observed within a certain distance downstream of the slots. Similarly, a reduction of up to 35% in local skin friction was observed in the direction numerical simulation (DNS) of turbulent channel flows with a frequency ranging from $f^+_c = 0.011$ to 0.044, and a fixed amplitude, $A/U_\infty = 0.2$, where A is the jet amplitude and U_∞ is the free-steam velocity, Araya et al. (2008, 2011).

Jets with a non-zero net mass flux were also investigated. Park and Choi (1999) performed direct numerical simulations of turbulent boundary layers with uniform blowing or suction. Their results show that uniform blowing lifts streamwise vortices and weakens their interaction with the wall. As a result, it significantly reduces skin friction in the vicinity of the slot. The lifted vortices, hence, become stronger downstream, leading to increased turbulence intensity and skin friction downstream of the slot. In contrast, uniform suction has the opposite effect. Similarly, Kametani et al. (2015) performed large-eddy simulations of a turbulent boundary layer with uniform blowing or suction to investigate the variations in skin friction drag. Turbulent channel flows with spanwise opposed wall jets were investigated by direct numerical simulations in the work by Yao et al. (2017, 2018). They observed a maximum drag reduction of about 18.6% at $A^+ = 0.015$. However, at a very large jet amplitude, friction drag increases due to the downwash at the swirl sides. Cheng et al. (2021) and Zhang et al. (2022) experimentally investigated the effect of periodic blowing through streamwise slits on turbulent boundary layers. They found that the effect of amplitudes on local drag reduction depended on frequency. The maximum local drag reduction of about 70% was archived at $A^+ = 1.42$ and $f^+ = 0.42$.

Although numerous relevant studies have been conducted over the years, there are still few recent papers on experimental investigations in the near-wall region of turbulent boundary layers involving synthetic jets. This study aims to investigate the impact of synthetic jets on near-wall turbulence to enhance understanding of the mechanisms of turbulence attenuation. The primary focus is on how synthetic jets modify the turbulent intensity and burst events in the near-wall region. Burst characteristics, including intensity, duration, and frequency, were assessed using the variable-interval time-averaging (VITA) technique by Blackwelder and Kaplan (1976). Round synthetic jets with a frequency from $f^+ = 0.025$ to 0.063 at two amplitudes, $A/U_\infty = 0.1$ and 0.2 or $A^+ = 2.23$ and 4.47 were considered to manipulate a turbulent boundary layer at $Re_\theta \approx 1050$. In aircraft design, orifices on aircraft surfaces, such as wings and fuselages, tend to cause less local damage than slits or slots. Therefore, round synthetic jets were implemented to influence the turbulent boundary layers. In the following section, the details of the experimental setup and synthetic jet characteristics are presented. Section 3 presents the results, where turbulent statistics and kinetic energy are discussed. The article concludes with final remarks.

2. Experimental methods

2.1. Wind tunnel facility and measurement method

Experiments were carried out at the University of Adelaide using a closed-return wind tunnel. The wind tunnel has a maximum velocity of 30 ms^{-1} and maintains a low-level turbulence intensity of around 0.5%. Its test section is rectangular, measuring 500 mm × 500 mm in cross-section and 2000 mm in length. A flat plate was inserted into the test section as shown in Fig. 1. Because the wind tunnel width exceeds the boundary layer thickness more than 10 times, the additional strain-rate effect resulting from the finite width is considered negligible, in accordance with the recommendation by Nickels et al. (2005). The blockage ratio created by a probe holder and a Pitot tube inside the test section

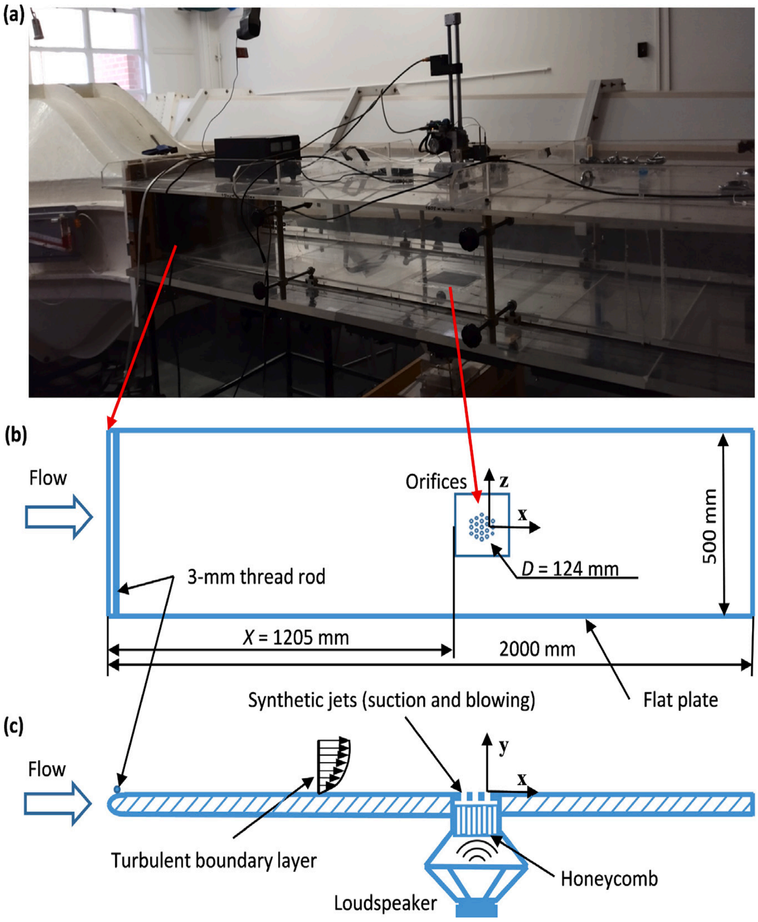

Fig. 1. (a) Photo of the test section, (b) Top view, and (c) Side view of the schematic diagram of the test section and the synthetic jet actuator.

was 1.8%, which is smaller than a threshold of 4% recommended by Mondal and Alam (2023) to avoid the blockage effect. To maintain a zero-pressure gradient along the test section, the side walls were adjusted to achieve an acceleration parameter, $\wedge = (\nu/U_\infty^2)(dU_\infty/dx)$, in the order of 10^{-7}, which was selected in the consideration of the previous work by De Graaff and Eaton (2000), Schultz and Flack (2003) and Hyun Shin and Song (2015). The selected acceleration parameters are smaller than the threshold of 3.5×10^{-6}, suggested for the occurrence of relaminarization of a turbulent boundary layer (Moretti and Kays, 1965). To ensure fully developed boundary layer conditions, the inlet flow was tripped using a 3 mm rod positioned 140 mm from the leading edge, which is similar to the method proposed by Silvestri et al. (2018).

Flow velocities and turbulence were measured using a single miniature wire probe, specifically the Dantec 55P15 model with a diameter of 5 μm and a length of 1.25 mm. The probe is operated by a Dantec Dynamics Streamline Pro. The ratio of wire length to diameter, approximately 240, exceeded the recommended maximum threshold of 200 by Hutchins et al. (2009). This large ratio, however, applied to both the baseline and controlled cases, so it may not affect the considerations in the paper. The length of the hot-wire probe in viscous units denoted as $l^+ = lU_\tau/\nu$, where l is the probe length, was about 19, which is smaller than the maximum threshold of 20 recommended by Hutchins et al. (2009). The probe's sensor has the capability to detect velocities within a range from a few centimetres to several hundred metres per second, with an accuracy of ±0.5% for readings above 5 m/s, as documented by Jørgensen (2005). The measurements were conducted at a sampling frequency f_s of 40 kHz, with a measurement duration of 30 s, equivalent to a viscous-scaled sample interval, $\Delta t^+ = (1/f_s)U_\tau^2/\nu$, ranging about 0.1. This non-dimensional sample interval was kept smaller than the minimum timescale of $t^+ = tU_\tau^2/\nu = 3$ for resolving energetic turbulent fluctuations, as recommended by Hutchins et al. (2009). A third-order Butterworth filter, set at a filtering frequency of $f_c = 19$ kHz, was employed to low-pass filter the measured signals. The viscous-scaled filtering frequency, $f_c^+ = f_c\nu/(U_\tau^2)$, was about 4.8, surpassing the recommended minimum threshold of 0.33 suggested by Hutchins et al. (2015). Calibration of the probe was carried out using a Pitot-static tube connected to a 10 Torr Baratron pressure transducer. Two calibrations were conducted at the beginning and end of each measurement. Each calibration contained twenty-two freestream velocities from 0 m/s to 25 m/s measured using both the hotwire probe and the Pitot-static tube simultaneously. Calibration coefficients were estimated through a 5th-order polynomial fit, enabling the conversion of probe-measured voltage to velocity. The variance in ambient temperature during calibration and measurements was below 1 °C, allowing for the assumption of constant ambient temperature throughout the experiments. To position the probe at various wall-normal locations, a Mitutoyo dial/mechanical-digit counter height gauge with a travel range of 0 to 300 mm and an accuracy of ±0.03 mm was utilized. The gauge motor was controlled by a Matlab code. To minimize the impact of any gear backlash, a laser displacement sensor was employed to position the gauge sensor back to its origin location.

2.2. Synthetic jet actuators and experiments

The synthetic jet actuator includes a signal generator (a laptop), a digital to analog converter (Focusrite Scarlett 18i20), a power amplifier, an oscilloscope, and a loudspeaker, as shown in Fig. 2. The laptop generated a digital sinusoidal signal of a frequency f_S ranging from 50 to 300 Hz via the Matlab Audio Toolbox. The digital signal was then converted into an analog signal by the Focusrite, which was then

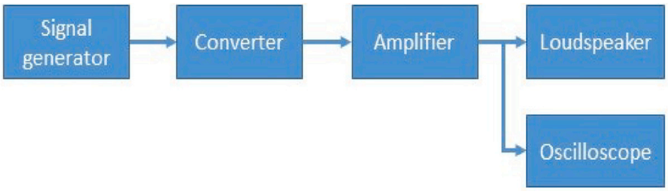

Fig. 2. Schematic diagram of the main actuator components.

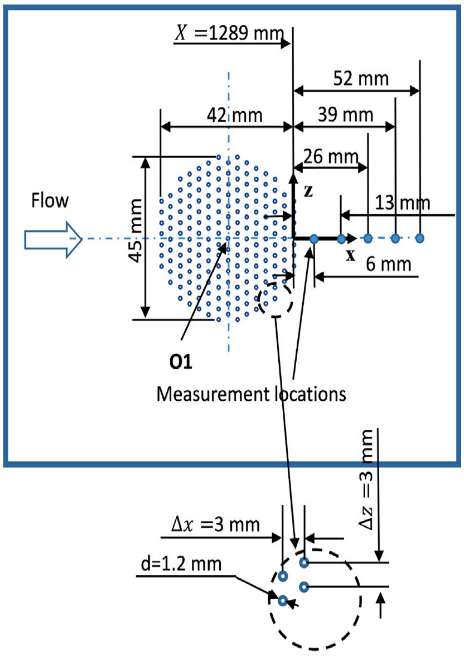

Fig. 3. Schematic diagram of the staggered orifice array and the measurement locations.

used to drive the loudspeaker via the power amplifier to enhance the signal amplitude via the input voltage, V_S. The input voltage was also monitored by an oscilloscope.

The synthetic jets were introduced through the outlet of the actuator which was located at $X = 1205$ mm from the leading edge of the test section, as shown in Fig. 1. The outlet was made from polylactic acid plastic and manufactured using 3D printing. It contained a staggered orifice array with 187 orifices arranged in a hexagonal shape as shown in Fig. 3. The hexagon was 42 mm long in the downstream direction and 45 long in the spanwise direction, which was equal to about 700 and 750 viscous units, respectively. The orifice diameter, d_0, and depth, h_0, were 1.2 and 3 mm, respectively, which resulted in a depth-to-diameter ratio of $h_0/d_0 = 2.5$. Based on the viscous length scale, $l_v = \nu/U_\tau = 0.006$ mm, in the undisturbed turbulent boundary layer, the orifice diameter, $d_0^+ = d_0/l_v$, and depth, $d_0^+ = h_0/l_v$, were about 20, respectively. The orifice spacing in both streamwise and spanwise directions was 3 mm. In viscous units, the orifice spacings, $\Delta x^+ = \Delta z^+ = \Delta z/l_v$, were approximately 50. The hexagon size and the orifice spacings were chosen to manipulate the low-speed streaks in the turbulent boundary layers. The separation between adjacent low-speed streaks, distributed randomly, ranged from approximately 80 to 120 in viscous units in the spanwise direction (Kim et al., 1971; Gupta et al., 1971). This spacing remained unaffected by the Reynolds numbers. Furthermore, the length of these streaks in the streamwise direction could exceed 1000 viscous units, as noted by Blackwelder and Eckelmann (1979) and Cantwell (1981). The measurement locations are located at 6 mm, 13 mm, 26 mm, 39 mm, and 52 mm from the last row of the orifice array as shown in Fig. 3.

The suction and blowing velocities of the synthetic jets were measured by a hot-wire probe which was placed above and at 0.1±0.03 mm from the orifice in quiescent air as shown in Fig. 4(a). The sampling frequency was set to 40 kHz and the sampling duration was 10 s. Fig. 4(b) shows jet instantaneous velocities as a function of time in five signal periods, T_s, with an input signal at $f_S = 100$ Hz and $V_S = 1$ V. The generated jet velocities clearly showed two peaks, all with positive values as the hotwire probe was not able to measure negative values. The largest peak was considered to be the maximum velocity for blowing while the lower peak was at the maximum velocity for suction.

The characteristics of synthetic jets include both the jet frequency and the jet amplitude. The suction and blowing were generated by the oscillating diaphragm of the loudspeaker, so the jet frequency, f, was equal to the signal frequency, f_S. The jet amplitude was defined as the time-averaged maximum blowing velocity, which was given as follows:

$$A = \frac{1}{N}\sum_{j=1}^{N} v_{bj,max}, \tag{1}$$

where N was the number of jet cycles and $v_{bj,max}$ was the maximum blowing velocity of a jet cycle.

All measurements were conducted at a freestream velocity of $U_\infty \approx 5.5$ m/s and at the Reynolds number of $Re_\theta = \theta U_\infty/\nu = 1057$, where θ was the momentum thickness of the unperturbed turbulent boundary layer. Streamwise velocities without the jet actuator were assessed at two positions along the streamwise direction of the smooth plexiglass plate. Locations $x = -50$ mm and $x = 6$ mm are aligned with the leading and trailing edges of the jet actuator. The main flow parameters of the turbulent boundary layers over a flat plate are presented in Table 1, where θ is the momentum thickness, δ^* is the displacement thickness, and C_f is the friction coefficient estimated using the near-wall velocity

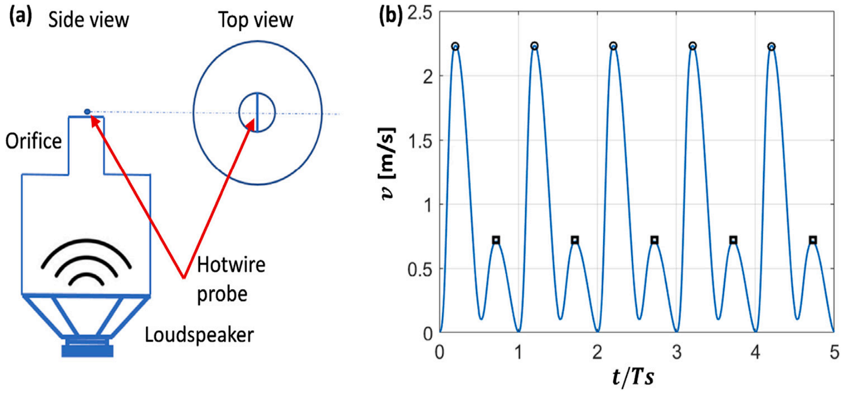

Fig. 4. (a) Schematic diagram of the synthetic jet measurement and (b) jet instantaneous velocities as a function of time. The circular marker represents the maximum velocity for blowing and the square marker represents the maximum velocity for suction.

Table 1
Flow parameters for the turbulent boundary layers over a smooth plate.

U_∞ (m/s)	x (mm)	Re_θ	Re_τ	θ (mm)	δ^* (mm)	δ_{99} (mm)	ν/U_τ (μm)	U_τ (m/s)	C_f (10^{-3})
5.48	−50	1057	467	2.94	4.38	28.6	61.1	0.249	4.01
5.52	6	1132	476	3.13	4.62	29.5	62.1	0.246	3.97

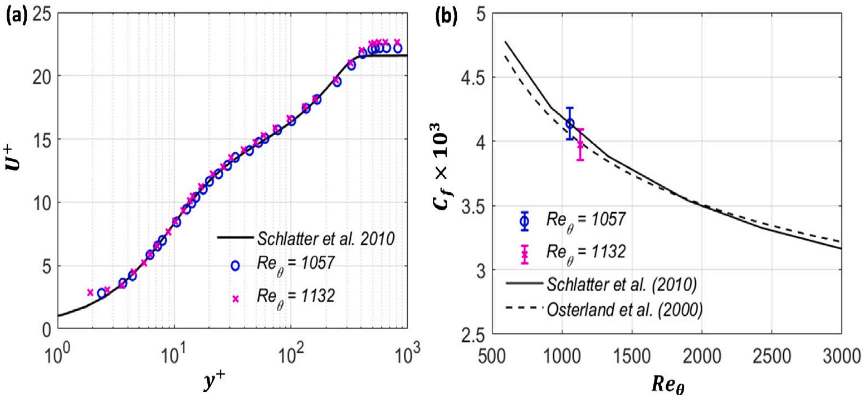

Fig. 5. (a) Viscous-scaled velocity profiles of the unperturbed turbulent boundary layers at $Re_\theta = 1057$ and 1132 and the DNS turbulent boundary layer at $Re_\theta = 1000$ by Schlatter et al. (2010) and (b) Friction coefficients as a function of Reynolds numbers. The solid black line represents friction coefficients from the DNS data by Schlatter et al. (2010). The dashed black line represents friction coefficients estimated by a semi-empirical relationship, $C_f = 1/2 \times (1/0.384 \times \ln(Re_\theta) + 4.08)^{-2}$, by Österlund et al. (2000). The error bars represent the experimental uncertainties.

gradient technique in Section 2.3. The unperturbed turbulent boundary layer at $x = 6$ mm was considered as a baseline case for comparison with those controlled by synthetic jets.

Fig. 5(a) shows the viscous-scaled velocity profiles of the unperturbed turbulent boundary layer and the DNS data by Schlatter et al. (2010) at a similar range of Reynolds numbers of $Re_\theta = 1000$. The velocity profiles show good agreement with the DNS data at $y^+ \geq 3$. Fig. 5(b) shows the friction coefficients of the turbulent boundary layers as a function of the Reynolds numbers, compared with the friction coefficients from the DNS data (Schlatter et al., 2010) and the experimental data (Österlund, 1999). The calculated friction coefficients of the two turbulent boundary layers demonstrated good agreement with both the DNS and the experimental data in the experimental uncertainties.

The synthetic jets operated at a frequency of 100 Hz $\leq f \leq$ 250 Hz, and at amplitudes of $A = 0.55$ and 1.1 m/s. The viscous-scaled frequency, $f^+ = f\nu_0/U_{\tau 0}^2$, is from 0.025 to 0.063 and the operating amplitude corresponds to $A/U_\infty = 0.1$ and 0.2 or $A^+ = A/U_{\tau 0} = 2.23$ and 4.47, based on the friction velocity, $U_{\tau 0}$, and the kinetic viscosity of the air, ν_0, in the baseline case. The origin of the coordinate axes was set at the center of the last row of the orifice array, which was at $X = 1289$ mm from the leading edge of the test section, as shown in Fig. 1. The measurement location was at $x = 6$, 13, 26, 39, and 52 mm or $x/\delta^* = 1.3$, 2.8, 5.6, 8.4, and 11.3, as shown in Fig. 3.

2.3. Determination of friction coefficients

The friction coefficient can be estimated as

$$C_f = \frac{\tau_w}{\rho U_\infty^2/2}, \tag{2}$$

where τ_w is the wall-shear stress and ρ is the density of air. The wall-shear stress is given as $\tau_w = \mu\frac{du}{dy}$, where μ is the dynamic viscosity of air, u is the instantaneous velocities in the viscous sublayer of turbulent boundary layers, and y is the wall-normal location. This formula requires two simultaneous measurements in the viscous sublayer of turbulent boundary layers, which can be very challenging; hence, an assumption of a non-slip condition at the wall was applied to simplify the technique. As a result, the wall-shear stress can be estimated as $\tau_w = \mu u/y$. The details of this technique can be found in the work by Hutchins and Choi (2002). The wall-shear stresses were indirectly estimated via hotwire measurements in the near-wall region of $y^+ = yU_\tau/\nu = 3.5$ to 5.5.

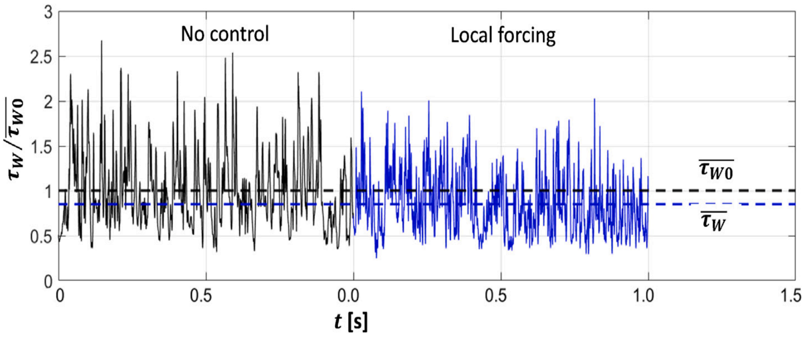

Fig. 6. Instantaneous wall-shear stresses of the turbulent boundary layers in the baseline case and the controlled case with a jet frequency of f^+ = 0.063 and amplitude of A/U_∞ = 0.2. The dashed lines represent the mean values.

Fig. 6 shows the instantaneous wall-shear stresses of the turbulent boundary layers in the baseline case and the controlled case with a jet frequency of f^+ = 0.063 and amplitude of A/U_∞ = 0.2. The ratio between the variance and mean of the instantaneous wall-shear stresses, $\mathrm{rms}(\tau'_W)/\overline{\tau_W}$, for the baseline controlled cases were 0.41 and 0.38, respectively. These values agree with a universal value of 0.4 recommended by Örlü and Schlatter (2011). The mean value of the instantaneous wall-shear stresses for the controlled case was smaller than the one for the baseline case, $\overline{\tau_W}/\overline{\tau_{W0}} \approx 0.84$, which indicates a reduction in the wall shear stresses due to synthetic jets.

3. Results and discussion

3.1. Turbulent boundary layer statistics

Fig. 7(a) shows the effect of the synthetic jet frequency on the displacement thickness of turbulent boundary layers at two jet amplitudes. The results show a systematic increase in the displacement thickness of the controlled boundary layers when the synthetic jet frequency increases. For example, when the synthetic jet frequency increased from f^+ = 0.025 to 0.063, the increase in the displacement thickness increased from about 1.9% to 5.9% of the displacement thickness of the turbulent boundary layer in the baseline case. When the jet frequency increased, the displacement thicknesses with a jet amplitude of A/U_∞ = 0.2, increased faster than those with a jet amplitude of A/U_∞ = 0.1. For example, an increase of about 5.9% in the displacement thickness of the turbulent boundary layer was observed at A/U_∞ = 0.2 and f^+ = 0.063, which is larger than an increase of about 3.5% at A/U_∞ = 0.1 and the same jet frequency. Fig. 7(b) shows similar effects of jet frequency on the shape factor of turbulent boundary layers. When the jet frequency increased from f^+ = 0.025 to 0.063, the increase in the displacement thickness increased from about 2% to 3.5% at A/U_∞ = 0.2 and from about 1% to 2% at A/U_∞ = 0.1. The increase in the displacement thicknesses and shape factors of turbulent boundary layers with synthetic jets was also observed in the work by Park et al. (2001) and Lu et al. (2020).

Fig. 8 shows the shape factor of turbulent boundary layers with synthetic jets at A/U_∞ = 0.1 and 0.2 compared with those of the undisturbed turbulent boundary layers, the turbulent boundary layers with a zero pressure gradient (Monkewitz et al., 2008), and the turbulent boundary layers with increasing adverse pressure gradients (Monty et al., 2011). The results show that when the jet amplitude increased, the shape factors increased along with an increase in the Reynolds number. This finding was also found in the work with $f^+ \leq 0.044$ by Park et al. (2001). When Reynolds numbers increase, the shape factors of turbulent boundary layers with a zero pressure gradient reduce (Monkewitz et al., 2008). In contrast, Monty et al. (2011) found an increase in the shape factor along with an increase in the Reynolds number of the turbulent boundary layers when the adverse pressure gradient increased. It, thus, is suggested that the behavior of the shape factor of the turbulent boundary layers with synthetic jets is similar to those with an adverse pressure gradient. The similarities between the changes observed in the boundary layer due to wall-normal blowing and those occurring in the presence of an adverse pressure gradient were also reported by Kornilov (2015).

Fig. 9(a) shows the effect of the jet frequency on the reduction in friction coefficients, $(C_f - C_{f0})/C_{f0}$, where C_f is the friction coefficient for the turbulent boundary layers with synthetic jets and C_{f0} is the friction coefficient for the baseline case with turbulent boundary layers over a flat plate. The friction coefficient is estimated from the mean wall-shear stress as $C_f = \overline{\tau_W}/(1/2\rho U_\infty^2)$. When the jet frequency increases from f^+ = 0.025 to 0.063, the reduction in friction coefficients for the turbulent boundary layers with a jet amplitude of A/U_∞ = 0.1 increases from about 5% to 15%. Similarly, the reduction in friction coefficients for the turbulent boundary layers with a jet amplitude of A/U_∞ = 0.2 increases from about 8% to 16.5%. These reductions agree with the reduction in turbulence intensity in the near-wall region in Fig. 14, the burst intensity and durations in Fig. 17. It is suggested that when the jet frequency or amplitude increases, the upwash motions during blowing phases may block the incoming flow more frequently, leading to a reduction in the mean local streamwise velocities in the vicinity of the orifices. When the mean local streamwise velocities were reduced, the local static pressure would increase. This could result in a larger local adverse pressure gradient in the vicinity of the orifices in the downstream direction and a larger increase in the shape factors as shown in Fig. 8. The larger adverse pressure gradient results in a larger reduction in the skin-friction drag of the turbulent boundary layers as reported by Monty et al. (2011). Fig. 9(b) illustrates the distribution of the friction coefficients, C_f, normalized by the one in the undisturbed case, C_{f0}, along the downstream locations at two frequencies of f^+ = 0.038 and 0.063, compared to the data by Park et al. (2001). The results show that the skin friction drag gradually recovers to the one in the undisturbed case. The effect of the jet frequency persists along the downstream location. For example, the normalized friction coefficient increased from 0.9 at x/δ^* = 1.3 to about 0.98 at x/δ^* = 11.3 in the cases with f^+ = 0.038 while it increased from about 0.83 to 0.96 in the case with f^+ = 0.063. The results show good agreement with the work by Park et al. (2001).

3.2. Time-averaged flow field and turbulence intensity

The instantaneous velocity signals were decomposed with a Reynolds decomposition as $u = U + u'$, where U is the time-averaged components and u' is the fluctuating components. Fig. 10 shows the effect of the jet frequency on the viscous-scaled time-averaged velocity profiles, $U^+ = U/U_{\tau 0}$ and $y^+ = yU_{\tau 0}/\nu 0$ at A/U_∞ = 0.1 and 0.2, respectively. The friction velocity was normalized by the local friction velocity in the baseline case, $U_{\tau 0}$. The results show a good agreement between the velocity profile of the baseline case and the logarithmic law at $30 \leq y^+ \leq 60$. As the Reynolds number of $Re_\theta \approx 1100$ is

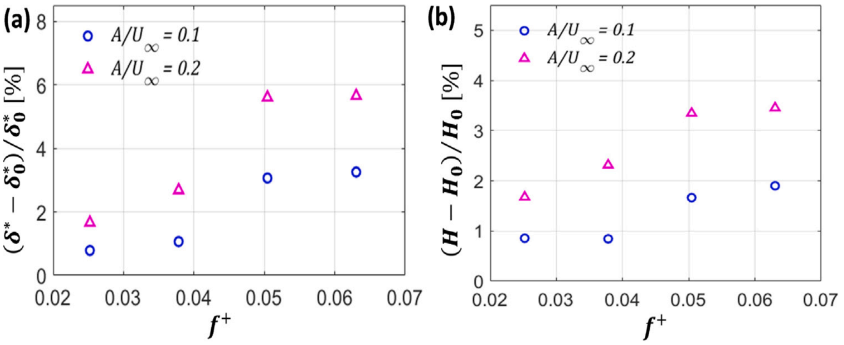

Fig. 7. Increases in (a) the displacement thicknesses, δ^*, and (b) shape factors, H, of the turbulent boundary layers with synthetic jets at $x/\delta^* = 1.3$ with respect to those of the unperturbed turbulent boundary layer, δ^*_0 and H_0, as a function of jet frequency.

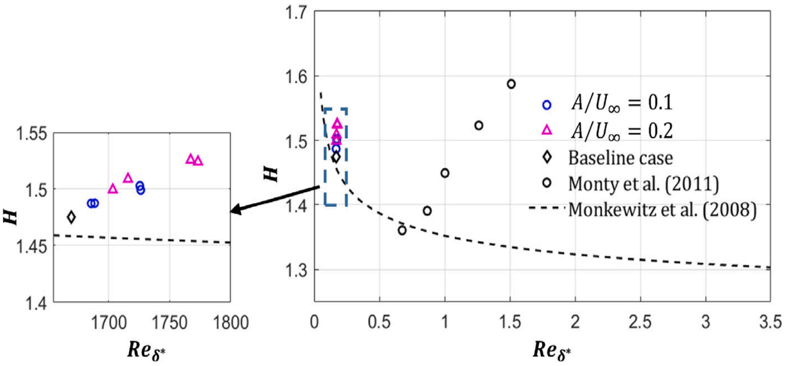

Fig. 8. The shape factors as a function of Reynolds number are based on displacement thicknesses of the turbulent boundary layers at $x/\delta^* = 1.3$. The dashed black line represents friction coefficients estimated by a semi-empirical relationship, $H = (1 - 7.11/(\ln(Re_{\delta^*})/0.384 + 3.11))^{-1}$, by Monkewitz et al. (2008).

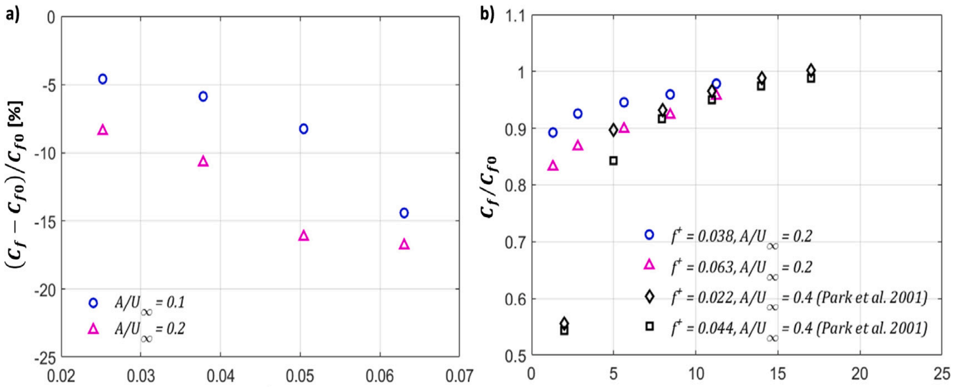

Fig. 9. (a) Friction drag reduction of the turbulent boundary layers with synthetic jets at $x/\delta^* = 1.3$ compared with the baseline case as a function of the jet frequencies and (b) Normalized friction coefficients as a function of the normalized downstream locations. Diamond and square markers are reproduced from the data by Park et al. (2001).

relatively low, the logarithmic layer is thin. This finding is consistent with the work by Österlund et al. (2000). A clear reduction in the viscous-scaled velocities in the near-wall and logarithmic regions of the turbulent boundary layers due to the synthetic jets was observed. When the jet frequency increased, the reduction increased. The reduction in the viscous-scaled velocities at $A/U_\infty = 0.2$ was more pronounced than those at $A/U_\infty = 0.1$ with a similar jet frequency. This finding was also observed in the work by Park et al. (2001) and Lu et al. (2020).

Fig. 11 shows the viscous-scaled velocity profiles of the turbulent boundary layers with a jet frequency of $f^+ = 0.038$ and 0.063 at four downstream locations. The friction velocity was normalized by the local friction velocity in the baseline case, $U_{\tau 0}$. When the turbulent boundary layer went downstream, the velocity profile gradually recovered to the undisturbed profile. The controlled velocity profile was identical to the undisturbed one at $x/\delta^* = 11.3$. When the jet frequency increased from $f^+ = 0.038$ to 0.063, a reduction in the streamwise velocity from $y^+ \leq 100$ increased. This increase was preserved downstream up to $x/\delta^* = 11.3$. A similar trend of reduction in the streamwise velocity downstream was observed by Park et al. (2001) and Lu et al. (2020).

Fig. 12 shows the turbulence intensity profiles of the turbulent boundary layers with the synthetic jets compared with those in the baseline case. The results show a steady increase in velocity fluctuations at $15 < y^+ \leq 60$ when the jet frequency increased in the cases with a jet amplitude of $A/U_\infty = 0.1$ in comparison to those in the baseline case. The increases in the cases with a jet amplitude of $A/U_\infty = 0.2$ were observed at $20 < y^+ \leq 70$, which were more significant than those with a jet amplitude of $A/U_\infty = 0.1$. The larger jet amplitude and frequency pushed the peak in the turbulence intensity further from the wall. The

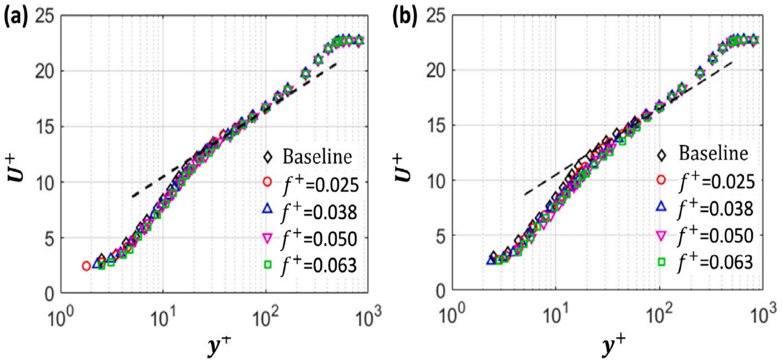

Fig. 10. Viscous-scaled velocity profiles of the turbulent boundary layers with different synthetic jet frequencies at $x/\delta^* = 1.3$ compared with the one of the unperturbed turbulent boundary layer at a jet amplitude of (a) $A/U_\infty = 0.1$ and (b) $A/U_\infty = 0.2$. The dashed lines represent the logarithmic law, $U^+ = 1/\kappa \ln(y^+) + B$, where $\kappa = 0.384$ and $B = 4.17$ (Monkewitz et al., 2007).

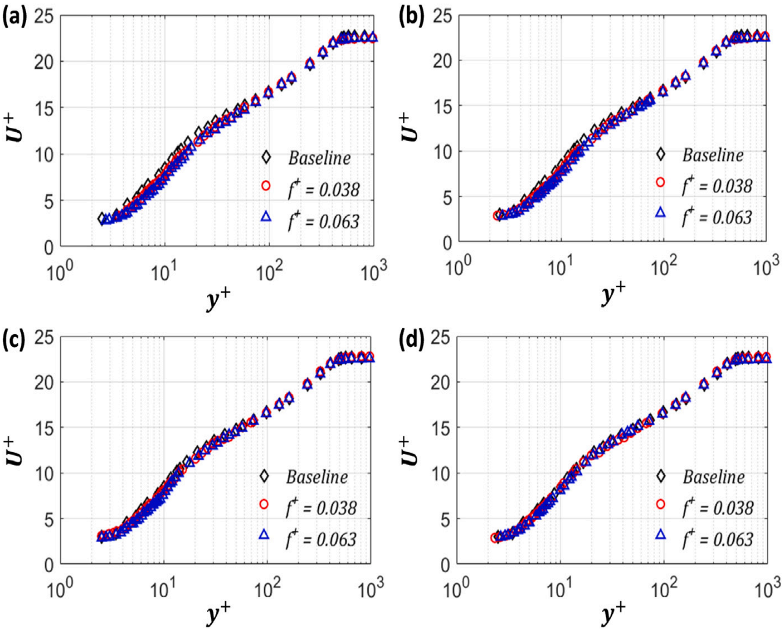

Fig. 11. Viscous-scaled velocity profiles of the turbulent boundary layers at $A/U_\infty = 0.2$ compared with the one of the unperturbed turbulent boundary layer at (a) $x/\delta^* = 2.8$, (b) $x/\delta^* = 5.6$, (c) $x/\delta^* = 8.4$, and (d) $x/\delta^* = 11.3$.

increase in velocity fluctuations could result from the generation of vortical structures in both blowing and suction. The upwash motions during blowing temporarily block the incoming free stream, which reduces the pressure in the vicinity of the orifices. Consequently, the surrounding ambient fluid fills up the area around the vicinity of the orifice and forms a vortex-like structure (Murugan et al., 2016). As the suction phase commences, the vortex-like structure moves away from the orifice due to its self-induced velocity. This vortical structure is then raised off the wall and another vortical structure is generated (Lawson and Dawson, 2013). When the jet frequency increased, the process of the generation of vortical structures became faster and a larger number of vortical structures were generated and lifted away from the wall (Belanger et al., 2020). As a result, the turbulence intensity increased. In contrast, the velocity fluctuations reduced at $y^+ \leq 12$ in both cases with $A/U_\infty = 0.1$ and 0.2, when the jet frequency increased. These decreases could be due to the lifting of the vortical structures from the wall and the temporary blocking of the incoming freestream flows. This finding agrees with the work by Park et al. (2001), Lu et al. (2020) and Cheng et al. (2021). Their results show that the movement of the turbulence intensity peak to a higher y^+ and the reduction in the turbulence intensity were associated with a reduction in skin friction drag of the turbulent boundary layers with synthetic jets.

The effect of the jet frequency on viscous-scaled turbulence intensity profiles at four downstream locations is presented in Fig. 13. The turbulence intensity profiles were normalized by the local friction velocity in the baseline case, $U_{\tau 0}$. The synthetic jets resulted in a reduction in the inner peak of turbulence intensity and a hump in the logarithmic region. When the jet frequency increased from $f^+ = 0.038$ to 0.063, both the reduction in the inner peak and the hump increased. This reduction and the hump were preserved until $x/\delta^* = 11.3$.

Fig. 14 shows the reduction in the averaged turbulence intensity of the turbulent boundary layers due to the synthetic jets in the near wall region, $y^+ \leq 12$. The averaged turbulence intensity in the near-wall region is given as:

$$TI = \frac{1}{y^+_{max}} \int_0^{y^+_{max}} \mathrm{rms}(u')^+ dy^+, \tag{3}$$

where $y^+_{max} = 12$ is the selected upper limit of the near-wall region. The results show that when the jet frequency increased, the reduction in the turbulence intensity in the near wall region became larger. For example, the reduction increased from about 6% at $f^+ = 0.025$ to about 10% at $f^+ = 0.063$ for the cases with $A/U_\infty = 0.1$. Similarly, the increase in the jet frequency resulted in a larger reduction in the turbulence intensity in the near-wall region. The maximum reduction of

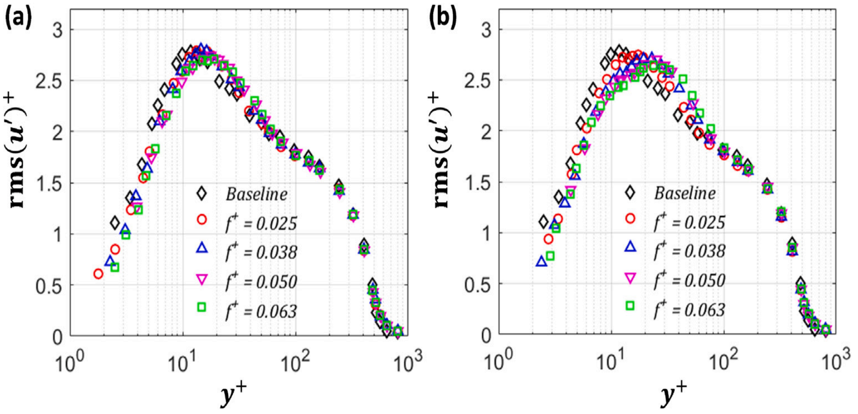

Fig. 12. Viscous-scaled turbulence intensity profiles of the turbulent boundary layers with different synthetic jet frequencies at $x/\delta^* = 1.3$ compared with that of the unperturbed turbulent boundary layer at a jet amplitude of (a) $A/U_\infty = 0.1$ and (b) $A/U_\infty = 0.2$.

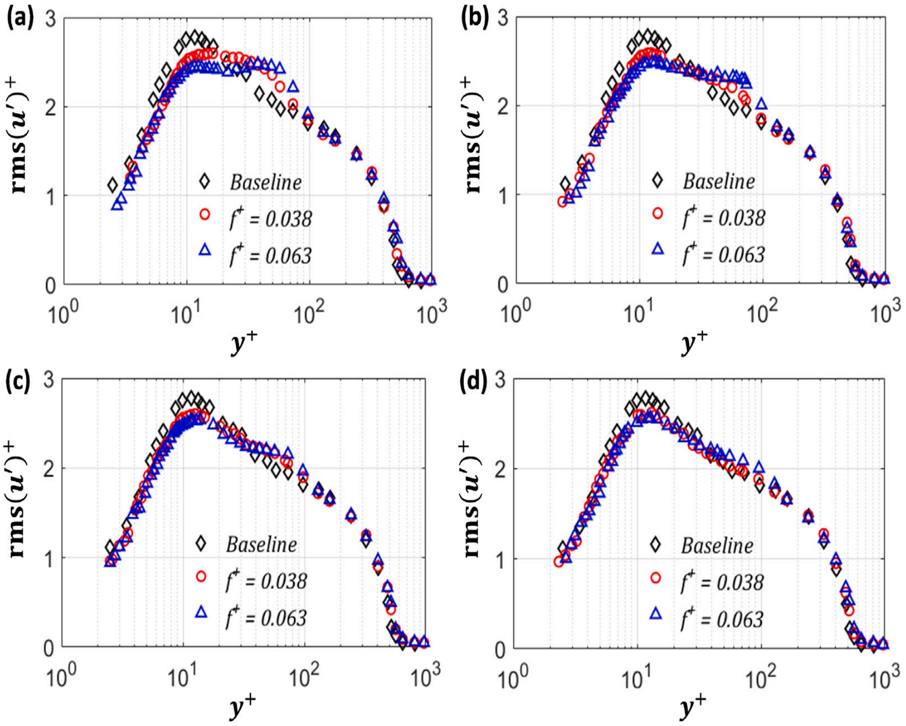

Fig. 13. Viscous-scaled turbulence intensity profiles of the turbulent boundary layers with different synthetic jet frequencies at $A/U_\infty = 0.2$ compared with that of the unperturbed turbulent boundary layer at (a) $x/\delta^* = 2.8$, (b) $x/\delta^* = 5.6$, (c) $x/\delta^* = 8.4$, and (d) $x/\delta^* = 11.3$.

about 14% was observed at $f^+ = 0.063$ and $A/U_\infty = 0.2$. The reduction in the turbulence intensity in the near-wall region would result in a reduction in the shear stresses and the friction drag. Hence, an increase in the jet frequency or amplitude would result in the increase in the drag reduction.

3.3. Burst events

Burst events including ejections and sweeps play an important role in the turbulence generation of turbulent boundary layers. They have a strong relationship with the level of turbulence intensity, especially in the near-wall region (Kim et al., 1971). Synthetic jets generate periodic disturbances in the turbulent boundary layer, impacting its coherent structures. Consequently, synthetic jets are likely to influence the burst process. The burst characteristics and profiles of the turbulent boundary layers were estimated by the Variable Interval Time Averaging (VITA) technique, as presented in Appendix.

Fig. 15(a) and (b) show the burst signatures at $y^+ = 7$ for the baseline case and controlled cases with different jet frequencies and amplitudes of $A/U_\infty = 0.1$ and 0.2, respectively. It was shown that the burst intensity in the controlled cases was smaller than the one in the baseline case. When the jet frequency or amplitude increased, the burst intensity reduced. Fig. 15(c) and (d) show the burst signatures at $y^+ = 30$ for the baseline case and controlled cases with different jet frequencies and amplitudes of $A/U_\infty = 0.1$ and 0.2, respectively. The results show that synthetic jets increased burst intensity at $y^+ = 30$. The increase in jet frequency or amplitude enhanced the burst intensity. Hence, it is suggested that the synthetic jets weakened the bursts in the near-wall regions but promoted the bursts in the outer region of the turbulent boundary layers.

Fig. 16 shows the burst profiles of the perturbed turbulent boundary layers with the synthetic jets compared with those of the unperturbed turbulent boundary layers in the baseline cases. Fig. 16(a) and (e) show the effect of jet frequency on the burst intensity profiles, $I_b^+ = I_b/U_\tau$,

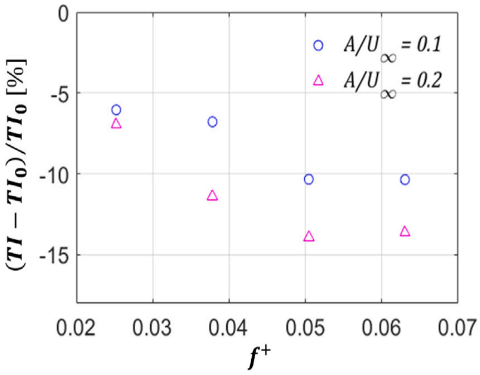

Fig. 14. The reduction in the averaged turbulence intensity, TI, in the near-wall region, $y^+ \leq 12$, of the turbulent boundary layers with the synthetic jets at $x/\delta^* = 1.3$ compared with the undisturbed turbulent boundary layer, TI_0.

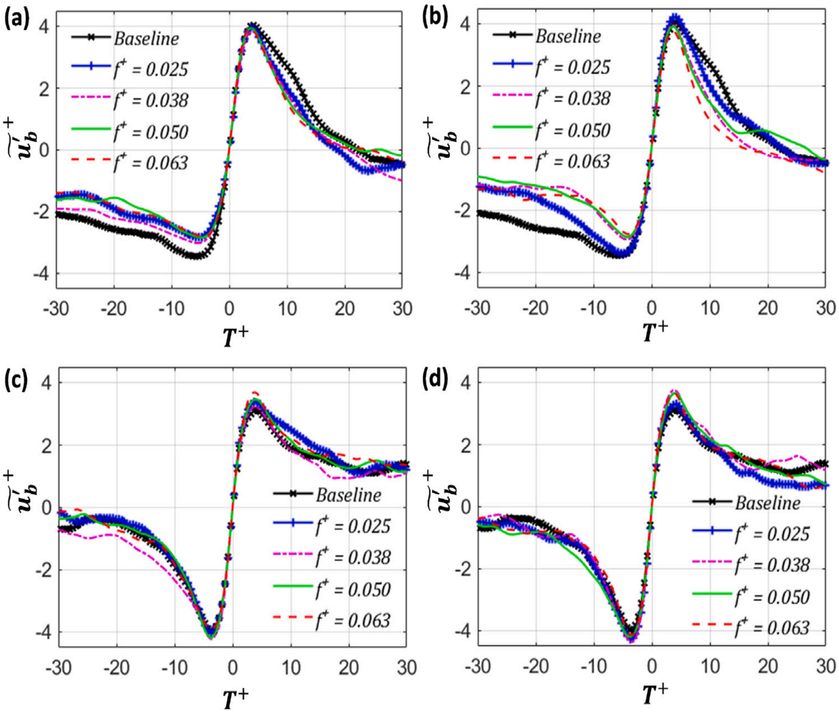

Fig. 15. Mean viscous-scaled burst signatures, $\tilde{u}_b'^+$, with VITA parameters, $T_W^+ = 10$ and $k = 1.2$, for the baseline and controlled cases with different jet frequencies and amplitudes at $x/\delta^* = 1.3$. (a) and (b) represent for the controlled cases with $A/U_\infty = 0.1$ and 0.2 at $y^+ = 7$, respectively. (c) and (d) represent for the controlled cases with $A/U_\infty = 0.1$ and 0.2 at $y^+ = 30$, respectively.

at $A/U_\infty = 0.1$ and 0.2, respectively. When the jet frequency increased from 0.025 to 0.063, the burst intensity increased at $15 < y^+ \leq 60$ for the cases with $A/U_\infty = 0.1$ and at $20 < y^+ \leq 70$ for the cases with $A/U_\infty = 0.2$. The burst intensity reduced at $y^+ \leq 12$ for the cases with both $A/U_\infty = 0.1$ and 0.2. These effects are similar to the variations of the turbulence intensity of the velocity fluctuations for the synthetic jets cases as shown in Fig. 12. The increase in the burst intensity at higher wall-normal locations agrees with the outer peak of turbulence intensity in the previous part which suggests that the synthetic jets weaken the streamwise vortices near the wall but enhance them in the outer region. Fig. 16(b) and (f) show the burst duration profiles, $T_b^+ = T_b U_\tau^2/\nu$, of the turbulent boundary layers with the synthetic jets compared with those of the baseline case. The results show that when the jet frequency increased, the burst duration reduced at $y^+ \leq 12$ in the cases with both $A/U_\infty = 0.1$ and 0.2. The reduction in the cases with $A/U_\infty = 0.2$ was more pronounced than those in the cases with $A/U_\infty = 0.1$.

In contrast, the effect of the viscous scaled jet frequency on the burst frequencies, $f_b^+ = f_b \nu/U_\tau^2$, was the opposite of the effect on the burst duration, as shown in Fig. 16(c) and (g). When the jet frequency increased, the burst frequencies significantly increased at $y^+ \leq 20$. Fig. 16(d) and (h) show the effect of jet frequency on the ratio between averaged burst duration and the averaged time between two consecutive bursts, $T_b f_b$. It was shown that the synthetic jets reduced the averaged time between two consecutive bursts at $y^+ \leq 20$ but had no effect at $y^+ > 20$. When the jet frequency or amplitude increased, the ratio increased. The decrease in bursting intensity and duration in the near-wall region suggests a weakening of the dynamic interactions between the wall streaks and the streamwise vortices. This leads to a reduction in turbulence production near the wall, ultimately resulting in decreased skin friction drag. Weakened burst events associated with a reduction in the friction drag of the turbulent boundary layers with synthetic jets were also reported in the previous work (Lu et al., 2020).

Fig. 17(a)-(b) show the reductions in the averaged viscous-scaled burst intensity, $\langle I_b^+ \rangle$, and durations, $\langle T_b^+ \rangle$, in the near-wall region, $y^+ \leq 12$, of the turbulent boundary layers with the synthetic jets compared with those of the undisturbed turbulent boundary layers as a function of the jet frequency at two jet amplitudes of $A/U_\infty = 0.1$ and 0.2. The

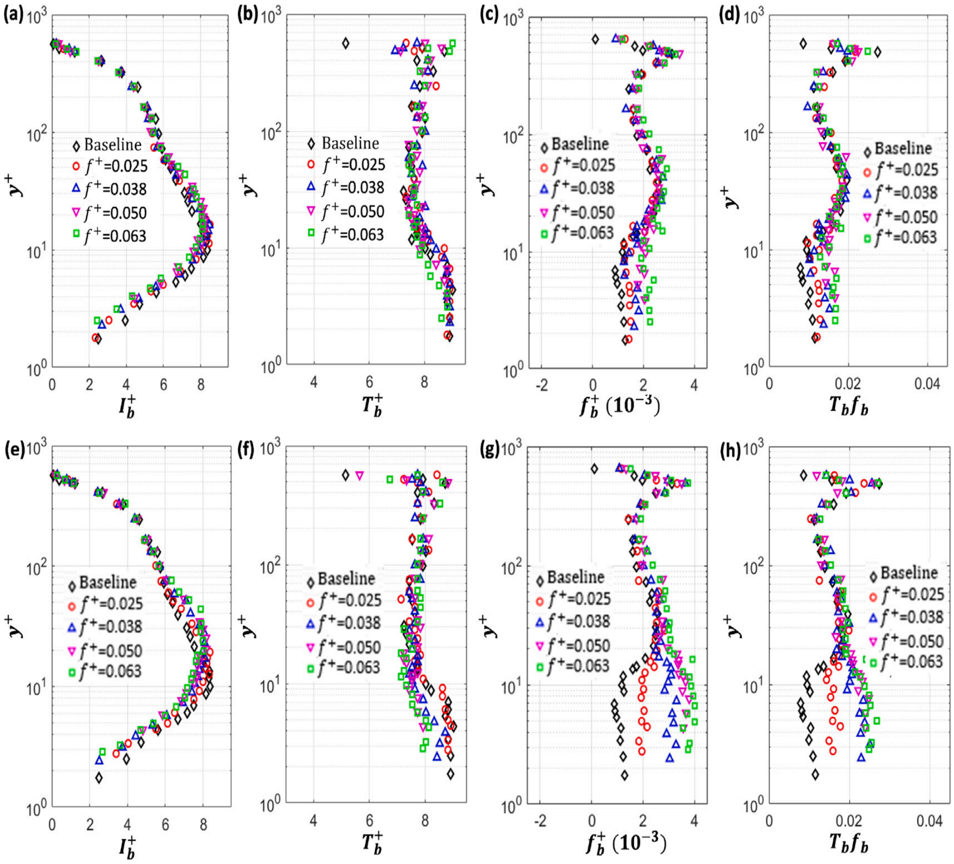

Fig. 16. Burst profiles with VITA parameters, $T_W^+ = 10$ and $k = 1.2$, for the control data with different jet frequencies and amplitudes at $x/\delta^* = 1.3$. (a), (b), (c), and (d) represent the profiles for the cases with the jet amplitude of $A/U_\infty = 0.1$. (e), (f), (g), and (h) represent the profiles for the cases with the jet amplitude of $A/U_\infty = 0.2$.

averaged burst intensity and duration in the near-wall region is given as:

$$\langle I_b^+ \rangle = \frac{1}{y_{max}^+} \int_0^{y_{max}^+} I_b^+ dy^+; \quad \langle T_b^+ \rangle = \frac{1}{y_{max}^+} \int_0^{y_{max}^+} T_b^+ dy^+. \tag{4}$$

where $y_{max}^+ = 12$. Fig. 17(a) shows that the synthetic jets reduced the burst intensity in the near-wall region of the turbulent boundary layers. While the jet frequency increased, the reduction in the burst intensity became more pronounced. For example, the reduction increased from about 5% at $f^+ = 0.023$ to about 14.5% at $f^+ = 0.063$ at $A/U_\infty = 0.2$. Similarly, when the jet amplitude increased, the reduction in the burst intensity became more significant. Fig. 17(b) illustrates the effect of jet frequency and amplitude on the burst durations of the turbulent boundary layers. The results show that when the jet frequency increased, the reduction in the burst duration became larger. For instance, the reduction in the burst duration increased from about 0% at $f^+ = 0.023$ to about 10% at $f^+ = 0.063$ at $A/U_\infty = 0.2$. Similarly, the effect of the jet amplitude on the burst duration became more significant when the jet amplitude increased. For example, the reduction in the burst duration increased from about 4.5% at $A/U_\infty = 0.1$ to about 10% at $A/U_\infty = 0.2$ for cases with $f^+ = 0.063$. Thus, the effects of the jet frequency and amplitude on the burst event mirror their effect on the turbulence intensity in the near-wall region, as shown in Fig. 14, which indicates a strong relationship between the burst events and the turbulent generation of the turbulent boundary layers in the near-wall region. This relationship was also reported by the previous work (Kim et al., 1971; Tang and Jiang, 2020).

3.4. Spectral content

A similar energy reorganization in the turbulent boundary layer, shifting towards the outer region, can be observed when examining the pre-multiplied power spectral densities (PSDs), $(k_x\Phi_{uu})^+ = k_x\Phi_{uu}/U_{\tau 0}^2$, where the power spectral density, Φ_{uu}, is estimated using the Welch algorithm with a 50% overlap and a Hamming window; $k_x = \omega/U$ is the wavenumber in the streamwise direction; ω is the angular frequency in the frequency domain. The convection velocity is equal to the local freestream velocity, following Taylor's hypothesis. The pre-multiplied PSDs were smoothed as:

$$(k_x\Phi_{uu})_{smooth}^+ = \frac{1}{N} \sum_{i=1}^{i=N} (k_x\Phi_{uu})_i^+ \tag{5}$$

where N is the number of data points between the smoothed intervals. Fig. 18 shows the pre-multiplied PSDs of the streamwise velocity fluctuations at $y^+ = 15$ in the turbulent boundary layer with a jet frequency of 100 Hz. The initial pre-multiplied PSDs clearly show the peak at the jet frequency of 100 Hz but it is hard to see this peak in color contours in the frequency domain because the peak occurs at only one frequency. Hence, the pre-multiplied PSDs were smoothed for better visualization of their color contours. The results show that when the smoothing span increases, the peak of the pre-multiplied PSDs reduces. As the span is applied to all cases, the selection of the span would not change the consideration of the analysis. Hence, the span, $N = 50$, is selected for all cases.

Fig. 19(a)–(d) and (i)–(l) show the pre-multiplied PSDs, $(k_x\Phi_{uu})^+ = k_x\Phi_{uu}/U_\tau^2$, as a function of the viscous-scaled wavelength, λ_x^+, and the viscous-scaled wall-normal locations, y^+, for both the baseline and controlled cases. The pre-multiplied PSDs for the baseline case show an inner-peak at $y^+ \approx 13$ and $\lambda_x^+ \approx 1500$, which is similar to the inner-peak at $y^+ \approx 15$ and $\lambda_x^+ \approx 1000$ in the pre-multiplied PSDs for the turbulent boundary layers over a smooth flat plate, observed by Mathis et al. (2009) and Hutchins and Marusic (2007). The scatter could be due to the uncertainties of the smoothing process and the estimation

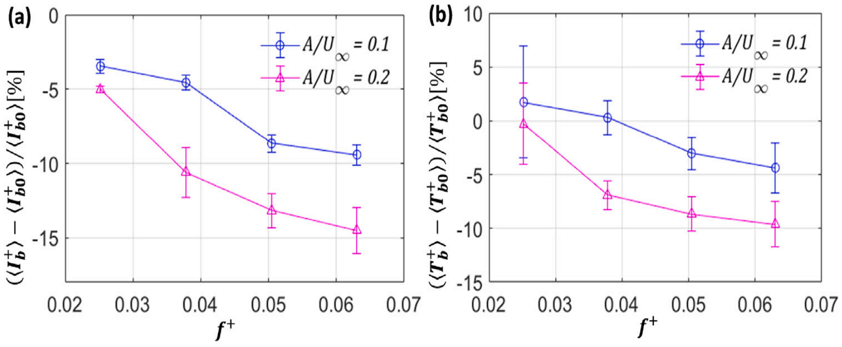

Fig. 17. Reductions in (a) the averaged viscous-scaled burst intensity, $\langle I_b^+\rangle$ and (b) the averaged burst duration, $\langle T_b^+\rangle$, in the near-wall region, $y^+ \le 12$, of the turbulent boundary layers with synthetic jets at $x/\delta^* = 1.3$ as a function of the jet frequency compared with the averaged viscous-scaled burst intensity, $\langle I_{b0}^+\rangle$, and frequency, $\langle T_{b0}^+\rangle$, of the undisturbed turbulent boundary layer. The error bars represent the variation of the VITA parameter with $1 \le k \le 1.5$ and $10 \le T_W^+ \le 20$.

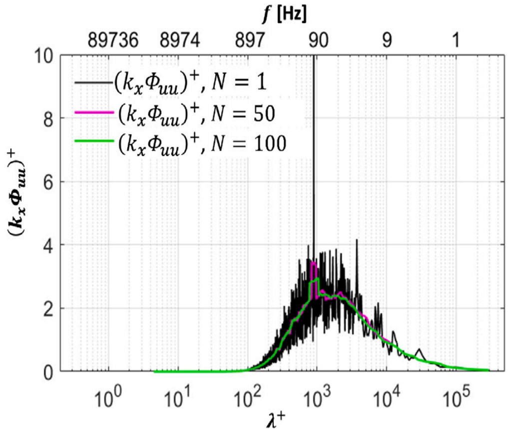

Fig. 18. Initial values and smoothed values of the pre-multiplied PSDs of streamwise velocity fluctuations at $y^+ = 15$ in the turbulent boundary layer with a jet frequency of 100 Hz.

of the friction velocities. These uncertainties, however, applied to both the baseline and controlled cases, so they would not affect the consideration of these results. From left to right, Fig. 19(a)–(d) and (i)–(l) show that when the jet frequency increased, the inner peak of the pre-multiplied PSDs was lifted to a higher y^+ for the case with both $A/U_\infty = 0.1$ and 0.2. Similar effects of the jet amplitude on the inner peak were also observed. When the jet amplitude increased, the inner peak moved further from the wall. These indicate that the synthetic jets lifted the turbulent kinetic energy further from the wall and expanded the inner region, which resulted in the reduction in the turbulent kinetic energy as well as the shear stresses in the near-wall region. As a result, the synthetic jets reduced the local skin friction drag of the turbulent boundary layers. Lifting the inner peak and expanding the inner region along with a reduction in the skin-friction drag was also observed in other turbulent boundary layer controls, such as spanwise wall forcing (Chandran et al., 2023; Rouhi et al., 2023).

Fig. 19(e)–(h) and (n)–(p) show the difference between the pre-multiplied PSDs of the streamwise velocity fluctuations of the turbulent boundary layers with the synthetic jets, $(k_x\Phi_{uu})^+$, and those of the undisturbed boundary layer, $(k_x\Phi_{uu})_0^+$. The difference is given as:

$$\Delta(k_x\Phi_{uu})^+ = (k_x\Phi_{uu})^+ - (k_x\Phi_{uu})_0^+. \tag{6}$$

The results show a clear increase in the pre-multiplied PSD of the turbulent boundary layers with different jet frequencies. When the jet frequency increased, the pre-multiplied PSD at $y^+ > 15$ increased at all wavelengths. These increases agree with the increase in turbulence intensity and burst intensity at $y^+ > 15$, as shown in Fig. 12, Fig. 16(a) and (d), respectively. These increases in the pre-multiplied PSDs shift the energy peak further from the wall. In contrast, the near-wall region, $y^+ \le 12$, illustrates the different effects of synthetic jets on small-scale and large-scale energy. When the jet frequency or amplitude increased, the scale structures of $\lambda_x \le 3\delta$, became more energetic but the scale structures of $\lambda_x > 3\delta$ became less energetic.

4. Conclusion

This paper conducted hot-wire experiments to examine the effects of synthetic jets on burst events in the near-wall region of turbulent boundary layers at $Re_\theta \approx 1050$ to understand the mechanism of turbulent drag reduction with synthetic jets. Different characteristics of synthetic jets including jet frequencies, $f_W^+ = 0.025$ to 0.063, and two different jet amplitudes, $A/U_\infty = 0.1$ and 0.2 were considered. The study's findings are outlined below.

Burst events in the near-wall region of the turbulent boundary layers with synthetic jets experienced a reduction up to about 15% in the burst strength and a reduction up to about 10% in the burst duration in the near-wall region, $y^+ \le 12$, suggesting that synthetic jets lifted the turbulent kinetic energy away from the wall. This results in a reduction up to nearly 14% in the turbulence intensity in the near-wall region, which would reduce the shear stresses in the near-wall region as well as the skin-friction drag. An increase in synthetic jet frequencies or amplitudes results in the modification of the near-wall burst event being more pronounced.

A reduction up to about 16.5% of the local friction drag was observed in the turbulent boundary layer manipulated by the synthetic jets with $f^+ = 0.063$ and $A/U_\infty = 0.2$. This local skin friction drag reduction has to be taken with care and does not conclusively imply a total drag reduction as the skin-friction drag was not measured directly. However, the reductions in the turbulence intensity, the burst events, and the very large-scale energy in the near-wall region provide

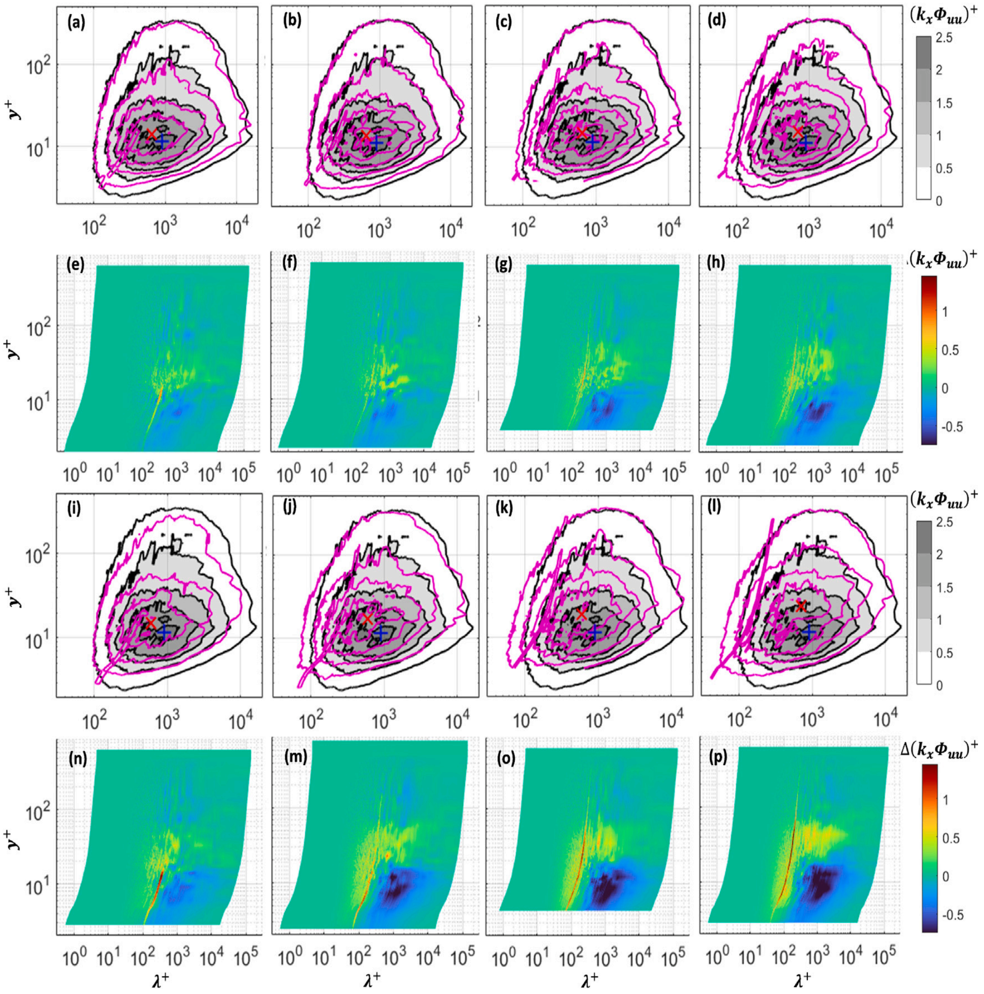

Fig. 19. The pre-multiplied PSDs of the streamwise velocity fluctuations, $(k_x\Phi_{uu})^+$; (a)–(d) $A/U_\infty = 0.1$; (i)–(l) $A/U_\infty = 0.2$; and the difference between the pre-multiplied PSDs of the turbulent boundary layers with synthetic jets at $x/\delta^* = 1.3$ with respect to one of the undisturbed boundary layers, $\Delta(k_x\Phi^+_{uu})$; (e)–(h) $A/U_\infty = 0.1$; (n)–(p) $A/U_\infty = 0.2$. The magenta lines represent for the controlled cases with $(k_x\Phi_{uu})^+ = 0$–2.5 in steps of 0.5. The black contours represent for the baseline case. The blue "+" markers represent the inner-peak location of the pre-multiplied PSDs for the baseline case. The red "x" markers represent the inner-peak location of the pre-multiplied PSDs for the controlled cases. From left to right, the four columns represent for the cases with $f^+ = 0.025$, 0.038; 0.050; and 0.063 respectively.

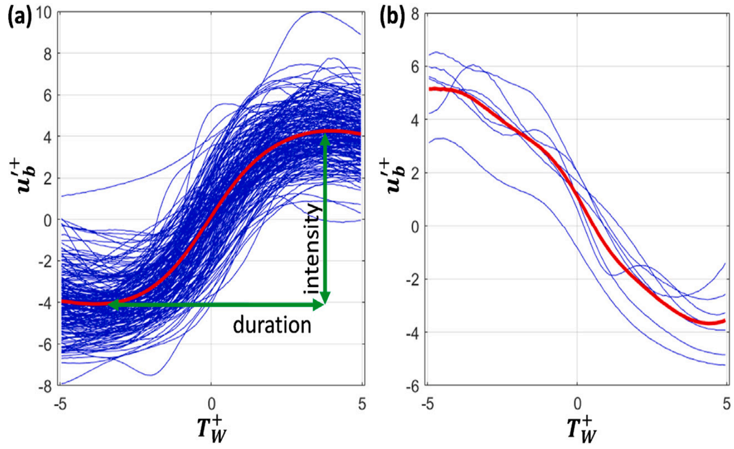

Fig. 20. Viscous-scaled burst signatures, $u_b'^+$, with VITA parameters, $T_W^+ = 10$ and $k = 1.2$ for the baseline data at $y^+ = 15$. (a) the sweep signatures and (b) the ejection signatures. The red lines represent the mean signatures. (For interpretation of the references to color in this figure legend, the reader is referred to the web version of this article.)

evidence of skin-friction drag reduction in the turbulent boundary layer with synthetic jets.

Future extensions of this study could concentrate on investigating the influence of orifice spacing and diameter of synthetic jet actuators

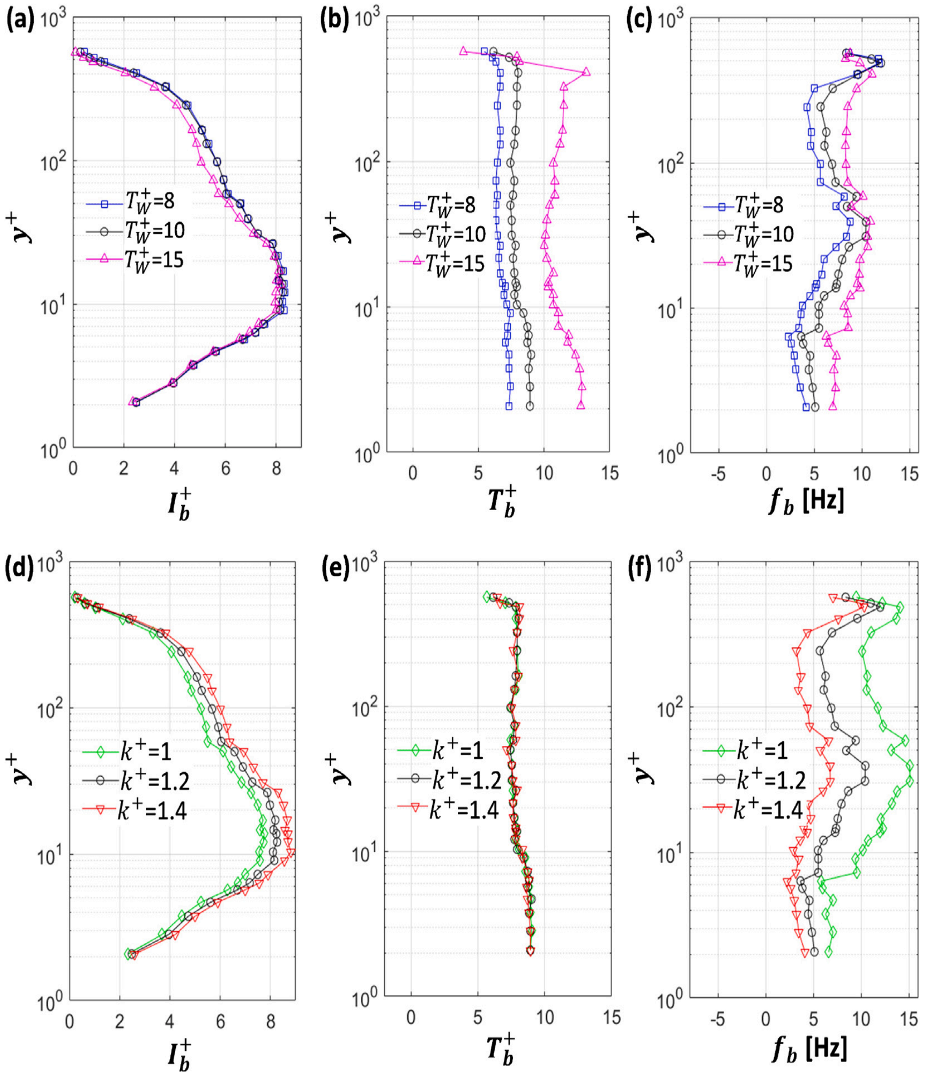

Fig. 21. Burst profiles with different VITA parameters for the baseline data. (a), (b) and (c) represent the profiles with different T_W^+ and k = 1.2. (d), (e) and (f) represent the profiles with different k and T_W^+ = 10.

on turbulent boundary layers at different flow conditions to enhance the understanding of the drag reduction mechanism.

CRediT authorship contribution statement

Van Thuan Hoang: Writing – review & editing, Writing – original draft, Visualization, Validation, Software, Resources, Methodology, Investigation, Funding acquisition, Formal analysis, Data curation, Conceptualization. **Azadeh Jafari:** Writing – review & editing, Visualization, Validation, Supervision, Methodology, Investigation, Formal analysis, Conceptualization. **Benjamin Cazzolato:** Writing – review & editing, Visualization, Validation, Supervision, Methodology, Investigation, Formal analysis, Conceptualization. **Maziar Arjomandi:** Writing – review & editing, Visualization, Validation, Supervision, Project administration, Methodology, Investigation, Funding acquisition, Formal analysis, Conceptualization.

Declaration of competing interest

The authors declare that they have no known competing financial interests or personal relationships that could have appeared to influence the work reported in this paper.

Acknowledgments

This research was supported by the Australian Government Research Training Program (RTP) and the Australian Government through the Australian Research Council (ARC DP-200101961).

Appendix. Estimation of burst profiles

Burst events, including sweep and ejection events, can be detected by the Variable Interval Time Averaging (VITA) technique (Whalley, 2011). A burst is detected when the local variance, $\mathrm{Var}(t, T_W)$, in a window, T_W, is larger than the variance of an entire signal of velocity fluctuations, $\mathrm{Var}(t)$, manipulated by a threshold, k. The local variance can be given as:

$$\mathrm{Var}(t, T_W) = \hat{u^2}(t, T_W) - (\hat{u^2}(t, T_W))^2, \tag{7}$$

where $\hat{Q}(t, T_W)$ is the local mean, $\hat{Q}(t, T_W) = \frac{1}{T_W}\int_{t-\frac{1}{2}T_W}^{t+\frac{1}{2}T_W} Q dt$. The detection function, $D(t)$, of burst events can be given as (Whalley, 2011):

$$D(t) = \begin{cases} 1 & \text{if } \mathrm{Var}(t, T_W) \geq k \times \mathrm{Var}(t) \;\&\; du/dt > 0 \text{ (sweeps)} \\ 0 & \text{if } \mathrm{Var}(t, T_W) < k \times \mathrm{Var}(t) \text{ (no events)} \\ -1 & \text{if } \mathrm{Var}(t, T_W) \geq k \times \mathrm{Var}(t) \;\&\; du/dt < 0 \text{ (ejections)} \end{cases} . \tag{8}$$

Changing the VITA parameters, k and T_W^+, has no impact on the considerations in this report, as shown in the following paragraphs, so $k = 1.2$ and $T_W^+ = 10$ were selected.

Fig. 20 shows the burst signatures of the velocity fluctuations for the baseline case at $y^+ = 15$ with VITA parameters, $T_W^+ = 10$ and $k = 1.2$. The velocity signal duration was 30 s at a sampling frequency of 40 kHz. Fig. 20(a) illustrates the instantaneous sweep signatures and Fig. 20(b) shows the instantaneous ejection signatures. While 189 sweep events were detected, only 7 ejection events were found. This indicates that sweep events were the main contributors to the bursts. This finding is consistent with the work by Orlandi and Jiménez (1994) and Whalley (2011). The characteristics of sweep events were considered as the characteristics of burst events. The intensity of bursts, I_b, was the magnitude difference between the maximum and minimum points of the mean burst profiles, and the duration of the bursts, T_b, was calculated from the time separation of the peaks of the mean signature of the events, as shown in Fig. 20(a). The burst frequency, f_b, is the number of bursts in a second.

Fig. 21 shows the burst profiles including the intensity, duration, and frequency profiles of the velocity fluctuations through the boundary layer for the baseline case with three different T_W^+ from 8 to 15 and k from 1 to 1.4. The results are consistent throughout the turbulent boundary layer from the wall to the boundary layer edge. The effect of T_W^+ on the burst profiles was the opposite of the effect of k. Fig. 21(a–c) show that when T_W^+ increased from 8 to 15, the burst intensity profile reduced but both burst duration and frequency profiles increased throughout the boundary layer. In contrast, when k increased from 1 to 1.4, the burst intensity profile increased but the burst frequency profile reduced. The burst duration profile did not show any effect of k. Modifying the VITA parameters does not change the considerations outlined in this study, so the VITA parameters were selected as $T_W^+ = 10$ and $k = 1.2$ to detect bursts for both the baseline and synthetic jet cases. These VITA parameters were also used by Blackwelder and Kaplan (1976) and Whalley (2011).

Data availability

Data will be made available on request.

References

Aider, J.L., Beaudoin, J.F., Wesfreid, J.E., 2010. Drag and lift reduction of a 3d bluff-body using active vortex generators. Exp. Fluids 48, 771–789. http://dx.doi.org/10.1007/s00348-009-0770-y.

Araya, G., Leonardi, S., Castillo, L., 2008. Numerical assessment of local forcing on the heat transfer in a turbulent channel flow. Phys. Fluids 20, 1–22. http://dx.doi.org/10.1063/1.2963140.

Araya, G., Leonardi, S., Castillo, L., 2011. Steady and time-periodic blowing/suction perturbations in a turbulent channel flow. Physica D 240, 59–77. http://dx.doi.org/10.1016/j.physd.2010.08.006.

Belanger, R., Zingg, D.W., Lavoie, P., 2020. Vortex structure of a synthetic jet issuing into a turbulent boundary layer from a finite-span rectangular orifice. In: AIAA Scitech 2020 Forum. p. 1815. http://dx.doi.org/10.2514/6.2020-1815.

Blackwelder, R.F., Eckelmann, H., 1979. Streamwise vortices associated with the bursting phenomenon. J. Fluid Mech. 94, 577–594. http://dx.doi.org/10.1017/S0022112079001191.

Blackwelder, R., Kaplan, R., 1976. On the wall structure of the turbulent boundary layer. J. Fluid Mech. 76, 89–112. http://dx.doi.org/10.1017/S0022112076003145.

Cannata, M., Cafiero, G., Iuso, G., 2020. Large-scale forcing of a turbulent channel flow through spanwise synthetic jets. AIAA J. 58, 2042–2052. http://dx.doi.org/10.2514/1.J059047.

Cannata, M., Iuso, G., 2008. Spanwise directed synthetic jets for wall turbulence control. In: The 4th AIAA Flow Control Conference. p. 4205. http://dx.doi.org/10.2514/6.2008-4205.

Cantwell, B.J., 1981. Organized motion in turbulent flow. Annu. Rev. Fluid Mech. 13, 457–515. http://dx.doi.org/10.1146/annurev.fl.13.010181.002325.

Chandran, D., Zampiron, A., Rouhi, A., Fu, M.K., Wine, D., Holloway, B., Smits, A.J., Marusic, I., 2023. Turbulent drag reduction by spanwise wall forcing. part 2. High-Reynolds-number experiments. J. Fluid Mech. 968, A7. http://dx.doi.org/10.1017/jfm.2023.498.

Cheng, X., Qiao, Z., Zhang, X., Quadrio, M., Zhou, Y., 2021. Skin-friction reduction using periodic blowing through streamwise slits. J. Fluid Mech. 920, A50. http://dx.doi.org/10.1017/jfm.2021.439.

Corke, T.C., Thomas, F.O., 2018. Active and passive turbulent boundary-layer drag reduction. AIAA J. 56, 3835–3847. http://dx.doi.org/10.2514/1.J056949.

De Graaff, D.B., Eaton, J.K., 2000. Reynolds-number scaling of the flat-plate turbulent boundary layer. J. Fluid Mech. 422, 319–346. http://dx.doi.org/10.1017/S0022112000001713.

Guo, H., Borodulin, V., Kachanov, Y., Pan, C., Wang, J., Lian, Q., Wang, S., 2010. Nature of sweep and ejection events in transitional and turbulent boundary layers. J. Turbul. 11, N34.

Gupta, A., Laufer, J., Kaplan, R., 1971. Spatial structure in the viscous sublayer. J. Fluid Mech. 50, 493–512. http://dx.doi.org/10.1017/S0022112071002726.

Heinemann, P., Panagiotou, P., Vratny, P., Kaiser, S., Hornung, M., Yakinthos, K., 2017. Advanced tube and wing aircraft for year 2050 timeframe. In: 55th AIAA Aerospace Sciences Meeting. p. 1390.

Hutchins, N., Choi, K.S., 2002. Accurate measurements of local skin friction coefficient using hot-wire anemometry. Prog. Aerosp. Sci. 38, 421–446. http://dx.doi.org/10.1016/S0376-0421(02)00027-1.

Hutchins, N., Marusic, I., 2007. Evidence of very long meandering features in the logarithmic region of turbulent boundary layers. J. Fluid Mech. 579, 1–28. http://dx.doi.org/10.1017/S0022112006003946.

Hutchins, N., Monty, J., Hultmark, M., Smits, A., 2015. A direct measure of the frequency response of hot-wire anemometers: temporal resolution issues in wall-bounded turbulence. Exp. Fluids 56, 1–18.

Hutchins, N., Nickels, T.B., Marusic, I., Chong, M., 2009. Hot-wire spatial resolution issues in wall-bounded turbulence. J. Fluid Mech. 635, 103–136.

Hyun Shin, J., Song, S.Jin., 2015. Pressure gradient effects on smooth and rough surface turbulent boundary layers—part i: Favorable pressure gradient. J. Fluids Eng. 137, 011203. http://dx.doi.org/10.1115/1.4027474.

Iuso, G., Di Cicca, G.M., 2007. Interaction of synthetic jets with a fully developed turbulent channel flow. J. Turbul. 8, N11. http://dx.doi.org/10.1080/14685240601110088.

Jørgensen, F.E., 2005. How To Measure Turbulence with Hot-Wire Anemometers. Technical Report, Dantec A/S.

Kametani, Y., Fukagata, K., Örlü, R., Schlatter, P., 2015. Effect of uniform blowing/suction in a turbulent boundary layer at moderate reynolds number. Int. J. Heat Fluid Flow 55, 132–142. http://dx.doi.org/10.1016/j.ijheatfluidflow.2015.05.019.

Kim, H., Kline, S., Reynolds, W., 1971. The production of turbulence near a smooth wall in a turbulent boundary layer. J. Fluid Mech. 50, 133–160. http://dx.doi.org/10.1017/S0022112071002490.

Kornilov, V., 2015. Current state and prospects of researches on the control of turbulent boundary layer by air blowing. Prog. Aerosp. Sci. 76, 1–23. http://dx.doi.org/10.1016/j.paerosci.2015.05.001.

Krein, A., Williams, G., 2012. Flightpath 2050: Europe's vision for aeronautics. In: Innovation for Sustainable Aviation in a Global Environment: Proceedings of the Sixth European Aeronautics Days. http://dx.doi.org/10.3233/978-1-61499-063-5-63.

Lawson, J.M., Dawson, J.R., 2013. The formation of turbulent vortex rings by synthetic jets. Phys. Fluids 25, http://dx.doi.org/10.1063/1.4825283.

Lu, L., Li, D., Gao, Z., Cao, Z., Bai, Y., Zheng, J., 2020. Characteristics of array of distributed synthetic jets and effect on turbulent boundary layer. Acta Mech. Sin. 36, 1171–1190. http://dx.doi.org/10.1007/s10409-020-01001-x.

Mathis, R., Hutchins, N., Marusic, I., 2009. Large-scale amplitude modulation of the small-scale structures in turbulent boundary layers. J. Fluid Mech. 628, 311–337. http://dx.doi.org/10.1017/S0022112009006946.

Mondal, R., Alam, M.M., 2023. Blockage effect on wakes of various bluff bodies: A review of confined flow. Ocean Eng. 286, 115592. http://dx.doi.org/10.1016/j.oceaneng.2023.115592.

Monkewitz, P.A., Chauhan, K.A., Nagib, H.M., 2007. Self-consistent high Reynolds number asymptotics for zero-pressure-gradient turbulent boundary layers. Phys. Fluids 19, 115101.

Monkewitz, P.A., Chauhan, K.A., Nagib, H.M., 2008. Comparison of mean flow similarity laws in zero pressure gradient turbulent boundary layers. Phys. Fluids 20, 105102. http://dx.doi.org/10.1063/1.2972935.

Monty, J.P., Harun, Z., Marusic, I., 2011. A parametric study of adverse pressure gradient turbulent boundary layers. Int. J. Heat Fluid Flow 32, 575–585. http://dx.doi.org/10.1016/j.ijheatfluidflow.2011.03.004.

Moretti, P., Kays, W., 1965. Heat transfer to a turbulent boundary layer with varying free-stream velocity and varying surface temperature—an experimental study. Int. J. Heat Mass Transfer 8, 1187–1202. http://dx.doi.org/10.1016/0017-9310(65)90062-1.

Murugan, T., Deyashi, M., Dey, S., Rana, S.C., Chatterjee, P., 2016. Recent developments on synthetic jets. Def. Sci. J. 66, doi: https://api.semanticscholar.org/CorpusID:73587359.

Nickels, T., Marusic, I., Hafez, S., Chong, M., 2005. Evidence of the k_{-1}^{1} law in a high-Reynolds-number turbulent boundary layer. Phys. Rev. Lett. 95, 074501.

Orlandi, P., Jiménez, J., 1994. On the generation of turbulent wall friction. Phys. Fluids 6, 634–641. http://dx.doi.org/10.1063/1.868303.

Örlü, R., Schlatter, P., 2011. On the fluctuating wall-shear stress in zero pressure-gradient turbulent boundary layer flows. Phys. Fluids 23, http://dx.doi.org/10.1063/1.3555191.

Österlund, J.M., 1999. Experimental Studies of Zero Pressure-Gradient Turbulent Boundary Layer Flow (Ph.D. thesis). Department of Mechanics, Royal Institute of Technology.

Österlund, J.M., Johansson, A.V., Nagib, H.M., Hites, M.H., 2000. A note on the overlap region in turbulent boundary layers. Phys. Fluids 12, 1–4.

Park, J., Choi, H., 1999. Effects of uniform blowing or suction from a spanwise slot on a turbulent boundary layer flow. Phys. Fluids 11, 3095–3105. http://dx.doi.org/10.1063/1.870167.

Park, S., Lee, I., Sung, H.J., 2001. Effect of local forcing on a turbulent boundary layer. Exp. Fluids 31, 384–393. http://dx.doi.org/10.1007/s003480100305.

Park, Y.S., Park, S.H., Sung, H.J., 2003. Measurement of local forcing on a turbulent boundary layer using piv. Exp. Fluids 34, 697–707. http://dx.doi.org/10.1007/s00348-003-0604-2.

Rouhi, A., Fu, M.K., Chandran, D., Zampiron, A., Smits, A.J., Marusic, I., 2023. Turbulent drag reduction by spanwise wall forcing, part 1. large-eddy simulations. J. Fluid Mech. 968, 6. http://dx.doi.org/10.1017/jfm.2023.499.

Scarano, F., Jacob, M.C., Gowree, E.R., 2023. Drag reduction by means of an array of staggered circular cavities at moderate Reynolds numbers. Int. J. Heat Fluid Flow 102, 109142. http://dx.doi.org/10.1016/j.ijheatfluidflow.2023.109142.

Schatzman, D.M., Wilson, J.S., Chandrasekhara, M.S., 2016. Synthetic jet and turbulent boundary layer interaction quantification. In: The 8th AIAA Flow Control Conference. p. 4238. http://dx.doi.org/10.2514/6.2016-4238.

Schlatter, P., Li, Q., Brethouwer, G., Johansson, A.V., Henningson, D.S., 2010. Simulations of spatially evolving turbulent boundary layers up to Re_θ=4300. Int. J. Heat Fluid Flow 31, 251–261.

Schultz, M.P., Flack, K.A., 2003. Turbulent boundary layers over surfaces smoothed by sanding. J. Fluids Eng. 125, 863–870. http://dx.doi.org/10.1115/1.1598992.

Silvestri, A., Ghanadi, F., Arjomandi, M., Cazzolato, B., Zander, A., 2018. The application of different tripping techniques to determine the characteristics of the turbulent boundary layer over a flat plate. J. Fluids Eng. 140.

Soleimani, S., Eckels, S., 2021. A review of drag reduction and heat transfer enhancement by riblet surfaces in closed and open channel flow. Int. J. Thermofluids 9, 100053. http://dx.doi.org/10.1016/j.ijft.2020.100053.

Tang, Z., Jiang, N., 2020. The effect of a synthetic input on small-scale intermittent bursting events in near-wall turbulence. Phys. Fluids 32, 015110. http://dx.doi.org/10.1063/1.5129042.

Thomas, F.O., Corke, T.C., Duong, A.H., 2023. Airfoil friction drag reduction with net power savings using pulsed-direct-current plasma actuation. AIAA J. 61, 4045–4055. http://dx.doi.org/10.2514/1.J062627.

Whalley, R.D., 2011. Turbulent Boundary-Layer Control with DBD Plasma Actuators using Spanwise Travelling-Wave Technique (Ph.D. thesis). University of Nottingham.

White, C.M., Mungal, M.G., 2008. Mechanics and prediction of turbulent drag reduction with polymer additives. Annu. Rev. Fluid Mech. 40, 235–256. http://dx.doi.org/10.1146/annurev.fluid.40.111406.102156.

Yao, J., Chen, X., Hussain, F., 2018. Drag control in wall-bounded turbulent flows via spanwise opposed wall-jet forcing. J. Fluid Mech. 852, 678–709. http://dx.doi.org/10.1017/jfm.2018.553.

Yao, J., Chen, X., Thomas, F., Hussain, F., 2017. Large-scale control strategy for drag reduction in turbulent channel flows. Phys. Rev. Fluids 2, 062601. http://dx.doi.org/10.1103/PhysRevFluids.2.062601.

Ye, Z., Jiang, Y., Zhang, Y., Zou, J., Zheng, Y., 2019. Effects of synthetic jet array on turbulent boundary layer. Int. J. Heat Technol. 37, 893–898. http://dx.doi.org/10.18280/ijht.370327.

Zhang, X., Wong, C., Cheng, X., Zhou, Y., 2022. Dependence of skin-friction reduction on the geometric parameters of blowing jet array. Phys. Fluids 34, http://dx.doi.org/10.1063/5.0101289.

Chapter 6

Acoustic impedance of a perforated plate

6.1 Chapter overview

Extensive research gaps exist regarding how the relationship between wall-normal velocities and pressure at the wall affects the turbulent boundary layers over a perforated plate with a backing cavity. The relationship between wall-normal velocities and pressure at the wall can be represented by wall impedance, but how the wall impedance of the perforated plate modifies the turbulent boundary layer in a way that reduces friction drag has not been fully understood. To address this gap, different wall impedances generated by a perforated plate with a backing cavity were used to control turbulent boundary layers. The correlation between the wall impedance and the modification of the burst events, turbulence intensity, and turbulence energy of the turbulent boundary layers with the wall impedance also needs to be discussed. Therefore, Chapter 6 addresses this gap by investigating the impact of the wall impedance of a perforated plate on near-wall turbulence.

The absolute normalised specific acoustic impedance at the frequency of the near-wall cycles varied from 5.5 to 69.6 at a particular impedance angle of $\angle(Z_{pnc}) \approx 0.5\pi$. The particular acoustic impedance was selected to be in the range of $0.4\pi \leq \angle(Z_{pnc}) \leq 1.4\pi$

for the suppression of the near-wall cycles. The results show that when turbulence intensity in the near-wall region decreases, the normalised specific acoustic reactance increases. The results show that when turbulence intensity in the near-wall region decreases, the normalised specific acoustic reactance rises. Within the near-wall region, a maximum decrease of roughly 7.8% in sweep intensity and 7% in ejection intensity was observed at a normalised specific acoustic reactance of 69.6. These reductions are associated with an approximate 7% decrease in the near-wall region's turbulence intensity and an approximate 8% decrease in the estimated local friction drag. It is suggested that the increase in the normalised specific acoustic impedance causes the normal-wall velocities at the wall to be more sensitive to the pressure fluctuations, which makes the normal-wall velocities at the wall become more fluctuated. This can result in an increase in both the frequency and amplitude of the normal-wall velocities, which lifts the turbulence kinematic energy farther away from the wall. By weakening sweep and ejection events in the near-wall region, these wall-normal velocities also reduce the near-wall cycles. Consequently, turbulence intensity, shear stress in the vicinity of the wall, and friction drag are all reduced.

6.2 Statement of Authorship

Statement of Authorship

Title of Paper	Impacts of acoustic impedance of a perforated plate on near-wall turbulence
Publication Status	☑ Published ☐ Accepted for Publication ☐ Submitted for Publication ☐ Unpublished and Unsubmitted work written in manuscript style
Publication Details	Hoang, V., Jafari, A., Cazzolato, B., and Arjomandi, M. (2025). Impacts of acoustic impedance of a perforated plate on near-wall turbulence. *Physics of Fluids,* 37, 025102.

Principal Author

Name of Principal Author (Candidate)	Van Thuan Hoang		
Contribution to the Paper	Impacts of acoustic impedance of a perforated plate on near-wall turbulence		
Overall percentage (%)	75		
Certification:	This paper reports on original research I conducted during the period of my Higher Degree by Research candidature and is not subject to any obligations or contractual agreements with a third party that would constrain its inclusion in this thesis. I am the primary author of this paper.		
Signature		Date	04/02/2025

Co-Author Contributions

By signing the Statement of Authorship, each author certifies that:

i. the candidate's stated contribution to the publication is accurate (as detailed above);
ii. permission is granted for the candidate in include the publication in the thesis; and
iii. the sum of all co-author contributions is equal to 100% less the candidate's stated contribution.

Name of Co-Author	Azadeh Jafari		
Contribution to the Paper	Supervised the development of the research, helped in developing ideas, contributed in academic discussion and manuscript review.		
Signature		Date	19/02/2025

Name of Co-Author	Benjamin Cazzolato		
Contribution to the Paper	Supervised the development of the research, helped in developing ideas, contributed in academic discussion and manuscript review.		
Signature		Date	19/02/2025

Name of Co-Author	Maziar Arjomandi		
Contribution to the Paper	Supervised the development of the research, participated in developing ideas and concepts, helped in interpretation of results, provided critical revision o		
Signature		Date	19/02/2025

6.3 Impacts of acoustic impedance of a perforated plate on near-wall turbulence

This chapter consists of the following published journal article:

Hoang, V., Jafari, A., Cazzolato, B., and Arjomandi, M. (2024). Impacts of acoustic impedance of a perforated plate on near-wall turbulence. *Physics of Fluids*, 37, 025102. (Published)

The article is identical to its published format with the following exceptions:

- The numbering of figures, tables and equations have been altered to include the chapter number.
- The position of some figures and tables have been changed to improve legibility.

Physics of Fluids ARTICLE pubs.aip.org/aip/pof

Impacts of acoustic impedance of a perforated plate on near-wall turbulence

Cite as: Phys. Fluids **37**, 025102 (2025); doi: 10.1063/5.0249382
Submitted: 18 November 2024 · Accepted: 6 January 2025 ·
Published Online: 3 February 2025

Van Thuan Hoang (Hoàng Văn Thuần),[1,a)] Azadeh Jafari,[2] Benjamin Cazzolato,[1] and Maziar Arjomandi[1]

AFFILIATIONS

[1]School of Electrical and Mechanical Engineering, The University of Adelaide, Adelaide, South Australia 5005, Australia
[2]School of Mechanical and Mining Engineering, The University of Queensland, St Lucia, Queensland 4072, Australia

[a)]Author to whom correspondence should be addressed: vanthuan.hoang@adelaide.edu.au

ABSTRACT

In this paper, the impact of wall acoustic impedance on near-wall turbulence of boundary layers is presented. Different acoustic impedances of a perforated plate with a backing cavity are used to control near-wall turbulence. It was shown that the specific acoustic impedance of the perforated plate correlates with sweeps and ejections in the near-wall region. A reduction of up to 7.8% in sweep intensity and 7% in ejection intensity was observed at a normalized specific acoustic reactance of 69.6 and an impedance angle of approximately 0.5π, which is associated with a reduction of about 7% in the inner peak of the turbulence intensity profiles. At this impedance angle, the wall-normal velocity is in phase with the pressure at the wall leading to transpiration through the perforated plate. This transpiration decreases the near-wall cycles by interacting with sweep and ejection events and reducing their effects. Consequently, turbulence intensity, shear stress in the near-wall region, and local friction drag are all reduced.

I. INTRODUCTION

Turbulent skin friction reduction in wall-bounded flows is a significant challenge in many engineering applications. If the friction drag can be effectively reduced, the energy consumption decreases across various modes of transport, including aircraft, road vehicles, and ships, which helps reduce CO_2 emissions (Ricco *et al.*, 2021). For example, in the aviation industry, a 10% decrease in total drag can lead to a roughly 6% reduction in fuel consumption (Heinemann *et al.*, 2017).

Skin friction drag in wall-bounded flows is mostly caused by the interaction between the flow and the wall in boundary layers. The near-wall region of these boundary layers is where turbulence is primarily generated (Kim *et al.*, 1971). Shear stress and turbulent momentum transfer are significantly influenced by coherent structures, such as horseshoe vortices, streaks, and quasi-streamwise vortices (Guo *et al.*, 2010). These streamwise vortices, which include both sweep and ejection events and revolve in the direction of the flow, are essential components of coherent structures in the near-wall region. While sweeps create flow momentum in the direction of the wall, ejections lift the streamwise vortices away from it. Skin friction drag is mainly increased by the burst events produced by these ejection and sweep events (Guo *et al.*, 2010). As a result, the majority of flow control techniques reduce skin friction drag by controlling sweeps and ejections which are known as bursts to reduce near-wall cycles, turbulence generation, and Reynolds shear stresses.

Studies conducted in the last decade have demonstrated that perforated plates have the potential for skin friction drag reduction in turbulent boundary layers. Silvestri *et al.* (2017a) conducted experiments to investigate the effect of perforated plates on turbulence intensity and sweep events in turbulent boundary layers. Their findings demonstrate that a maximum reduction of 13% and 14% in sweep and turbulence intensity, respectively, is available for $d^+ \approx 60$. Gowree *et al.* (2019) found that perforated plates could reduce drag by as much as 10%. They discovered that for $d/h \leq 1$, where h is the orifice depth, the skin friction drag reduces, while for $d/h \geq 1$, it increases. The authors proposed that the mechanism of skin friction drag reduction of the perforated plate was comparable to that of riblets by adjusting the transverse velocities. Scarano *et al.* (2022, 2023) examined how various perforated configurations affected turbulent boundary layer modification and skin friction drag reduction. Their findings demonstrate a notable decrease in local skin friction drag of up to roughly 30%. Skin friction reduction and boundary layer alterations became more noticeable as the open area ratio (OAR) increased. They noted that as the orifice diameter increased, the friction drag reduced. The instantaneous upward and downward velocity components were observed in the numerical simulation of a turbulent boundary layer over a perforated plate by Bhat *et al.* (2021). They showed that the interaction of reciprocating vertical component of velocity results in lifting the quasi-streamwise vortices, which results in increasing by this blowing effect, increasing energy in the outer region, and creating a second burst intensity hump. The low-momentum fluid carried by these structures as they move upward then alters the mean velocity in a way that lessens skin friction. Kornilov (2015) proposed a similar process of skin friction decrease in turbulent boundary layers due to wall-normal blowing.

Recent studies show that adding a backing cavity can increase the performance of a perforated plate in controlling turbulent boundary layers. Silvestri *et al.* (2018b) found that the sweep intensity reduction increases with an increase in the backing cavity volume, V, before reaching a threshold of $V^+ = V(U_\tau/\nu)^3 = 5\times 10^6$. The mechanism of sweep reduction is proposed to be caused by the dissipation of sweep energy in the backing cavity and when flow passes through the orifices. According to Jafari *et al.* (2022), at large scales, a backing cavity significantly reduces the pre-multiplied spectrum of streamwise velocity fluctuations by up to 80%. The authors propose that turbulent boundary layers may be reorganized by unsteady transpiration via the orifices. They also speculate that the turbulent boundary layer flows across the orifices, which may provide acoustic excitation within the cavity, causing unsteady transpiration. As a resonator, the cavity produces flow suction and ejection through the orifices when it is substantially stimulated (Ghanadi *et al.*, 2015; Dacome *et al.*, 2024). According to Hoang *et al.* (2024), near-wall turbulent structures are significantly affected by the presence of a backing cavity. Within the near-wall region, $y^+ \le 30$, there was a reduction of up to about 9% in sweep and ejection intensity, a decrease in about 25% in ejection frequency, and a decrease in roughly 33.5% in sweep frequency. These observations suggest that the perforated plate weakens burst events in this region. The decrease in near-wall turbulence was more noticeable as the viscous-scaled cavity volume increased.

Wall acoustic impedance is used as a boundary condition in modeling the interaction between a wall-bounded flow and the wall. Fukagata *et al.* (2008) applied wall-shear-driven impedance in direction number simulations (DNS) of turbulent boundary layers over a compliant surface. Their results show that the wall-shear-driven impedance which accounts for both pressure and wall shear could generate a reduction of up to 8% in the friction drag. Józsa *et al.* (2019) used DNSs of turbulent channel flows at $Re_\tau = 180$ and 1000 to study the mechanics of compliant surfaces driven by wall shear stresses with only in-plane velocity response. They discovered that while small-scale passive spanwise wall motions result in significant drag penalties, large-scale passive streamwise wall fluctuations can reduce friction drag by at least $3.7 \pm 1\%$. Jafari *et al.* (2023) investigated the drag reduction in turbulent boundary layers over a perforated plate using a resolvent analysis with impedance boundary conditions. They discovered that the near-wall cycle and very-large-scale motion modes can be suppressed at the wall acoustic impedance which reduces the phase difference the wall-normal velocity and the pressure at the wall. Consequently, friction drag and Reynolds stress are reduced. Jafari *et al.* (2024) used a resolvent analysis with a boundary condition of a measured acoustic impedance to examine passive perforated surfaces at the frequency of the near-wall cycles. It was discovered that the range of 0.4π to 1.4π was the preferable value of the wall acoustic impedance angle for controlling near-wall turbulence. This range of the impedance angle causes the pressure and wall-normal fields at the wall in phase. Hence, this phase difference is the main determinant of the suppression or amplification of the near-wall cycles (Jafari *et al.*, 2024).

The published studies have shown the potential for a perforated plate to reduce turbulence in boundary layers by changing the acoustic wall impedance (Jafari *et al.*, 2023, 2024). However, there is a lack of experimental studies of the relationship between the acoustic impedance of the perforated plate and near-wall turbulence. This study conducted experiments to investigates the impact of the acoustic impedance of a perforated plate with a backing cavity on near-wall turbulence. The primary focus is on the correlation between wall impedance and turbulent kinematic energy and burst events in the near-wall region. The variable interval time averaging (VITA) technique was used to estimate burst parameters, including intensity, duration, and frequency. An extensive description of the experimental methods is given in Sec. II. The effects of acoustic impedance on near-wall turbulence are then shown in Sec. III, and Sec. IV contains closing thoughts.

II. EXPERIMENTAL METHODS

A. Experimental rig and measurement method

A closed-return wind tunnel was used for the experiments at the University of Adelaide. The wind tunnel maintains a low-level turbulence intensity of about 0.5% and can reach a maximum velocity of 30 ms^{-1}. Its test section is rectangular, with dimensions of 2000 mm in length and $600\times 500\,\mathrm{mm}^2$ in cross section. As illustrated in Fig. 1, a flat plate was placed into the test section. According to the advice by Nickels *et al.* (2005), the additional strain-rate effect arising from the finite width is deemed insignificant because the wind tunnel width is more than ten times greater than the boundary layer thickness. To maintain a zero-pressure gradient along the test section, the side walls were adjusted to achieve an acceleration parameter, $\wedge = (\nu/U_\infty^2)\times(dU_\infty/dx)$, on the order of 10^{-7}. This value of the acceleration parameter was also used in the earlier work by De Graaff and Eaton (2000); Schultz and Flack (2003) and Hyun Shin and Jin Song (2015). Similar to the technique suggested by Silvestri *et al.* (2018a), the inlet flow was tripped using a 3 mm rod placed 140 mm from the leading edge to guarantee fully developed boundary layer conditions.

A single miniature wire probe, the Dantec 55P15 type, with 5 μm in diameter and 1.25 mm in length, was used to measure flow velocities and turbulence. The wire length to diameter ratio of about 240 was higher than the minimum of 200 suggested by Hutchins *et al.* (2009) to avoid the error due to the insufficient ratio of wire length to

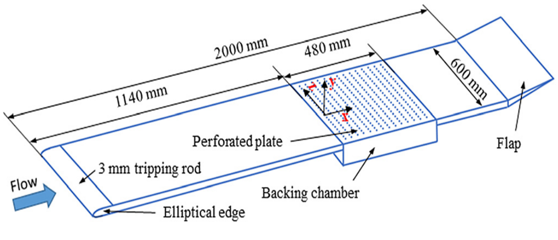

FIG. 1. Schematic diagram of the test model with the perforated plate.

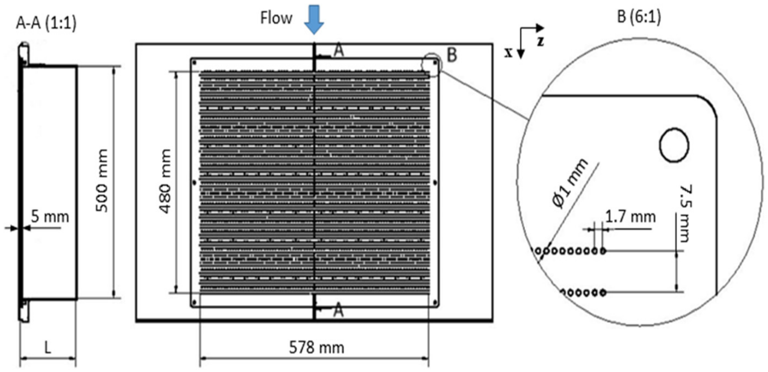

FIG. 2. Schematic of the perforated plate with a backing cavity and the main dimensions.

diameter ratio. The hot-wire probe's length, expressed in viscous units as $l^+ = lU_\tau/\nu$, where l is the probe length, was around 19. This is less than the maximum threshold of 20 proposed by Hutchins *et al.* (2009) to avoid the effects of spatial resolution. The sampling frequency, f_s, of the measurement is 40 kHz and the measurement duration is 30 s. This corresponds to a viscous-scaled sample interval, $\Delta t^+ = (1/f_s)U_\tau^2/\nu$, with a range of around 0.1. As advised by Hutchins *et al.* (2009), this non-dimensional sample interval was kept below the minimal time-frame of $t^+ = tU_\tau^2/\nu = 3$ for resolving energetic turbulent fluctuations. The measurements were low-pass filtered using a third-order Butterworth filter with a cutoff frequency of $f_c = 19$ kHz. The non-dimensional cutoff frequency, $f_c^+ = f_c\nu/(U_\tau^2)$, was around 4.8, exceeding Hutchins *et al.* (2015) proposed minimum threshold of 0.33. A pitot-static tube coupled to a 10 Torr Baratron pressure transducer was used to calibrate the hot-wire probe. Before and after every measurement, two calibrations were performed. Twenty-two freestream velocities ranging from 0 m/s to 25 m/s were measured concurrently with the pitot-static tube and the hotwire probe in each calibration. By estimating calibration coefficients using a fifth-order polynomial fit, the probe-measured voltage could be converted to velocity. The ambient temperature remained constant during the experiments because the difference between the calibration and measurement temperatures was varying by less than 1 °C. A Mitutoyo dial/mechanical-digit counter height gauge with a travel range of 0 to 300 mm and an accuracy of ±0.03 mm was used to place the probe at different wall-normal positions. A laser displacement sensor, aWenglor CP35MHT80, which has an accuracy of ±0.05 mm, was used to move the gauge sensor back to its starting position to lessen the effect of any gear backlash.

B. Perforated plate geometries and test cases

The perforated structure was placed at 1140 mm from the test section's leading edge, as shown in Fig. 1. It has 64 rows and 340 columns of circular orifices which were manufactured by the laser cutting method to ensured a good shape of the orifice edge. Similar manufacturing method of the orifice edges was used in the work by Silvestri *et al.* (2017a). The orifices have a diameter of $d = 1$ mm, a depth of $h = 5$ mm, and spacings of $\Delta x = 7.5$ mm in the streamwise directions and $\Delta z = 1.7$ mm in the spanwise directions, as shown in Fig. 2. Silvestri *et al.* (2017a) investigated the impacts of different orifice diameters on the reduction in turbulence boundary layers due to a perforated plate. They found that a large orifice diameter could create flow separation at the wall and increase turbulence intensity. In this study, the orifice diameter, expressed in viscous units, $d^+ = d \times U_\tau/\nu$, ranged from 15 to 26, which are smaller than the threshold of $d^+ = 60$ suggested by Silvestri *et al.* (2017a) to avoid separation of the flow at the wall. In the streamwise direction, the orifice spacing ranged from 113 to 192 in viscous units, $\Delta x^+ = \Delta x \times U_\tau/\nu$. In the span-wise direction, the orifice spacing ranged from 25 to 44 in viscous units, $\Delta z^+ = \Delta z \times U_\tau/\nu$. These spacings were used to control the low-speed streaks of turbulent boundary layers. In the spanwise direction, the distance between two nearby low-speed streaks varies randomly, ranging from about 80 to 120 viscous units (Smith and Metzler, 1983). Reynolds numbers have no effect on this spacing. Furthermore, these streaks can be longer than 1000 viscous units in a streamwise direction Smith and Metzler (1983).

To investigate the turbulence in the near-wall region, two free-stream velocities of $U_\infty = 5.5$ m/s and 9.7 m/s were considered. This

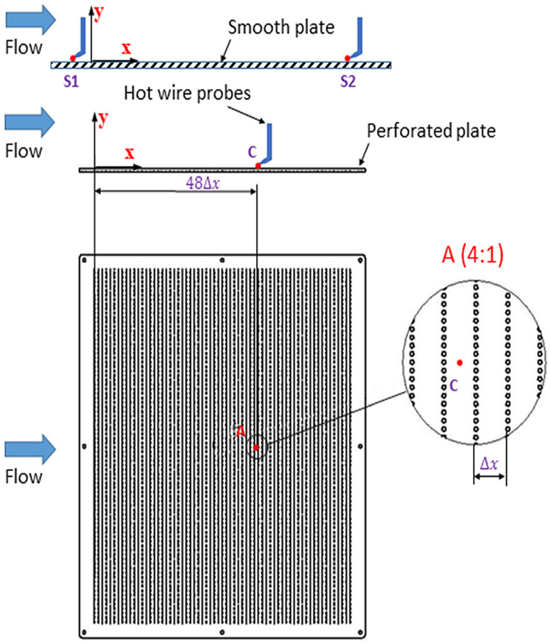

FIG. 3. Schematic of the measurement locations for the turbulent boundary layers over the smooth plate, including S1 and S2, and the ones over the perforated structures.

TABLE I. Flow parameters for the turbulent boundary layers over a smooth plate.

U_∞ (m/s)	Locations	Re_θ	Re_τ	θ (mm)	δ^* (mm)	δ_{99} (mm)	H	l^+	ν/U_τ (μm)	U_τ (m/s)	C_f (10^{-3})
5.5	S1	1154	501	3.25	4.73	31.1	1.45	20.1	62.1	0.249	4.11
5.5	S2	1499	587	4.20	6.08	37.8	1.44	19.4	64.3	0.240	3.80
9.7	S1	2267	870	3.64	5.14	33.4	1.41	32.6	38.4	0.403	3.49
9.7	S2	2802	1022	4.44	6.21	39.9	1.40	32.1	39.0	0.395	3.31

equals the Reynolds numbers of $Re_\tau = 587$ and 1022, respectively. These Reynolds numbers are smaller than the threshold of $Re_\tau \leq 4200$, reported by Marusic *et al.* (2010), at which the contribution of the near wall region to turbulence kinetic energy production is dominant. As seen in Fig. 3, the measurement points for the turbulent boundary layers over the smooth plate were S1, $x = -40$ mm, and S2, $x = 480$ mm. The Reynolds numbers varied from 1499 to 2802 according to momentum thicknesses, $Re_\theta = \theta U_\infty/\nu$, where θ is the momentum thickness, δ^* is the displacement thickness, and C_f is the friction coefficient which is estimated using the near-wall velocity gradient technique proposed by Hutchins and Choi (2002). The friction coefficient was estimated as $C_f = \frac{\tau_w}{\rho U_\infty^2/2}$, where τ_w is the wall-shear stress and ρ is the density of air. The wall-shear stress is given as $\tau_w = \mu \frac{du}{dy}$, where μ is the dynamic viscosity of air, u is the instantaneous velocities in the viscous sublayer of turbulent boundary layers, and y is the wall-normal location. The technique was simplified by assuming a non-slip condition at the wall because this formula necessitates two simultaneous measurements in the viscous sublayer of turbulent boundary layers. Consequently, $\tau_w = \mu u/y$ was used to determine the wall-shear stress. The work by Hutchins and Choi (2002) contains the specifics of this method. Through hotwire measurements in the near-wall region of $y^+ = yU_\tau/\nu = 3.5$ to 5.5, the wall-shear stresses were indirectly estimated. Table I shows the primary flow parameters of the turbulent boundary layers over a flat plate.

Figure 4(a) shows the viscous-scaled velocity profiles, $U^+ = U/U_\tau$, of the unperturbed turbulent boundary layer as a function of the viscous-scaled wall-normal locations, $y^+ = yU_\tau/\nu$ in comparison with the DNS data by Schlatter *et al.* (2010) at a comparable range of Reynolds numbers. The results show good agreement between the velocity profiles and the experimental and DNS data. The measured profiles are the same as the DNS profiles at $3.5 \leq y^+ \leq 5.5$, but a significant scatter was observed at $y^+ \leq 3$ due to the wall effect as mentioned by Hutchins and Choi (2002). Figure 4(b) compares the experimental results (Österlund *et al.*, 2000) with the friction coefficients of the turbulent boundary layers over a smooth flat plate as a function of Reynolds numbers. Within the measurement uncertainties, the computed friction coefficients for the turbulent boundary layers show good agreement with both the DNS and experimental data.

In the perforated plate cases, at each flow condition, different backing cavity depths of $L = 30$ and 50 mm were considered, which equates to the cavity volume for each orifice, $V^+ = V/(\nu/U_\tau)^3/N$, from 1.55×10^6 and 11.5×10^6, where $N = 21760$ is the number of orifices. These volumes were selected to generate the normalized specific acoustic impedance angle in a range suggested by Jafari *et al.* (2024) for drag reduction. Figure 3 shows only one streamwise measurement location at $x = 304$ mm and $x/\Delta x \approx 40$. This is because adding more streamwise measurement locations would not change the conclusion of this study. In the work by Hoang *et al.* (2024), five measurement locations in the streamwise direction of the leading edge of the perforated plate were conducted. We found that the modification of near-wall turbulence is more significant at further downstream locations of the leading edge of the perforated plate. However, a similar trend in the effect of the perforated plate on near-wall turbulence was observed at all five measurement locations. In addition, this measurement location is located at $x/\delta_0 \approx 80$, where δ_0 is the boundary layer thickens in the baseline cases, which is larger than a threshold of $\delta_0 \approx 15$ proposed by Efros and Krogstad (2011) for the internal thickness to reach the boundary layer thickness.

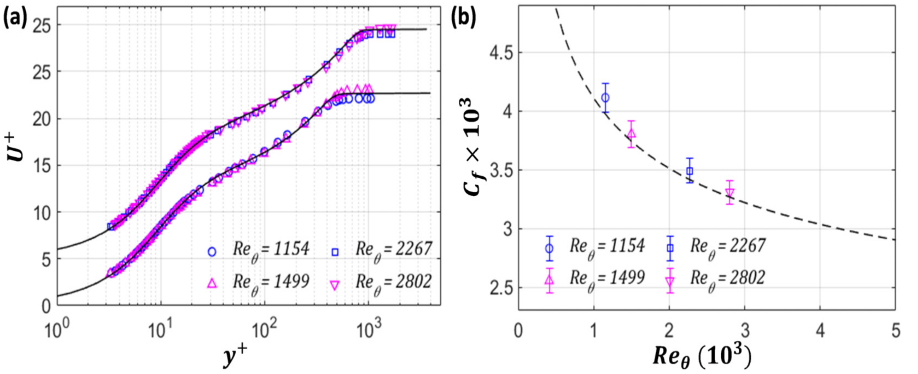

FIG. 4. Turbulent boundary layers over a smooth flat plate: (a) mean velocity profiles and (b) friction coefficients. The dashed and black solid lines are reproduced from the DNS data of Schlatter *et al.* (2010) at similar Reynolds numbers. The black dashed–dotted line is reproduced from the semi-empirical relationship, $C_f = 1/2 \times [1/0.384 \times \ln(Re_\theta) + 4.08]^{-2}$, by Österlund *et al.* (2000).

C. Acoustic impedance of the perforated plate

Jafari *et al.* (2023) and Jafari *et al.* (2024) used wall acoustic impedance as a boundary condition in resolvent analysis of turbulent boundary layers over a perforated plate. They found that the near-wall cycles and large-scale structures can be suppressed with a desired acoustic impedance. Dacome *et al.* (2024) experimentally investigates how a resonator change its acoustic impedance and dynamics of the grazing flow. They found that the resonator with a desired wall impedance can reduce more than 20% of the lower-frequency (larger scale) energy. To estimate wall acoustic impedance, the perforated plate with a backing cavity can be modeled as an array of resonators. The specific acoustic impedance of the equivalent resonator of the perforated plate can be given as (Lee and Ih, 2003): $Z_r = \Delta p/v_o$, where Δp is the difference pressure between two sides of the perforated platee and v_o is the particle velocity inside the orifice. The specific acoustic impedance of a perforated plate with a backing cavity can be given as $Z_p = Z_r/OAR$, where OAR is the open area ratio or the porosity of the perforated plate. The normalized specific acoustic impedance of the equivalent resonator is given as $Z_{rn} = Z_r/(\rho c)$, where ρ is the air density and c is the speed of sound. The normalized specific acoustic impedance of the resonator can be decomposed into the normalized specific acoustic impedance of the orifice, Z_{on}, and the contribution of the cavity, Z_{cn}, as

$$Z_{rn} = Z_{on} + Z_{cn}. \tag{1}$$

The orifice normalized specific acoustic impedance can be decomposed into the normalized specific acoustic resistance, R_{on}, and reactance, I_{on}, as $Z_{on} = R_{on} + jI_{on}$. The normalized specific acoustic resistance and reactance of a resonator with a grazing flow can be given as (Seo *et al.*, 2018),

$$\begin{cases} R_{on} = k\delta_\nu\left(2+\dfrac{h}{a}\right) + \dfrac{1}{4}(ka)^2 + R_{NL} + R_f, \\ I_{on} = k\left(h + \dfrac{16}{3\pi}\Phi_I\Phi_G\Phi_R\right) + k\delta_\nu\left(2+\dfrac{h}{a}\right), \end{cases} \tag{2}$$

where k is the wavenumber, $\delta_\nu = \sqrt{2\nu/\omega}$ being the viscous boundary layer thickness, h is the thickness of the perforated plate, $a = d/2$ is the orifice radius, $R_{NL} = u_0/c$ is the resistance contribution of the sound pressure, u_0 is the particle velocity in the orifice, R_f is the resistance contribution of the grazing flow, and Φ_I, Φ_G, Φ_R are the correlation for the neck length. The particle velocity in the orifice is given as (Ingard and Ising, 1967)

$$u_0 = \frac{c \times OAR}{1 - OAR^2}\left(\sqrt{0.25 + 2\frac{P_i(1-OAR^2)}{\rho c^2 OAR^2}} - 0.5\right), \tag{3}$$

where P_i is the incident sound pressure amplitude. The impedance contribution of the grazing flow is given as (Seo *et al.*, 2018)

$$\begin{cases} R_f = \dfrac{u_0}{2cC_{D_e}^2}, \\ C_{D_e}^2 = 3.64\left(\dfrac{u_0}{U_\infty}\right)^{0.5}\left(\dfrac{\delta_\nu}{2a}\right)^{0.1}. \end{cases} \tag{4}$$

Based on the effects of the incident sound pressure and the grazing mean flow, the correction terms for neck length were empirically determined as (Ingard, 1953; Groeneweg, 1969; Rice, 1973)

$$\Phi_I = 1 - 1.41\sqrt{OAR}, \quad \Phi_G = \frac{1 + 5\times 10^3 M_0^2}{1 + 10\times 10^3 M_0^2}, \quad \Phi_R = \frac{1}{1 + 305M^3}, \tag{5}$$

where $M_0 = u_0/c$ being the Mach number of the particle velocity and $M = U_\infty/c$ being the Mach number of the grazing flow.

The contribution of the backing cavity to the specific acoustic impedance of the resonator is not affected by the grazing flow and can be given as (Seo *et al.*, 2018)

$$Z_{cn} = -jS_o/(kV), \tag{6}$$

where $S_o = \pi d^2/4$ is the cross-sectional area of the orifice, d is the orifice diameter, and V is the volume of the cavity.

The resonant frequency of the resonator can be given as (Vér and Beranek, 2005)

$$f_0 = \frac{c}{2\pi}\sqrt{\frac{S_a}{V(h + 16a/(3\pi))}}. \tag{7}$$

Figure 5(a) shows the normalized specific acoustic resistance of the perforated plate with a backing cavity at $U_\infty = 9.7$ m/s as a function of frequency at the incident sound pressure level of $L_{P_i} = 125$ dB referenced to 20 μPa, compared with the work by Seo *et al.* (2018). The result shows a clear reduction of the current study in comparison with the published data, which could result from a different resonator configuration. For example, Seo *et al.* (2018) used a resonator with a neck diameter of 8 mm and a neck length of 10 mm while this current study used an equivalent resonator with a neck diameter of 1 mm and a neck length of 5 mm. Figure 5(b) shows the normalized specific acoustic resistance of the perforated plate with a backing cavity at $U_\infty = 9.7$ m/s as a function of the incident sound pressure level at the resonant frequency of $f_0 = 985$ Hz compared with the work by Seo *et al.* (2018). Although there is a noticeable variation at $L_{P_i} \leq 125$ dB referenced to 20 μPa, the current data show good agreement with the published data at $L_{P_i} > 125$ dB referenced to 20 μPa. The difference at low incident sound pressure levels could be due to the different resonator configurations, which results in different resonant frequencies.

Figure 6(a) shows the normalized specific acoustic resistance of the perforated plate with a backing cavity as the viscous-scale wavelength at different viscous-scaled backing volumes. The results showed that the backing cavity did not affect the normalized specific acoustic resistance of the perforated plate with a backing cavity. For example, at $R_\theta = 1499$, the normalized specific acoustic resistance at $V^+ = 1.55 \times 10^6$ is identical to those at $V^+ = 6.95 \times 10^6$. When the Reynolds number increases, the normalized specific acoustic resistance increases. For instance, When the viscous-scaled backing volume increases from $V^+ = 1.55 \times 10^6$ at $R_\theta = 1499$ to $V^+ = 6.95 \times 10^6$ at $R_\theta = 2802$ at the same dimensional backing volume, the normalized specific acoustic resistance became more pronounced. Figure 6(b) shows the effect of the backing volume on the normalized specific acoustic reactance of the perforated plate with a backing cavity as the viscous-scale wavelength. The results show that at high wavelength numbers, an increase in the viscous-scaled backing volume increases results in the normalized specific acoustic reactance becoming more pronounced. Figure 6(c) shows the absolute normalized specific acoustic impedance of the

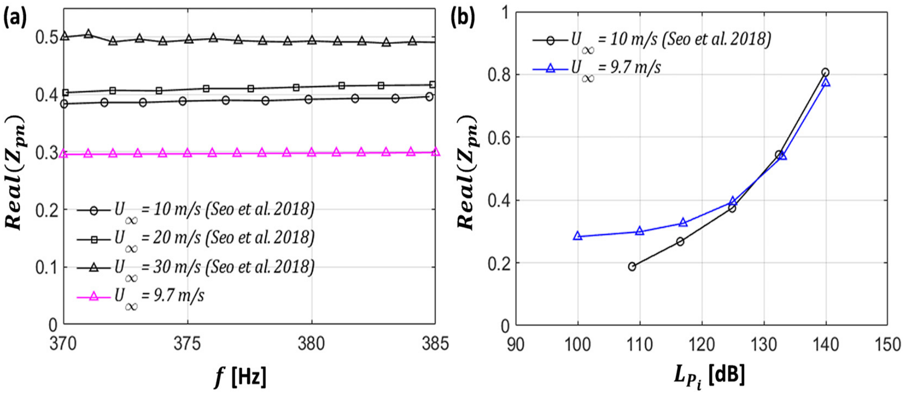

FIG. 5. Normalized specific acoustic resistance of the perforated plate with a backing cavity as a function of (a) frequencies at the incident sound pressure level of $L_{P_i} = 125$ dB and (b) the incident sound pressure level at the resonant frequency.

perforated plate with a backing cavity as the viscous-scale wavelength at different viscous-scaled backing volumes. The results show that the absolute impedance reduces as the frequency increases up to a critical frequency, f_c. At $f \geq f_c$, an opposite trend was observed. As the viscous-scaled backing volume increases, the critical frequency increases. Figure 6(d) shows the angle of the normalized specific acoustic impedance of the perforated plate with a backing cavity as the viscous-scale wavelength at different viscous-scaled backing volumes. The results show that the angle of the normalized specific acoustic impedance is constant at 0.25 and −0.25 for the frequency range of $f \leq f_0$ and $f \geq f_0$, respectively. At the vicinity of the critical frequency, the angle sharp changed from 0.25 to −0.25. This is because the change in the normalized specific acoustic reactance is much larger than the change in the normalized specific acoustic resistance as shown in Figs. 6(a) and 6(b).

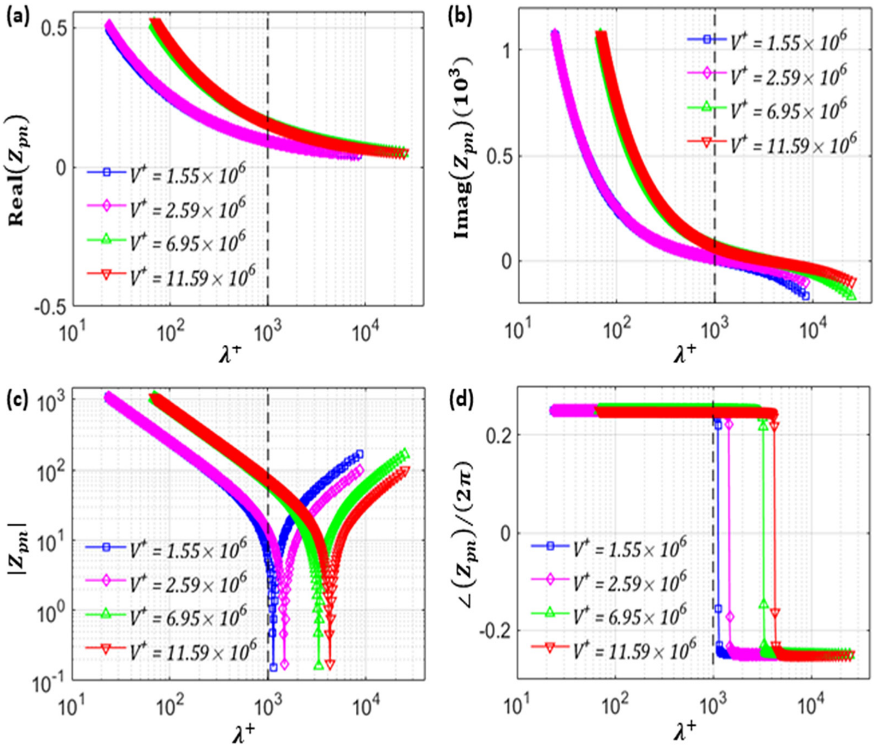

FIG. 6. (a) The resistance, (b) the reactance, (c) the absolute value, and (d) the angle of the normalized specific acoustic impedance of the perforated plate with a backing cavity, Z_{pn}, as a function of the viscous-scale wavelength, $\lambda^+ = \lambda U_{\tau 0}/\nu_0$, for the controlled cases. The dashed black lines represent the frequency of the near-wall cycles of $\lambda^+ = 1000$.

TABLE II. Impedance of the perforated plate at the near-wall frequency.

Case	Re_θ	V^+ (10^6)	Z_{pnc}	$\angle(Z_{pnc})/(2\pi)$
1	1499	1.55	$0.09 + 5.53j$	0.247
2	1499	2.59	$0.09 + 13.47j$	0.249
3	2802	6.95	$0.16 + 66.82j$	0.250
4	2802	11.58	$0.16 + 69.56j$	0.250

The near-wall cycles are the most energetic structures in the near-wall region. Therefore, the normalized specific acoustic impedance, Z_{pnc}, at the frequency of the near-wall cycles is selected to represent the normalized specific acoustic impedance of the perforated plate. This can be decomposed into the resistance, R_{pnc}, and the reactance, I_{pnc}, as $Z_{pnc} = R_{pnc} + jI_{pnc}$. Table II shows the normalized specific acoustic impedance at the frequency of the near-wall cycles of four cases. The particular acoustic impedance was selected to fall in a range of $0.4\pi \leq \angle(Z_{pnc}) \leq 1.4\pi$ suggested by Jafari *et al.* (2024) for the suppression of the near-wall cycles.

III. RESULTS AND DISCUSSION

A. Turbulent boundary layer statistics

Figure 7 shows the increases in the momentum thicknesses of the turbulent boundary layers over the perforated structure, $(\theta - \theta_0)/\theta_0$, where θ is the momentum thickness for the perforated cases and θ_0 is the momentum thickness for the undisturbed boundary layers, as a function of the normalized specific acoustic reactance. The result shows that at the same Reynolds number, when the normalized specific acoustic reactance increases, the momentum thickness increases too. For example, an increase in about 8% is observed at $I_{pnc} = 13.5$, which is larger than about 7.5% at $I_{pnc} = 5.5$ at $Re_\theta = 1499$. When Reynolds numbers increase, the effect of normalized specific acoustic reactance on momentum thickness reduces. For instance, when the Reynolds number increases from $Re_\theta = 1499$ to $Re_\theta = 2802$, the increase in the momentum thickness reduces from 8% at $I_{pnc} = 13.5$ to about 4% at $I_{pnc} = 69.6$. The increase in the momentum thickness of the turbulent boundary layers over a perforated plate was also observed in the work by Gowree *et al.* (2019), Scarano *et al.* (2023) and Hoang *et al.* (2024). One hypothesis is that the momentum thickening is increased by the wall-normal velocities produced by the interaction between the backing cavity and the turbulent boundary layer. These wall-normal velocities change the pressure fluctuations and shear at the wall which is affected by the normalized specific acoustic impedance. In the turbulent boundary layer over the perforated structure with a backing cavity, Bhat *et al.* (2021) found unsteady wall-normal velocities through the orifices at a comparable Reynolds number. These wall-normal jets would increase the momentum thickness of the turbulent boundary layer as reported in the work by Park *et al.* (2001).

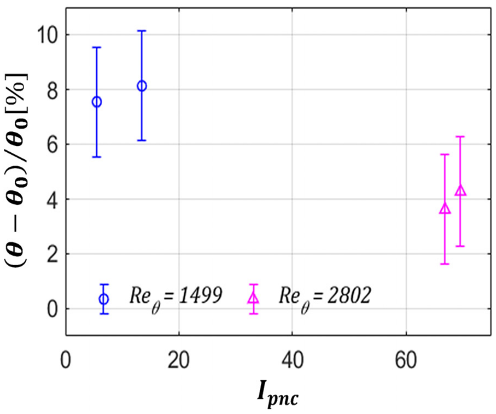

FIG. 7. Variations in momentum thicknesses, θ, of the turbulent boundary layers over the perforated plate compared to those in the baseline cases, θ_0, as a function of the normalized specific acoustic reactance, I_{pnc}.

Figure 8(a) shows the friction drag reduction as a function of the viscous-scaled backing volume. The results show that when the viscous-scaled backing volume increases, the friction reduction becomes more pronounced. This is consistent with the work by Hoang *et al.* (2024). Figure 8(b) shows the reduction in the estimated local friction drag as a function of normalized specific acoustic reactance. The results show that an increase in the normalized specific acoustic reactance causes friction reduction more significant. For example, the friction reduction increases from about 4% at $I_{pnc} = 5.5$ to about 8% at $I_{pnc} = 69.6$. As the normalized specific acoustic reactance increases from $I_{pnc} = 5.5$ to $I_{pnc} = 69.5$ at the angle of the normalized specific acoustic impedance of the perforated plate of $\angle(Z_{pnc}) \approx 0.25 \times (2\pi)$. This finding agrees with the work by Jafari *et al.* (2024) who found that the angle of normalized specific acoustic impedance of $0.2 \leq \angle(Z_{pnc})/(2\pi) \leq 0.7$ results in a reduction in shear stress. They reported that this normalized specific acoustic impedance range suppresses the near-wall cycles and consequently reduces shear stress in the turbulence boundary layers. The impedance angle of $\angle(Z_{pnc}) \approx 0.25 \times (2\pi)$ would reduce the phase difference between the wall-normal velocity and the pressure fluctuations at the wall. Fukagata *et al.* (2008); Luhar *et al.* (2015); and Toedtli *et al.* (2019) also reported that the wall acoustic impedance which cause the wall-normal velocity needs to be in phase with the wall pressure can suppress the near-all cycles and reduce friction drag.

B. Mean velocity and turbulence intensity profiles

Figure 9 shows the impact of the normalized specific acoustic impedance of the perforated plate on the viscous-scaled mean velocity profiles of the turbulent boundary layers at the two Reynolds numbers of $Re_\theta = 1499$ and 2802. In the wake region of the turbulent boundary layers over the perforated structure, the mean velocity profiles were higher than those in the baseline case. When the normalized specific acoustic impedance rises, this impact becomes more noticeable. The increases in the viscous-scaled mean velocities are due to the reduction in the skin friction drag. This finding agrees with the work by Scarano *et al.* (2023) and Hoang *et al.* (2024).

Figure 10 shows the Hama roughness function, $\Delta U^+ = U^+_{e0} - U^+_e$, where U^+_{e0} is the viscous-scaled mean velocity at the edge of the undisturbed boundary layers over a smooth plate and U^+_e is the viscous-scaled mean velocity at the edge of the boundary layers over the perforated structure, as a function of the normalized specific acoustic reactance, I_{pnc}. The findings indicate that the Hama roughness function decreases as I_{pnc} increases. For instance, when the normalized specific acoustic reactance increases from $I_{pnc} = 13.5$ to $I_{pnc} = 69.6$, the Hama roughness function reduces from −0.2 to −0.8. The findings

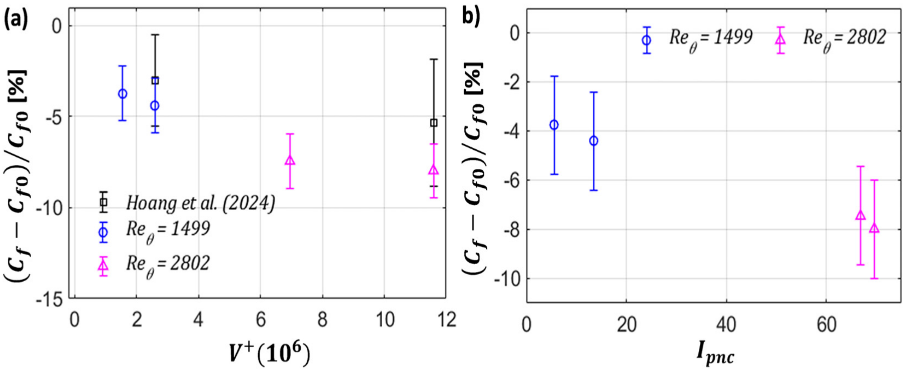

FIG. 8. Reduction in the local friction coefficients of the turbulent boundary layers due to the perforated plate with a backing cavity as a function of (a) the viscous-scaled backing volume and (b) the normalized specific acoustic reactance.

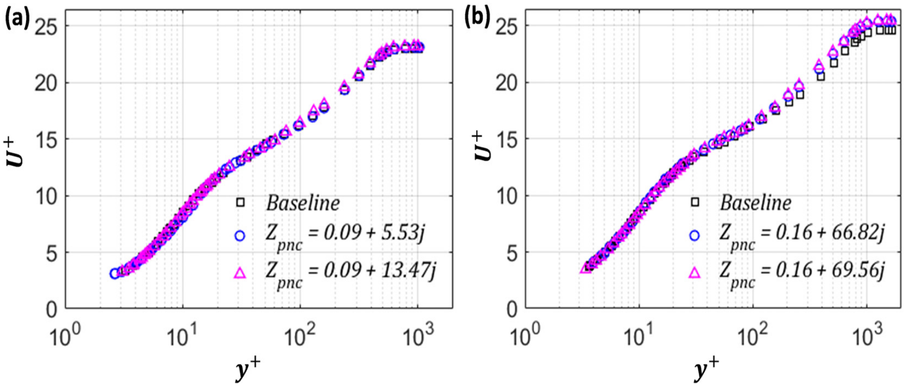

FIG. 9. Viscous-scaled velocity profiles of turbulent boundary layers with different normalized specific acoustic impedance compared with those of the baseline cases at (a) $Re_\theta = 1499$ and (b) $Re_\theta = 2802$.

indicate a reduction in the roughness function of the boundary layers with the normalized specific acoustic reactance, which is associated with a reduction in the local friction drag as shown in Fig. 8(b). The relationship between a reduction in the roughness function and the local friction drag was also reported in the work by Gómez-de Segura and García-Mayoral (2019) and Hoang *et al.* (2024).

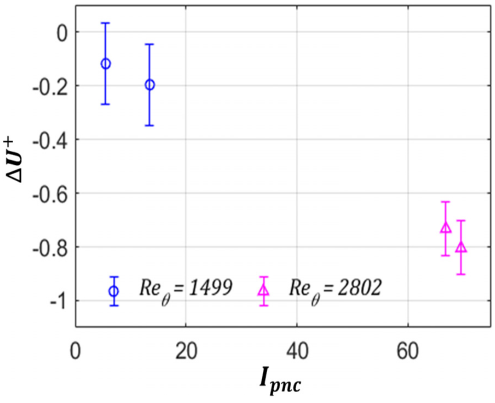

FIG. 10. Roughness functions of the turbulent boundary layers over the perforated plate as a function of the normalized specific acoustic reactance, I_{pnc}.

Figure 11 illustrates the turbulence intensity profiles of the turbulent boundary layers with different normalized specific acoustic impedances and the baseline cases at $Re_\theta = 1499$ and 2802. The result shows that the perforated plate with these normalized specific acoustic impedances reduces the inner peak but increases the outer peak in the turbulence intensity profiles. When the Reynolds number increases, the effect of the perforated plate on the turbulence intensity profile becomes more pronounced. The reduction in the inner peak of the turbulence intensity profiles could result from the suppression of the near-wall cycles due to the wall impedance, which as discussed by Luhar *et al.* (2015) and Jafari *et al.* (2023) suppresses the near-wall mode through reducing the phase difference the wall-normal velocity and the pressure at the wall.

Figure 12 shows the reduction in the inner peak of the turbulence intensity profiles of the turbulent boundary layers over the perforated plate compared to those in the baseline case as a function of the normalized specific acoustic reactance, I_{pnc}. The inner peak is considered as the averaged turbulence intensity, *TI*, in the near-wall region, $10 \le y^+ \le 20$, as shown in Fig. 11. The averaged turbulence intensity is given as

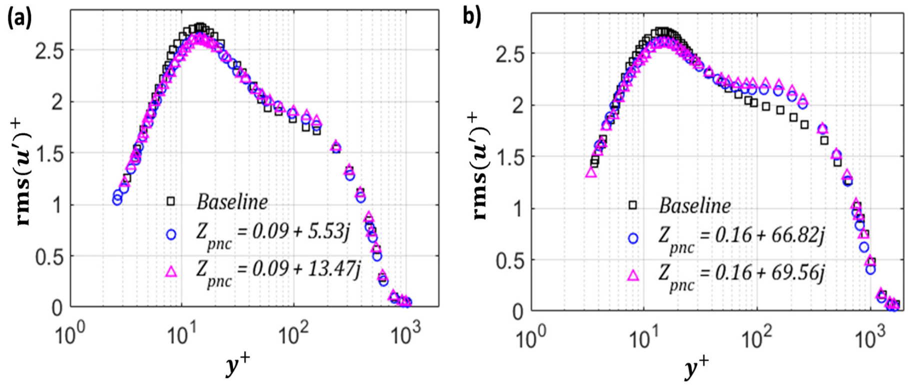

FIG. 11. Turbulence intensity profiles of the turbulent boundary layers over the perforated plate compared with those of the unperturbed turbulent boundary layer at (a) $Re_\theta = 1499$ and (b) $Re_\theta = 2802$.

$$TI = \frac{1}{(y^+_{\max} - y^+_{\min})}\int_{y^+_{\min}}^{y^+_{\max}} \mathrm{rms}(u)^+ dy^+, \tag{8}$$

where $y^+_{\min} = 10$ and $y^+_{\max} = 20$. The results show that the inner peak reduces when the normalized specific acoustic reactance increases. For example, the reduction in the inner peak increases from about 4.1% at $I_{pnc} = 5.5$ to 7% at $I_{pnc} = 69.6$. The reduction in turbulence intensity indicates that at these specific acoustic impedance angles of $\angle(Z_{pnc}) \approx 0.25 \times (2\pi)$, the wall-normal velocities interact with the pressure at the wall in a way to reduce turbulence production in turbulence boundary layers. This finding is consistent with the work by Jafari *et al.* (2024).

C. Burst events

Burst events within turbulent boundary layers, including sweeps and ejections, play a major role in generating turbulence. Kim *et al.* (1971) found that they are strongly associated with turbulence intensity in the near-wall region. Perforated plates have been found to reduce turbulence in turbulent boundary layers (Scarano *et al.*, 2022; Jafari *et al.*, 2024; Hoang *et al.*, 2024). As a result, the sweeps and ejections events are probably influenced by the perforated plate. As shown in Appendix, the variable interval time averaging (VITA) technique was used to estimate the burst characteristics. Appendix also shows the effect of varying VITA parameters on the burst estimation.

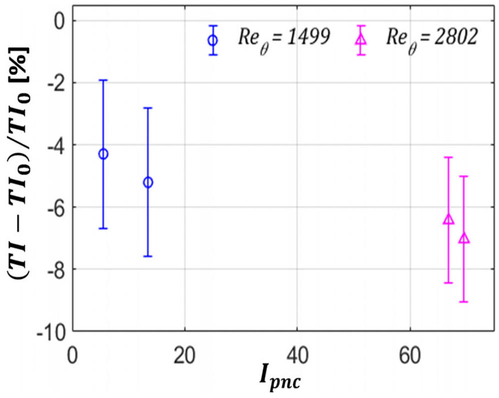

FIG. 12. Reductions in the averaged turbulence intensity, *TI*, in the near-wall region, $10 \le y^+ \le 20$, of the turbulent boundary layers over the perforated plate compared to those of the undisturbed turbulent boundary layer as a function of the normalized specific acoustic reactance, I_{pnc}.

The ejection and sweep profiles of the turbulent boundary layers over the perforated plate are displayed in Fig. 13 in comparison to the baseline case at a Reynolds number of $Re_\theta = 2802$. Figures 14(a) and 14(d) show that both the sweep and ejection intensity dropped at $y^+ \approx 15$ due to the perforated plate. Similar impacts of the perforated structure on the sweep frequency profiles are shown in Fig. 14(c). The findings show that the perforated plate weakens the sweep and ejection intensity. As a result, it suppressed the near-wall cycles in the turbulent boundary layers. These reductions agree with the reduction in the turbulence intensity as shown in Fig. 11. In contrast, the perforated plate has little effect on the sweep and ejection durations, as shown in Figs. 14(b) and 14(e).

The effect of the specific acoustic impedance of the perforated structure on the sweep and ejection events in the near-wall region of the turbulent boundary layers over the perforated plate compared to those of the undisturbed turbulent boundary layers as a function of the are shown in Fig. 14. The averaged burst intensity, $\bar{I}_b$, and averaged burst frequency, $\bar{f}_b$, in the near-wall region, $10 \le y^+ \le 20$, are given as

$$\bar{I}_b = \frac{1}{(y^+_{\max} - y^+_{\min})}\int_{y^+_{\min}}^{y^+_{\max}} I_b^+ dy^+, \tag{9}$$

where $y^+_{\min} = 10$ and $y^+_{\max} = 20$ for the inner peak.

Figure 14(a) shows the effect of the viscous-scaled orifice diameter on the reduction in the sweep intensity due to the perforated plate in comparison with the work by Silvestri *et al.* (2017a). The result shows that the decrease in sweep intensity increases from around 3.5% to 5% as the viscous-scaled orifice diameter increases from roughly 15 to 26. This finding is consistent with the work by Silvestri *et al.* (2017a). Figure 14(b) shows the reduction in sweep intensity due to the perforated structure as a function of the viscous-scaled backing volume. The findings indicate that the sweep intensity decreases as the viscous-scaled backing volume rises. This finding agrees with the work by Silvestri *et al.* (2017b, 2018b).

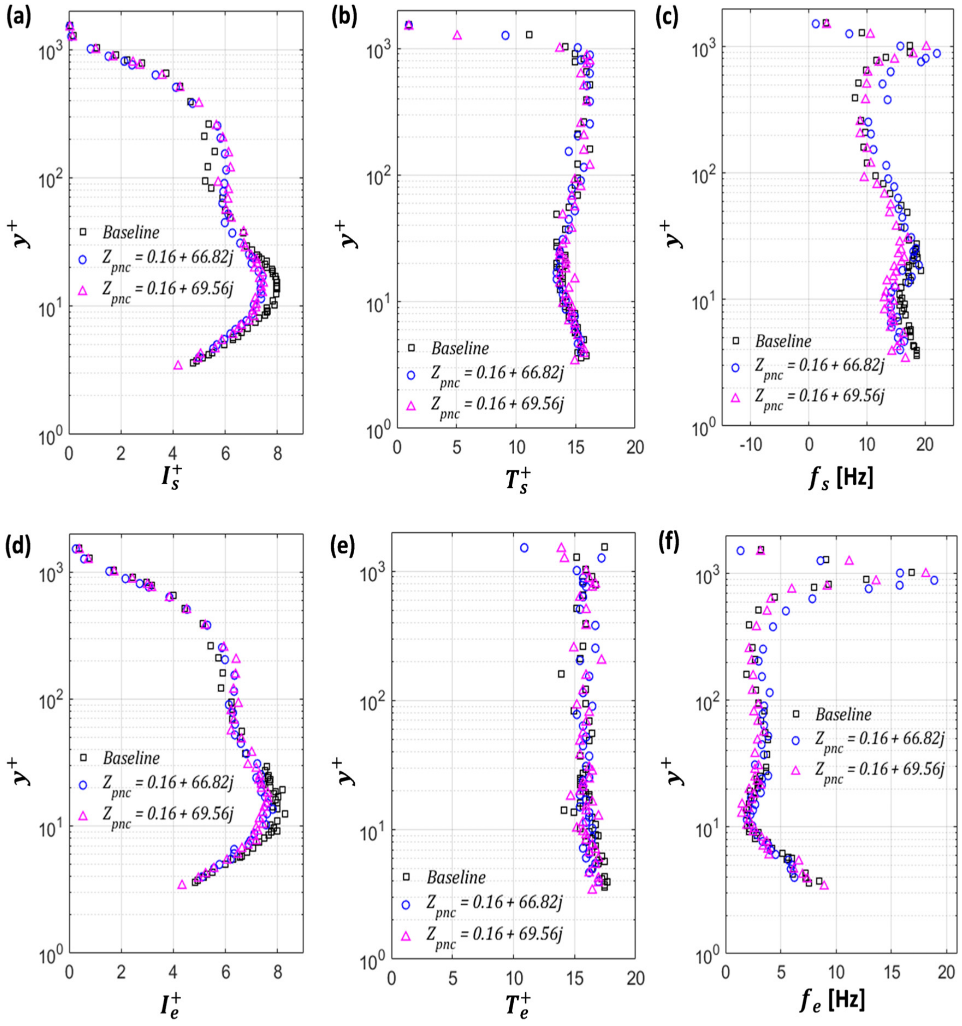

FIG. 13. [(a) and (d)] The burst intensity, [(b) and (e)] the burst durations, and [(c) and (f)] the burst frequencies as a function of the wall-normal locations for the turbulent boundary layers over the perforated plate compared with those in the baseline cases for the cases at a Reynolds number of $Re_\theta = 2802$. The top row represents the sweep events. The bottom row represents the ejection events.

Figure 15 shows the reduction in the sweep and eject intensity of the turbulent boundary layers over the perforated plate compared to those of the baseline cases as a function of the normalized specific acoustic reactance, I_{pnc}. Figure 15(a) shows that at the same Reynolds number when the normalized specific acoustic reactance increases, the reduction in the sweep events becomes more significant. For example, at $Re_\theta = 2802$ when the normalized specific acoustic reactance increases from $I_{pnc} = 13.5$ to $I_{pnc} = 69.6$, the reduction in the sweep intensity increases from 4.1% to about 7.8%. Figure 15(b) shows the reduction in the ejection events of turbulent boundary layers due to the perforated plate as a function of the normalized specific acoustic reactance, I_{pnc}. The results illustrate that when the normalized specific acoustic reactance increases, the ejection intensity reduces. For instance, the reduction in the ejection intensity increases from about 4.1% at $I_{pnc} = 5.5$ to about 6.8% at $I_{pnc} = 69.6$. These findings indicate that the perforated plate with the normalized specific acoustic reactance from $I_{pnc} = 5.5$ to $I_{pnc} = 69.6$ at the impedance angle of $\angle(Z_{pnc}) \approx 0.25 \times (2\pi)$, can weaken burst events and consequently reduces the turbulence intensity as shown in Fig. 12. Hence, it is hypothesized that at these specific acoustic impedances the wall-normal velocities at the wall interact with the pressure fluctuations at the wall in a way that suppresses the burst events and consequently reduces the near-wall cycles and near-wall turbulence.

D. Spectral content

The pre-multiplied power spectral densities (PSDs) show a similar energy reorganization with the turbulence intensity modification in the turbulent boundary layers. The PSD can be given as $(k_x\Phi_{uu})^+ = k_x\Phi_{uu}/U_{\tau0}^2$, where $k_x = \omega/U_c$ is the wavenumber in the streamwise direction; ω is the angular frequency in the frequency domain; U_c is the convection velocity which is equivalent to the local

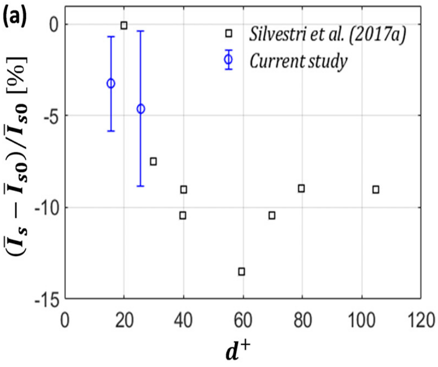

FIG. 14. Variance in the averaged sweep intensity of the turbulent boundary layers over the perforated compared to the undisturbed turbulent boundary layer in the near-wall region, $y^+ \leq 30$, as a function of (a) the viscous-scaled orifice diameter, d^+, and (b) the viscous-scaled chamber volume, V^+. The black squares are reproduced from the data of Silvestri *et al.* (2017a). The black triangles are reproduced from the data of Silvestri *et al.* (2017b). The green diamonds are reproduced from the data of Silvestri *et al.* (2018b). The blue error bars represent the variation in the backing volumes. The magenta error bars represent the variation due to experimental uncertainties.

freestream velocity, according to Taylor's theory; and Φ_{uu} is the power spectral density estimated using the Welch algorithm with a 50% overlap and a Hamming window.

Figure 16(a) shows the contours of the PSD of the streamwise velocity fluctuations for the baseline case at $Re_\theta = 2802$. The result shows an inner peak at $y^+ \approx 15$ and $\lambda^+ \approx 1000$, which is consistent with the work by Hutchins and Marusic (2007). Figures 16(b) and 16(c) show the contours of the PSD of the streamwise velocity fluctuations of the turbulent boundary layers over the perforated plate of $Z_{pnc} = 0.09 + j \times 5.5$, and $Z_{pnc} = 0.09 + j \times 13.5$. Figures 16(d) and 16(e) show the difference between the pre-multiplied PSDs of the streamwise velocity fluctuations of the turbulent boundary layers over the perforated plate, $(k_x\Phi^+_{uu})$, and those of the undisturbed boundary layer, $(k_x\Phi^+_{uu})_0$, at $Re_\theta = 2802$. The difference is given as

$$\Delta(k_x\Phi^+_{uu}) = (k_x\Phi^+_{uu}) - (k_x\Phi^+_{uu})_0. \tag{10}$$

The results show that when the normalized specific acoustic reactance increases from $I_{pnc} = 5.5$ to $I_{pnc} = 13.5$, the inner peak at $y^+ \approx 15$ and $\lambda^+ \approx 1000$ reduces. This is consistent with the reduction in the near-wall turbulence as shown in Fig. 11. In contrast, there was an increase in the turbulent kinematic energy at $y^+ \approx 150$, which is consistent with the turbulence intensity hump as shown in Fig. 11. These humps are accounted for the large-scale structures in the logarithmic region, suggesting that at these normalized specific acoustic reactance, the interaction between the wall-normal velocities and the pressure at the wall encourages the development of the large-scale structures in the logarithmic region. It is suggested that the wall-normal velocities lift the turbulent kinematic energy further from the wall. These wall-normal velocities suppress the near-wall cycles by weakening sweep and ejection events. Consequently, they reduce turbulence intensity, shear stress in the near-wall region as well as friction drag. The suppression of the near-wall region by applying a specific acoustic impedance boundary was also reported in the work by Fukagata *et al.* (2008); Luhar *et al.* (2015); and Jafari *et al.* (2023).

IV. CONCLUSIONS

This study investigates the effects of the acoustic impedance of a perforated plate with a backing cavity on near-wall turbulence at two Reynolds numbers, $Re_\theta = 1499$ and $Re_\theta = 2802$. Acoustic impedance

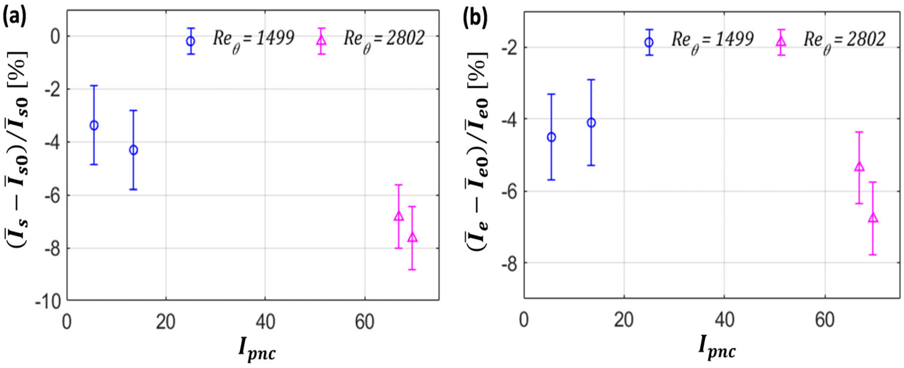

FIG. 15. Reductions in (a) the averaged sweep intensity, $\bar{I}_s$, and (b) the averaged ejection intensity, $\bar{I}_e$, of the turbulent boundary layers over the perforated plate compared to those of the undisturbed turbulent boundary layers at $10 \leq y^+ \leq 20$ as a function of the normalized specific acoustic reactance, I_{pnc}. The subscript of 0 represents the values of the undisturbed turbulent boundary layers.

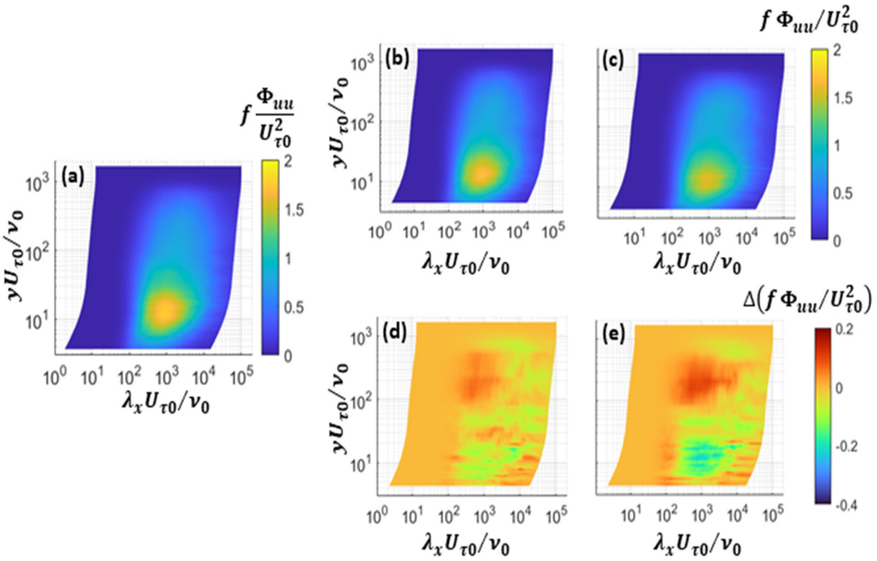

FIG. 16. Contours of the pre-multiplied PSDs, $k_x\Phi_{uu}^+$ at $Re_\theta = 1499$ for (a) the baseline case, (b) and (c) the perforated cases, and (d) and (e) the difference between the pre-multiplied PSDs of the turbulent boundary layers over the perforated plate with respect to one of the undisturbed boundary layers, $\Delta(k_x\Phi_{uu}^+)$. The columns from central to right represent the cases with $Z_{pnc} = 0.09 + j \times 5.5$ and $Z_{pnc} = 0.09 + j \times 13.5$, respectively.

was varied by the use of a perforated plate with a backing cavity, providing normalized specific acoustic reactance of $5.5 \le I_{pnc} \le 69.6$ at the angle of the acoustic impedance of $\angle(Z_{pnc}) \approx 0.25 \times (2\pi)$ at a specific frequency of the near-wall cycle, $\lambda^+ = 1000$. The turbulent boundary layers were generated in a wind tunnel and measured by hot-wire anemometry. The following summarizes the study's findings.

The perforated plate with the considered acoustic impedance can supress the sweep and ejection events in the near-wall region. When the normalized specific acoustic reactance increased, a maximum reduction of about 7.8% in sweep intensity and 7% in ejection intensity within the near-wall region of $10 \le y^+ \le 20$ was observed at $I_{pnc} \le 69.6$. As a result, the turbulence intensity in the near-wall region reduced up to 7%. This indicates that the perforated suppressed the near-wall cycles and consequently reduced the near-wall turbulence.

The acoustic impedance of the perforated plate with a backing cavity has a correlation with the local friction drag. As the normalized specific acoustic reactance increases, the reduction in the estimated local friction drag becomes more pronounced. A maximum reduction of about 8% in the estimated local friction drag was found at the normalized specific acoustic reactance of $I_{pnc} = 69.6$ and the impedance angle of $\angle(Z_{pnc}) \approx 0.25 \times (2\pi)$. The turbulent kinematic energy spectrum indicates a reduction in the near-wall region but an increase in the outer region. It is suggested that the increase in the normalized specific acoustic impedance induces wall-normal velocity fluctuation at the wall in a way that the wall-normal velocities lift the turbulence

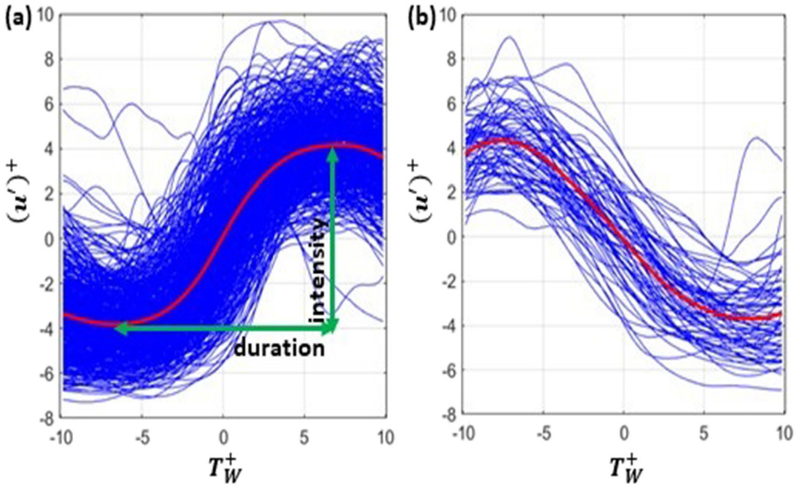

FIG. 17. Burst signatures with VITA parameters, $T_W^+ = 20$ and $k = 1.2$ for the baseline data at $y^+ = 15$. (a) the sweep events and (b) the ejection events. The red lines represent the mean signatures.

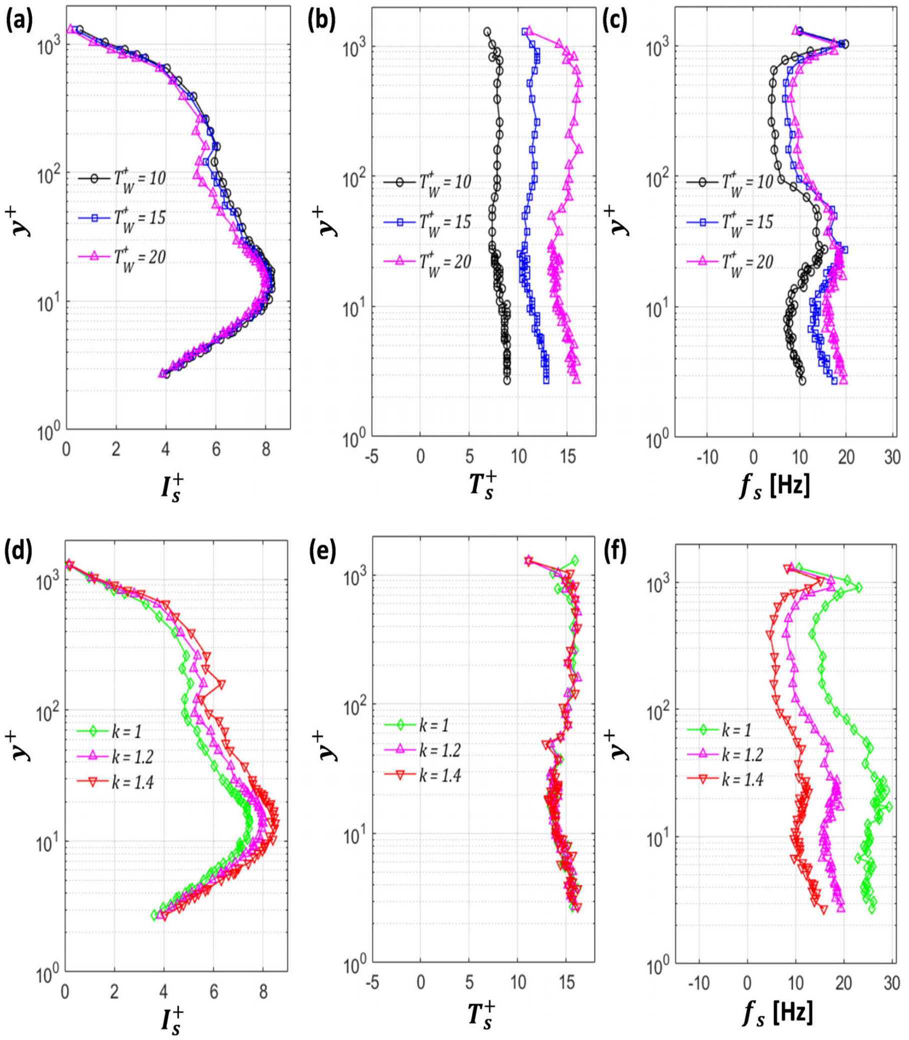

FIG. 18. Sweep profiles with different VITA parameters for the baseline data. (a), (b), and (c) represent the profiles with different T_W^+ and $k = 1.2$. (d), (e), and (f) represent the profiles with different k and $T_W^+ = 20$.

kinematic energy further from the wall. These wall-normal velocities also suppress the near-wall cycles by weakening sweep and ejection events in the near-wall region. As a result, friction drag, shear stress in the near-wall area, and turbulence intensity are all decreased.

This study investigates the effect of acoustic impedance on near-wall turbulence at low Reynolds numbers. When the Reynolds number increases, large-scaled structures become more pronounced and affect the near-wall region. Consequently, the effects of wall-normal velocity fluctuations on the flow will change. Hence, the further work is to investigate the effect of acoustic impedance on turbulence statistics at high Reynolds numbers of $Re_\theta \geq 6000$. The interaction between wall-normal velocity and the pressure at the wall plays an important role in controlling near-wall turbulence. To validate the hypotheses in this study, future research may use μ-PIV or a comprehensive DNS to estimate the wall-normal velocity and pressure fields at the wall in the turbulent boundary layers over the perforated plate, which can be used to determine the optimal acoustic impedance of a perforated plate for the control of near-wall turbulence.

ACKNOWLEDGMENTS

This research was supported by the Australian Government Research Training Program (RTP) and the Australian Government through the Australian Research Council (No. ARC DP-200101961).

AUTHOR DECLARATIONS

Conflict of Interest

The authors have no conflicts to disclose.

Author Contributions

Van-Thuan Hoang: Conceptualization (equal); Data curation (equal); Formal analysis (equal); Investigation (equal); Methodology (equal); Resources (equal); Software (equal); Validation (equal); Visualization (equal); Writing – original draft (equal); Writing – review & editing (equal). **Azadeh Jafari:** Conceptualization (equal); Formal analysis (equal); Investigation (equal); Methodology (equal); Resources (equal); Supervision (equal); Validation (equal); Visualization (equal); Writing – review & editing (equal). **Benjamin Cazzolato:** Conceptualization (equal); Formal analysis (equal); Investigation (equal); Methodology (equal); Resources (equal); Supervision (equal); Validation (equal); Visualization (equal); Writing – review & editing (equal). **Maziar Arjomandi:** Conceptualization (equal); Formal analysis (equal); Funding acquisition (equal); Investigation (equal); Methodology (equal); Project administration (equal); Resources (equal); Software (equal); Supervision (equal); Validation (equal); Visualization (equal); Writing – review & editing (equal).

DATA AVAILABILITY

The data that support the findings of this study are available from the corresponding author upon reasonable request.

APPENDIX: ESTIMATION OF BURST PROFILES

The variable interval time averaging (VITA) technique of Blackwelder and Kaplan (1976) can be used to detect burst events including sweep and ejection events. A burst is identified when the local variance, Var (t, T_W), in a window, T_W, exceeds the variance of a whole signal of velocity fluctuations, Var(t), which is controlled by a threshold, k. The local variance can be given as

$$\mathrm{Var}(t, T_W) = \widehat{u'^2}(t, T_W) - \left(\widehat{u'^2}(t, T_W)\right)^2, \tag{A1}$$

where $\widehat{Q}(t, T_W)$ is the local mean and $\widehat{Q}(t, T_W) = \frac{1}{T_W}\int_{t-\frac{1}{2}T_W}^{t+\frac{1}{2}T_W} Q dt$. The detection function, $D(t)$, of burst events can be given as (Whalley, 2011)

$$D(t) = \begin{cases} 1 \text{ if } \mathrm{Var}(t, T_W) \geq k \times \mathrm{Var}(t) \,\&\, du/dt > 0 \,(\text{sweeps}) \\ 0 \text{ if } \mathrm{Var}(t, T_W) < k \times \mathrm{Var}(t) \,(\text{noevents}) \\ -1 \text{ if } \mathrm{Var}(t, T_W) \geq k \times \mathrm{Var}(t) \,\&\, du/dt < 0 \,(\text{ejections}). \end{cases} \tag{A2}$$

Varying the VITA parameters, k and T_W^+, has no impact on the considerations in this study, as shown in the following paragraphs, so $k = 1.2$ and $T_W^+ = 20$ were selected.

The burst signatures of the velocity fluctuations for the baseline case at $y^+ = 15$ with VITA parameters, $T_W = 20$ and $k = 1.2$, are displayed in Fig. 17. The velocity signal was measured at a sample frequency of 40 kHz for 30 s. The instantaneous sweep signatures are depicted in Fig. 17(a), whereas the instantaneous ejection signatures are shown in Fig. 17(b). Only 56 events were discovered, compared to 516 sweep occurrences. This suggests that the primary cause of the bursts was sweep events. The characteristics of sweep events were considered as the characteristics of burst events. The findings of Orlandi and Jiménez (1994) and Whalley (2011) are in agreement with this one. As illustrated in Fig. 17(a), the duration of the sweeps, T_s, was computed from the time separation of the peaks of the mean signature of the events, and the intensity of the sweeps, I_s, was the magnitude difference between the highest and minimum points of the mean sweep profiles. The number of sweeps per second is known as the sweep frequency, or f_b. Similar definitions were applied to the ejection intensity, I_e, duration, T_e, and frequency, f_e.

Different VITA parameters were used to estimate the burst profile of the undisturbed boundary layers. While Blackwelder and Kaplan (1976) and Whalley (2011) detected burst events with $T_W^+ = 10$, Scarano *et al.* (2022) used the value of $T_W^+ = 15$. A VITA window of $T_W^+ = 20$ was used in the work by Scarano *et al.* (2023) and Hoang *et al.* (2024). Hence, different windows including $T_W^+ = 10$, 15, and 20 were considered. For the baseline case with three different T_W from 10 to 20 and k from 1 to 1.4, Fig. 18 displays the sweep profiles, which include the intensity, duration, and frequency profiles of the velocity fluctuations over the boundary layer. From the wall to the boundary layer edge, the outcomes are the same across the turbulent boundary layer. In contrast to k, T_W had the opposite effect on the sweep profiles. As T_W rose from 10 to 20, the sweep intensity profile decreased, while the sweep duration and frequency profiles increased across the boundary layer, as seen in Figs. 18(a)–18(c). On the other hand, the sweep intensity profile rose while the sweep frequency profile decreased when k climbed from 1 to 1.4. k had no effect on the sweep duration profile. Therefore, the VITA parameters were chosen as $T_W = 20$ and $k = 1.2$ to identify bursts for both the baseline and perforated plate cases in this work. These selections were consistent with the work by Scarano *et al.* (2023) and Hoang *et al.* (2024).

REFERENCES

Bhat, S., Silvestri, A., Cazzolato, B., and Arjomandi, M., "Mechanism of control of the near-wall turbulence using a micro-cavity array," Phys. Fluids **33**(7), 075114 (2021).

Blackwelder, R. and Kaplan, R., "On the wall structure of the turbulent boundary layer," J. Fluid Mech. **76**(1), 89–112 (1976).

Dacome, G., Siebols, R., and Baars, W., "Small-scale Helmholtz resonators with grazing turbulent boundary layer flow," J. Turbul. **25**, 461 (2024).

De Graaff, D. B. and Eaton, J. K., "Reynolds-number scaling of the flat-plate turbulent boundary layer," J. Fluid Mech. **422**, 319–346 (2000).

Efros, V. and Krogstad, P.-Å., "Development of a turbulent boundary layer after a step from smooth to rough surface," Exp. Fluids **51**, 1563–1575 (2011).

Fukagata, K., Kern, S., Chatelain, P., Koumoutsakos, P., and Kasagi, N., "Evolutionary optimization of an anisotropic compliant surface for turbulent friction drag reduction," J. Turbul. **9**, N35 (2008).

Ghanadi, F., Arjomandi, M., Cazzolato, B. S., and Zander, A. C., "Analysis of the turbulent boundary layer in the vicinity of a self-excited cylindrical Helmholtz resonator," J. Turbul. **16**(8), 705–728 (2015).

Gómez-de Segura, G. and García-Mayoral, R., "Turbulent drag reduction by anisotropic permeable substrates–analysis and direct numerical simulations," J. Fluid Mech. **875**, 124–172 (2019).

Gowree, E. R., Jagadeesh, C., and Atkin, C. J., "Skin friction drag reduction over staggered three dimensional cavities," Aerosp. Sci. Technol. **84**, 520–529 (2019).

Groeneweg, J. F., "Current understanding of Helmholtz resonator arrays as duct boundary conditions," in *Basic Aerodynamic Noise Research: A Conference Held at NASA Headquarters, Washington, DC, July 14–15* (Scientific and Technical Information Division, National Aeronautics and Space Administration, 1969), pp. 357–368.

Guo, H., Borodulin, V., Kachanov, Y., Pan, C., Wang, J., Lian, Q., and Wang, S., "Nature of sweep and ejection events in transitional and turbulent boundary layers," J. Turbul. **11**, N34 (2010).

Heinemann, P., Panagiotou, P., Vratny, P., Kaiser, S., Hornung, M., and Yakinthos, K., "Advanced tube and wing aircraft for year 2050 timeframe," AIAA Paper No. 2017-1390, 2017.

Hoang, V., Jafari, A., Cazzolato, B., and Arjomandi, M., "Modification of near-wall turbulence in turbulent boundary layers due to a perforated structure," Phys. Fluids **36**(7), 075173 (2024).

Hutchins, N. and Choi, K.-S., "Accurate measurements of local skin friction coefficient using hot-wire anemometry," Prog. Aerosp. Sci. **38**(4–5), 421–446 (2002).

Hutchins, N. and Marusic, I., "Large-scale influences in near-wall turbulence," Philos. Trans. R. Soc. London, Ser. A **365**(1852), 647–664 (2007).

Hutchins, N., Monty, J., Hultmark, M., and Smits, A., "A direct measure of the frequency response of hot-wire anemometers: Temporal resolution issues in wall-bounded turbulence," Exp. Fluids **56**(1), 1–18 (2015).

Hutchins, N., Nickels, T. B., Marusic, I., and Chong, M., "Hot-wire spatial resolution issues in wall-bounded turbulence," J. Fluid Mech. **635**, 103–136 (2009).

Hyun Shin, J. and Jin Song, S., "Pressure gradient effects on smooth and rough surface turbulent boundary layers—Part I: Favorable pressure gradient," J. Fluids Eng. **137**(1), 011203 (2015).

Ingard, U., "On the theory and design of acoustic resonators," J. Acoust. Soc. Am. **25**(6), 1037–1061 (1953).

Ingard, U. and Ising, H., "Acoustic nonlinearity of an orifice," J. Acoust. Soc. Am. **42**(1), 6–17 (1967).

Jafari, A., Cazzolato, B., and Arjomandi, M., "Finite-length porous surfaces for control of a turbulent boundary layer," Phys. Fluids **34**(045115), 1–34 (2022).

Jafari, A., McKeon, B. J., and Arjomandi, M., "Frequency-tuned surfaces for passive control of wall-bounded turbulent flow–a resolvent analysis study," J. Fluid Mech. **959**, A26 (2023).

Jafari, A., McKeon, B. J., Cazzolato, B. C., and Arjomandi, M., "A resolvent analysis of the effect of passive perforated surfaces on wall-bounded turbulence," Int. J. Heat Fluid Flow **106**, 109315 (2024).

Józsa, T., Balaras, E., Kashtalyan, M., Borthwick, A., and Viola, I. M., "Active and passive in-plane wall fluctuations in turbulent channel flows," J. Fluid Mech. **866**, 689–720 (2019).

Kim, H., Kline, S., and Reynolds, W., "The production of turbulence near a smooth wall in a turbulent boundary layer," J. Fluid Mech. **50**(1), 133–160 (1971).

Kornilov, V., "Current state and prospects of researches on the control of turbulent boundary layer by air blowing," Prog. Aerosp. Sci. **76**, 1–23 (2015).

Lee, S.-H. and Ih, J.-G., "Empirical model of the acoustic impedance of a circular orifice in grazing mean flow," J. Acoust. Soc. Am. **114**(1), 98–113 (2003).

Luhar, M., Sharma, A. S., and McKeon, B., "A framework for studying the effect of compliant surfaces on wall turbulence," J. Fluid Mech. **768**, 415–441 (2015).

Marusic, I., Mathis, R., and Hutchins, N., "High Reynolds number effects in wall turbulence," Int. J. Heat Fluid Flow **31**(3), 418–428 (2010).

Nickels, T., Marusic, I., Hafez, S., and Chong, M., "Evidence of the k^{1}_{-1} law in a high-Reynolds-number turbulent boundary layer," Phys. Rev. Lett. **95**(7), 074501 (2005).

Orlandi, P. and Jiménez, J., "On the generation of turbulent wall friction," Phys. Fluids **6**(2), 634–641 (1994).

Österlund, J. M., Johansson, A. V., Nagib, H. M., and Hites, M. H., "A note on the overlap region in turbulent boundary layers," Phys. Fluids **12**(1), 1–4 (2000).

Park, S., Lee, I., and Sung, H. J., "Effect of local forcing on a turbulent boundary layer," Exp. Fluids **31**, 384–393 (2001).

Ricco, P., Skote, M., and Leschziner, M. A., "A review of turbulent skin-friction drag reduction by near-wall transverse forcing," Prog. Aerosp. Sci. **123**, 100713 (2021).

Rice, E., "A model for the pressure excitation spectrum and acoustic impedance of sound absorbers in the presence of grazing flow," in *Aeroacoustics Conference, Seattle, WA, USA* (American Institute of Aeronautics and Astronautics, 1973), pp. 995-1004.

Scarano, F., Jacob, M. C., Gojon, R., Carbonneau, X., and Gowree, E. R., "Modification of a turbulent boundary layer by circular cavities," Phys. Fluids **34**(6), 065134 (2022).

Scarano, F., Jacob, M. C., and Gowree, E. R., "Drag reduction by means of an array of staggered circular cavities at moderate Reynolds numbers," Int. J. Heat Fluid Flow **102**, 109142 (2023).

Schlatter, P., Li, Q., Brethouwer, G., Johansson, A. V., and Henningson, D. S., "Simulations of spatially evolving turbulent boundary layers up to $Re_\theta = 4300$," Int. J. Heat Fluid Flow **31**(3), 251–261 (2010).

Schultz, M. P. and Flack, K. A., "Turbulent boundary layers over surfaces smoothed by sanding," J. Fluids Eng. **125**(5), 863–870 (2003).

Seo, S.-H., Kim, Y.-H., and Kim, K.-J., "Design of silencer using resonator arrays with high sound pressure and grazing flow," Appl. Acoust. **138**, 188–198 (2018).

Silvestri, A., Ghanadi, F., Arjomandi, M., Cazzolato, B., and Zander, A., "Attenuation of sweep events in a turbulent boundary layer using micro-cavities," Exp. Fluids **58**, 1–13 (2017a).

Silvestri, A., Ghanadi, F., Arjomandi, M., Cazzolato, B., and Zander, A., "The application of different tripping techniques to determine the characteristics of the turbulent boundary layer over a flat plate," J. Fluids Eng. **140**(1), 011204 (2018a).

Silvestri, A., Ghanadi, F., Arjomandi, M., Cazzolato, B., Zander, A., and Chin, R., "Mechanism of sweep event attenuation using micro-cavities in a turbulent boundary layer," Phys. Fluids **30**(5), 055108 (2018b).

Silvestri, A., Ghanadi, F., Arjomandi, M., Chin, R., Cazzolato, B., and Zander, A., "Attenuation of turbulence by the passive control of sweep events in a turbulent boundary layer using micro-cavities," Phys. Fluids **29**(11), 115102 (2017b).

Smith, C. and Metzler, S., "The characteristics of low-speed streaks in the near-wall region of a turbulent boundary layer," J. Fluid Mech. **129**, 27–54 (1983).

Toedtli, S. S., Luhar, M., and McKeon, B. J., "Predicting the response of turbulent channel flow to varying-phase opposition control: Resolvent analysis as a tool for flow control design," Phys. Rev. Fluids **4**(7), 073905 (2019).

Vér, I. L. and Beranek, L. L., *Noise and Vibration Control Engineering: Principles and Applications* (John Wiley & Sons, 2005).

Whalley, R. D., "Turbulent boundary-layer control with DBD plasma actuators using spanwise travelling-wave technique," Ph.D. thesis (University of Nottingham, 2011).

Chapter 7

Conclusions and future work

The potential of a perforated surface for skin friction drag in turbulent boundary layers has been investigated in this research. The findings were based on extensive experimental measurements in a wind tunnel to generate boundary layers over a perforated plate. This thesis significantly contributes to understanding the mechanisms of the reduction in the near-wall turbulence of turbulent boundary layers over a perforated plate. The results show that the perforated plate weakens the burst events in the near-wall region, consequently reducing near-wall turbulence and friction drag. In addition, the effects of the perforated plate on different turbulent scales were determined. The findings illustrate that the perforated plate increases the large-scale modulation of the small scales in the near-wall region of the turbulent boundary layer. The increase in the large-scale amplitude modulation of the samll scales in the near-wall region is associated with a reduction in friction drag. This contributes to the understanding of the mechanisms of drag reduction in turbulent boundary layers over a perforated plate with a backing cavity. Furthermore, this research analysed the effect of wall-normal velocities with a zero-mass flux through a perforated plate on the near-wall turbulence of turbulent boundary layers. The results show that wall-normal velocities reduce near-wall turbulence and lift the turbulence energy further away from the wall, which contributes to the reduction in near-wall turbulence and friction drag. Finally, the effects of acoustic impedance of the perforated plate on near-wall turbulence were estimated. The results show that when the normalised specific acoustic reactance of the perforated plate increases, the near-wall cycle suppression due to the perforated plate becomes momre significant. Also a direct correlation between the wall acoustic impedance and friction drag was observed. With the increase in the normalised specific acoustic reactance, the local skin friction was reduced. The work presented in this thesis developed an understanding of the mechanisms of friction drag reduction in turbulent boundary layers over a perforated plate with a backing cavity. The following sections summarize the main findings and achievements of this research in relation to the defined objectives and conclude with recommendations for future work.

7.1 Near-wall turbulence in the turbulence boundary layers over the perforated plate

Near-wall turbulence has a strong relationship with turbulence generation and skin friction drag in the turbulent boundary layers. Turbulence generation and shear stresses account for burst events, which are formed by ejections and sweep events in the near-wall region. Consequently, these events primarily contribute to the creation of turbulence and skin friction drag. A perforated plate with a backing cavity has been shown to reduce turbulence intensity; however, the mechanisms underlying this reduction in turbulence are not entirely understood. Therefore, an understanding of how a perforated plate with a backing cavity modifies burst events in the near-wall region is investigated in Chapter 3.

Hot-wire experiments were conducted to investigate how a perforated plate with a backing cavity affects the near-wall turbulences of turbulent boundary layers at two Reynolds numbers, $Re_\theta = 1165$ and 2294. Different inner-scaled cavity volumes from $V^+ = 2.4 \times 10^6$ to 11.5×10^6 were used to manipulate turbulent boundary layers. The results show that the near-wall turbulence of the turbulent boundary layers experienced a decrease of approximately 9% in sweep intensity, 9.3% in ejection intensity, 25% in ejection frequency, and up to 33.5% in sweep frequency within the near-wall region, $y^+ \leq 30$, indicating that the perforated structure weakened turbulent activities near the wall. Consequently, the turbulence intensity in this region decreased by nearly 9%. Moreover, a decrease in turbulent kinetic energy near the wall, coupled with an increase at $y^+ \geq 30$, implies that the perforated structure redistributes turbulent energy from the near-wall region to the outer region, probably leading to a reduction in shear stresses and skin friction drag. Furthermore, the backing cavity plays an important role in reducing near-wall turbulence. The increase in the cavity volume results in a decrease in the local skin friction drag, suggesting that the larger the backing cavity, the more kinetic energy is damped. Consequently, the sweeps are weakened and the near-wall turbulence intensity is reduced. It is suggested that the wall-normal velocities at the perforated surface exchange the turbulence kinetic energy between the inside and outside of the cavity and play an important role in reducing the near-wall turbulence of the turbulent boundary layers over the perforated structure.

7.2 Interection between small and large scales in the turbulent boundary layers over a perforated plate

Large scales in the outer region directly modify the small-scale structures in the near-wall regions and thus alter friction drag in turbulent boundary layers. Even at relatively low Reynolds numbers, a perforated plate increases the large scales in turbulent boundary layers. Comparatively less research had been done on the interaction between small and large scales in turbulent boundary layers over a perforated plate with a backing cavity. Therefore, Chapter 4 explores how friction drag is decreased by the interaction between the large scales in the outer region and the small scales in the near-wall region. This work accumulates knowledge of drag reduction mechanisms in turbulent boundary layers over a perforated plate with a backing cavity.

The effect of a perforated plate with a backing cavity on the large-scaled amplitude modulation of small-scaled structures in turbulent boundary layers at different Reynolds numbers, $Re_\theta = 1499$, 2802, and 4409 was investigated using hot-wire experiments. Turbulent boundary layers were manipulated using varying viscous-scaled cavity volumes ranging from $V^+ = 2.7 \times 10^6$ to 31.3×10^6. The results illustrate that the perforated surface reduces turbulence intensity in the near-wall region, $y^+ \leq 30$, but creates a hump in the turbulence energy in the outer region at $y^+ \approx 150$. The analysis of the shear stresses and turbulence production shows that the shear stresses were weakened throughout the boundary layers, which results in a reduction in the turbulence production due to the perforated surfaces, in the near-wall region at $y^+ \leq 30$. This reduction agrees with the redistribution of the turbulent kinetic energy on that the turbulence energy was reduced in the near-wall region but increased in the outer region. When the Reynolds number increased, these effects became more pronounced. The reduction in the turbulence energy and the shear stresses in the near-wall region is associated with a reduction in skin friction drag due to the perforated surface. In addition, the perforated surface significantly increases the turbulence energy of the large-scale structures in the outer region of the turbulent boundary layers. Consequently, the large-scale amplitude modulation of small-scale structures in the turbulent boundary layers was more pronounced in the turbulent boundary layers over the perforated surface. A clear increase in the modulation was observed at $20 \leq y^+ \leq 150$ in comparison with those in the baseline cases. In addition, the modulation was reduced at $y^+ \leq 10$. This suggests that the perforated surface lifts the large-scale motions further from the wall, which diminishes large-scale structures in the near-wall region but increases them in the logarithmics region. When the Reynolds number increased, the effects of the perforated surface on modulation became more significant. The wall-normal location at which the amplitude modulation is zero moves away from the wall in the turbulent boundary layer over the perforated surface, which results in a reduction in skin friction drag compared with those in the unperturbed turbulent boundary layer.

7.3 Wall-normal velocities through the perforated plate

In turbulent boundary layers, a perforated plate with a backing cavity produces wall-normal velocities with a zero-mass flux. However, the turbulence properties of turbulent boundary layers with wall-normal velocities through a perforated plate are not fully understood. To develop an understanding of the mechanisms of near-wall turbulence, Chapter 5 thus explored the effects of wall-normal velocities with a zero-mass flux generated by the perforated plate on near-wall turbulence.

Hot-wire experiments were conducted to examine the effects of synthetic jets on burst events in the near-wall region of turbulent boundary layers at $Re_\theta \approx 1050$ to understand the mechanism of turbulent drag reduction with synthetic jets. Different characteristics of synthetic jets including jet frequencies, $f_W^+ = 0.025$ to 0.063, and two different jet amplitudes, $A/U_\infty = 0.1$ and 0.2 were considered. The findings are outlined below. The results show that burst events in the near-wall region of the turbulent boundary layers with synthetic jets experienced a reduction up to about 15% in the burst strength and a reduction up to about 10% in the burst duration in the near-wall region, $y^+ \leq 12$, suggesting that synthetic jets lifted the turbulent kinetic energy away from the wall. This results in a reduction up to nearly 14% in the turbulence intensity in the near-wall region, which would reduce the shear stresses in the near-wall region as well as the skin-friction drag. An increase in synthetic jet frequencies or amplitudes results in the modification of the near-wall burst event being more pronounced. Furthermore, a reduction up to about 16.5% of the local friction drag was observed in the turbulent boundary layer manipulated by the synthetic jets with $f^+ = 0.063$ and $A/U_\infty = 0.2$. Since skin friction drag was not directly measured, this local drag reduction may not fully represent the total drag reduction. However, the reductions in the turbulence intensity, the burst events, and the very large-scale energy in the near-wall region provide evidence of skin-friction drag reduction in the turbulent boundary layer with synthetic jets.

7.4 Acoustic impedance of the perforated plate

In wall-bounded flows, wall acoustic impedance represents the interaction between wall-normal velocities and pressure at the wall. It has been shown that when wall-normal velocities are in phase with the pressure at the wall, the near-wall cycles are suppressed and consequently friction drag is reduced. However, there is a lack of knowledge about how the relationship between wall-normal velocities and pressure at the wall affects the turbulent boundary layers over a perforated plate with a backing cavity. Therefore, chapter 6 investigates the relationship between the acoustic impedance of a perforated plate with a backing cavity and near-wall turbulence.

Acoustic impedance was varied by the use of a perforated plate with a backing cavity, providing normalised specific acoustic reactance of $5.5 \leq I_{pnc} \leq 69.6$ at the angle of the acoustic impedance of $\angle(Z_{pnc}) \approx 0.25 \times (2\pi)$. The turbulent boundary layers were generated in a wind tunnel and measured by hot-wire anemometry. The results show that the acoustic impedance of the perforated plate with a backing cavity has a correlation with near-wall turbulence. When the normalised specific acoustic reactance increases, the turbulence intensity in the near-wall region reduces. A reduction of up to 7% in the turbulence intensity in the near-wall region was observed at $I_{pnc} \leq 69.6$. This turbulence reduction could result from the reduction in sweep and ejection intensity in the near-wall region. A maximum reduction of about 7.8% in sweep intensity and 7% in ejection intensity within the near-wall region of $10 \leq y^+ \leq 20$ was observed at $I_{pnc} \leq 69.6$. This indicates that the perforated suppressed the near-wall cycles and consequently reduced the near-wall turbulence. Furthermore, the acoustic reactance of the perforated plate with a backing cavity has a correlation with the estimated friction drag. As the normalised specific acoustic reactance increases, the reduction in the estimated local friction drag becomes more pronounced. A maximum reduction of about 8% in the estimated local friction drag was found at the normalised specific acoustic reactance of $I_{pnc} = 69.6$ and the impedance angle of $\angle(Z_{pnc}) \approx 0.25 \times (2\pi)$. The turbulent kinematic energy spectrum indicates a reduction in the near-wall region but an increase in the outer region. It is suggested that the increase in the normalised specific acoustic impedance affects the relationship between the wall-normal velocities and the pressure at the wall in a way that the wall-normal velocities lift the turbulence kinematic energy further from the wall. These wall-normal velocities also suppress the near-wall cycles by weakening sweep and ejection events in the near-wall region. As a result, friction drag, shear stress in the near-wall area, and turbulence intensity are all decreased.

7.5 Recommendations for future work

The findings of this thesis have shown demonstrated the potential of a perforated plate with a backing cavity for reducing drag in turbulent boundary layers. However, the interaction between the flow and the perforated plate with a backing cavity is complicated. Further work is needed to use this method in practical settings. Suggestions for further investigations are discussed below.

1. This research shows a reduction in burst events including ejections and sweeps by applying the VITA technique to analyse hot-wire measurement data. Hot-wire anemometry was used to quantify the flow velocities precisely but only single-point

measurements were made. To model the full volume of flow and assess the impact of the perforated plate on the burst event in the near-wall zone, flow visualisation is required. Coherent structures inside the backing cavity and above the perforated plate could be visualised with this kind of analysis. Direct numerical simulations (DNS) or micro-particle image velocimetry (μ-PIV) could be used to do this numerically or experimentally. Utilising these two methods would yield results that are needed to improve our knowledge of the flow both inside and outside the backing chamber, especially in the area around the orifices.

2. Through this research, the wall-normal velocities with a zero-mass flux generated by a perforated plate with a backing cavity present the interaction between the flow inside and outside the backing cavity. Although the effects of wall-normal velocities with a zero-mass flux on the turbulent boundary layer were reported, the characteristics of these unsteady wall-normal velocities have not been understood. This gap can be solved by DNS of the turbulent boundary layers over the perforated plate with a backing cavity, or experiments with pressure sensors to detect acoustic excitation inside and outside the backing cavity. The results of the characteristics of wall-normal velocities contribute to the understanding of the mechanisms of the reduction in near-wall turbulent and friction drag.

3. In this study, the velocity gradient technique was used to determine friction drag indirectly from the velocities obtained by a hot-wire anemometer. Even though the velocities were measured precisely, the wall-shear stresses and the skin friction values were not directly measured. Direct measures of friction drag, such as oil film interferometry and the force balance method, can be used to tackle this issue. One may consider the directly measured friction values to be a proof of concept.

4. Through this study, the effects of a perforated plate on turbulent boundary layers were investigated at low and moderate Reynolds numbers. At high Reynolds numbers, the large scales in the outer region of turbulent boundary layers increase to form the outer peak in the turbulence intensity profile. This would affect the interaction between the perforated plate and the near-wall region of the turbulent boundary layer. To address this gap, turbulent boundary layers at high Reynolds

numbers will be generated in a wind tunnel to investigate the effect of the perforated plate on the turbulence boundary layers.

5. This study shows a correlation between the acoustic impedance of the perforated plate and friction drag. Geometric parameters of the perforated plate play an important role in generating the acoustic impedance. Changing geometric parameters of the perforated plate, such as the backing volume would change the acoustic impedance. Hence, further work is to investigate the configuration of the perforated plate to generate a preferable wall impedance for friction drag reduction.

The results presented in this thesis provide a substantial body of work demonstrating the potential of a perforated plate with a backing cavity as a passive flow control device to reduce skin friction drag in turbulent boundary layers. Completing the recommended future work would significantly further advance this area of research.